SISSA
Scuola
Internazionale
Superiore di
Studi Avanzati

Physics Area - PhD course in
Astrophysics and Cosmology

Probing the Evolution of Dusty Star-Forming Galaxies at the Cosmic Noon via Strong Gravitational Lensing

Candidate:
Marika Giulietti

Supervisors:
Prof. Andrea Lapi
Dr. Marcella Massardi

Academic Year 2022-23

Declaration of Authorship

I, Marika Giulietti, declare that this thesis titled *Probing the Evolution of Dusty Star-Forming Galaxies at the Cosmic Noon via Strong Gravitational Lensing*, and the work presented in it are my own. I confirm that:

- This work was done wholly or mainly while in candidature for a research degree at SISSA.
- Where any part of this thesis has previously been submitted for a degree or any other qualification at SISSA or any other institution, this has been clearly stated.
- Where I have consulted the published work of others, this is always clearly attributed.
- Where I have quoted from the work of others, the source is always given. With the exception of such quotations, this thesis is entirely my own work.
- I have acknowledged all main sources of help.
- Where the thesis is based on work done by myself jointly with others, I have made clear exactly what was done by others and what I have contributed myself.

Abstract

Probing the Evolution of Dusty Star-Forming Galaxies at the Cosmic Noon via Strong Gravitational Lensing

by Marika Giulietti

The primary objective of this thesis is to explore the early stages of the evolution of Dusty Star-Forming Galaxies (DSFGs) by leveraging the physical phenomenon of strong gravitational lensing. This population of galaxies represents the ideal testing laboratories for galaxy evolution studies, as they constitute the bulk population at the peak of Cosmic Star Formation History and they have been identified as the progenitors of massive quiescent early-type galaxies. The magnification effect induced by a foreground lens, such as a low-redshift massive elliptical galaxy, offers a unique opportunity to investigate the intricate morphology of distant and compact galaxies such as DSFGs, overcoming the resolution and sensitivity limits imposed by the current instrumentation. Strong lensing therefore enables us to gain unprecedented insights into the processes that guided the evolution of star-forming progenitors toward becoming the massive elliptical galaxies we observe today.

To achieve this objective, this work aims to explore the *in-situ* scenario for galaxy-black hole co-evolution by testing its predictive capabilities to self-consistently interpret the outcomes obtained from observational analyses.

In my research, I employed a composite approach, combining the exploration of empirical relationships within samples of strongly lensed DSFGs with a detailed investigation into the morphological and physical characteristics of individual objects. Both methodologies benefit from the advantages offered by gravitational lensing. The former allows the study of fainter luminosity regimes, while the latter provides access to intricate structures of distant and compact objects like DSFGs.

The investigation began with a sample of sub-millimeter-selected (candidate) strongly lensed DSFGs identified within the *Herschel*-ATLAS survey. The sample was originally selected based on a straightforward flux density threshold of $S_{500\,\mu\mathrm{m}} > 100$ mJy, resulting in redshifts spanning $1 \lesssim z \lesssim 4.5$ and apparent Infrared (IR) luminosities in the range of $10^{13} \lesssim L_{\mathrm{IR}}/\mathrm{L}_\odot \lesssim 10^{14}$. These properties make this sample an ideal testing ground for investigating the evolution of DSFGs during the cosmic noon and the interplay between black holes and their host galaxies.

This work also emphasises the significance of multi-wavelength broad-band and spectroscopic observations in studying the evolution of massive star-forming progenitors of early-type galaxies, spanning from the UV/optical to the radio regime. To achieve this, I integrated data available in the literature, public surveys or telescopes, and high-quality archival and proprietary data. This included data from telescopes such as HST in the optical/NIR, the *Spitzer* and *Herschel* space observatories in the MIR-to-FIR range, interferometric ALMA (sub-)millimetric continuum and spectroscopic observations, and proprietary radio data from the ATCA telescope. My work complemented these high-quality multi-wavelength observations with modern analysis techniques, including lens modelling and source reconstruction methods, to reveal the unlensed structure of DSFGs down to sub-kpc scales, and Spectral Energy Distribution fitting to access the integrated physical properties of these objects.

In this work, I investigated the interplay between galaxy formation and nuclear activity by examining the Far-Infrared/Radio correlation (FIRRC) of a sample of (candidate) strongly lensed DSFGs with radio counterparts. Gravitational lensing allowed for the observation of such a relation over a wide range of redshifts and luminosities. Our resulting trend of the FIRRC indicates a transition from an earlier phase of dust-obscured star formation to a later, radio-loud quasar phase. Simultaneously, the strong lensing effect enabled a detailed analysis of the reconstructed source-plane morphology and sizes, the ISM content (dust and gas), and integrated properties (luminosities, masses, ages, and kinematics) of an individual strongly lensed DSFG at $z\sim3$. These results precisely pinpointed the evolutionary phase of the galaxy in accordance with the predictions yielded by the *in-situ* scenario.

In conclusion, this research contributes significantly to our understanding of DSFGs by exploiting the gravitational lensing effect to investigate their evolution, morphology, and physical properties. It also highlights the importance of empirical relationships among samples and the detailed examination of individual objects as a multi-faceted approach to deepen our comprehension of galaxy evolution during the peak of the Cosmic Star Formation History.

This Ph.D. thesis is based on the following publications and submitted papers:

1. The Far-Infrared/Radio Correlation for a Sample of Strongly Lensed Dusty Star-Forming Galaxies Detected by *Herschel*, **Giulietti M.**; Massardi, M.; Lapi, A.; Bonato, M.; Enia, A. F. M.; Negrello, M.; D'Amato, Q.; Behiri, M.; and De Zotti, G.; *Monthly Notices of the Royal Astronomical Society, Volume 511, Issue 1, pp.1408-1419, February 2022.*
2. ALMA Resolves the First Strongly Lensed Optical/Near-IR-dark Galaxy, by **Giulietti M.**; Lapi, A.; Massardi, M.; Behiri, M.; Torsello, M.; D'Amato, Q. ; Ronconi, T.; Perrotta, F.; Bressan, A.; *The Astrophysical Journal, Volume 943, Issue 2, id.151, 15 pp., February 2023.*
3. The Way of Water: ALMA Resolves H2O Emission Lines in a Strongly Lensed Dusty Star-Forming Galaxy at z~3.1, by Perrotta F., **Giulietti, M.**; Massardi, M.; Gandolfi, G.; Ronconi, T.; Zanchettin, M. V.; D'Amato, Q.; Behiri, M.; Torsello, M.; Gabrielli, F.; Boco, L.; Galluzzi, V.; and Lapi, A., *The Astrophysical Journal, Volume 952, Issue 1, id.90, 16 pp., July 2023.*
4. GalaPy, the highly optimised C++/Python spectral modelling tool for galaxies, by Ronconi, T.; Lapi, A; Torsello, M.; Bressan, A; Donevski, D; Pantoni, L; Behiri, M.; Boco, L.; Cimatti, A.; D'Amato, Q.; **Giulietti, M**; Danese, L.; Perrotta, F.; Silva, L.; Talia, M.; Massardi, M; *The Astrophysical Journal, submitted.*

Other publications, submitted and forthcoming papers:

1. Illuminating the Dark Side of Cosmic Star Formation Two Billion Years after the Big Bang, by Talia, M.; Cimatti, A.; **Giulietti, M.**; Zamorani, G.; Bethermin, M.; Faisst, A.; Le Fèvre, O.; and Smolçić, V., *The Astrophysical Journal, Volume 909, Issue 1, id.23, 11 pp., March 2021.*
2. An ALMA view of 11 Dusty Star-Forming Galaxies at the Peak of Cosmic Star Formation History, by Pantoni, L. Massardi, M.; Lapi, A.; Donevski, D.; D'Amato, Q.; **Giulietti, M.**; Pozzi, F.; Talia, M.; Vignali, C.; Cimatti, A.; Silva, L.; Bressan, A.; and Ronconi, T.; *Monthly Notices of the Royal Astronomical Society, Volume 507, Issue 3, pp.3998-4015, November 2021.*
3. A New Estimate of the Cosmic Star Formation Density from a Radio-selected Sample, and the Contribution of H-dark Galaxies at $z \geq 3$, by Enia, A. F. M.; Talia, M.; Pozzi, F.; Cimatti, A.; Delvecchio, I.; Zamorani, G.; D'Amato, Q.; Bisigello, L.; Gruppioni, C.; Rodighiero, G.; Calura, F.; Dallacasa, D.; **Giulietti, M.**; Barchiesi, L.; Behiri, M.; and Romano, M.; *The Astrophysical Journal, Volume 927, Issue 2, id.204, 16 pp., March 2022.*
4. In pursuit of giants: II. Evolution of dusty quiescent galaxies over the last six billion years from the hCOSMOS survey, by Donevski, D.; Damjanov, I.; Nanni, A.; Man, A.; **Giulietti, M.**; Romano, M.; Lapi, A.; Narayanan, D.; Davé, R.; Shivaei, I.; Sohn, J.; Junais; Pantoni, L.; and Li, Q.; *Astronomy & Astrophysics, in press.*

5. Illuminating the Dark Side of Cosmic Star Formation II. A second date with RS-NIRdark galaxies in COSMOS, by Behiri, M.; Talia, M.; Cimatti, A.; Lapi, A.; Massardi, M.; Enia, A. F. M.; Vignali, C.; Bethermin, M.; Faisst, A.; Gentile, F.; **Giulietti, M.**; Gruppioni, C.; Pozzi, F.; and Zamorani, G.; *The Astrophysical Journal, in press.*

6. Illuminating the Dark Side of Cosmic Star Formation III: Building the largest homogeneous sample of Radio-Selected Dusty Star-Forming Galaxies in COSMOS with PhoEBO, by Gentile, F.; Talia, M., Behiri, M., Zamorani, G.; Vignali, C.; Barchiesi, L.; Pozzi, F.; Bethermin, M.; Enia, A. F. M.; Faisst, A.; **Giulietti, M.**; Gruppioni, C.; Lapi, A.; Massardi, M.; Smolçić, V.; Vaccari, M.; and Cimatti, A.; *The Astrophysical Journal, submitted.*

7. SHORES: Serendipitous H-ATLAS-fields Observations of Radio Extragalactic Sources with the ATCA. I: Catalogue generation and analysis, by Massardi, M.; Galluzzi, V.; Behiri, M.; D'Amato, Q.; **Giulietti, M.**; Baccigalupi, C.; Ekers, R.; Mahony, E.; Murphy, T.; Perrotta, F.; Prandoni, I.; Ronconi, T.; Sadler, E.; Torsello, M.; Zanchettin M. V.; and Lapi, A., *in preparation*.

8. SHORES: Serendipitous H-ATLAS-fields Observations of Radio Extragalactic Sources with the ATCA. II: The Deep Field, by Behiri, M., Massardi, M.; Galluzzi, V.; D'Amato, Q.; **Giulietti, M.**; Baccigalupi, C.; Ekers, R.; Mahony, E.; Murphy, T.; Perrotta, F.; Prandoni, I.; Ronconi, T.; Sadler, E.; Torsello, M.; Zanchettin M. V.; Lapi, A., *in preparation.*

9. SHORES: Serendipitous H-ATLAS-fields Observations of Radio Extragalactic Sources with the ATCA. III: Polarization Properties, by Galluzzi, V., Massardi M., Behiri, M., D'Amato, Q.; **Giulietti, M.**; Baccigalupi, C.; Ekers, R.; Mahony, E.; Murphy, T.; Perrotta, F.; Prandoni, I.; Ronconi, T.; Sadler, E.; Torsello, M.; Zanchettin M. V.; Lapi, A., *in preparation.*

10. Observing Galaxies at the Cosmic Noon through Gravitational Lensing: Perspectives from New Generation Telescopes, by **Giulietti, M**.; Gandolfi, G.; Massardi, M.; Behiri, M.; and Lapi, A., Galaxies, Special Issue, *in preparation.*

11. Observations and Identifications of Dusty Star-Forming Galaxies across the Radio-to-Sub-mm Spectral Range, by Massardi, M.; Behiri, M.; **Giulietti, M.**; and Lapi, A., Galaxies, Special Issue, *in preparation.*

12. Resolving Stellar and Dust Sub-Kiloparsec Emission of Three Strongly Lensed Dusty Star-Forming Galaxies at z~3, by **Giulietti, M.**; Lapi, A.; Massardi, M.; Behiri, M.; Torsello, M.; Ronconi, T.; Perrotta, F.; *in preparation*.

Contents

List of Figures

List of Tables

List of Abbreviations

AGN	**A**ctive **G**alactic **N**uclei
ALMA	**A**tacama **L**arge **M**illimeter/submillimeter **A**rray
APEX	**A**tacama **P**athfinder **EX**periment
BEARS	**B**right **E**xtragalactic **A**LMA **R**edshift **S**urvey
BELLS	**B**OSS **E**mission-**L**ine **L**ens **S**urvey
BOSS	**B**aryon **O**scillation **S**pectroscopic **S**urvey
CARMA	**C**ombined **A**rray for **R**esearch in **M**illimeter-wave **A**stronomy
CASTLeS	**C**fA-**A**rizona **S**pace **T**elescope **Le**ns **S**urvey
CDM	**C**old **D**ark **M**atter
CFHTLenS	**C**anada-**F**rench **H**awaii **T**elescope **L**ensing **S**urvey
CIE	**C**ollisional **I**onisation **E**quilibrium
CIGALE	**C**ode **I**nvestigating **GA**laxy **E**mission
CLASS	**C**osmic **L**ens **A**ll **S**ky **S**urvey
COSMOS	**COSM**ic Ev**O**lution **S**urvey
DSFG	**D**usty **S**tar-**F**orming **G**alaxy
EVLA	**E**xpanded **V**ery **L**arge **A**rray
FIR	**F**ar **I**nfra**R**ed
FIRRC	**F**ar**I**nfrared/**R**adio **C**orrelation
FWHM	**F**ull **W**idth at **H**alft **M**aximum
GALEX	**G**alaxy **E**evolution **E**xplorer
GBT	**G**reen **B**ank **T**elescope
GMC	**G**iant **M**olecular **C**loud
GMRT	**G**iant **M**eterwave **R**adio **T**elescope
H-ATLAS	**H**erschel **A**strophysical **T**erahertz **L**arge **A**rea **S**urvey
HeLMS	**H**erschel **L**arge **M**ode **S**urvey
HerBS	**Her**schel **B**right **S**ources
HerMES	**H**erschel **M**ulti-tired **E**xtragalactic **S**urvey
HerS	**H**erschel **S**tripe 82 **S**urvey
HSC	**H**yper **S**upreme-**C**am
HST	**H**ubble **S**pace **T**elescope
IGM	**I**nter**G**alactic **M**edium
IRAC	**I**nfra**R**ed **A**rray **C**amera
ISM	**I**nter**S**tellar **M**edium
KiDS	**Ki**lo-**D**egree **S**urvey
LABOCA	**L**arge **A**PEX **BO**lometer **CA**mera
LOFAR	**LO**w **F**requency **AR**ray

(Continued)

LoTSS	**Lo**FAR **T**wo-metre **S**ky **S**urvey
LTE	**L**ocal **T**hermodynamic **E**quilibrium
MBB	**M**odified **B**lack **B**ody
MIGHTEE	**M**eerKAT **I**nternational **G**Hz **T**iered **E**xtragalactic **E**xploration
MIR	**M**id **I**nfra**R**ed
MUSCLES	**M**ajor **U**KIDSS-**S**DSS **C**osmic **L**ens **S**urvey
NGP	**N**orth **G**alactic**P**ole
NIR	**N**ear **I**nfra**R**ed
NOEMA	**N**orthern **E**xtended **M**illimeter **A**rray
PACS	**P**hotodetector **A**rray **C**amera and **S**pectrometer
QSO	**Q**uasi-**S**tellar **O**bject
SAMs	**S**emi-**A**nalytic **S**chemes
SCUBA	**S**ubmillimetre **C**ommon-**U**ser **B**olometer **A**rray
SDP	**S**cience **D**emonstration **P**hase
SDSS	**S**loan **D**igital **S**ky **S**urvey
SED	**S**pectral **E**nergy **D**istribution
SFH	**S**tar **F**ormation **H**istory
SFR	**S**tar **F**ormation **R**ate
SFRD	**S**tar **F**ormation **R**ate **D**ensity
SGP	**S**outh **G**alactic**P**ole
SIE	**S**ingular **I**sothermal **E**llipsoid
SKA	**S**quare **K**ilometer **A**rray
SL2S	**S**trong **L**ensing **L**egacy **S**urvey
SLACS	**S**loan **L**ens **A**CS
SMA	**S**ub**M**illimeter **A**rray
SMBH	**S**uper **M**assive **B**lack **H**ole
SMD	**S**tellar **M**ass **D**ensity
SPIRE	**S**pectral and **P**hotometric **I**maging **R**eceiver
SPT	**S**outh **P**ole **T**elescope
SQLS	**S**loan Digital Sky Survey **Q**uasar **L**ens **S**earch
UKIDSS	**UK**IRT **I**nfrared **D**eep **S**ky **S**urvey
UKIRT	**U**nited **K**ingdom **I**fra**R**ed **T**elescope
VIKING	**VI**STA **K**ilo-degree **IN**frared **G**alaxy
VISTA	**V**isible and **I**nfrared **S**urvey **T**elescope for **A**stronomy
VLA	**V**ery **L**arge **A**rray
VLT	**V**ery **L**arge **T**elescope array
WISE	**W**ide-field **I**nfrared **S**urvey **E**xplorer
ZEUS	**z** **E**arly **U**niverse **S**pectrometer

List of Physical Constants

Speed of Light	$c = 2.99792458 \times 10^{10}\,\mathrm{cm\,s^{-1}}$
Constant of Gravitation	$G = 6.67 \times 10^{8}\,\mathrm{g}^{-1}\,cm^{3}\,s^{-2}$
Solar Mass	$\mathrm{M}_{\odot} = 1.99 \times 10^{33}\,\mathrm{g}$
Solar Luminosity	$\mathrm{L}_{\odot} = 3.90 \times 10^{33}\,\mathrm{erg\,s^{-1}}$
Parsec	$\mathrm{pc}{=}\ 3.09 \times 10^{18}\,\mathrm{cm}$
Reduced Hubble Constant	$h = 0.67$
Hubble Constant	$H_0 = 100\,h\,\mathrm{km\,s^{-1}\,Mpc^{-1}}$
Mass Variance Parameter	$\sigma_8 = 0.81$ (on a scale of $8\,h^{-1}\,\mathrm{Mpc}$)
Baryon Density Parameter	$\Omega_{\mathrm{b}} = 0.05$
Total Matter Density Parameter	$\Omega_{\mathrm{M}} = 0.32$
Dark Energy Density	$\Omega_{\Lambda} = 0.63$
Proton Mass	$m_{\mathrm{P}} = 1.66 \times 10^{-24}\,\mathrm{g}$
Boltzmann Constant	$k_{\mathrm{B}} = 1.38 \times 10^{16}\,\mathrm{erg\,K^{-1}}$
Solar Metallicity	$Z_{\odot} = 0.0153$
Solar Oxygen Abundance	$12 + \log \mathrm{O}_{\odot}/\mathrm{H}_{\odot} = 8.76$

Chapter 1

Introduction

The exploration of galaxy formation and evolution stands as a dynamic topic of considerable interest and resonance in modern astrophysics. At its core, unravelling the complex story of galaxy formation and evolution involves grasping how ordinary matter transforms through gravitational interactions with dark matter over cosmic timescales.

This pursuit seeks to unveil how galaxies, emerging from the amorphous gas distribution in the Universe's primordial origins, ultimately acquire their present-day attributes. This scientific endeavour involves the complex interplay between gravity and baryonic physics and robust observations of galaxies across vast spatial and temporal scales, from the Epoch of Reionisation (EOR) to the present day. At the same time, the development of robust theoretical frameworks that simulate their formation and transformation is needed. Therefore, the interplay between observations and theoretical constructs constitutes a crucial role in shedding light on the mystery of how galaxies come into existence and evolve.

The past decades have witnessed unprecedented observational and theoretical advancements in this area. The deployment of cutting-edge ground-based and space-based telescopes across the entire electromagnetic spectrum has unveiled a previously inaccessible view of galaxies in the distant Universe. Likewise, theoretical models have taken a huge step forward, thanks to more advanced numerical simulations that depict the complex process of galaxy formation in the cosmic context.

A large number of galaxy surveys have been conducted. For example, the Sloan Digital Sky Survey (SDSS, York et al. 2000) provided a large amount of information about galaxies in the present Universe which is vital for studying how galaxies evolve. Also, multi-wavelength imaging surveys with the *Hubble* (HST), *Spitzer*, and *Herschel* space telescopes, ground-based facilities, such as the Very Large Telescope array (VLT), the Visible and Infrared Survey Telescope for Astronomy (VISTA), the Subaru telescope, and interferometers such as the Very Large Array (VLA) and the Atacama Large Millimeter/submillimeter Array (ALMA), provided a data on galaxies from the UV to radio bands. With the launch of the *James Webb* (JWST), these results have been expanded towards extremely high redshifts ($z \sim 13.2$; Robertson 2022, Curtis-Lake et al. 2023).

Spitzer and *Herschel*, revealed that dusty galaxies with star-formation rates

(SFRs) of order 100 $M_\odot$ yr^{-1} or more were abundant when the Universe was only 2-3 Gyr old (Barger et al. 1998, Daddi et al. 2005, Gruppioni et al. 2013). This discovery is also supported by galaxies' inferred ultraviolet (UV) luminosity function and its redshift evolution through ground and space-based observations. For example, studies conducted with the Galaxy Evolution Explorer (GALEX) have confirmed that star-formation activity was significantly higher in the past (Lilly et al. 1996, Le Floc'h et al. 2005, Schiminovich et al. 2005). Deep near-infrared (NIR) observations are now commonly used to select galaxies on the basis of their optical rest-frame light and to chart the evolution of the global stellar mass density (SMD) at $0 < z < 3$ (Dickinson et al. 2003). In the local Universe, various galaxy properties (colours, surface mass densities, and concentrations) have been observed by SDSS to be "bimodal" around a transitional stellar mass of 3×10^{10} $M_\odot$ (Kauffmann et al. 2003), showing a clear division between faint, blue, active galaxies and bright, red, passive systems.

The influx of new data has expanded galaxy classification according to their selection criteria and observed properties such as their colours and luminosity. However, the challenge persists in organising this information coherently due to the difficulty of observing evolving galaxy sub-groups across cosmic time and the partial interpretative nature of existing theories in astronomy.

1.1 Cosmological Framework

In standard cosmological scenarios, the formation of structures in the Universe is primarily driven by dark (non-baryonic) matter. Initially, density fluctuations in the early universe are amplified through gravitational instability caused by the presence of cold dark matter (CDM). As photons decouple from baryons, CDM perturbations attract baryons into gravitational potential wells, setting the stage for structure formation.

This process of structure formation follows a "bottom-up" growth (Peebles 1982). It begins with the virialisation of low-mass objects (halos), with larger halos forming subsequently by incorporating smaller ones through mergers. Matter outside the halo is also drawn in via accretion, with the most massive progenitor dominating the main halo's growth at any given time.

Across a spectrum ranging from ultra-faint dwarf galaxies to galaxy clusters, ordinary matter in the Universe adheres to the dynamics dictated by dark matter, until radiative, hydrodynamic, and star-formation processes become significant (White & Rees 1978a). The "dark side" of galaxy formation, where dark matter plays a central role, has been meticulously modelled using highly accurate N-body numerical simulations of increasing resolution and scope (e.g., Davis et al. 1985, Dubinski & Carlberg 1991, Springel 2005, Diemand et al. 2008, Springel et al. 2008, Tinker et al. 2008, Stadel et al. 2009, Klypin et al. 2011).

Despite the success in modelling the halo formation, the same does not hold for the complex phenomena involving the physics of baryons. These include the conversion of cold gas into stars and the mechanisms triggering the star-formation bursts, the dissipation of baryonic matter within developing CDM halos, the formation of both disk and spheroidal structures, the enrichment of chemical elements into gaseous matter spanning galactic and intergalactic scales through cosmic time, and the impact of "feedback" mechanisms – originating from the energy release of stars, supernovae (SNe), and massive black holes – in governing star formation and galactic outflows.

Various methodologies can be employed to address these intricate physical phenomena (Frenk & White 2012, Scannapieco et al. 2012, see also Somerville & Davé 2015 for a review).

Ideally, the higher level of realism is reached by the “subgrid modelling” implemented even in the more accurate cosmological hydrodynamic simulations (e.g. Katz et al. 1996, Navarro & Steinmetz 2000, Hopkins et al. 2012, Bekki 2013, Dubois et al. 2014, Hopkins et al. 2014, Vogelsberger et al. 2014, Bekki 2015, Khandai et al. 2015, Schaye et al. 2015, Dubois et al. 2016, McAlpine et al. 2016, Richardson et al. 2016, Zhukovska et al. 2016, Aoyama et al. 2017, Kaviraj et al. 2017, McKinnon et al. 2017, Pallottini et al. 2017, Aoyama et al. 2018, Hopkins et al. 2018, McKinnon et al. 2018, Springel et al. 2018, McAlpine et al. 2019, Torrey et al. 2019; for a review see Naab & Ostriker 2017 and reference therein) Nonetheless, hydrodynamic simulations are vulnerable to inaccurately defined parameters and are susceptible to multiple degenerations. These challenges can be mitigated by employing parametric prescriptions to offer reliable predictions grounded in specific observations. An additional issue involves the computational time consumption required by the in-depth exploration of the parameter space.

Another approach involves semi-analytic schemes (SAMs), which analogously to hydrodynamic simulations, treat the complex baryonic processes through a purely phenomenological approach (White & Frenk 1991, Kauffmann et al. 1993, Lacey & Cole 1993, Cole et al. 2000, Croton et al. 2006, Arrigoni et al. 2010, Benson 2012, De Lucia et al. 2014, Porter et al. 2014, Cousin et al. 2016, Hirschmann et al. 2016, De Lucia et al. 2017, Fontanot et al. 2017, Popping et al. 2017, Collacchioni et al. 2018, Lagos et al. 2018, Forbes et al. 2019; see also Somerville & Davé 2015 and related references for a review). SAMs are built upon CDM merger trees extracted from or calibrated against N-body simulations. The underlying physics governing galaxy evolution within dark halos is then described using a series of parametric expressions that are partly informed by observations.

SAMs are computationally less demanding than hydrodynamic simulations, providing clearer insights into the relative contributions of distinct physical processes. However, the use of adjustable parameters in SAMs can lead to degenerate solutions, diminishing their predictive precision. SAMs also lack the comprehensive physical realism found in hydrodynamic simulations, often excluding fluid dynamics and intricate feedback mechanisms.

Finally, analytic models can address some specific problems related to the global evolution of the baryonic content in galaxies, such as the chemical evolution in relation to supernovae feedback and gas inflow/outflow (Tinsley 1974, Pagel & Patchett 1975, Hartwick 1976, Chiosi 1980, Matteucci & Greggio 1986, Edmunds 1990, Greggio 2005, Mollá et al. 2015, Recchi & Kroupa 2015, Andrews et al. 2017, Gioannini et al. 2017, Spitoni et al. 2017, Vincenzo et al. 2017, Weinberg et al. 2017, Grisoni et al. 2018), dust and metal production and abundances in local and high redshift galaxies (Dwek 1998, Hirashita 2000, Chiappini et al. 2001, Draine 2003, Inoue 2003, Zhukovska et al. 2008, Valiante et al. 2009, Draine 2011, Dwek & Cherchneff 2011, Asano et al. 2013, Forbes et al. 2014, Feldmann 2015, Hirashita et al. 2015, Mancini et al. 2015) and their connection with gas regulation, star formation, stellar mass, and halo mass (Schmidt 1963, Talbot & Arnett 1971, Erb 2008, Bouché et al. 2010, Davé et al. 2012, Lilly et al. 2013, Dekel & Mandelker 2014, Pipino et al. 2014, Rodríguez-Puebla et al. 2016, Imara et al. 2018, Tacchella et al. 2018, Dekel et al. 2019). Analytic solutions are valuable for gaining insights into fundamental aspects of galaxy formation and evolution. However, their simplicity can also be a limitation, as they rely on approximations often involving spatial and time averaging of the astrophysical processes. These models are particularly effective for addressing specific questions and generating qualitative insights, but they may lack the accuracy and precision of more complex numerical simulations.

Nevertheless, providing a detailed description of the intricate baryonic physics governing the processes behind star formation and BH accretion requires knowledge across vast time and spatial scales. Understanding the complete sequence of events that occurred from the formation of the first stars after the cosmic dark ages to the galaxies of various forms, sizes, masses, colours, luminosities, metal content, and clustering properties that exist in the present day is, therefore, a challenging task even with the aforementioned methods, which are still inadequate to make accurate predictions.

What has become evident in the latest decades of investigations, is the necessity of gaining a collective view of the different emission properties of galaxies, racking the evolution of galaxy luminosity density across cosmic time from far-UV (FUV) to radio wavelengths.

This approach aims to address relevant questions in galaxy formation and evolution, without delving into the complex physical mechanisms behind the evolutionary stages of individual galaxy sub-populations.

These include identifying a characteristic cosmic epoch for star and heavy element formation, quantifying the fraction of luminous baryons locked in early galaxies, assessing the validity of a universal IMF, determining the role of galaxies in the Universe's reionisation at $z > 6$, explaining the origin of all metals produced throughout cosmic time, and comparing the Cosmic Star-Formation History (CSFH) with the accretion history onto massive black holes as observed through luminous quasars.

The answers to these questions are based on key attributes of stellar populations and dust-rich starburst galaxies.

Specifically, on the one hand, the light coming from short-lived massive stars is predominantly traced by the rest-frame UV-continuum emission, which can be a direct measure of the instantaneous star-formation rate density (SFRD). Also, UV emission is absorbed by the interstellar dust and re-emitted as thermal infrared radiation, rendering the FIR emission from dusty starburst galaxies a sensitive tracer of young stellar populations and SFRD. Radio emission serves as another significant indicator of star formation. Its primary component emerges from massive stars that explode as Type II supernovae, primarily radiating their energy in the radio band through synchrotron emission at the end of their life. Additionally, the radio emission contains a secondary component, originating from the free-free emission of the hot and ionised HII regions.

On the other hand, the bulk of the galaxy's stellar mass is constituted by evolved near-solar massive stars, whose light can be traced in the rest-frame NIR emission.

For all these reasons, multi-wavelength observations and modelling of emissions from galaxy components up to very high redshifts ($z \simeq 10$) are nowadays considered the most promising approach to address the open questions in galaxy populations description across cosmic time.

1.2 The Cosmic Star Formation History

It is now well-established that the peak of star-formation activity and the mass build-up occurred about 10 billion years ago (corresponding to z ~2), rising from $z = 0$ (Madau & Dickinson 2014, Oesch et al. 2018). During this phase, also called "cosmic noon", the comoving SFRD was an order of magnitude higher than what is observed in the local Universe (see Madau & Dickinson 2014 and references therein).

At higher redshifts, the situation is less clear (e.g. Casey et al. 2014, Magnelli et al. 2019). Studies based on UV-selected samples such as Lyman-break galaxies (LBGs) point towards a rapid decline of the SFRD towards higher redshift (Bouwens et al. 2015, McLeod et al. 2016, Ishigaki et al. 2018,). While long-wavelength observations seem to point toward a flatter decline at z$\gtrsim$ 3 (Gruppioni et al. 2013, Rowan-Robinson et al. 2016, Gruppioni et al. 2020, Talia et al. 2021, Enia et al. 2022).

During the cosmic noon, about half of the stellar mass observed in present-day galaxies was formed in just about 3.5 Gyr, in a redshift range $1 \lesssim z \lesssim 3$.

The trend of the SFRD is mirrored by the comoving rate of SMBH accretion (Boyle & Terlevich 1998, Franceschini et al. 1999, Heckman et al. 2004, Marconi et al. 2004, Shankar et al. 2009, Silverman et al. 2009, Aird et al. 2010, Delvecchio et al. 2014, Madau & Dickinson 2014, Aird et al. 2015, Mancuso et al. 2016b), suggesting the idea of the co-evolution of central black holes and their host galaxies (see Figure 1.1).

Several tight relations suggest a connection between these components during the early stages of galaxy formation, particularly when star formation happened at extremely high rates. For example the black hole mass and galaxy properties such as the velocity dispersion found in the local Universe, the luminosity, morphological indicators, and old stars' stellar masses (Kormendy & Richstone 1995, Ferrarese & Merritt 2000, Gebhardt et al. 2000, Tremaine et al. 2002, Marconi & Hunt 2003, Häring & Rix 2004, McLure & Dunlop 2004, Ferrarese & Ford 2005, Graham 2007, Greene & Ho 2007, Lauer et al. 2007, Gültekin et al. 2009, Kormendy & Bender 2009, Shankar et al. 2009, Vika et al. 2009, Graham et al. 2011, Beifiori et al. 2012, Kormendy & Ho 2013, McConnell & Ma 2013, Ho & Kim 2014).

During cosmic history, the change in average SFRs is reflected in the characteristics of individual SFGs. Around $z \sim 2$, these galaxies exhibited star formation

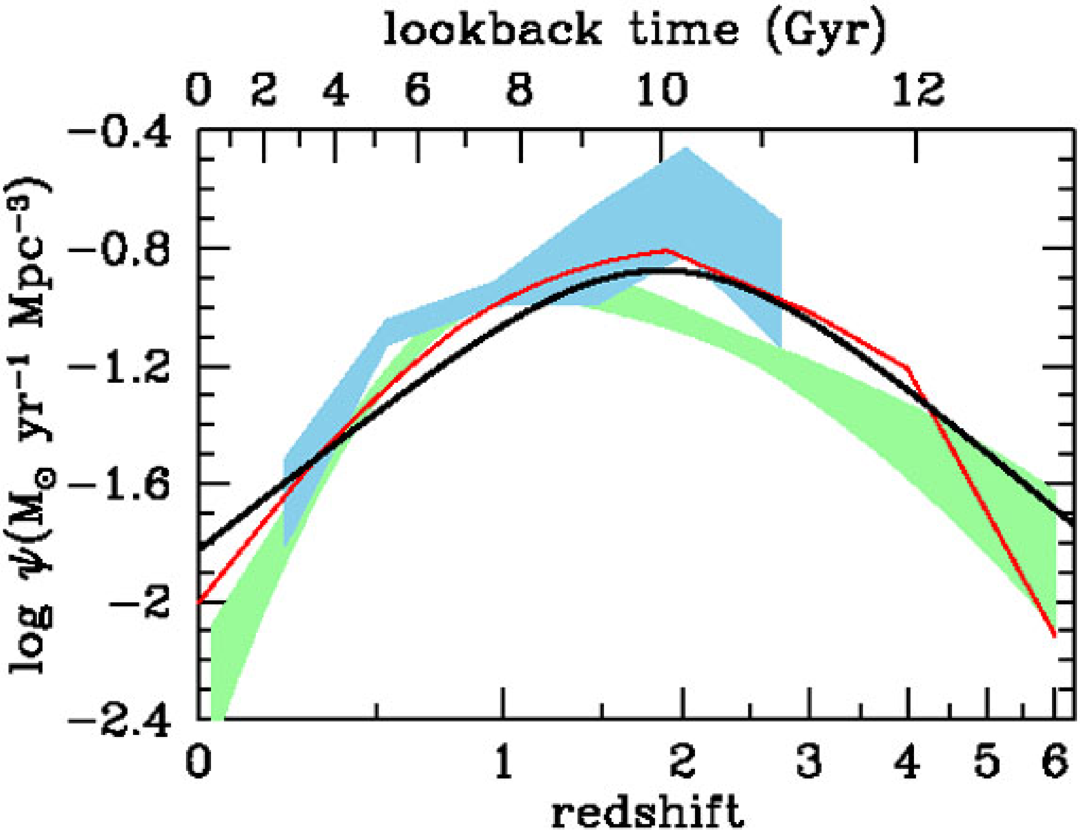

Figure 1.1: Comparison between the star formation history (black line) and the SMBH accretion history. The BH accretion rates from X-ray are represented with the red line and the green shaded area (Shankar et al. 2009, Aird et al. 2010). The light blue shaded area represents the BH accretion rates from IR measurements (Delvecchio et al. 2014). Shaded areas span the 1σ uncertainty range on the total bolometric luminosity density. Note that, for visual purposes, the comoving rates of black hole accretion have been scaled up by a factor of 3300. Image credits: Madau & Dickinson 2014.

and black hole feeding rates roughly 10 times higher than today. Most SFGs follow a linear and relatively tight *main sequence* (MS) correlation between stellar mass and SFR up (i.e., SFR$\propto M_\star^\alpha$) (Brinchmann et al. 2004, Daddi et al. 2007, Elbaz et al. 2007, Noeske et al. 2007, Rodighiero et al. 2011, Speagle et al. 2014). This relation is valid up to at least $z \sim 3$, and its normalisation slightly varies with redshift as $0.6 \lesssim \alpha \lesssim 1$, with $\alpha \propto (1-z)^{\sim 3.5}$, and flattening at $z > 3$ (Daddi et al. 2007, Rodighiero et al. 2010, Karim et al. 2011). A minority of starburst galaxies exhibiting elevated specific star formation rates (sSFRs) show a deviation from the MS. Additionally, there is a rising population of quiescent galaxies falling below this MS.

Aside from the MS, other scaling relations are observed at $z \sim 2-3$. These relations involve the evolution of size, kinematics, metal content, and gas (e.g., van der Wel et al. 2014, Übler et al. 2017, Maiolino & Mannucci 2019, Tacconi et al. 2020).

1.2.1 Dusty Star-Forming Galaxies

During the cosmic noon, SFGs exhibited intense star formation within dust-rich environments, arising from rapid gas collapse within central regions of DM halos. This phase saw vigorous star formation and supernova explosions, which enriched inner regions with dust and facilitated accelerated feeding of central black holes. These objects are heavily obscured by dust and are therefore named Dusty Star-Forming Galaxies (DSFGs, see Casey et al. 2014 for a review).

When first discovered in the local Universe by the IRAS satellite, dusty systems were thought to be rare. However, over the past two decades, various surveys and observations have provided new insights into DSFGs. The Submillimetre Common-User Bolometer Array (SCUBA) camera on the James Clerk Maxwell Telescope (JCMT), revealed that these galaxies are extremely bright in sub-millimetre (sub-mm) wavelengths (at 850 micrometre), for this reason, are labelled Sub-millimetre Galaxies (SMGs) and mostly abundant at high redshift (Smail et al. 1997, Barger et al. 1998, Hughes et al. 1998,Blain et al. 2002).

These objects are found to be $\sim$ 1000 times more abundant at high redshifts with respect to the nearby Universe, dominating the cosmic star formation at $z \sim 2$ (e.g. Gruppioni et al. 2013), even though their volume density at higher redshifts is still unconstrained. DSFGs feature extreme properties, such as incredibly high star formation rates (100-1000 $\mathrm{M}_\odot\ \mathrm{yr}^{-1}$), clumpy morphologies, and high mass content ($M_\star \gtrsim 10^{10}\,\mathrm{M}_\odot$).

The ease of the detection of these galaxies at high redshift is because their sub-mm emission exhibits a negative K-correction due to the characteristics of dust emission, which follows a Modified Black Body peaking around 100micrometre. In the Rayleigh-Jeans regime, the flux density behaves like $\nu^{2+\beta}/(4\pi D_\mathrm{L}^2)$, resulting in a roughly constant observed brightness for high-redshift galaxies ($z = 1-8$), even as their luminosity distance increases. This behaviour is due to the interplay of redshift effects, rest-frame wavelength shifts, and the dust emissivity spectral index (β), with typical values of $\beta = 1.5-2.0$ for dusty galaxies.

The peak in the number density of DSFGs mirrors the peaks in both the Cosmic

Star Formation History and Black Hole Accretion History. Moreover, the majority of DSFGs are also found to lie on and above the MS relation. These findings suggest that DSFGs have made a substantial contribution to the Universe's SFRD and overall SMD.

Observations strongly imply that DSFGs underwent a transition to become Early-Type Galaxies (ETGs) observed in the local Universe (see e.g., Peng et al. 2010, Cimatti et al. 2008, Behroozi et al. 2013, Simpson et al. 2014, Toft et al. 2014, Aversa et al. 2015, Mancuso et al. 2016a, Oteo et al. 2017, Scoville et al. 2017b). This transformation involved shifting from an active phase of star formation to a more passive state.

1.2.2 Theoretical Frameworks of Galaxy Evolution

The significance of DSFGs extends to several key aspects of cosmic evolution. They play a central role in the evolution of AGN, the formation of galactic spheroids, and the development of massive ETGs. By serving as a bridge between actively star-forming and passive galaxies, DSFGs have a pivotal role in shaping our understanding of early cosmic star formation.

Nonetheless, understanding the observed properties of these galaxies and unravelling the mechanisms governing the co-evolution of galaxies and black holes remains a topic of ongoing discussion. In pursuit of this challenge, three primary theoretical frameworks have emerged.

The first scenario affirms that the starbursting phenomenon is driven by the *merging* among dark matter halos and associated baryons; specifically, it envisages the merging of gas-rich spirals at high redshift as the main route toward building up massive ellipticals and triggering their star formation and BH activity (e.g. Bower et al. 2006, Croton et al. 2006, Hopkins et al. 2006, Benson 2010, Fanidakis et al. 2012, Somerville & Davé 2015).

The second, alternative framework assumes that star formation and BH accretion are driven by steady cold gas streams along filaments of the cosmic web (Dekel et al. 2009, Bournaud et al. 2011).

Finally, the third scenario envisages the star-formation and nuclear processes to occur *in situ* and is mainly governed by self-regulated baryonic physics, in particular by energy feedback from SNe and the central nucleus (e.g., Granato et al. 2004, Lapi et al. 2006, 2011, Aversa et al. 2015, Mancuso et al. 2016a). In this view, the merging events play a minor role in the late slow stage of the evolution of the quenched galaxy and are mainly involved in the mass increase to the values observed in the local Universe (Lapi et al. 2018).

In this thesis, I aim to explore this latter scenario as a viable sequence of processes describing the evolution of star-forming progenitors into local ETGs. The primary objective is to uncover significant observational support for its ability to predict actual occurrences.

1.3 Relevant Astrophysical Processes Involved in the In-Situ Scenario

In this Section, I will provide a summary of the sequence of physical baryonic processes that constitute the fundamental elements shaping the evolution of a massive ETG progenitor. Further details on this model (referred as the *in-situ* scenario) are provided in Lapi et al. (2018) (see Figure 1.2; see also Mancuso et al. 2016a; Mancuso et al. 2016b, 2017, Pantoni et al. 2019).

Astrophysical gas undergoes various processes for cooling and heating. Adiabatic mechanisms involve gas contraction or expansion, while gravitational-induced interactions, such as shocks, can heat the gas. Additional processes include emission, absorption, radiation scattering, and interaction with cosmic rays, all contributing to gas heating and cooling. A detailed description of the relevant processes presented here and in the course of this thesis is provided in Appendix A.

1.3.1 Biased collapse, cooling and fragmentation

At the top of the early fast evolution of a massive ETG progenitor, there is the *biased collapse* of the low angular momentum gaseous baryonic component in the inner regions of the host DM halo (e.g. Fall 2002, Romanowsky & Fall 2012, Shi et al. 2017). In this scenario, the formation of stars is predicted to primarily occur within the inner regions of the halo, whereas the outer regions are expected to predominantly contain gas and produce only a limited number of stars.

For the scaling relations presented in this Section, the star-formation efficiency $f_\star$ is normalised to ≈ 0.2 and the infall fraction is normalised $f_{\rm inf}$ to ≈ 0.6, using these values as references for a mass of $M_\star \approx 10^{11}\,{\rm M}_\odot$, and $z \approx 2$ is chosen as the fiducial redshift of the ETG progenitor formation. $f_{\rm inf}$ represents the fraction of baryons initially present in the DM halo and experimenting *infall*. The halo-radius is defined as

$$R_{\rm H} \sim 160 f_{\rm inf,0.2}^{1/3} M_{\star,11}^{1/3} [E_z/E_{z=0}]^{-1.3}\,{\rm kpc}, \tag{1.1}$$

where $E_z = \Omega_\Lambda + \Omega_{\rm M}(1-z)^3$ is a redshift-dependent term. The gas is subjected to cooling, fragmentation and infall within the infall-radius

$$R_{\rm inf} \sim f_{\rm inf} R_{\rm H} \sim 96 f_{\rm inf,0.6} f_{\star,0.2}^{-1/3} M_{\star,11}^{1/3}. \tag{1.2}$$

The value of $R_{\rm inf}$ aligns with the scale at which both observations (Hodge et al. 2013, Karim et al. 2013, Simpson et al. 2015, Hill et al. 2018) and high-resolution simulations (Narayanan et al. 2015) suggest gas inflow occurs towards the central regions of galaxy halos. The corresponding infall time scale is

$$t_{\rm dyn}(R_{\rm H} \simeq \frac{\pi}{2}\sqrt{\frac{R_{\rm H}^3}{G M_{\rm H}}} \approx 8.5\times 10^8 [E_z/E_{z=2}]^{-1/2}\,{\rm yr}. \tag{1.3}$$

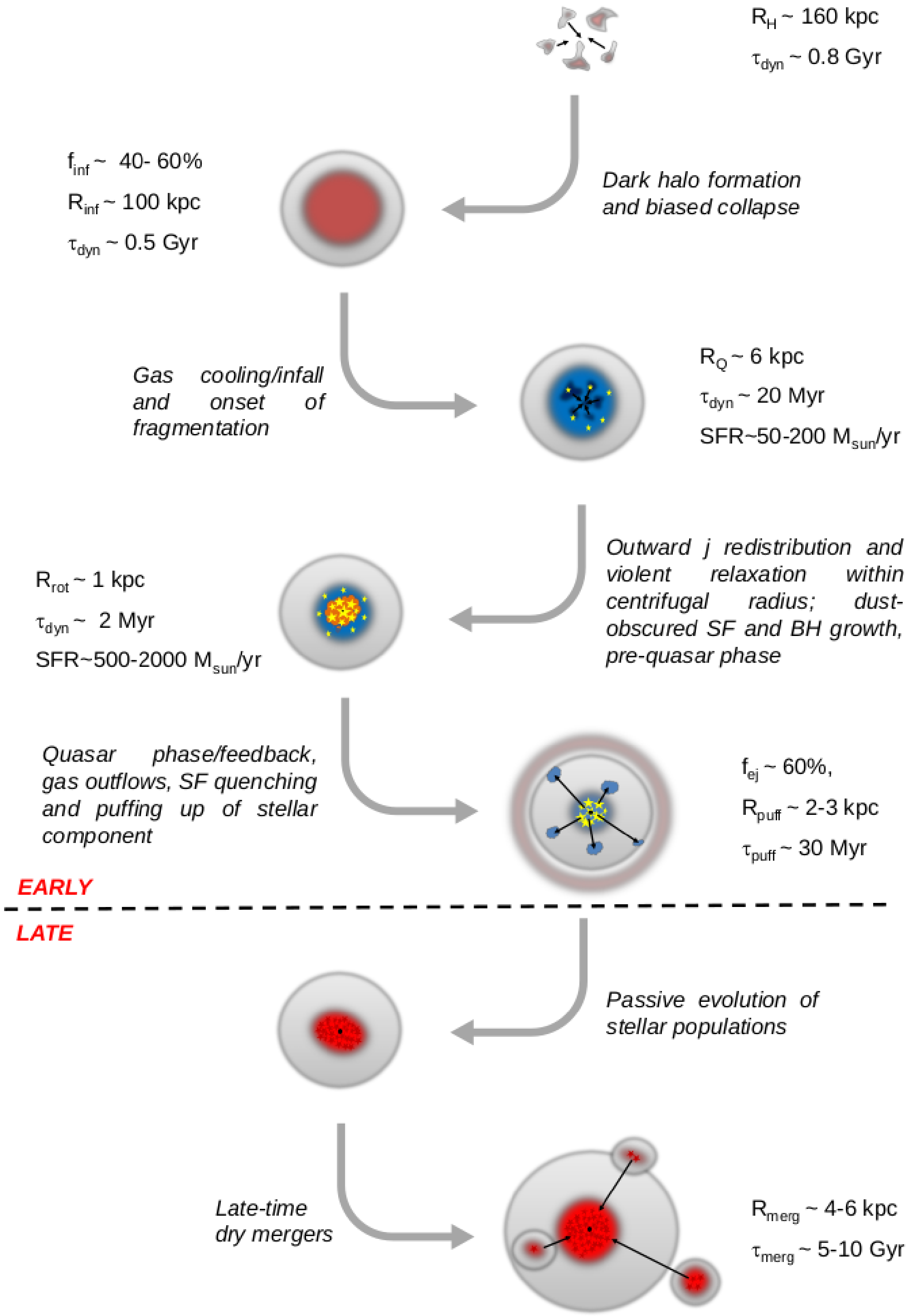

Figure 1.2: Schematic view of the size and timescale evolution of a massive ($M_\star \sim 10^{11}\,\mathrm{M}_\odot$) ETG progenitor. The early-fast ($\sim 10^8$ yr) and late-slow (several Gyr) evolution are separated by the dashed line. Image credits: Lapi et al. (2018).

The gas is then subjected to cooling and fragmentation processes. The radiative cooling time reads as

$$t_{\mathrm{cool}} \simeq \frac{2.5 \times 10^8}{\Lambda_{-23}(T,Z)} \frac{T_6}{n_{-3} C_{10}} \mathrm{yr} \sim 4 \times 10^8 (r/R_{\mathrm{inf}})^{-2}\,\mathrm{yr} \tag{1.4}$$

with $T_6 \equiv T/10^6\,\mathrm{K}$ being the temperature, $n_{-3} \equiv n/10^{-3}\,\mathrm{cm}^{-3}$ the gas density, $C_{\infty}, \equiv C/10$ the clumping factor, and $\Lambda_{-23} \equiv \Lambda(T,Z)/10^{-23}\,\mathrm{cm}^3\mathrm{s}^{-1}\mathrm{K}$ the cooling function. The latter expression is derived for typical values of ETG progenitors and within $r \lesssim R_{\mathrm{inf}}$. The cooling time is therefore comparable to or shorter than the dynamical time, enabling the gas to cool efficiently and infall over $t_{\mathrm{dyn}}(R_{\mathrm{inf}})$. In summary, the scenario predicts the infall to set in a time scale $t_{\mathrm{dyn}}(R_{\mathrm{inf}})$ of $\approx 10^8$ yr and drives the subsequent evolution of the ETG progenitor within the infall radius $R_{\mathrm{inf}} \lesssim 10^2\,\mathrm{kpc}$.

During the infall, only a fraction of gas is available to form stars. This fraction is determined by the gravitational fragmentation of the rotating material, regulated by the Toomre (1964) parameter $Q \equiv \sqrt{2}\Omega\sigma/\pi G\Sigma$, where $\Omega \equiv v/R \simeq j/R^2$ is the angular rotation velocity, σ is the gas velocity dispersion and $\Sigma \simeq M_{\mathrm{gas}}(< R)/\pi R^2$ is the gas surface density. The rotating disc remains stable as long as Q is higher than the critical values $0.7 - 1 - 2$, respectively for thick, thin and composite discs. The stability radius is then defined for $Q \sim 1$ and reads as

$$R_{\mathrm{Q}} \approx 6.3 Q \sigma_{60}^{-1} \lambda_{0.035} f_{\mathrm{inf},0.6}^{s} \times \times f_{\star,0.2}^{-2/3} M_{\star,11}^{2/3} \left[E_z/E_{z=2}\right]^{-1/6}\,\mathrm{kpc}, \tag{1.5}$$

with $\sigma_{60} \equiv \sigma/60\mathrm{km\,s}^{-1}$. The corresponding dynamical time at the stability radius is :

$$t_{\mathrm{dyn}}(R_{\mathrm{Q}} \approx 2.2 \times 10^7 Q^{3/2} \sigma_{60}^{-3/2} \lambda_{0.035}^{3/2} \times f_{\mathrm{inf}\,,0.6}^{(3s-1)/2} f_{\star,0.2}^{-1/2} M_{\star,11}^{1/2} \left[E_z/E_{z=2}\right]^{-1/4}\,\mathrm{yr}. \tag{1.6}$$

The infalling gas is then subjected to cooling and fragmentation processes down to the radius set by the centrifugal barrier (R_{Q}), corresponding to $\lesssim 10$ kpc. Once this scale is reached, a gaseous clumpy ($M_{\mathrm{clumps}} \leq 10^{-1} M_{\mathrm{inf}}$) and unstable disc forms with a ratio of rotation velocity to velocity dispersion $(v/\sigma)_{\mathrm{Q}} \gtrsim 3$.

As a consequence of the biased collapse, the centre of the galaxy experiences a rapid compaction within a few tens of Myr, driven by the migration of clumps and gas. The migration timescale is

$$t_{\mathrm{migr}}\left(R_{\mathrm{Q}}\right) \simeq \frac{2.1 Q^2}{\delta_{\mathrm{gas}}^2\left(R_{\mathrm{Q}}\right)} t_{\mathrm{dyn}}\left(R_{\mathrm{Q}}\right) \approx 3.2 \times 10^8\,\mathrm{yr}. \tag{1.7}$$

In this process, the dynamical friction, gravitational torquing and viscosity effects are negligible near R_{Q}, given that the gas possesses insufficient specific angular momentum to counteract the gravitational pull. During this phase, gas and clumps approximately maintain their initial specific angular momentum, and are expected to feature moderate star formation activity, which proceeds over a timescale

$$t_{\mathrm{SFR}} \simeq (50 - 100) \times t_{\mathrm{dyn}}\,(R_{\mathrm{Q}}) \approx 1 - 2 \times 10^9\,\mathrm{yr}. \tag{1.8}$$

The SFR is regulated by energy/momentum feedback of supernovae and stellar winds originating outflow. This effect is described through the mass loading factor ϵ_{out}, which is defined as the ratio between the outflow mass loss rate and the SFR (e.g. Thompson et al. 2005, Feldmann 2015).

The average SFRs around R_{Q} based on mass conservation arguments is estimated as

$$\mathrm{SFR}(R_{\mathrm{Q}} \simeq \frac{1}{1 - \mathcal{R} + \epsilon_{\mathrm{out}}} \frac{M_{\mathrm{inf}}}{t_{\mathrm{SFR}}} \lesssim 50 - 200\,\mathrm{M}_{\odot}\,\mathrm{yr}^{-1}, \tag{1.9}$$

where $\mathcal{R}$ is the return fraction of the gas from the formed stars. The estimated approximations are consistent with the values measured from optical/NIR observations of massive, star-forming galaxies at $z \sim 1 - 2$ (e.g. Genzel et al. 2014, van Dokkum et al. 2015, Barro et al. 2016a).

1.3.2 Compaction

The infall process of gas and clumps continues within R_{Q} for $\sim 10^7$ yr, maintaining its specific angular momentum (j_{inf}), down to a radius R_{rot} which corresponds to the radius where gravity and centrifugal support balance, strongly depending on the spin parameter λ of the host dark matter halo and the baryonic mass contrast $\delta(R_{\mathrm{rot}}) \equiv M_{\mathrm{inf}}/M_{\mathrm{tot}}(< R_{\mathrm{rot}})$:

$$R_{\mathrm{rot}} \approx \frac{j_{\mathrm{inf}}^2}{G M_{\mathrm{inf}}} \delta(R_{\mathrm{rot}}) \approx 1.3 \lambda_{0.035}^2 f_{\mathrm{inf},0.6}^{2s-1} \times f_{\star,0.2}^{-1/3} M_{\star,11}^{1/3} \left[E_z/E_{z=2}\right]^{-1/3}\,\mathrm{kpc}, \tag{1.10}$$

The above expression implies $R_{\mathrm{rot}} \lesssim 1$ kpc, which is indicative of an extremely high gas mass concentration. The gas kinematics is largely dominated by rotational velocities of the order of hundreds of km s^{-1}, corresponding to $v/\sigma \lesssim 10$.

The dynamical time at R_{rot} is

$$t_{\mathrm{dyn}} \simeq \frac{\pi}{2} \sqrt{\frac{R_{\mathrm{rot}}^3}{G M_{\mathrm{inf}}}} \approx 2 \times 10^6 \lambda_{0.035}^3 \times f_{\mathrm{inf}\;,0.6}^{3s-2} \left[E_z/E_{z=2}\right]^{-1/2}\,\mathrm{yr}\;. \tag{1.11}$$

The dynamical friction may transfer the angular momentum toward the outer regions, originating further gas collapse over a migration timescale $\lesssim 10^6$ yr.

The star formation within R_{rot} occurs over a time scale

$$t_{\mathrm{SFR}}(R_{\mathrm{rot}} \approx (50 - 100) \times t_{\mathrm{dyn}}(R_{\mathrm{rot}}) \approx (1 - 2) \times 10^8\,\mathrm{yr} \tag{1.12}$$

at a rate

$$\mathrm{SFR}(R_{\mathrm{rot}}) \simeq \frac{1}{1 - \mathbf{R} + \epsilon_{\mathrm{out}}} \frac{M_{\mathrm{inf}}}{t_{\mathrm{SFR}}(R_{\mathrm{rot}}}) \lesssim 500 - 2000\,M_{\odot}\mathrm{yr}^{-1}. \tag{1.13}$$

The high star formation activity is expected to occur in a dust-enshrouded environment which has been rapidly enriched with metals. During the *compaction* phase, most of the stellar mass is accumulated ($M_\star$ reaches from several to many $10^{10}\,M_\odot$) within $R_{\rm rot}$. As $t_{\rm migr}(R_{\rm rot}) \lesssim t_{\rm dyn}(R_{\rm rot})$ the system is driven toward a bulge-like configuration in virial equilibrium through violent relaxation processes, maintaining residual rotational support. During this phase, the galaxy is expected to lie above the MS relationship given that the stellar mass is growing (Mancuso et al. 2016b), and the high SFR can result in partial disruption of clumps and molecular clouds and may be subject to the Eddington limit for starburst (Andrews & Thompson 2011, Simpson et al. 2015).

The overall galaxy star formation activity is expected to be limited and mildly obscured in the region between $R_{\rm Q}$ and $R_{\rm rot}$, and a much stronger and dust-obscured in the innermost regions within $R_{\rm rot}$. For this reason, UV and FIR data are expected to probe different spatial distributions and irregular and clumpy morphologies. These analytical estimates are consistent with measurements from FIR/sub-mm continuum and CO spectral line observations of star-forming galaxies at $z \sim 1-2$ (Barro et al. 2016a, Hodge et al. 2016, Barro et al. 2017, Tadaki et al. 2017a, Talia et al. 2018), and for multi-wavelengths source reconstruction of a limited number of strongly lensed galaxies (Dye et al. 2018, Enia et al. 2018, Massardi et al. 2017).

At the end of the collapse, the baryons dominate the innermost regions of the galaxy, this creates favourable physical conditions for gas inflows towards the centre. This triggers the formation and accretion onto a central supermassive black hole, thickening the reservoir, particularly the dusty torus of the active galactic nucleus. This process leads to the emergence of an active galactic nucleus in the central regions, profoundly impacting the system's future evolution. The radius of the baryonic-dominated region is

$$R_{\rm b} \approx 18.8 f_{{\rm inf},0.6}^{1/2} f_{*,0.2}^{1/3} M_{*,11}^{1/3} \left[E_z/E_{z=2}\right]^{-1/3}\ {\rm kpc}, \tag{1.14}$$

with $R_{\rm b}$ being larger than both $R_{\rm rot}$ and $R_{\rm Q}$.

1.3.3 Feedback and stellar evolution

The size evolution of ETG progenitors is shaped by feedback events that expel gaseous material from their inner regions. These events are triggered by phenomena like supernovae, stellar winds, and emissions from the central SMBH during its quasar phase. They play a critical role in regulating or even quenching star formation activity. This phase, known as the *puffing-up* phase, leads to changes in the gravitational potential, causing the stellar component to settle into an extended equilibrium state. The final size of the galaxy depends on the comparison between the timescale of gas expulsion ($\tau_{\rm exp}$) and the dynamical time of the initial configuration ($\tau_{\rm dyn}$).

In the case of a fraction of the infalling mass is ejected ($f_{\rm out}$) from the central star-forming regions, an approximation of the final size $R_{\rm puff}$ after puffing up can be derived in relation to the initial size $R_{\rm in}$ by following Ragone-Figueroa & Granato (2011):

$$\begin{aligned} \frac{R_{\rm puff}}{R_{\rm in}} &\simeq \left(1+\frac{\chi f_{\rm out}}{1-\psi f_{\rm out}}\right) && \text{for } R_{\rm in} \approx 3\text{kpc}, \\ \frac{R_{\rm puff}}{R_{\rm in}} &\propto \left(\frac{R_{\rm in}}{2.7\text{kpc}}\right)^{-\phi} && \text{for } f_{\rm out} \gtrsim 0.4. \end{aligned} \tag{1.15}$$

In the above expression $f_{\rm out} \equiv M_{\rm out}/M_{\rm inf}$ is the ejected fraction of mass, $\chi = \psi^{-1} \approx 1.1$ and $\phi \approx 0.7$ for an impulsive ejection, $\chi = \psi \approx 0.8$ and $\phi \approx 0$ for a slow ejection. From the above expressions, follows that a considerable fraction of gas ($f_{\rm out} \approx 0.5 - 0.7$) is expected to be ejected, with a consequent puffing up of the stellar distribution to a radius $R_{\rm puff} \sim 3 - 5\,$kpc. This radius can be significantly larger than $R_{\rm rot}$ as a consequence of the presence of the dark matter component within the halo which enhances the puffing-up process in galaxies that were initially more compact. Consequently to the size expansion, the mass within $R_{\rm rot}$ is less concentrated in quiescent galaxies with respect to their star-forming progenitors.

The expected expansion is foreseen to follow gas ejection within a relatively short period, spanning from a few to several tens of millions of years. This suggests that the puffing-up process likely began operating in compact, quiescent galaxies at high redshifts ($z \gtrsim 2$), as these systems are estimated to be older than half a billion years ($\gtrsim 0.5\,$Gyr). From the kinematic point of view, while the stellar velocity dispersion is mildly affected by the puffing-up process, the rotational velocity significantly decreases because of the expansion in size, giving $v/\sigma \lesssim 0.5$.

The resulting estimate of $R_{\rm puff}$ and stellar velocity ratio $(v/\sigma)_{\star,\rm puff}$ are in concordance with the quantities measured from optical/NIR observations for quiescent galaxies at $z \sim 1 - 2$ (e.g. van der Wel & van der Marel 2008, van de Sande et al. 2013, van der Wel et al. 2014, Belli et al. 2017, Glazebrook et al. 2017, Toft et al. 2017).

1.3.4 Late evolution

The late slow evolution features the passive ageing of stellar populations, followed by size and kinematic alterations through mass additions via dry merger events. The mass after merging can be estimated given that $M_{\rm merg} = M_{\rm in}(1+\eta)$, with $\eta \equiv M_{\rm acc}/M_{\rm in}$ in terms of the accreted and initial material mass. For $\epsilon = \eta^{1-\kappa}$, with $\kappa \approx 0.56$ in local ETGs, the fractional size variations can be estimated from the virial theorem and energy conservation as:

$$\frac{R_{\rm merg}}{R_{\rm in}} = \frac{(1+\eta)^2}{1+\eta^{2-\kappa}} \tag{1.16}$$

The final sizes $R_{\rm merg}$ for the most massive systems increases by $\sim 2-3$ from $z \sim 2$ to 0. The $(v/\sigma)_{\star,\rm merg}$ ratio decreases as a consequence of the size increase and of the angular momentum loss during the merging. Again, these estimates are consistent with those measured via optical/NIR observations of local ETGs (e.g. Shen et al. 2003, Cappellari et al. 2013, Cappellari 2016).

1.4 Goal of this Thesis

The primary objectives of this thesis, are to investigate and understand the properties and evolutionary processes of DSFGs at the peak of the Cosmic Star Formation History, by exploiting the phenomenon of strong gravitational lensing to gain unprecedented insights into the physical properties and structures of such systems.

By leveraging the unique magnification and spatial resolution provided by gravitational lensing, a gravitational distortion of light caused by massive structures in the universe, our research seeks to unveil details about DSFGs that would otherwise remain inaccessible.

In this thesis, I have exploited a sample of lensed galaxies, selected in the millimetric band. The lensing effect allows us to include sources which otherwise would not be extremely bright or peculiar and would remain undetected. Ancillary information located our targets at redshifts close to the cosmic noon and I have integrated the multi-wavelength observations available in the literature and in public surveys or telescope archives with proprietary data in the radio band. These data come from telescopes such as HST in the optical/NIR, the *Spitzer* and *Herschel* space observatories in the MIR-to-FIR and interferometers such as ALMA and Australia Telescope Compact Array (ATCA) in the millimetre and radio bands. Utilising the available information, we were able to extend the statistical analysis conducted on the entire sample of lensed galaxies to delve into a more comprehensive examination of specific targets.
Therefore the outline of the thesis is the following.

In Chapter 2 I will describe the analysis approach used in this thesis, providing a brief introduction to gravitational lensing and focusing on the lens modelling techniques utilised in the literature. I will describe how samples of strongly lensed DSFGs are selected, and the role of multi-wavelength and spectroscopic observations. The primary focus of my research will centre around the *Herschel*-ATLAS survey, which serves as the source of the core sample of strongly lensed galaxies examined in this study.

In Chapter 3, I will explore the Far-Infrared/Radio Correlation among a selection of (candidate) DSFGs strongly lensed by gravitational effects. By taking advantage of the amplification provided by gravitational lensing and exploiting sensitive radio observations, I aim to extend this analysis to redshifts higher than achievable and provide an evolutionary interpretation of their observed properties.

In Chapter 4 I will investigate the detailed physical properties of an individual strongly lensed DSFGs, exploiting high-quality photometric and spectroscopic data. To this purpose, I will also implement the lens modelling techniques mentioned above, which are essential to gain in-depth insights into these sources.

Finally, in Chapter 5 I will summarise the results and conclusions of this work, inferring indications to the development of evolutionary models, and identifying some future actions and perspectives that will be made possible by the analysis described in this thesis.

Chapter 2

Methodology-Strong Gravitational Lensing

2.1 Gravitational Lensing

Gravitational lensing emerges as a direct consequence of Einstein's General Relativity, wherein the distribution of matter and energy in the Universe bends the structure of space-time. Consequently, all matter and energy within this curved space-time adhere to paths dictated by its geometric nature. This intricate interplay between the fabric of the Universe and its contents shapes the structures that exist today. Photons coming from massive objects composed of baryons like planets, stars, and galaxies, are compelled to follow the trajectories suggested by space-time curvature. As a light ray traverses the space-time curvature it bends towards the massive object responsible for curving space-time. This bending gives rise to various significant phenomena, including the expectation of multiple images, distortions, magnification, and time delays. Over time, numerous cases of these phenomena have been observed, confirming Einstein's predictions.

Gravitational lensing presents two primary benefits when studying distant objects. Firstly, it conserves the source's surface brightness while simultaneously magnifying its apparent luminosity linearly with the magnification factor μ. This unique combination allows the observations of regions in the luminosity-redshift space of faint astrophysical sources that would otherwise remain inaccessible.

Next, gravitational lensing distorts the shapes of the sources. For instance, when an event is produced by a lensing galaxy, it leads to the observation of multiple images of the object, which appear elongated or "stretched" to the observer by a factor $\mu^{1/2}$. As a result, the angular sizes of the source are amplified, providing an enhanced view and enabling a more detailed examination of the object's features.

Gravitational lensing can manifest itself in three main ways. When the sizes of the lensing systems significantly exceed the sizes of the lenses involved, it is referred to as *microlensing*. Examples of such lenses include stars, planets, or any compact objects present in the Milky Way, and in some extreme cases, even in other galaxies (see right panel of Figure 2.1 for an example).

First detected in 1990 (Tyson et al. 1990), *weak* lensing events occur in the

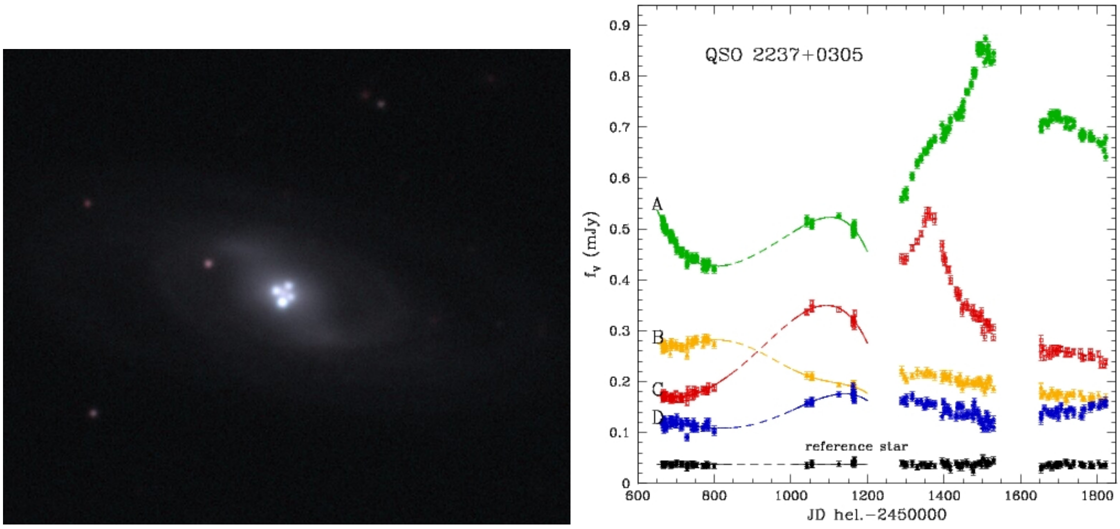

Figure 2.1: Left: the quadruply imaged QSO Q2237+0305. Credits: J.Rhoads, S.Malhotra, I.Dell'Antonio (NOAO)/WIYN/NOIRLab/NSF. Right: the light curve for Q2237+0305, this was the first object in which a microlensing event was ever detected (Irwin et al. 1989). Credits: OGLE Web Page: `http://ogle.astrouw.edu.pl/`.

presence of a significant angular separation between the source and the lens. The shape distortions in the images of the sources are incredibly subtle, to the point that they can only be measured by averaging over a group of extended sources (like galaxies) located behind the lens.

Finally, *strong lensing* occurs when the observer, the lens (a galaxy or a cluster of galaxies), and the background source are well aligned along the line of sight. This implies that the sky-projected sources are at a small angular distance with respect to the deflector's centre. As a result, the background sources may appear as multiple images whose separation depends on the mass distribution of the foreground lenses (see left panel of Figure 2.1 for an example of strong lensing of a QSO).

In this thesis, my primary focus will be on the latter scenario. The key astrophysical advantage is the opportunity to study high-redshift galaxies at sub-kpc scales, surpassing the constraints in angular resolution and sensitivity posed by the current instrumentation.

Gravitational lensing also becomes a means to detect minor sub-structures within the lenses through high-resolution imaging (e.g. Vegetti & Koopmans 2009, Hezaveh et al. 2016). These sub-structures, which can have low masses, offer an opportunity to test the cold dark matter scenario concerning the formation of structures on smaller scales.

Moreover, the statistical distribution of the lenses, together with the distribution and the extent of image separations, are influenced by both dark matter and dark energy components in the Universe. Thus, statistically significant samples of gravitational lenses can serve as valuable tools for constraining cosmological parameters. For instance, studies such as those by Grillo et al. (2008) and Eales (2015) have demonstrated the application of large gravitational lens samples in this regard.

2.2 Lens modelling

To maximise the scientific potential offered by gravitational lensing and reconstruct the properties of the lensed target, it is necessary to assume an appropriate lens model. This problem can be tackled from two different perspectives.

The first method is the so-called *parametric* approach. This consists in assuming an analytic model for both the lens and the source. For example, the lens mass profile can be described by a Singular Isothermal Sphere or Ellipsoide (SIE, e.g. Kormann et al. 1994, Muñoz et al. 2001) or a Navarro-Frenk-White (Navarro et al. 1996) profile, while the source's light can be modelled by a Sérsic profile. The effects from the environment are instead usually described by an external *shear* parameter. Each profile is described by a set of free parameters, each of them to be multiplied by the number of lens components. The best-fit parameters are obtained from a χ^2 fit statistics by minimising the term:

$$\chi^2_{\rm img} = \sum_i \frac{(f_i - M_i f_{\rm src})^2}{\sigma_i^2}, \tag{2.1}$$

Where $f_{\rm i}$ and $f_{\rm src}$ are the image and source flux respectively and σ_i is the associated uncertainty.

The main drawback of this approach is that it is highly reliant on the number of parameters utilised to describe the model, and even for the most basic lens and source descriptions, this quantity can become exceedingly large, leading to a considerable increase in computational cost.

Parametric methods encounter a further constraint when dealing with intricate source morphologies. This limitation becomes increasingly pronounced when the system is observed using high angular resolution instruments like HST, JWST and ALMA. In such instances, irregular and asymmetric morphologies cannot be accurately approximated using straightforward light profiles such as the Sérsic model. Even more sophisticated techniques like multi-Gaussian expansion or shapelets fail to capture the full complexity of these source morphologies. Furthermore, expanding the parameter space to reproduce more complex profiles could potentially lead to degeneracies.

Due to the aforementioned reasons, an alternative *semi-linear* inversion (SLI) approach has been developed over the past 20 years (e.g. Warren & Dye 2003). In this method, the source is pixelated, treating the pixel counts as free parameters, without making any assumptions about the intrinsic morphology of the source. By doing so, the challenge of finding an appropriate parameterisation for the source is eliminated, thus preventing any bias in the fitted mass profile that could result from a sub-optimal choice. The term "semi-linear" is attributed to this method because the source reconstruction involves a linear problem, while the mass modelling constitutes a non-linear problem.

2.2.1 The SLI method formalism

Pixelisation reconstructs the light from the source by employing an adaptive pixel grid. In this approach, once a fixed mass profile is established, the pixelated source light distribution that yields the lowest χ^2 value through linear inversion is determined. Subsequently, the mass profile is fine-tuned to minimise the χ^2 values obtained from these linear inversions. As a result, this technique can proficiently handle complex source morphologies, ensuring an unbiased solution by avoiding source smoothing during the process.

For a given mass model parameters, the inversion consists of the linear problem, for which the goodness of the fit is quantified by the merit function G, defined as:

$$G = \chi^2_{\rm img} = \sum_{j=1}^{J} \left(\frac{\sum_{i=1}^{I} s_i f_{ij} - d_j}{\sigma_j} \right)^2 , \tag{2.2}$$

where s_i is the surface brightness of the *i-th* source pixel, f_{ij} is the *j-th* pixel of the lensed and PSF-convolved image of source pixel i. d_j are the counts and σ_j is the statistical uncertainty of observed image pixel j. The set of I equations minimising each source's term is written as:

$$\frac{1}{2}\frac{\partial G}{\partial s_i} = 0 = \sum_{j=1}^{J} \left(\frac{f_{ij} \sum_{k=1}^{I} s_k f_{kj} - f_{ij} d_j}{\sigma_j^2} \right) , \tag{2.3}$$

which, in matrix form, are:

$$\mathbf{FS} = \mathbf{D}. \tag{2.4}$$

The elements s_j are contained in the column matrix $\mathbf{S}$ of length I. $\mathbf{F}$ is a symmetric I×I matrix defined by the elements $\mathrm{F}_{ik} = \sum_{j=1}^{J} f_{ij} f_{kj} / \sigma_j^2$, and $\mathbf{D}$ is a column vector of length I defined as $\mathrm{D}_i = \sum_{j=1}^{J} f_{ij} d_j / \sigma_j^2$. By matrix inversion, it is possible to solve for the source's pixel counts by the matrix product of the two linear matrices:

$$\mathbf{S} = \mathbf{F}^{-1}\mathbf{D}. \tag{2.5}$$

The covariance matrix between source pixels i and k for independent image pixels is:

$$\sigma_{ik}^2 = \sum_{j=1}^{J} \sigma_j^2 \frac{\partial s_i}{\partial d_j} \frac{\partial s_k}{\partial d_j} , \tag{2.6}$$

which, from Equation 2.2.1, can be written as:

$$\sigma_{ik}^2 = \sum_{j=1}^{J} \sigma_j^2 \sum_{l=1}^{I} C_{il} \frac{f_{ij}}{\sigma_j^2} \sum_{m=1}^{I} C_{km} \frac{f_{mj}}{\sigma_j^2} = C_{ik} \tag{2.7}$$

The former equation implies $\mathbf{C}$=$\mathbf{F}^{-1}$, which is the covariance matrix for $\mathbf{S}$.

Although the inversion process is exceptionally well-suited for conducting comprehensive analyses of a lens galaxy's mass, it involves a deconvolution and, because of source plane pixels' independence, it can introduce artefacts into the solution due to the noise. A prior is applied to the solution to address this issue, ensuring a certain degree of smoothness. This is called *regularisation* term, it is defined as the linear combination of terms $s_i s_k$ and is added to the merit function:

$$G = \chi^2 + \lambda G_L = \chi^2 + \lambda \sum_{i,k} a_{ik} s_i s_k. \tag{2.8}$$

Following the previous methodology, this leads to:

$$\mathbf{S} = [\mathbf{F} + \lambda \mathbf{H}]^{-1} \mathbf{D}, \tag{2.9}$$

where λ is the *regularisation constant* and $\mathbf{H}$ is the *regularisation matrix*, defined as:

$$H_{ik} = \frac{1}{2} \frac{\partial^2 G_L}{\partial s_i \partial s_k}. \tag{2.10}$$

Analogously to Equation 2.2.1, the covariance matrix for the regularised case is:

$$\sigma_{ik}^2 = \sum_{j=1}^{J} \sigma_j \frac{\partial s_i}{\partial d_j} \frac{\partial s_k}{\partial d_j} = \mathrm{R}_{ik} - \lambda \sum_{l=1}^{I} \mathrm{R}_{\mathrm{il}} [\mathbf{RH}]_{\mathrm{kl}}. \tag{2.11}$$

2.2.2 Adaptive semi-linear inversion

The discretisation of the source plane that is used in the inversion process is completely free of constraints. For this reason, rectangular pixelisation is not always the optimal approach to source reconstruction. One notable issue is that it utilises only a small subset of the source pixels to perform the reconstruction. Moreover, the vast majority of pixels used in the reconstruction are often positioned far away from the actual source and, consequently, the remaining pixels merely contribute to fitting noise.

This approach is inefficient, leading to longer analysis runtimes. Additionally, it compromises the effectiveness of regularisation. Therefore, the solution is a pixelisation scheme that concentrates its pixels in regions where more data are present, such as the highly magnified areas in the source plane. This is called *adaptive* pixelisation scheme, it employs fewer pixels for reconstruction enhancing the computational efficiency (Nightingale & Dye (2015)).

With a fixed mass model, the centres of the image plane pixels are traced back to the source plane and grouped using a k-means clustering algorithm, defining new pixel centres in the source plane. These clusters with newly determined centres are then approximated to (for example) Voronoi or Delauney cells. As a result, regions with higher magnification will be probed by a greater number of cells, while regions with lower magnification will have fewer cells assigned to them.

How does the adaptive scheme influence the regularisation? When using the rectangular grid, each source pixel undergoes regularisation with its four neighbouring pixels. The fluxes are then determined, the differences are summed up and the solutions with significant discrepancies are penalised. In contrast, adopting an adaptive grid each source pixel is compared with all other source pixels sharing a direct vertex. Consequently, different source pixels may undergo regularisation with varying numbers of source pixels, depending on the number of neighbours they have. This approach increases the adaptability of the regularisation process, allowing for more flexible adjustments to the source reconstruction.

The formalism to describe this approach is the same, with the exception that the regularisation term is expressed as:

$$G_L = \sum_{i=1}^{I} \sum_{n=1}^{N_v} [s_i - s_{i,v}]^2, \tag{2.12}$$

where N_v is the number of neighbouring tassels for each cluster determined by the h-cluster centres.

2.2.3 Extending the SLI to visibilities

The SLI formalism can also be extended to interferometry (Dye et al. 2018, Enia et al. 2018, Maresca et al. 2022), modelling a set of visibility data, i.e. the result of the correlation of signals coming from an astrophysical source and collected by an array of antennae operating in the radio-to-mm band regime as an interferometer, whose Fourier transform gives the source surface brightness distribution. Performing an inversion directly on the Fourier space (or *uv*-plane) circumvents the issue of dealing with artefacts and noise correlation arising in the image as a consequence of poor sampling of the *uv*-plane.

Following a similar formalism concerning the one used in Dye et al. (2018), the fluxes of the *i-th* pixel in the source plane and the respective *j-th* image-plane pixel are, as in the previous section, contained in the rectangular matrix f_{ij}. Analogously, complex visibilities from the lensed image are collected rectangular matrix g_{ij}, which are the Fourier transform of the *i-th* source pixels in unit surface brightness computed at the *j-th* visibility point in the *uv*-plane. For each *j-th* visibility corresponding to the source pixel surface brightness s_i, the model visibility set can be described as $\sum_i s_i g_{ij}$.

Given a set of observed visibilities V_{obs}, the merit function can be described as:

$$G = \frac{1}{2}\chi^2 = \frac{1}{2}\sum_{j=1}^{J}\left(\frac{\left|\sum_{i=1}^{I} s_i g_{ij} - V_{obs,j}\right|^2}{\sigma_j^2}\right) + \lambda\frac{1}{2}\mathbf{S}^T\mathbf{HS}, \tag{2.13}$$

computed over a total of I pixels and J visibilities. σ_j are the 1σ uncertainties on the observed visibilities [1]. As in Equation 2.2.1, the last term in the expression describes the *regularisation*, where λ is a constant determining the strength of the regularisation, and **H** the regularisation matrix. Following the same procedure as in Section 2.2.1, the values s_i, represented by the vector **S** which best reproduces

---

[1] In the analysis described in Chapter 4 of this thesis, the 1σ uncertainties are rescaled adopting the CASA task `statwt` to match their absolute value.

the observed image-plane visibilities, can therefore be derived by minimising the merit function G. The solution to this linear problem is given by:

$$\mathbf{S} = [\mathbf{F} + \lambda \mathbf{H}]^{-1}\mathbf{D}, \tag{2.14}$$

where $\mathbf{F}$ and $\mathbf{D}$ are respectively the matrices $F_{ij} = \sum_{n=1}^{J}(g^{\mathbb{R}}_{in}g^{\mathbb{R}}_{jn} + g^{\mathbb{I}}_{in}g^{\mathbb{I}}_{jn}/\sigma^2_n)$ and $D_i = \sum_{n=1}^{J}(g^{\mathbb{R}}_{in}V^{\mathbb{R}}_n + g^{\mathbb{I}}_{in}V^{\mathbb{I}}_n/\sigma^2_n)$.

2.3 Observations of strongly lensed galaxies

Occurrences of strong lensing events are infrequent, requiring an exceptionally precise alignment between the observer and the lensing system composed of two objects at distinct redshifts. As a result, building statistically significant samples of strongly lensed galaxies requires extensive photometric and spectroscopic large-area surveys and effective identification techniques.

Over several decades, extensive datasets from optical and radio observations have been available for exploration in this pursuit. These datasets feature a sub-arcsecond spatial resolution, which is necessary for identifying distinctive characteristics associated with strong gravitational lensing, such as multiple images, arcs, and rings (Treu 2010).

Historically, the systematic identification of strongly lensed systems in the radio regime began with the MIT-Green Bank (MG)-VLA survey (Lawrence et al. 1986), leading to the discovery of a few radio-loud lensed quasars exploiting the VLA sub-arcsecond angular resolution. Almost 20 years later, 22 new AGNs were discovered in the Cosmic Lens All-Sky Survey (CLASS; Browne et al. 2003). HST imaging follow-ups of $\sim$ 100 galaxy-scale lenses were conducted in CLASS and other similar surveys as part of the CfA-Arizona-Space-Telescope-LEns-Survey (CASTLES; Munoz et al. 1999). CASTLES was also the first uniform sample of high-resolution images of known galaxy-scale lens systems, including both galaxy-quasar and galaxy-galaxy lens configurations.

In the optical regime, 85 galaxy-galaxy lenses were discovered in the Sloan Lens ACS (SLACS; Bolton et al. 2006) Survey exploiting the large volume of spectroscopic data from the SDSS survey and followed up with HST/ACS imaging (Auger et al. 2009). The SLACS for the Masses sample (Shu et al. 2015) added 40 new lensing systems with lower lens masses.

Additional sets of data generated from the SDSS survey include the SDSS Quasar Lens Search (SQLS) sample, which comprises 28 galaxy-scale multiply-imaged quasars selected through multi-colour imaging (Oguri et al. 2006). Furthermore, the Major UKIDSS-SDSS Cosmic Lens Survey (MUSCLES) sample (Jackson et al. 2012) identified several more galaxy-quasar lens systems by leveraging data from both SDSS and the UKIRT Infrared Deep Sky Survey (UKIDSS). 35 galaxy-galaxy lensing systems were discovered inside the Strong Lensing Legacy Survey (SL2S; More et al. 2012), exploiting data from the Canada-French Hawaii Telescope Lensing Survey (CFHTLenS; Gavazzi et al. 2012). From the latter, newer lensing samples have emerged (More et al. 2016a, Paraficz et al. 2016).

The BOSS Emission-Line Lens Survey (BELLS; Brownstein et al. 2012) identified approximately 30 galaxy-galaxy systems within the Baryon Oscillation Spectroscopic Survey (BOSS) and obtained high-resolution imaging from HST (Brownstein et al. 2012). This effort later expanded into the BELLS GALLERY survey, which focuses on Lyα emitters as source galaxies (Shu et al. 2016). Furthermore, a subset of 13 strongly lensed quasars has been uncovered using BOSS data (More et al. 2016b).

Usually, optical observations lead to the identification of nearby lensed systems ($z < 1$), where the lensed objects are often found in more advanced stages of their evolution featuring lower amounts of dust with respect to star-forming systems at higher redshifts. This is a straightforward consequence of the obscuration effect of the dust, making SFGs less likely to be detected. In order to identify highly star-forming objects, the best strategy is to search for DSFGs in the mm regime, complementing these observations with multi-wavelength data.

2.4 Multiwavelength Observations of Sub-millimetre Selected Strongly Lensed DSFGs

As discussed in Section 1.2 of the previous Chapter, DSFGs provide a unique window into the processes driving intense star formation, galaxy interactions, and feedback mechanisms in the early Universe. By studying these extreme objects, one can gain insights into the processes that shape galaxies over billions of years, shedding light on the overall story of galaxy evolution.

Over the last twenty years, observations have provided insights into the nature of DSFGs, uncovering their statistical characteristics as a result of larger numbers being identified through wide-area surveys ($> 0.1-100 deg^2$; e.g. Smail et al. 1997, Bakx et al. 2018, Scott et al. 2008, Eales et al. 2010, Aretxaga et al. 2011, Casey et al. 2012a,b) conducted with both ground-based (e.g. the JCMT), and space-based facilities (e.g. the *Spitzer* and *Herschel* Space Observatories).

Nonetheless, grasping the intricate spatial distribution and dynamics of individual molecular clumps, often on sub-kiloparsec scales, remains challenging.

The advent of ALMA in recent years has significantly advanced our understanding (see e.g. Hodge & da Cunha 2020). For instance, ALMA continuum observations provided insights into the properties of the bulk of dust content (composed by the coldest dust grains) by tracing the Rayleigh-Jeans tail of thermal dust emission of DSFGs at $z \sim 2-3$.

However, a comprehensive understanding of these galaxies goes beyond evaluating their integrated properties retrieved only in sub-mm bands, as vital evolutionary processes occur on sub-galactic scales, encompassing stellar and AGN feedback, star formation triggers and quenching, spheroid formation, and galaxy-black hole co-evolution, requiring a variety of multi-wavelength data.

In this sense, high-resolution ALMA observations, with sub-arcsecond spatial resolution, have been of great impact. High-z DSFGs found both above and on the MS, have been found to host a compact ($\sim 1-5$ kpc; Simpson et al. 2015, Barro et al. 2016a, Oteo et al. 2016, Barro et al. 2017, Fujimoto et al. 2017, Tadaki et al. 2017a,b, Talia et al. 2018, Nelson et al. 2019, Pantoni et al. 2021) and central concentrated dust continuum. The sizes of this compact dust component, are often found to be consistent with the sizes inferred from radio emission, however, they differ from optical measurements ($\sim 2-10$ kpc; Rujopakarn et al. 2016, Nelson et al. 2019, Pantoni et al. 2021). Yet a fraction ($\sim 20\%$) of sub-mm-selected DSFGs remains undetected in deep HST imaging (e.g. Franco et al. 2018, Wang et al. 2019a, Gruppioni et al. 2020; see also Section 4.1).

Further complexities arise from the multi-wavelength morphology of these galaxies. Recent studies employing ALMA and HST imaging have highlighted clumps in the optical rest-frame and smoother FIR rest-frame emissions with compact cores and extended disks. Clumpy structures have also been observed with ALMA in the FIR rest-frame continuum, while larger scales reveal isolated and disturbed morphologies, often requiring multiple-component models for multi-wavelength emission.

Spatially-resolved radio emission provides insights to distinguish between the stellar emission from AGN contributions, though such studies are limited due to extensive integration times required for high-redshift analysis.

From the point of view of the central SMBH, X-ray observations of DSFGs have unveiled the gradual growth, which continues until the mass and power is high enough to manifest as a quasar and quench star formation and cleaning the surrounding interstellar medium (ISM; see e.g. Mullaney et al. 2012, Page et al. 2012, Delvecchio et al. 2015, Rodighiero et al. 2015, Stanley et al. 2015, 2017; Hickox & Alexander 2018 and references therein).

Despite progress, a complete physical understanding of high-z DSFGs remains elusive. A comprehensive approach involving galaxy property characterisation, molecular spectral lines, and spatially-resolved multi-band imaging is crucial. This approach provides insights into mechanisms and processes across evolutionary stages, offering clarity on the role of DSFGs within the broader context of galaxy formation and evolution.

Strong gravitational lensing, therefore, offers an exceptional opportunity to investigate the properties of such objects. In FIR/sub-mm bands, high-z lensed dusty galaxies are exceptionally bright, while a negligible signal comes from the foreground lens, which is often a massive evolved elliptical at $z \lesssim 1$. Also, the obscuration from the foreground lens that limits the investigation of the background galaxy in the optical is negligible in the FIR/sub-mm domain.

Models (Blain 1996, Perrotta et al. 2002, Lapi et al. 2006, Negrello et al. 2007; Negrello et al. 2010, Lapi et al. 2011) predict a steep luminosity function for SMGs, resulting in a sharp drop in the number counts at the brightest fluxes ($\simeq 80-100$ mJy at 500 μm). Beyond this threshold, various galaxy populations can be detected, such as low-redshift ($z \lesssim 0.1$) late-type galaxies, flat spectrum radio sources, HyLIRGs, and gravitationally lensed DSFGs at $z \gtrsim 1$.

By adopting this simple flux density threshold, combined with shallow optical and radio data to identify and remove contaminants, gravitational lensing systems can be efficiently selected. Given the low predicted surface density of these systems ($\lesssim 0.5$ deg^{-2}), large area surveys are required to detect a significant number of lensing events.

In this sense, the capabilities of the *Herschel* Space Observatory and the comprehensive *Planck* all-sky survey at sub-mm wavelengths (Pilbratt et al. 2010, Cañameras et al. 2015), along with the achievements of the SPT in the mm frequency bands (Vieira et al. 2010, Carlstrom et al. 2011, Mocanu et al. 2013), has been amply proved.

The SPT-Sunyaev–Zel'dovich survey identified 81 strongly lensed DSFGs over an area of 2500 deg^2 by adopting a slightly different selection method ($S_{1.4mm} > 20$ mJy; Vieira et al. 2013, Weiß et al. 2013, Spilker et al. 2016, Everett et al. 2020, Reuter et al. 2020). Wardlow et al. (2013) identified 11 lensed galaxies over the 95 deg^2 of the HerMES survey (Oliver et al. 2012); other 77 candidate lensed galaxies were found by Nayyeri et al. (2016) in the HeLMS survey (Oliver et al. 2012), and in the HerS survey (Viero et al. 2014).

In the context of sub-mm/mm selected lensed galaxies, it is important to emphasise that the interference stemming from the foreground lens – typically a passive elliptical galaxy – with the sub-mm emission of the background galaxy is minimal. Consequently, the process of modelling the lensed morphology remains largely unaffected by uncertainties associated with lens subtraction, a predicament often encountered in optically chosen lensing systems.

Furthermore, this selection method exclusively harnesses the attributes of the background galaxy itself, specifically its sub-mm flux density. As a result, any potential bias against the lens's redshift and mass is circumvented. Notably, a handful of confirmed lenses already exist with redshifts surpassing $z > 1$. This avenue opens up the opportunity to investigate the mass distribution and the abundance of dark matter substructures in galaxies reaching significantly high redshifts compared to previous studies (e.g., Dye et al. 2014; Hezaveh et al. 2016).

2.4.1 The *Herschel*-ATLAS survey

The H-ATLAS survey (Eales et al. 2010) is the widest area (600 deg^2) extragalactic survey undertaken by *Herschel* and has provided a sample of more than a hundred thousand dusty galaxies at high redshift. During the Science Demonstration Phase (SDP), covering a 16 deg^2 portion of the sky, Negrello et al. (2010) selected the first sample of 5 strongly lensed galaxies in H-ATLAS. The area is divided into three well-studied sky fields, visible in Figure 2.2, located in regions uncontaminated by the dust in the Galactic plane. The North Galactic Pole (NGP) is centred at R.A. 13h18m and dec +29°130′ (J2000) and extends over 180.1 deg^2, covering the Coma Cluster The equatorial fields cover the GAMA survey along ∼ 9h, 12h, and 15h, measuring 161.6 deg^2. Finally, the South Galactic Pole (SGP) covers 317 deg^2 and it is centred at R.A. 0h6m and dec -32° 440′ (J2000). Negrello et al. (2017) further exploited this survey to extract a catalogue of 80 candidate strongly lensed dusty star-forming galaxies brighter than 100 mJy at 500 μm, and, with the recent Third Data Release Ward et al. (2022) found 11 more candidates in the SGP.

The SPIRE photometry is obtained from the point-source *Herschel*/SPIRE catalogues of the H-ATLAS Data Release 1 and 2, described in Valiante et al. (2016) and Maddox et al. (2017). The catalogues have been created identifying the 2.5 σ peaks in the SPIRE 250 μm maps, which are then used as position priors to

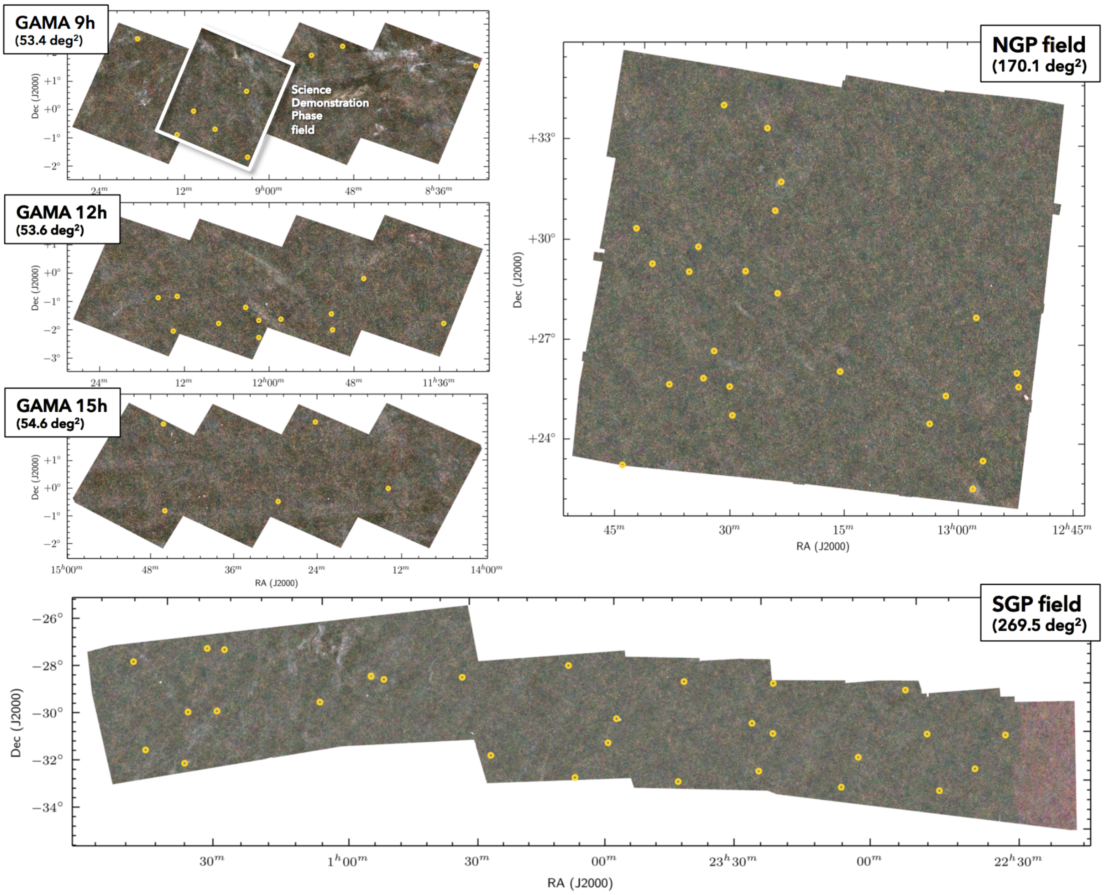

Figure 2.2: *Herscel*/SPIRE maps of the H-ATLAS fields. Yellow circles represent the centroids of the 80 candidate strongly lensed galaxies selected by Negrello et al. (2017). Credits: Negrello et al. (2017).

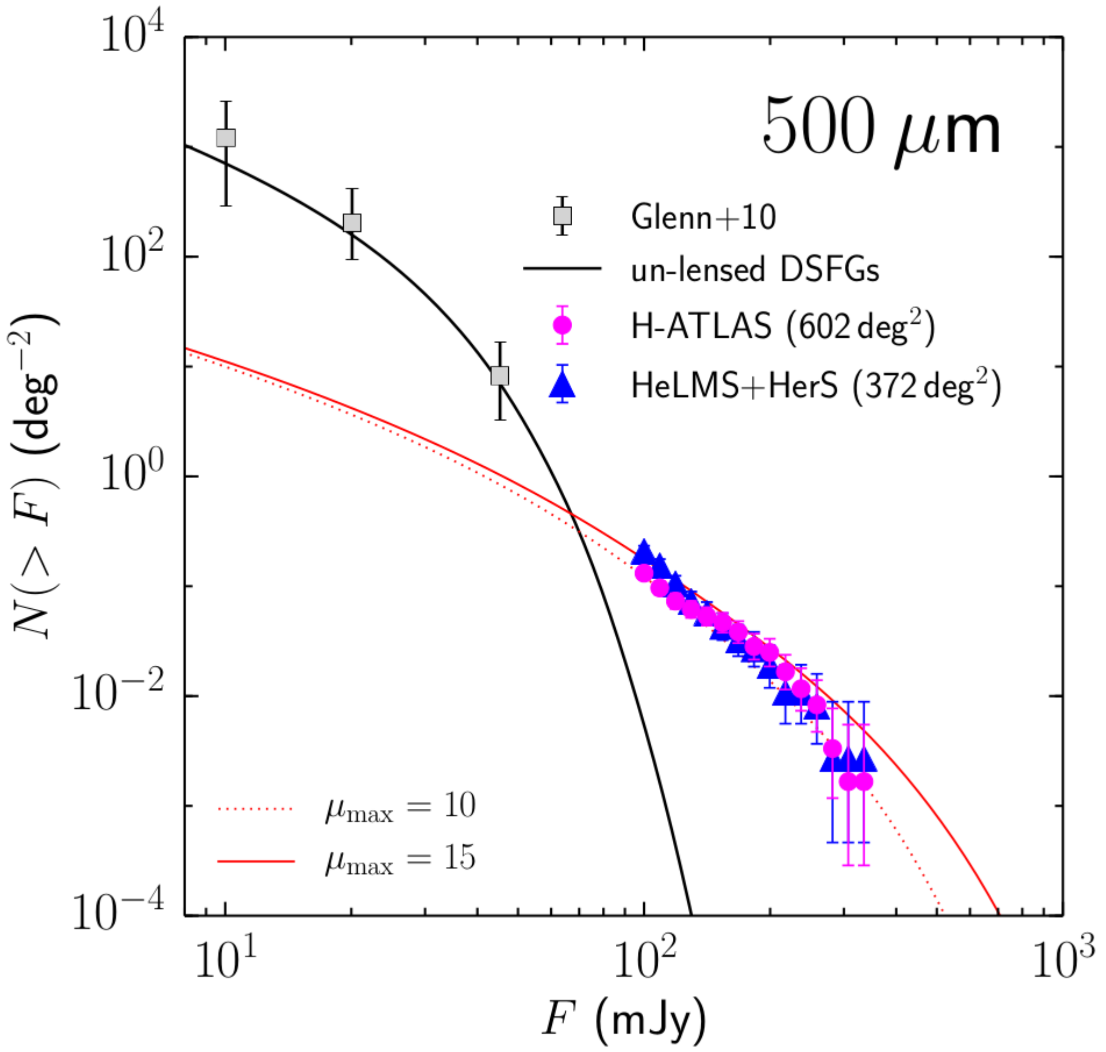

Figure 2.3: Integral number counts of the candidate lensed galaxies with $F_{500\mu m} > 100$ mJy from the sample of Negrello et al. (2017) (purple dots), compared to other candidate lensed galaxies derived by Nayyeri et al. (2016) from HeLMS+HerS (blue triangles). Error bars correspond to the 95 % confidence interval. The black line represents the prediction for the abundance of unlensed DSFGs at z$\gtrsim$1.5 from the model predictions of Cai et al. 2013. The red line represents the predicted number counts of lensed sources for different values of the maximum magnification factor μ. Grey squares represent measurements of the number density of unlensed DSFGs derived from P(D) analysis (Glenn et al. 2010). Image credits: Negrello et al. (2017).

measure flux densities in the other SPIRE bands. The instrumental and confusion noise has been minimised through the use of a matching filter for the creation of the maps from which fluxes have been extracted. Only sources with a signal-to-noise ratio > 4 in at least one of the three SPIRE bands have been included in the final catalogue. As described in Negrello et al. (2017), extended sources have been detected through optical images and treated as contaminants and, therefore are not included in the sample of 80 candidate lensed galaxies. The sample galaxies feature FIR (8-1000 μm) luminosities in the range $13 \lesssim \log(L_{\mathrm{FIR}}/L_{\odot}) \lesssim 14$ (uncorrected for lens magnification). They span a redshift range $1 \lesssim z \lesssim 4.5$ with a median value $z_{\mathrm{med}} = 2.5$. However, at the beginning of our analysis, only 21 of the 80 candidates in Negrello et al. (2017) sample were confirmed to be genuine strongly lensed objects through detailed optical/NIR (with HST and *Keck*; Fu et al. 2012, Calanog et al. 2014, Messias et al. 2014) or sub-mm (with SMA and ALMA; Bussmann et al. 2013, Massardi et al. 2017, Enia et al. 2018, Dye et al. 2022, Maresca et al. 2022) images of their structure, together with spectroscopic redshift measurements of the background lensed galaxy and of the foreground lens. For 8 sources, the lensing scenario is strongly supported by the redshift difference of optical/NIR and sub-mm galaxies along the line of sight. The remaining objects were classified as uncertain because they still missed proper follow-up that could confirm their lensed nature.

Bakx et al. (2018) extended the selection criteria adopted by Negrello et al. (2017) by including DSFGs with (sub-)mm color-estimated photometric redshift $z_{\pm phot} > 2$, and $S_{500\mu m} > 80$ mJy. This sample, namely HerBS, is expected to contain both lensed and unlensed sources, given that for fluxes $S_{500\mu m} < 100$ the number density of unlensed DSFGs increases exponentially. In Section 5.2.1, I will provide further details regarding the HerBS survey and the recent ALMA follow-ups conducted for this sample.

2.5 Studying lensed DSFGs from observations

The gravitational amplification makes accessible to observations regions of the luminosity/redshift space that would otherwise be beyond the reach of current instrumentation or would require exorbitant amounts of observing time. Sub-mm-selected samples of lensed galaxies are ideal for follow-up observations aimed at understanding the detailed properties of starburst phenomena in distant galaxies.

The investigation of these properties can be pursued through two primary and complementary strategies, harnessing the potential of multi-wavelength data from lensed high-redshift DSFGs. In the following section, I outline the rationale and significant advantages underlying these two methods, which have culminated in the development of this study.

2.5.1 Studies of statistically significant samples

The first approach involves the analysis of statistically relevant samples of lensed DSFGs. This method is centred on the selection of a group of objects sharing common observational traits. The robustness of this method lies in its ability to yield a coherent and representative so to be statistically significant sample containing a substantial number of sources, which is essential for analysing physical attributes. However, a notable drawback is the scarcity of data, particularly in specific regions of the electromagnetic spectrum. This scarcity can introduce uncertainties in photometric redshifts, and in some cases, necessitate arbitrary assumptions regarding under-sampled galaxy properties.

However, when dealing with samples selected using instruments with low angular resolution, such as the case of lensed galaxies selected with *Herschel*, the issue of blending must also be taken into account. Blending in FIR observations, such as those conducted with the *Herschel* Space Observatory, refers to the situation where the emissions from multiple celestial sources overlap or blend within the telescope's spatial resolution. This can result in a single observed signal that is a combination of emissions from multiple individual sources, making it difficult to accurately identify and characterise each source separately.

The FIR emissions from galaxies, particularly DSFGs, are crucial for studying their physical properties, SFR, and dust content. However, due to the relatively large beam size of FIR telescopes like the Large APEX BOlometer CAmera (LABOCA) or *Herschel*/SPIRE (e.g. the SPIRE beam size is of ~ 30 arcsec, while the LABOCA beam size of ~ 20 arcsec), multiple galaxies within a single beam can contribute to the observed signal (Hodge et al. 2013). This blending effect can lead to several challenges, such as source identification, the flux measurement of the individual source, and therefore the correct estimation of the physical properties and photometric redshift, for example through SED fitting.

To mitigate the effects of blending, high-resolution follow-up observations at other wavelengths (e.g., using radio, sub-mm, or optical telescopes) are often conducted to resolve individual sources within the blended region. These observations help in accurately identifying and characterising the contributing galaxies, allowing for more reliable scientific analyses and interpretations.

In the context of gravitational lensing, this approach benefits from the inherent magnification in the flux density of the objects in question. Consequently, it offers the great advantage of broadening studies to encompass galaxies that possess intrinsically lower flux densities and often fall below the confusion limit. This expansion allows for an investigation of the fainter portion of the luminosity function, overcoming sensitivity and confusion limits.

Gravitational lensing also offers an extra advantage due to its unique systematic biases when contrasted with field sources. While observations in the field tend to be biased towards sources with high luminosity or low redshifts, gravitationally lensed sources are biased towards compact, higher redshift objects (typically $z > 1$). Moreover, they are less biased against high intrinsic luminosities (e.g. Swinbank et al. 2010).

However, the primary drawback when examining extensive sets of lensed DSFGs arises from the lack of uniformity in the angular resolution of the data.

This aspect becomes particularly critical in the determination of the intrinsic (demagnified) physical properties. Lens modelling is indeed a process that can be accomplished solely for objects with resolved spatial features. Consequently, when lens modelling isn't accessible for all objects within the sample, one must resort to making assumptions about the value of the magnification factor.

2.5.2 Studies of individual sources

The second method centres on the study of limited samples or individual objects that possess an extensive collection of high-quality photometric and spectroscopic data. This approach aims to achieve a profound understanding of the ongoing astrophysical processes.

In the present era, achieving high-resolution imaging is feasible in both the optical/NIR domain, especially thanks to HST and the new JWST, or adaptive optics systems, such as the *Keck* Observatory and in the mm/radio spectrum using ground-based interferometers such as ALMA and the VLA.

The combination of high-resolution imaging in both the long and short-wavelength regimes is particularly important in studying a lensing system. Indeed, one of the significant uncertainties relies on the determination of the stellar component of the background DSFG, whose light can be captured in the observed optical/NIR regime. However, the light of the lensing system at these wavelengths is intrinsically faint because of the dust obscuration and the redshift and is often dominated by the foreground lens' emission (Negrello et al. 2014). To overcome this issue, an accurate modelling and subtraction of the lens light profile is required to detect the faint emission from the background source. This is necessary to perform accurate SED-fitting and disentangle the contributions from galaxies in the lensing system, and can only be achievable with high-quality imaging.

Conversely, achieving high-resolution follow-up observations in the sub-mm and mm wavelengths is essential for unveiling the multiple images of the background source. Figure 2.4 pictures the situation described above.

Spectroscopic data are extremely important to confirm the source's redshift, kinematic, and gas content (e.g. Tadaki et al. 2015, Barro et al. 2016a,b, Decarli et al. 2016, Talia et al. 2018, Rizzo et al. 2020, Pantoni et al. 2021, Rizzo et al. 2021, 2022). Observing spectral lines in high-z DSFGs requires an enormous amount of time (several hours), even with ALMA, and therefore it is often only feasible for individual sources. The magnification offered by strong lensing improves the performance of these observations. For example, Neri et al. (2020) determined the redshifts of 13 bright galaxies identified in H-ATLAS with $S_{500\mu m} \gtrsim 80$ mJy, including several lensing systems. They established robust spectroscopic redshifts for 12 individual sources, relying on the identification of at least two emission lines. Building on the success of this initial study, a comprehensive and extensive survey, known as z-GAL (Cox et al. 2023), has recently been conducted employing the Northern Extended Millimeter Array (NOEMA). This survey yielded dependable redshifts for all 126 bright *Herschel*-selected SMGs with 500 μm fluxes exceeding 80 mJy. These sources were chosen from the H-ATLAS and HerMES fields situated

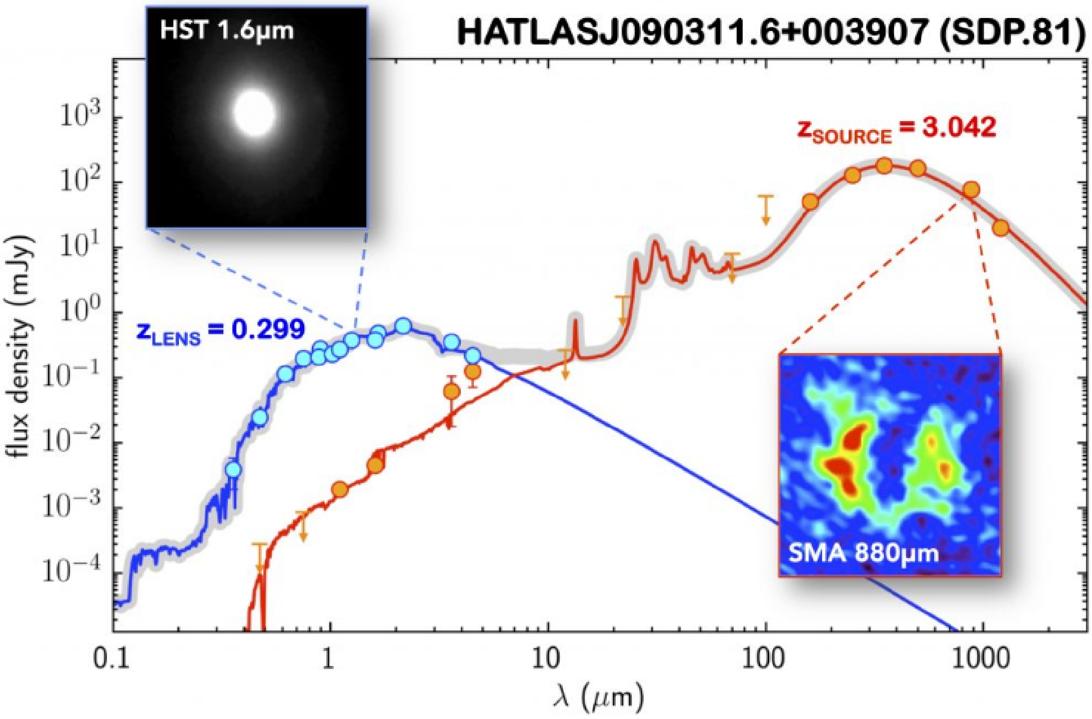

Figure 2.4: Example of the SED for a gravitational lensing system belonging to the H-ATLAS survey, namely HATLASJ090311.6+003907 or SDP.81 (Negrello et al. 2014). The SED of the lens and the background galaxy are depicted in blue and red respectively. The illustration demonstrates how observations at various wavelengths explore distinct elements of the lensing system. The foreground galaxy is studied in the optical/NIR range, as exemplified by the upper left inset featuring data from instruments like the HST. In contrast, the FIR to mm range, as observed by tools like the SMA (depicted in the lower right inset), uncovers details about the dust-obscured background galaxy. Image credits: `http://www.mattianegrello.com`

in the Northern and equatorial regions of the sky.

The BEARS survey is another recent redshift campaign (Urquhart et al. 2022, Bendo et al. 2023, Hagimoto et al. 2023) performed with ALMA using both the 12m and the Atacama Compact Array (ACA) arrays and targeting the brightest sources in the southern field of the H-ATLAS survey. While 81 sources were targeted, 142 objects were resolved and 71 were spectroscopically confirmed through the detection of [CI], CO, and H_2O lines. The outcomes of this redshift campaign open up several follow-up observations. Bendo et al. (2023) measured the continuum emission reconstructing the SED of these data, and Hagimoto et al. (2023) estimated the physical conditions of the ISM through the detected spectral lines [CI], CO, and H_2O lines.

Spectroscopic observations of strongly lensed sources can also be exploited to infer important dynamical properties of distant galaxies with unprecedented angular resolution. For instance, Rizzo et al. (2020) investigated the dynamics of the strongly gravitational lensed galaxy SPT-S J041839-4751.9 at $z = 4.2$. By applying a three-dimensional lens-kinematic modelling technique to ALMA data, they found evidence of a dynamically cold and highly star-forming disc.

This approach has been extended in Rizzo et al. (2021) for a sample of five strongly lensed DSFGs, exploiting ALMA spectroscopic [CII] data, and reconstructing their kinematics down to a scale of ~ 200 pc.

2.5.3 Examples of high-quality single source studies in the H-ATLAS field

Some of the sources in the H-ATLAS sample have been individually studied in detail exploiting multi-wavelength high-resolution observations. Here I provide details on the objects that have been analysed among the sample of Negrello et al. (2017).

- **J085358.9+015537 (G09v1.40)** has been the target of high-resolution follow-ups in NIR (*Keck*/NIRC2 Ks band and HST/WFC3 F110w) and sub-mm (SMA), exploited for source reconstruction (Bussmann et al. 2013, Calanog et al. 2014, Enia et al. 2018), together with high-resolution ALMA observations presented in Falgarone et al. (2017) and more recently in Butler et al. (2021). The latter revealed a massive outflow detected via the absorption $OH^+(1_1 - 1_0)$ line

- **HATLASJ090311.6+003907 (SDP.81)** has been the target of observations and modelling in the ALMA long-baseline campaign (Partnership et al. 2015, Dye et al. 2015, Hatsukade et al. 2015, Rybak et al. 2015b, Rybak et al. 2015a, Swinbank et al. 2015, Tamura et al. 2015, Hezaveh et al. 2016). These studies led to the reconstruction of the matter distribution of the foreground lens through the detection of low-mass substructures, together with the pixelated surface brightness distribution of dust in the lensed source. Thanks to ALMA CO and [CII] spectroscopic data, it was also possible to measure with high precision the gas mass distribution and the kinematics of the clumps, revealing a disturbed morphology of the stellar, gas, and dust components (Figure 2.6; see also Rybak et al. 2020).

- **HATLASJ090740.0-004200 (SDP.9)** Has been imaged in the Optical with the *Keck* telescope and in the NIR with HST at 1.1 and 1.6 μm (Dye et al. 2014, Negrello et al. 2014). ALMA high-resolution images of the continuum at 1.1 mm and of CO(6-5) (Wong et al. 2017) have been combined and modelled with X-ray band observations from Chandra to reconstruct the morphology and characterise the nuclear emission (Massardi et al. 2017, see Figure 2.5).

- **J091043.0-000322(SDP.11)** is another strongly lensed system discovered during the H-ATLAS Science Demonstration Phase (Negrello et al. 2010). The *Keck* and HST maps revealed the presence of a nearby spiral galaxy whose NIR emission partially overlaps with the one coming from SDP11. Massardi et al. (2017) observed this source with *Chandra*, finding an X-ray emission originating from the nucleus.

- **J114637.9-001132 (HATLAS12-00)** is a cluster-lensed galaxy identified cross-matching the Plank ERCSC (Planck Collaboration, 2011) and phase 1 release of H-ATLAS Examination. The *Keck* Adaptive Optics (K-band), SMA (880 μm), and JVLA CO(1-0) observations confirmed its lens nature (Fu et al. 2012), highlighting the presence of a heterogeneous distribution of various components in different photometric bands.

- **HATLASJ142413.9+022303 (ID141)** is one of the brightest lensed SMGs in the H-ATLAS field, with a SFR of ~2400 $M_{\odot}yr^{-1}$ and has been extensively analysed and modelled in several works (Cox et al. 2011, Bussmann et al. 2013, Omont et al. 2013, Dye et al. 2018, Enia et al. 2018, Cheng et al. 2020, Dye et al. 2022). The *Keck* K-band images analysed in Calanog et al. (2014) revealed two compact galaxies interior to the Einstein ring, each consistent with an early-type morphology. Dye et al. (2018, 2022) performed lens modelling and source reconstruction for the ALMA continuum, and several spectral lines such as CO, [CI], [CII], and H_2O; the analysis also includes kinematic modelling of the spectral components.

- **HATLASJ142935.3-002836 (H1429-0028)** is another extensively studied object among the sample of Negrello et al. (2017). Messias et al. (2014) studied the object adopting a broad range of multi-wavelength imaging, including ALMA Band 3 and Band 6 data at intermediate angular resolution (1.4 arcsec and 0.6 arcsec respectively). The *Keck* telescope Optical imaging (Calanog et al. 2014) revealed the foreground lens to be an edge-on spiral. Further studies (Dye et al. 2018) modelled ALMA Band 7 continuum at higher angular resolution (~ 0.1 arcsec), finding an extremely high SFR to dust mass ratio. Messias et al. (2019) presented new APEX observations of the system, assessing the ISM gas content and the complete CO-SLED of the background source.

- **J132427.0+284449** This peculiar object is another galaxy strongly lensed by a low redshift foreground cluster (George et al. 2013, Timmons et al. 2015).

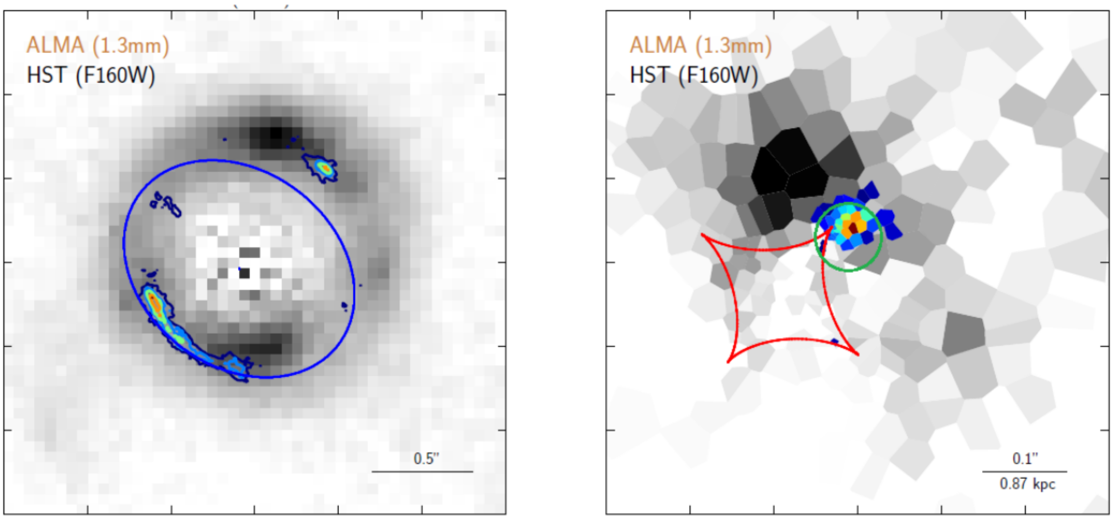

Figure 2.5: Image plane and reconstructed source plane of the strongly lensed DSFG SDP.9. Rainbow colour scale represents the 1.3 ALMA continuum map, HST/WFC3 1.6μm emission is shown in grey colours. The green circle represent the position of the reconstructed X-ray emission peak from *Chandra* observations. Credits: Massardi et al. (2017)

The gravitational distortion results in an extended arc ($\sim$ 1.5 arcsec) detected in HST/*Keck* optical/NIR images and the mm regime with SMM and ALMA. The first observations are presented in George et al. (2013), including dedicated follow-ups at 3.5 mm with the Combined Array for Research in Millimeter-wave Astronomy (CARMA) and VLA 7 GHz observations to trace its radio continuum emission. A detailed lens modelling, together with the derivation of the fundamental physical properties of J132427.0+284449 has been performed by Timmons et al. (2015).

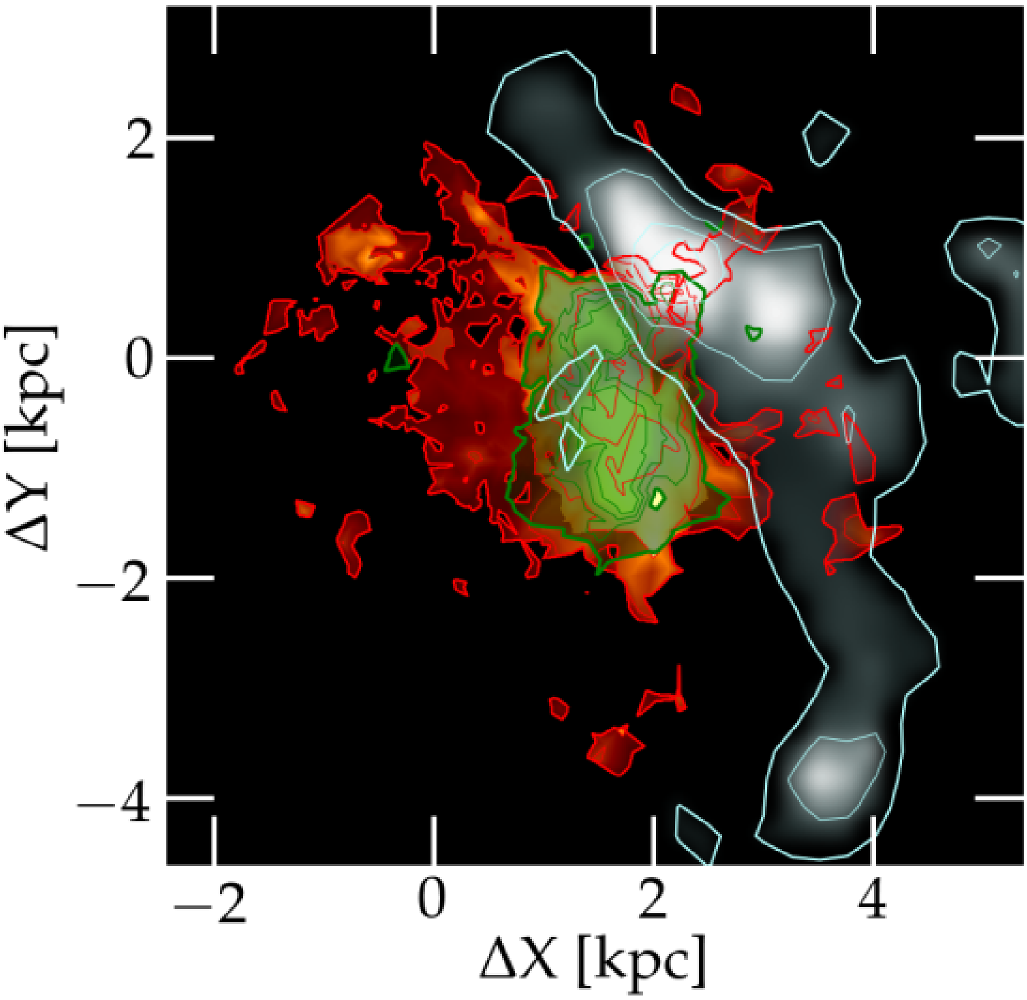

Figure 2.6: Reconstructed source plane of the strongly lensed DSFG SDP.81. Grey contours enclose the NIR emission from HST/WFC3 data, ALMA 1 mm continuum and the combined CO(5-4) and CO(8-7) emission is shown in green and red respectively. Credits: Rybak et al. (2015b)

Chapter 3

Investigating Radio Properties of a Sample of (Candidate) Strongly Lensed DSFGs

In this Chapter I will present the radio-FIR correlation for a sample of 28 (candidate) strongly lensed DSFGs in the redshift range $1 \lesssim z \lesssim 4$, observed in the HATLAS fields and selected from the sample of Negrello et al. (2017). As highlighted in Section 2.5, selecting a statistically significant sample of lensed galaxies can offer the major advantage of the enhancement of the source brightness as a consequence of lensing magnification. The radio information comes either from high-sensitivity dedicated ATCA observations at 2.1 GHz or from cross-matches with the VLA-Faint Images of the Radio Sky at Twenty-Centimeters (FIRST) survey at 1.4 GHz.

In Section 3.1 I will introduce the FIRRC and the physical mechanisms underlying this correlation and its redshift evolution. In Section 3.2 I will present our proprietary ATCA data, their observations, reduction and imaging to retrieve 2.1 GHz measurements of radio properties for the 30 candidate lensed galaxies in the H-ATLAS Southern field. In Section 3.3, by combining our data with VLA FIRST survey data and H-ATLAS catalogued data, I will present the derived FIRRC for the sample, its redshift evolution, and its luminosity dependence. In particular, I will compare the results to that of the lensed quasar sample by Stacey et al. (2018, 2019), highlighting the complementarity of the two selections and, finally presenting a physically-motivated interpretation in the framework of an in-situ galaxy evolution model (Section 3.4). Finally, I will summarise the results in Section 3.5). The content of this Chapter is primarily based on the findings published in Giulietti et al. (2022).

3.1 The FIRRC

For several decades the rest-frame 1.4 GHz radio luminosity density $L_{1.4\,\mathrm{GHz}}$ (W Hz^{-1}) emitted by bright dusty star-forming galaxies has been associated with their FIR luminosity L_{FIR} (8-1000 μm rest-frame) in terms of an empirical relation between these two quantities, namely the *FIR-radio correlation* (Helou et al. 1985, Yun et al. 2001). Such a relation is found to be roughly linear across ~ 3 orders of magnitude in luminosity $9 \lesssim \log(L_{\rm FIR}/{\rm L}_\odot) \lesssim 12.5$ with a rather low 1σ scatter $\lesssim 0.26$ dex; it is often described via the parameter $q_{\rm FIR}$ (e.g. Yun et al. 2001, Magnelli et al. 2015) defined as:

$$q_{\rm FIR} = \log\left(\frac{L_{\rm FIR}[{\rm W}]/3.75\times 10^{12}}{L_{1.4\,{\rm GHz}}[{\rm W\,Hz^{-1}}]}\right). \tag{3.1}$$

The tightness of this relation can be ascribed to the common origin of the radio and FIR emissions as interpreted by *calorimetric* models (Voelk 1989, Lacki & Thompson 2010). In this framework, cosmic ray electrons lose all of their energy prior to escaping the host galaxy, which is assumed to be optically thick to the UV light coming from young newborn stars. This UV light is absorbed by the interstellar dust within the galactic medium and subsequently emitted again in the FIR regime. At the end of their lives, the same massive stars explode as Type II supernovae producing cosmic ray electrons and positrons, radiating most of their energy in the radio band through synchrotron emission before escaping the galaxy. Additionally, a secondary component of the radio emission comes from the free-free contribution originated by the hot and ionised HII regions.

The FIR-radio correlation is well established in the local universe (Helou et al. 1985, Yun et al. 2001, Jarvis et al. 2010, Smith et al. 2014, Molnár et al. 2017, Wang et al. 2019b). Its apparent tightness encouraged the use of radio emission as an unbiased tracer of obscured star formation in dusty galaxies (Kennicutt & Evans 2012), and prospectively as a probe to obtain a comprehensive view of the cosmic star formation history up to very high redshift (Madau & Dickinson 2014, Delhaize et al. 2017, Novak et al. 2017). This is, in fact, one of the key science drivers of the SKA and of its pathfinder telescopes such as the Australian Square Kilometre Array Pathfinder (ASKAP) and MeerKAT (e.g., Jarvis et al. 2015) and of the next-generation Very Large Array (ngVLA), focused on the investigation of the emission mechanisms that power the radio continuum emission in galaxies (Murphy 2019).

For example, early science data at 1.3 GHz from the MeerKAT International GHz Tiered Extragalactic Exploration survey (MIGHTEE, Jarvis et al. 2016) have been recently analysed in An et al. (2021), together with radio data from the VLA and the GMRT, to investigate the radio spectral properties and the FIRRC for a sample of 2094 SFGs in the COSMOS field. Moreover, future observations with SKA will enable detailed investigations of magnetic fields in galaxies, which can be particularly relevant in the FIRRC, especially in the low SFR regimes (Schleicher & Beck 2016).

To achieve this goal, however, it is necessary to set on a firm basis the connection between radio and FIR emission (hence star formation), and to assess its redshift dependence, which has been strongly debated in the last decades. From a theoretical perspective, an evolution in redshift is expected as a consequence of either the additional energy losses of the cosmic rays interacting with the CMB photons through inverse Compton scattering (e.g. Lacki & Thompson 2010, Murphy 2009; see also Appendix A.3) or because of the co-evolution of AGNs in dusty environments with ongoing star formation in the early stages of galaxy evolution

(Lapi et al. 2018). In fact, sources whose radio emission is dominated by nuclear activity show up as outliers of the FIR-radio correlation (Sopp & Alexander 1991, Stacey et al. 2018). A $q_{\rm FIR} = 1.8$ was proposed by Condon et al. (2002) as the boundary between star-formation and (radio-loud) AGN-dominated radio emission.

From an observational point of view, evolution is far from being settled. On the one hand, different works found no significant evidence of a trend with redshift (e.g. Sargent et al. 2010). On the other hand, several authors pointed out the presence of a slight decline of the $q_{\rm FIR}$ parameter: Magnelli et al. (2015) report evidence of a weak redshift evolution in a mass-selected sample of galaxies, rendered as $q_{\rm FIR} \propto (1+z)^{-0.12\pm0.04}$; a similar result was found by Basu et al. (2015) for a sample of blue cloud galaxies at $z \leq 1.2$; Tabatabaei et al. (2016) studied the radio continuum emission from the KINGFISH sample of nearby galaxies finding that the FIR to 1-10 GHz luminosity ratio could decrease with the star formation rate, suggesting a decrease of the ratio at high redshifts where mostly luminous/star forming galaxies are detected; more recently, Ocran et al. (2020) analysed the radio properties of 1685 star-forming galaxies selected at 610 MHz with the GMRT, inferring an evolution $q_{\rm FIR} \propto 2.86 \pm 0.04(1+z)^{-0.20\pm0.02}$ up to $z \sim 1.8$; Delhaize et al. (2017) found $q_{\rm IR} \propto (1+z)^{-0.19\pm0.01}$ for galaxies selected with the VLA at 3 GHz; Calistro Rivera et al. (2017) obtained $q_{\rm FIR} \propto (1+z)^{-0.15\pm0.03}$ for a sample of star-forming galaxies obtained with Low Frequency Array (LOFAR) at 150 MHz.

This observed evolution would imply that high-z ($z \gtrsim 1$) star-forming galaxies somehow present a more pronounced radio emission (or a lower FIR luminosity) compared to their local counterparts. Other studies instead argued on the possibility that the observed trend with the redshift may be a consequence of selection effects (e.g. Sargent et al. 2010, Bourne et al. 2011, Molnár et al. 2021), which can be ascribed to the difference in depth between radio and FIR surveys and to flux-limited samples or to selections biased towards more massive galaxies, as recently reported by different authors (Delvecchio et al. 2021, Bonato et al. 2021, Smith et al. 2021). In fact, investigations at higher redshifts carried out up to $z \gtrsim 2$ (Ivison et al. 2010a, Thomson et al. 2014, Magnelli et al. 2015) have been limited by the availability of very deep radio data and/or redshift measurements. In this sense, selection biases can be minimised in homogeneous populations of FIR/sub-mm galaxies (e.g. Algera et al. 2020).

3.2 Radio observations of the H-ATLAS sample

3.2.1 ATCA follow-ups

The sample in the H-ATLAS SGP field comprises 30 sources with $22 < \text{RA} < 0$h and $-36 < \delta < -28$. All these are candidates, i.e. not yet confirmed at the time of observations, strongly lensed galaxies. Observations were centred at 2.1 GHz with a 2 GHz bandwidth and were carried out with the Australia Telescope Compact Array (ATCA) on 2017 December 14th and on 2019 July 31st respectively with 6 km and 750 m East-West configurations. The corresponding largest angular scales

(LAS) are 3.6 and 1.8 arcmin for the first and second configurations respectively. The expected resolution is ~ 10 arcsec if the farthest antenna, CA06, is included in the data, as in our case. In 2017 we got 12 allocated hours that allowed us to perform ~ 7 × 2min cuts on each target. In 2019 we performed 2 × 2min at least on each source for a total of 4 observing hours. The observing strategy allowed enough coverage of the uv plane to recover suitable images of the targets. The weather and system conditions were excellent in both the observing epochs.

I have performed data editing, calibration, and imaging using Miriad (Sault et al. 1995). Data flagging has been performed automatically through the task `PGFLAG` and I have followed the common calibration procedures for 16 cm data sets. I have manually checked that all the major RFI features were removed, flagging more than 30% of the data, but still recovering a 0.06 mJy beam^{-1} theoretical noise level (1σ). PKS1934-638 was observed as a bandpass and flux calibrator. Two-phase calibrators were observed during the 12-hour and 4-hour observations (PKS0008-421 and PKS2255-282) and their solutions are merged to correct the data phases as a function of time. The calibration process scheme with the tasks used is shown in Figure 3.1. The first step consists of determining the primary calibrator (PKS1934-638) corrections (the task used is `MFCAL`), as antenna gains, delays terms and passband responses, by averaging the data. The second task, `GPCAL` then is used to determine corrections for both antenna gains and instrumental polarisation from the primary calibrator. The solutions are then copied through the task `GPCOPY` into the phase (secondary) calibrator `GPCAL` is re-applied to solve for antenna gains and the XY phases as a function of time. `GPBOOT` bootstraps the flux density of the secondary calibrator by knowing the flux density of the primary. Finally, the calibration solutions are copied on the target.

I have combined the 2017 and 2019 data sets during the imaging process with the task `UVAVER` in order to improve the uv-sampling and the dynamic range of the final image. Furthermore, I have performed self-calibration in each observed field, exploiting the presence of several bright and point-like sources in the large field of view (22 arcmin FWHM), allowing the improvement of the overall signal-to-noise. Flux densities ($S_{\rm image}$) and image noise ($\sigma_{\rm image}$) are then extracted from the Briggs-weighted continuum images with a robust factor of 0.5. The average synthesised beam is ~ 7.4 × 3.9 arcsec. Noise is computed as

$$\delta S_{\rm image} = \sqrt{(\sigma_{\rm image})^2 + (0.05 \times S_{\rm image})^2} \tag{3.2}$$

to consider the calibration errors. For later use, I convert the ATCA flux densities from 2.1 GHz to 1.4 GHz assuming a power law spectrum $S_\nu = \nu^\alpha$ with average radio spectral index $\alpha = -0.7 \pm 0.14$, consistently with Stacey et al. (2018).

3.2.2 The FIRST catalog

The FIRST (Faint Images of the Radio Sky at Twenty-cm; Becker et al. 1995) survey, performed with the VLA reaches a typical rms of 0.15 mJy beam $^{-1}$ and a resolution ~ 5 arcsec comparable with those of ATCA observations. FIRST overlaps with the Equatorial and NGP H-ATLAS fields, thus complementing our

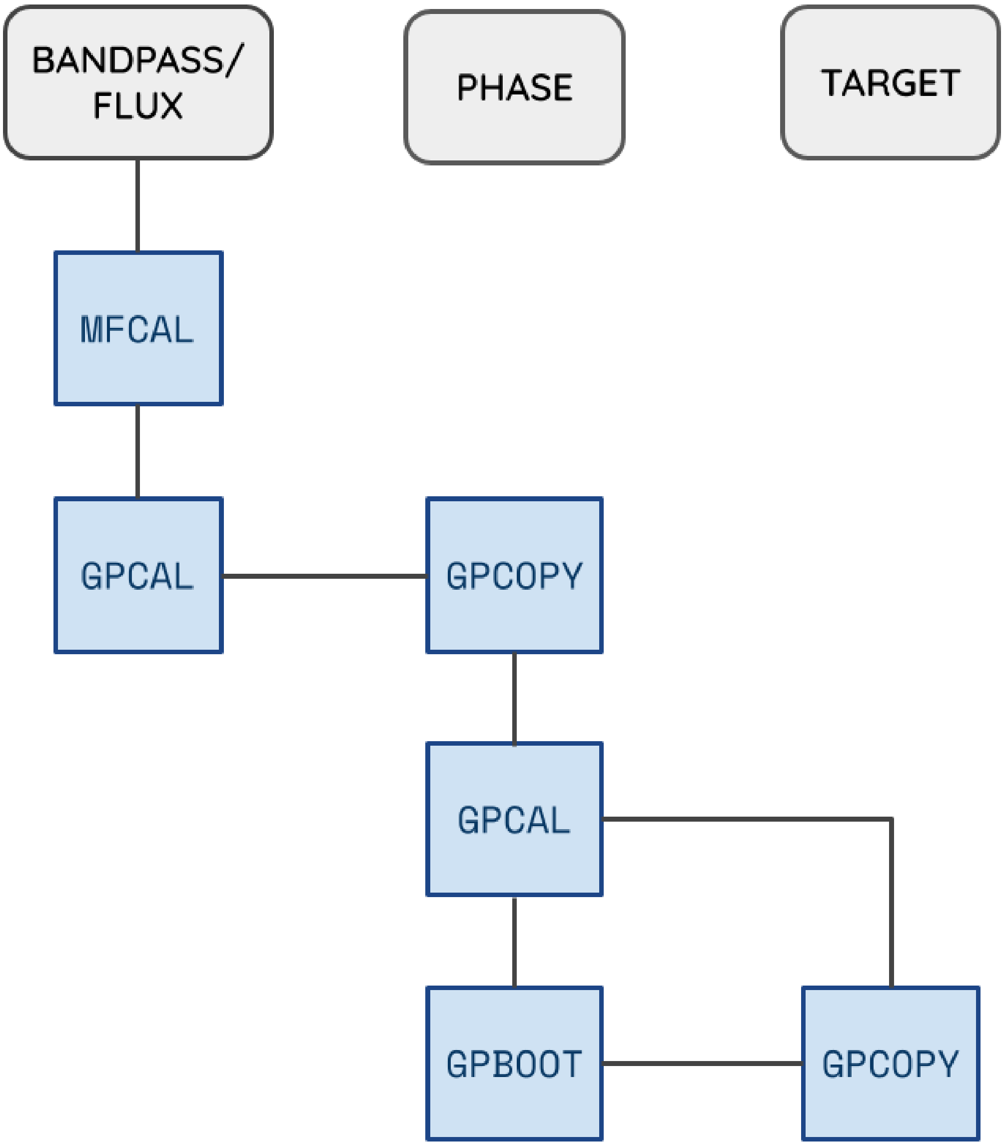

Figure 3.1: Flow chart of the calibration process. Blue cells show the tasks adopted and grey cells represent (from the left) the bandpass/flux calibrator, the phase calibrator and the target.

search for radio counterparts for the Negrello et al. (2017) sample. The cross-match with the FIRST catalogue within 10 arcsec of the *Herschel*-ATLAS position yields 8 potential counterparts, while 12 objects present a clear $\gtrsim 3\,\sigma$ signal in the FIRST maps, within the H-ATLAS beam size. For one of the matched sources, namely H-ATLAS J142935.3-002836, the FIRST flux density value has been replaced with the more reliable one coming from the JVLA 7 GHz high resolution (~ 0.3 arcsec) and high sensitivity (10 μJy beam^{-1}) observations described in Messias et al. (2014) (converted at 1.4 GHz).

Observations at 6.89 GHz from the JVLA are available for one additional source (H-ATLASJ133542.9+300401) and are described in detail by Nayyeri et al. (2017). The image reaches an rms of 7.8 μJy beam^{-1} and a beam size of 1.01×0.81 arcsec; for my analysis, I use the flux density at 1.4 GHz reported in Table 1 of Nayyeri et al. 2017.

H-ATLASJ090311.6+003907 (SDP.81) is detected in the FIRST catalogue, was observed by the Extended Very Large Array (EVLA) at 8.4 GHz (Valtchanov et al. 2011, Rybak et al. 2015b). However, its radio emission is likely to have originated from the AGN hosted by the foreground lens (Tamura et al. 2015, Rybak et al. 2020); for this reason it has been excluded a priori as a possible counterpart.

3.2.3 Selection of the radio counterparts

The detected sources display a variety of radio morphologies: some of them show a compact radio emission, and others instead feature a more extended structure or even multiple components, but the angular resolution of the observations is not enough to resolve any of the arcs possibly associated with lensing effects.

For this reason, in order to establish whether a radio source is correctly assigned as a counterpart of our selected *Herschel* sample, I selected radio detections with at least $> 3\sigma_{\rm image}$ confidence level and then consider their position with respect to the optical/IR and the mm high angular resolution imaging.

I consider as a counterpart only the component nearest to the SPIRE peak position, whose radio-detected emission overlaps with sources detected in NIR or mm, even though this can result in an underestimation of the radio luminosity in case of multiple component radio sources. In the NIR I exploit HST/WFC3 wide-J filter F110 maps described in Negrello et al. (2014) and more recent snapshot observations covering the Equatorial and Southern fields (PI: Marchetti L., 2019), both reaching an angular resolution of ~ 0.13 arcsec. The remaining sources are observed by the UKIDSS Large Area Survey (UKIDSS-LAS; Lawrence et al. 2007) and the VISTA Kilo-Degree Infrared Galaxy Survey (VIKING; Edge et al. 2013), reaching angular resolutions $\lesssim 1$ arcsec. Millimetric high-resolution images come from the ALMA Science Archive available at the time of this analysis: some of the sources located in the SGP have been targets of Band 4 follow-ups at ~ 1.7 arcsec, while for objects in the Northern and Equatorial fields, I made use of the images found in Bands 4, 6 and 7, with highest angular resolutions spanning from ~ 1.2 to < 0.1 arcsec. For sources without high-resolution imaging, I compared the uncertainties in the radio positional accuracy (Becker et al. 1995) with respect to the one from SPIRE/250 μm (Bourne et al. 2011), with a $\sim 3\sigma$ tolerance. I include only objects showing a superimposition between the two centroids and/or between the SPIRE positional uncertainty and the radio detection.

Following the above criteria I found 11 and 17 sources in ATCA and FIRST respectively, shown in Figure 3.2 and Figure 3.3. Please note that the HST/WFC3 maps reported here do not take into account the well-known positional offset between ALMA and HST counterparts (Dunlop et al. 2016, Rujopakarn et al. 2016). Therefore, combining ATCA follow-up and FIRST cross-matches I collected radio measurements for 28 out of the 80 galaxies in the original sample by Negrello et al. (2017). For the remaining objects, I have defined an upper limit for detection at 3σ from the noise at the position of the sources in the FIRST images and as $3\sigma_{\rm image}$ for ATCA images. Table 3.1 summarises the radio and FIR photometry for our sample. Finally, it should be emphasised that the focus of this analysis is solely on utilising the existing archived radio data, without delving into detailed descriptions of individual objects.

I have taken into account the information available in the literature for the confirmed cases at the time this analysis has been performed, but for the remaining unconfirmed ones in the absence of accurate lens modelling and/or higher angular resolution observations, it was not possible to confirm whether or in which fraction the radio emission is associated to the lensed object. This is also valid for the SPIRE flux densities in the unconfirmed cases. Indeed, as shown in Figures 3.2 and 3.3, multiple sources entering the *Herschel* beam are detected in the ALMA (sub-)mm maps, leading to a possible overestimation of the effective FIR luminosity of the actual counterpart. A fraction of low-resolution sub-mm detected sources is indeed expected to be composed of multiple ALMA sources (Hodge et al. 2013, Smail & Walter 2014, Bussmann et al. 2015). Here I have assumed that the observed SPIRE flux density mostly originated from the same object and that no strong FIR contamination from possible nearby sources is present. In any case, this should not affect the objects confirmed to be lensed. In fact, we expect the FIR luminosity of the lensed galaxies in our sample to be magnified by a factor spanning the range $\sim 3-10$ (Negrello et al. 2017, Enia et al. 2018), with a negligible contribution from possible additional unlensed sources entering the *Herschel* beam.

3.2.4 Physical properties of the sample

The rest-frame radio luminosity $L_{1.4\,\rm GHz}$ at 1.4 GHz for each source (see Table 3.2) is computed as

$$L_{\nu,\rm e} = \frac{4\pi D_{\rm L}^2(z)}{(1+z)^{1+\alpha}} \left(\frac{\nu_{\rm e}}{\nu_{\rm o}}\right)^{\alpha} S_{\nu,\rm o}\,, \tag{3.3}$$

where $S_\nu \propto \nu^\alpha$ is the monochromatic flux density at a certain frequency and α is assumed to be -0.7 as the typical value at 1.4 GHz for FIRST (Kimball & Ivezić 2008), $\nu_{\rm e}$ and $\nu_{\rm o}$ are the emitted and the observed frequency, and $D_{\rm L}$ is the luminosity distance computed for each redshift according to the adopted ΛCDM cosmology. Our 28 objects span a range $1.9\times10^{24} \lesssim L_{1.4\,\rm GHz} \lesssim 1.8\times10^{26}$ W Hz^{-1} (uncorrected for the lens magnification factor μ), with a median value of $L_{1.4\,\rm GHz} \sim 2.4\times10^{25}$ W Hz^{-1}.

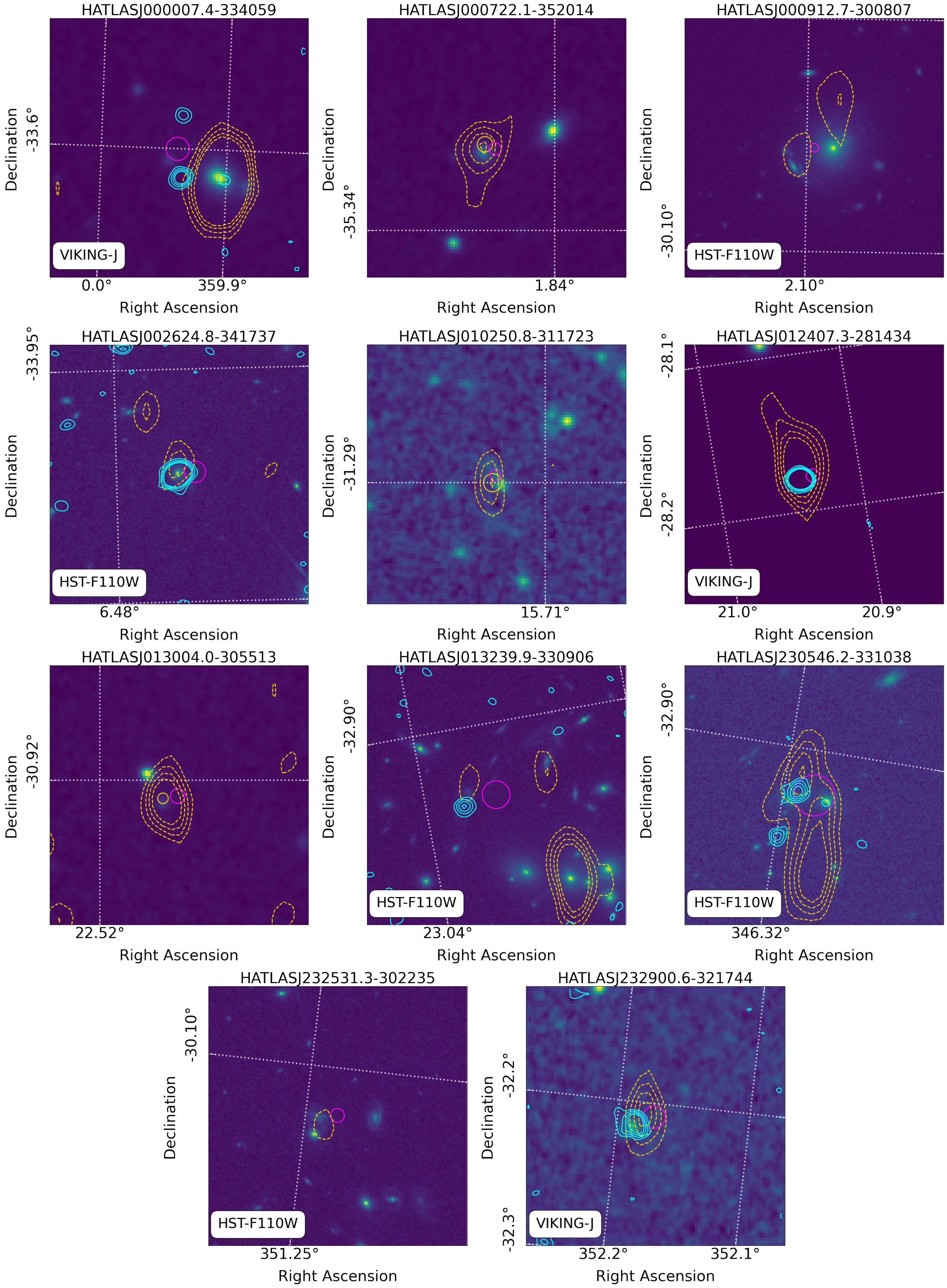

Figure 3.2: Cutouts of NIR images with the best available angular resolution centred on the *Herschel* positions for the 11 sources with an ATCA cross-match. Contours at 3,5,7,9σ levels are shown in gold for the radio and cyan for ALMA. Circles are the SPIRE position with a $3\sigma_{\rm pos}$ radius. RA and Dec are reported in Deg units. The postage stamps are 30×30 arcsec

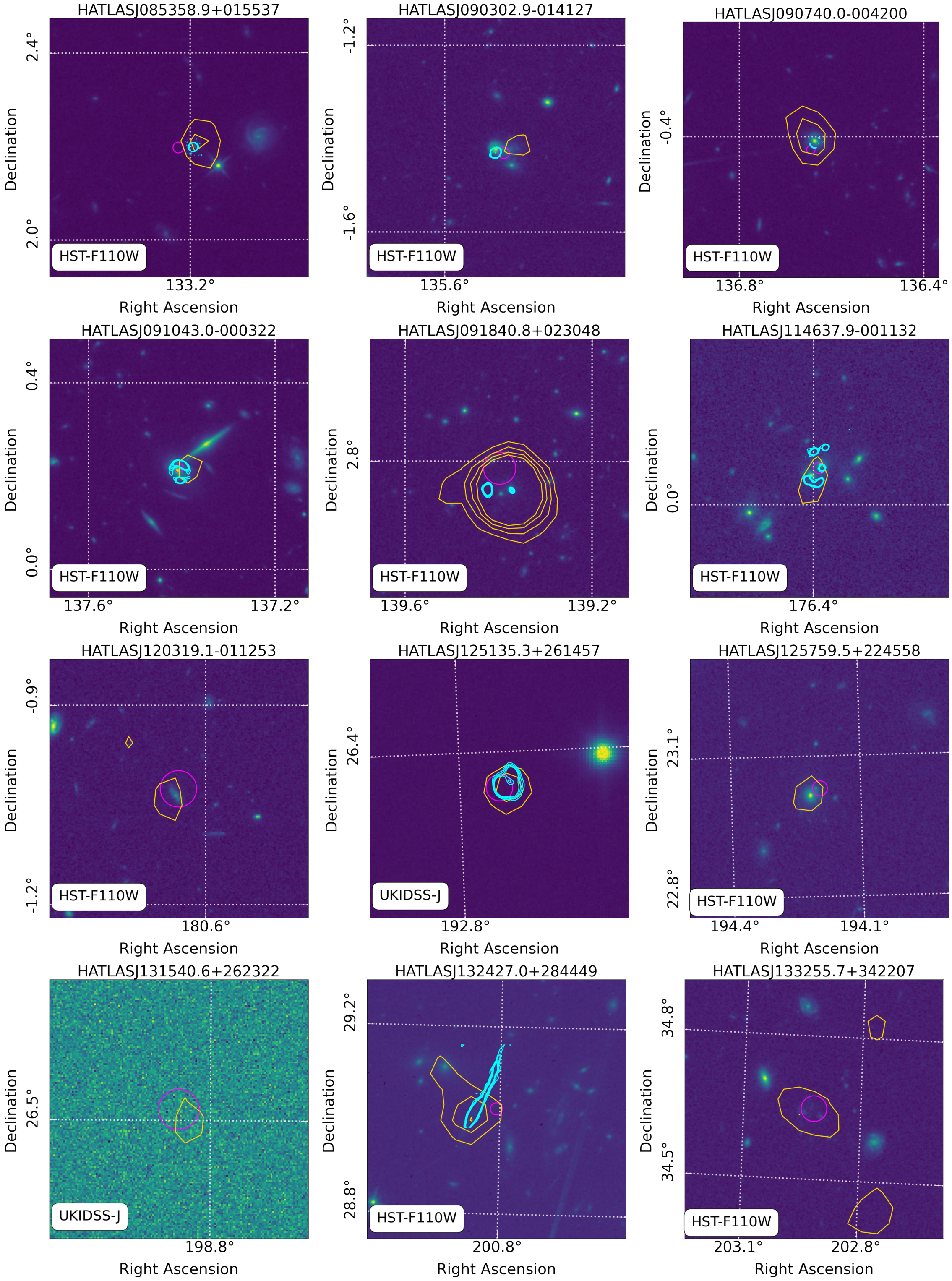

Figure 3.3: Cutouts of NIR images with the best available angular resolution centred on the *Herschel* positions for the 16 sources with a FIRST cross-match. Contours at 3,5,7,9σ levels are shown in gold for FIRST and cyan for ALMA. Circles are the SPIRE position with a 3$\sigma_{\rm pos}$ radius. RA and Dec are reported in Deg units. The postage stamps are 30x30 arcsec.

M14: Messias et al. (2014); N17: Nayyeri et al. (2017), † spectroscopic redshifts of H-ATLASJ130333.1+244643, H-ATLASJ131540.6+262322 and H-ATLASJ133255.7+342207 are taken from Neri et al. (2020).

#H-ATLAS ID	$S_{250\mu m}$ [mJy]	$S_{350\mu m}$ [mJy]	$S_{500\mu m}$ [mJy]	$z^{\dagger}$	lenscode	$S_{1.4\mathrm{GHz}}$ [mJy]	counterpart	dist [arcsec]
J000007.4-334059	130.3±5.4	160.1±5.9	116.2±6.5	2.56±0.43	C	1.91±0.2	ATCA image	6.6
J000722.1-352014	237.3±5.2	192.8±5.6	107.5±6.6	1.46±0.3	C	0.39±0.08	ATCA image	1.3
J000912.7-300807	352.8±5.4	272.6±6.1	156.1±6.8	1.39±0.29	C	0.20±0.05	ATCA image	2.2
J002624.8-341737	137.7±5.2	185.9±5.8	148.8±6.8	2.96±0.48	C	0.26±0.06	ATCA image	1.8
J010250.8-311723	267.9±5.2	253.1±5.7	168.1±7.1	1.92±0.35	C	0.29±0.06	ATCA image	0.9
J012407.3-281434	257.5±6	271.1±6	203.9±6.8	2.31 ±0.4	C	0.79±0.13	ATCA image	2.1
J013004.0-305513	164.4±4.3	147.5±5.1	100.6±5.9	1.84±0.34	C	0.65±0.11	ATCA image	1.7
J013239.9-330906	112±5.5	148.8±6.2	117.7±7	2.9 ±0.47	C	0.19±0.05	ATCA image	3.5
J085358.9+015537	396.4±7.6	367.9±8.2	228.2±8.9	2.0925	A	1.19±0.16	FIRST cat	2.0
J090302.9-014127(SDP.17)	354.1±7.2	338.8±8.1	220.2±8.6	2.3049	A	0.41±0.14	FIRST image	2.3
J090740.0-004200(SDP.9)	477.6±7.3	327.9±8.2	170.6±8.5	1.577	A	1.21±0.15	FIRST cat	2.1
J091043.0-000322(SDP.11)	420.8±6.5	370.5±7.4	221.4±7.8	1.786	A	0.97±0.19	FIRST image	1.3
J091840.8+023048	125.7±7.2	150.7±8.3	128.4±8.7	2.581	C	4.63±0.3	FIRST cat	2.2
J114637.9-001132	316±6.6	357.9±7.4	291.8±7.7	3.259	A	1.14±0.15	FIRST image	0.9
J120319.1-011253	114.3±7.4	142.8±8.2	110.2±8.6	2.26±0.39	C	0.82±0.15	FIRST image	1.8
J125135.3+261457	157.9±7.5	202.3±8.2	206.8±8.5	3.675	A	1.25±0.16	FIRST cat	0.9
J125759.5+224558	272.4±7.3	215±8.1	137.8±8.7	1.53±0.3	B	0.85±0.14	FIRST image	0.9
J131540.6+262322	94.1±7.4	116.1±8.2	108.6±8.7	2.4417	C	0.96±0.15	FIRST image	1.2
J132427.0+284449	342.4±7.3	371±8.2	250.9±8.5	1.6760	A	1.95±0.17	FIRST cat	3.9
J133255.7+342207	164.3±7.5	186.8±8.1	114.9±8.7	2.9268	C	1.00±0.16	FIRST image	1.9
J133542.9+300401	136.6±7.2	145.7±8.0	125.0±8.5	2.685	A	0.14±0.02	N17 obs	
J133649.9+291800	294.1±6.7	286±7.6	194.1±8.2	2.2024	A	0.87±0.15	FIRST image	1.2
J134429.4+303034	462±7.4	465.7±8.6	343.3±8.7	2.301	A	1.29±0.16	FIRST cat	0.6
J142413.9+022303	112.2±7.3	182.2±8.2	193.3±8.5	4.243	A	0.79±0.16	FIRST image	2.2
J142935.3-002836	801.8±6.6	438.5±7.5	199.8±7.7	1.027	A	2.8±0.67	M14	
J230546.2-331038	76.8±5.6	110.9±5.9	110.4±7	3.67±0.56	C	0.37±0.07	ATCA image	2.8
J232531.3-302235	175.5±4.3	227.0±4.7	175.7±5.7	2.8±0.46	C	0.105±0.03	ATCA image	1.9
J232900.6-321744	118.3±4.7	141.2±5.2	119.7±6.4	2.81±0.46	C	0.31±0.06	ATCA image	1.6

Table 3.1: Radio and FIR properties of the candidate and confirmed lensed galaxies with a counterpart in the radio bands. Columns are as follows: H-ATLAS IDs; *Herschel*/SPIRE flux densities; source redshift; lens classification from Negrello et al. (2017): (A) confirmed dusty lensed, (B) likely to be lensed, (C) uncertain; radio flux densities at 1.4 GHz; origin of the radio counterpart (images, catalogue or literature); distance (in arcseconds) of the radio peak from the *Herschel* position, if available.

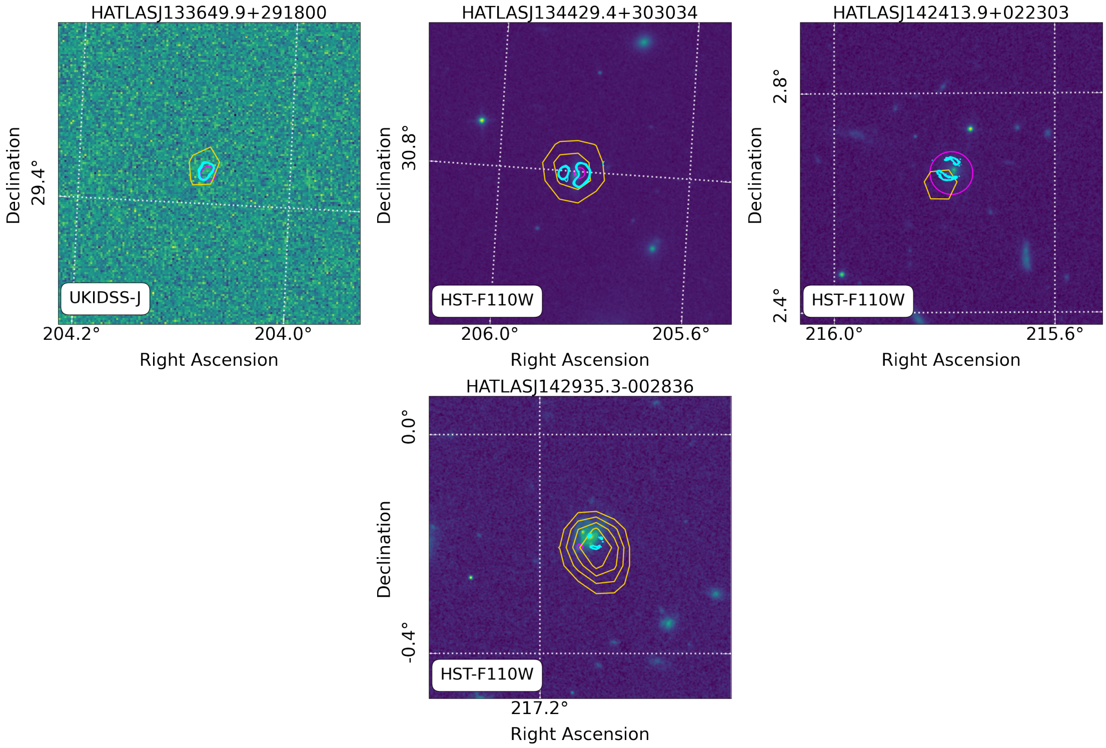

Figure 3.3: *Continued.*

The FIR luminosity $L_{\rm FIR}$ (see Table 3.2) is computed for each source in the main sample of Negrello et al. (2017) by fitting the *Herschel*/SPIRE photometry described in Section 2.4. I use a single-temperature modified black body under the optically-thin approximation with dust emissivity index $\beta = 1.5$ (Nayyeri et al. 2016, Negrello et al. 2017), the spectrum normalisation and the dust temperature ($\rm T_{dust}$) are kept as free parameters. The model ($S_{\nu,\rm best}$) which minimises the χ^2 is then integrated over the wavelength range 8-1000 μm as follows:

$$L_{\rm FIR} = \frac{4\pi D_L^2}{(1+z)} \int_{8\,\mu{\rm m}}^{1000\,\mu{\rm m}} S_{\nu,\rm best} d\nu. \tag{3.4}$$

The resulting FIR luminosities (uncorrected for lens magnification) and dust temperatures are shown in Figure 3.4. The FIR luminosities span the range $1.3 \times 10^{13} \lesssim L_{\rm FIR}/{\rm L}_{\odot} \lesssim 1.1 \times 10^{14}$, with a median value of $L_{\rm FIR} \sim 3.5 \times 10^{13}$ $L_{\odot}$. The median value of the dust temperature for the total sample of candidate strongly lensed galaxies is $T_{\rm dust} = 35.2 \pm 2.1$, consistently with what was found by Negrello et al. (2017) for the same sample.

3.3 The FIR-radio correlation for (candidate) lensed galaxies

In this Section, I will explore the correlation between the radio and the FIR luminosities for my sample of 28 (candidate) lensed dusty star-forming galaxies,

#H-ATLAS ID	$\log(L_{1.4GHz})$ $[L_\odot]$	$\log(L_{FIR})$ $[W\ Hz^{-1}]$	q_{FIR}
J000007.4-334059	25.86±0.04	13.40±0.05	1.55±0.15
J000722.1-352014	24.62±0.06	13.11±0.02	2.49±0.13
J000912.7-300807	24.29±0.10	13.24±0.01	2.96±0.23
J002624.8-341737	25.13±0.08	13.59±0.07	2.47±0.24
J010250.8-311723	24.77±0.07	13.41±0.03	2.64±0.17
J012407.3-281434	25.37±0.05	13.58±0.04	2.20±0.14
J013004.0-305513	25.07±0.05	13.15±0.03	2.08±0.12
J013239.9-330906	24.98±0.10	13.48±0.07	2.50±0.28
J085358.9+015537	25.46±0.06	13.68±0.03	2.22±0.14
J090302.9-014127	25.09±0.15	13.72±0.03	2.64±0.35
J090740.0-004200	25.19±0.05	13.57±0.01	2.39±0.12
J091043.0-000322	25.22±0.08	13.55±0.02	2.33±0.20
J091840.8+023048	26.25±0.02	13.39±0.06	1.14±0.15
J114637.9-001132	25.86±0.06	14.03±0.05	2.17±0.18
J120319.1-011253	25.54±0.08	13.40±0.06	1.86±0.23
J125135.3+261457	26.01±0.05	13.87±0.09	1.86±0.23
J125759.5+224558	25.01±0.07	13.21±0.02	2.20±0.17
J131540.6+262322	25.51±0.07	13.21±0.07	1.70±0.23
J132427.0+284449	25.46±0.04	13.37±0.04	1.91±0.12
J133255.7+342207	25.42±0.07	13.33±0.04	1.92±0.18
J133542.9+300401	24.75±0.07	13.45±0.05	2.70±0.20
J133649.9+291800	25.37±0.07	13.59±0.03	2.22±0.18
J134429.4+303034	25.59±0.05	13.83±0.04	2.24±0.15
J142413.9+022303	25.95±0.09	13.93±0.12	1.99±0.34
J142935.3-002836	25.13±0.10	13.57±0.01	2.44±0.23
J230546.2-331038	25.49±0.06	13.58±0.1	2.10±0.27
J232531.3-302235	24.69±0.11	13.63±0.06	2.95±0.30
J232900.6-321744	25.15±0.06	13.45±0.06	2.30±0.19

Table 3.2: 1.4 GHz and FIR luminosities (*uncorrected* for lensing magnification effects) and q_{FIR} parameter for the 28 galaxies in the presented sample.

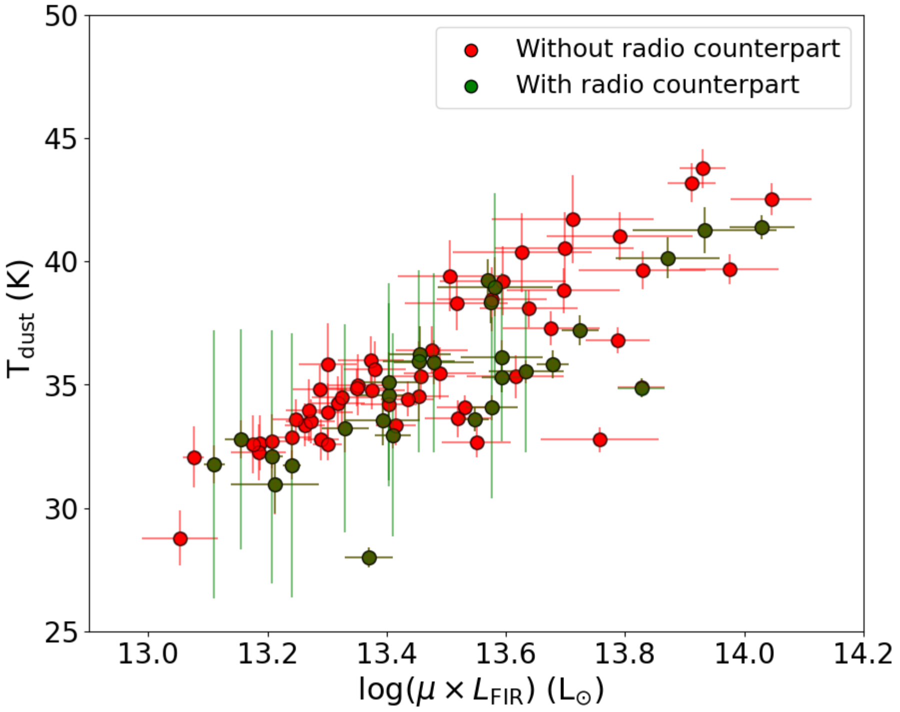

Figure 3.4: Dust temperatures against FIR luminosities (uncorrected for magnification) for the 80 (candidate) strongly lensed galaxies from Negrello et al. (2017). Green and red dots show respectively sources with and without radio counterparts.

focusing on the observed quantities uncorrected for lensing magnification effects. For each galaxy, I have computed the $q_{\rm FIR}$ parameter following equation 3.1.

Figure 3.5 shows the $q_{\rm FIR}$ parameter as a function of redshift. I find a weak yet appreciable decline of $q_{\rm FIR}$ with increasing z. My result is compared with the redshift evolution reported by Magnelli et al. (2015) and Delhaize et al. (2017) (red and green shaded areas respectively) and with the median value of the $\rm q_{FIR}$ parameter for star-forming radio galaxies from Ivison et al. (2010b). Magnelli et al. (2015) studied a mass-selected sample of star-forming galaxies up to $z \sim 2$, finding a slight evolution $q_{\rm FIR}(z) = (2.35 \pm 0.08)(1 + z)^{-0.12\pm0.04}$; in Figure 3.5 their relation is extended up to higher redshifts to ease the comparison with our sample. Similar results were obtained by Delhaize et al. (2017) from a radio-selected sample of star-forming galaxies extending up to $z \sim 6$, as described by the relation $q_{\rm FIR}(z) = (2.52 \pm 0.03)(1 + z)^{-0.21\pm0.01}$. The majority of our sources show values of $q_{\rm FIR}$ within the 2σ interval around the median value of Ivison et al. (2010b) for star-forming galaxies. Three sources lie below the limit of $q_{\rm FIR} \sim 1.8$ established by Condon et al. (2002) to separate between sources with radio emission powered by star formation and by AGN, respectively. The AGN-powered objects are all located at redshifts $z \gtrsim 2$.

Figure 3.6 I show the dependence of the $q_{\rm FIR}$ parameter on the radio luminosity (uncorrected for lensing magnification). A clear tendency of the $q_{\rm FIR}$ parameter to decrease with increasing radio power is visible. The radio excess follows from the definition given in Eq. 3.1 and, consequently, this observed trend can be ascribed to the presence of an AGN. Such behaviour is similar to what has been

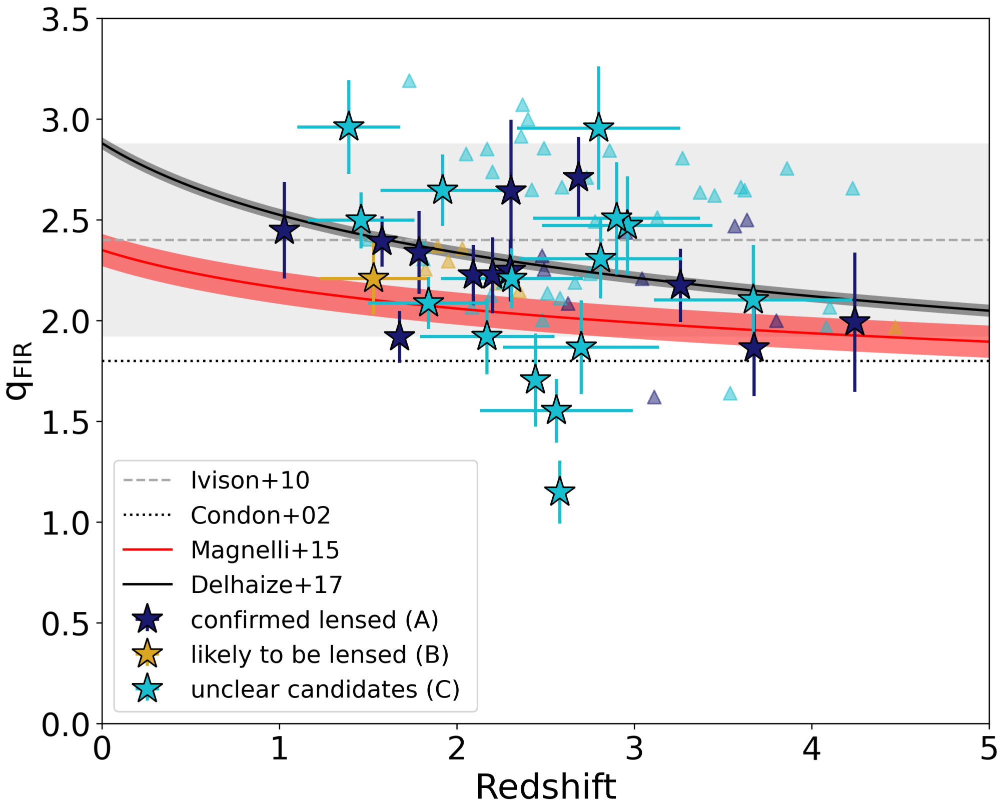

Figure 3.5: $q_{\rm FIR}$ parameter (see equation 3.1) as a function of redshift. The grey dashed line corresponds to the median $q_{\rm FIR}$ for star-forming galaxies as defined by Ivison et al. (2010b), and the grey shaded area represents the 2σ dispersion. Red and black shaded areas represent respectively the relation by Magnelli et al. (2015) and Delhaize et al. (2017). Stars are the 28 galaxies in my sample: (blue) the confirmed lensed objects, (yellow) the likely lensed objects, and (cyan) the uncertain objects. Triangles mark values of $q_{\rm FIR}$ computed with 3σ upper limits for the remaining undetected sources in the radio band.

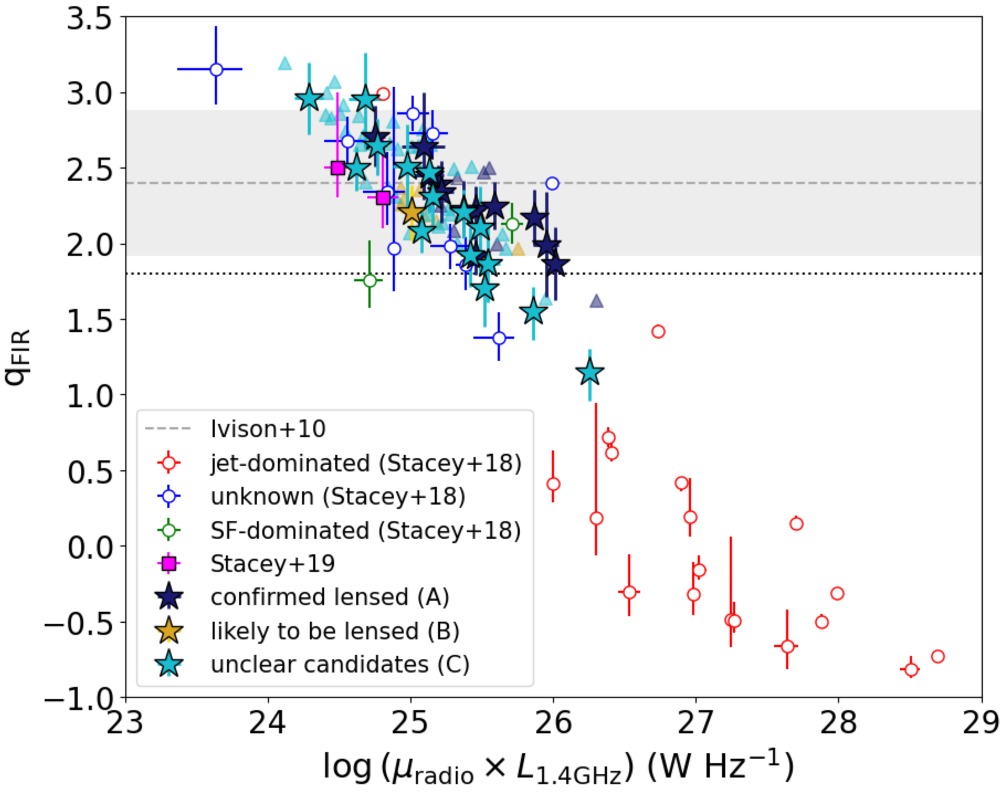

Figure 3.6: The q_{FIR} parameter, computed using the FIR luminosity, as a function of the logarithm of the 1.4 GHz luminosity (not corrected for lens magnification). Stars and triangles mark the same quantities as in Figure 3.5. Circles are the Stacey et al. (2018) lensed quasars classified according to the origin of their radio emission: (red) jets, (green) star formation, and (blue) unknown. Squares are from Stacey et al. (2019).

revealed by Stacey et al. (2018) observing a sample of strong gravitationally-lensed quasars. Their sample includes 104 quasars lensed by foreground galaxies, listed in the SQLS catalogue and CASTLES database (Kochanek et al. 1999, Munoz et al. 1999, Inada et al. 2012) and detected in a variety of optical and radio surveys. For clarity, in Figure 3.6 I have also reported their 31 detected sources that could be divided into three categories: jetted quasars, where high-resolution radio data confirmed the emission to be associated with AGN jets; non-jetted quasars, dominated by radio emission triggered by star-formation; quasars where the origin of the radio emission is unknown. They assumed a magnification factor of $\mu = 10^{+10}_{-5}$ for the majority of their sample, and the estimated median value of the total infrared luminosity amounts to $3.6^{+4.8}_{-2.4} x 10^{11}$ $\mathrm{L}_{\odot}$. Two additional sources are the gravitationally lensed radio-quiet quasars targeted by the LOFAR Two-metre Sky Survey (LoTSS) and detected by *Herschel* described in Stacey et al. (2019).

19 out of the 31 detected lensed quasars from Stacey et al. (2018) are located below the threshold of 1.8 and are mostly (with only one exception) classified as jet-dominated. For the remaining sources, only two quasars are confirmed to be star formation-dominated sources and are found to be above the 1.8 threshold within their uncertainties. The nature of the radio emission of the remaining one-third of the sample (10 sources) is still uncertain. Only the 25% of their sample has $q_{\mathrm{FIR}} < 1.8$ and lie in the same region of the jet-dominated quasars of Stacey et al. (2018), actually aligning onto their trend of q_{FIR} with radio luminosity. Most relevantly, the majority of our sources lie ($\sim 90\%$) in the region where radio emission is dominated by star formation, thus complementing the radio/optical selection adopted in Stacey et al. (2018) and actually extending to lower radio luminosities a consistent q_{FIR} vs. radio luminosity relation.

As a final remark, I note that the assumption that the FIR luminosity is not strongly affected by nearby objects entering the *Herschel* beam is reasonable. If not, the trend in Figure 3.6 should show a clear offset with respect to the confirmed lensed galaxies and/or with the points from Stacey et al. (2018, 2019). Another support to this assumption is given by the fact that our points are consistent within the uncertainties with the span of the $q_{\mathrm{FIR}} - L_{1.4\mathrm{GHz}}$ relation.

3.4 Physical interpretation

In the way of providing a physical interpretation, in Figure 3.7 we compared the observed FIR-radio correlation from this work and from Stacey et al. (2018, 2019) to the galaxy formation scenario by Lapi et al. (2014, 2018) described in Section 1.3 (see also Mancuso et al. 2017, Pantoni et al. 2019). As previously described in this thesis, this scenario envisages star formation and SMBH accretion in galaxies to be essentially *in-situ* and time-coordinated processes, triggered by the fast collapse of baryons in the host dark matter halos and subsequently controlled by self-regulated baryonic physics, in particular by energy/momentum feedback from SNe and from the central active nucleus.

The evolution of an individual massive galaxy (say the high-redshift star-forming progenitor of a present-day elliptical) predicted by the model consists of different stages (see Lapi et al. 2018, and Section 1.3). Early on, the balance between cooling, infall, compaction, and stellar feedback processes sets in a strong and dust-enshrouded star formation activity (SFR$\sim$ several 10^2 $M_\odot$ yr^{-1}), with a roughly constant behaviour in time (stellar mass increases almost linearly). Meanwhile, in the inner, gas-rich galaxy regions the central BH undergoes an exponential growth in Eddington-limited conditions. In this stage, the system behaves as a bright IR/(sub)mm galaxy with an X-ray active nucleus. When the central BH has grown to a significant mass, its energy output becomes so large as to eject gas and dust from the host and eventually quench the star formation and reduce the accretion onto itself to sub-Eddington values. In this stage, the system behaves as a powerful AGN with possible residual star formation. Thereafter, the stellar population evolves almost passively, and the system behaves as a red and dead massive quiescent galaxy; its further evolution in mass and size toward the present is mainly due to minor dry merger events.

In the early stages of the evolution when the central BH is still small and the nuclear power quite limited, the radio emission is mostly associated with the star formation in the host, implying modest $L_{1.4\,\mathrm{GHz}}$ and standard values $q_{\mathrm{FIR}} \approx 2.5$. Later on, when the BH mass has increased to substantial values, the radio emission from the nucleus progressively overwhelms that from the star formation, driving q_{FIR} toward values appreciably smaller than 2.5. Values smaller even than 1.8 are obtained when jetted emission is produced, preferentially in the late-stage of the evolution: this is because extraction of rotational energy to drive jets is favoured in sub-Eddington conditions that set in when the gaseous environment around the BH has been partially cleaned by the feedback from the nucleus itself (see above).

The typical model evolutionary track of a radio-loud AGN in the q_{FIR} vs. radio luminosity diagram is illustrated by the black line with arrows in Figure 3.7; the dark shaded area is the locus expected for such objects taking into account the relative contribution of sources with different masses, weighted by their statistics and timescales. For reference, the light-shaded area refers to the typical q_{FIR} parameter of star-forming galaxies with negligible contribution from AGNs to radio emission. The agreement of the model prediction with the data is pleasingly good and testifies that the behaviour of the FIR-radio correlation is physically driven by the onset of jetted radio emission, and consistent with a co-evolution scenario between star formation and BH growth.

3.5 Summary

In this Chapter, I have exploited a sample of sub-mm-selected (candidate) strongly-lensed galaxy with radio counterparts to investigate the FIR-radio correlation out to redshift $z \sim 4$. Specifically:

In Section 3.2 I cross-matched the Negrello et al. (2017) sample with the FIRST survey at 1.4 GHz and ran a dedicated follow-up with ATCA at 2.1 GHz, finding 16 and 11 matches, respectively; the addition of another source observed at ~ 7 GHz with the JVLA (analysed in detail by Nayyeri et al. 2017) led us to a sample

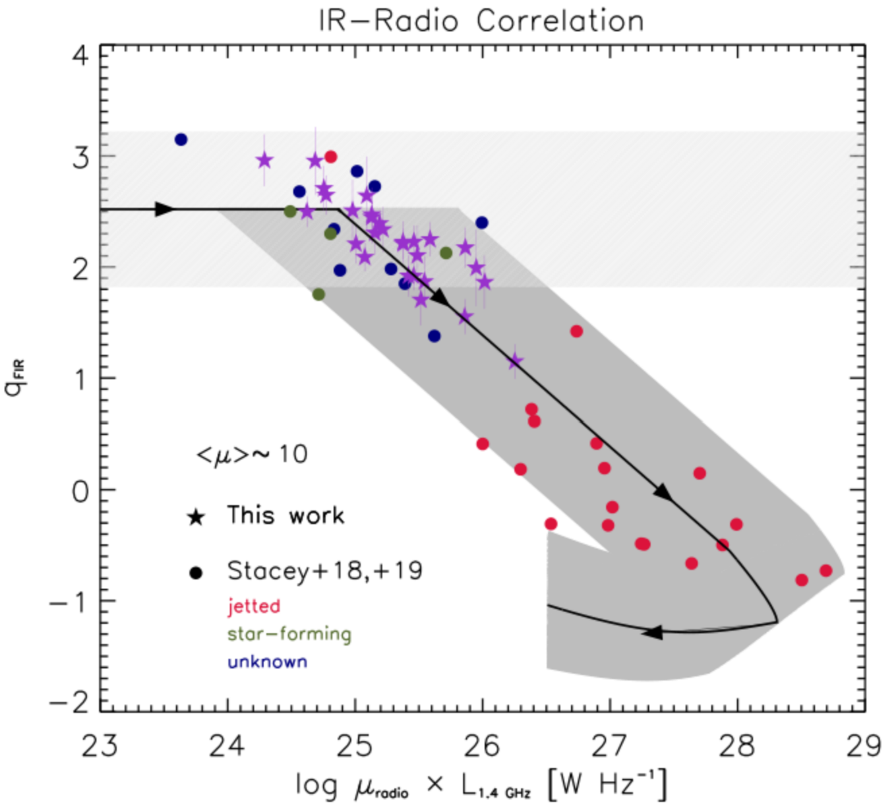

Figure 3.7: The FIR-radio correlation in terms of the $q_{\rm FIR}$ vs. radio luminosity (uncorrected for lensing magnification). Data from this work (stars) and from Stacey et al. (2018, 2019). Circles: red for jetted source, green for star-forming galaxies, and blue for uncertain ones) are compared with the prediction of the in-situ galaxy formation scenario by Lapi et al. (2014, 2018) for radio-loud AGNs. Specifically, the dark grey area represents the locus of radio-loud AGNs and the light-shaded area for SFGs without a significant AGN contribution to radio emission. The black line with arrows illustrates the typical evolution of an individual radio-loud AGN at $z \sim 2$. An average magnification $\langle\mu\rangle \sim 10$ (as estimated by Stacey et al. 2018) has been applied to the model predictions for a fair comparison with the data of gravitationally lensed sources.

of 28 candidate lensed dusty star-forming galaxies with a radio counterpart over the redshift range $1 \lesssim z \lesssim 4$. In Section 3.3 I derived the radio and the integrated FIR luminosities for the selected sample (uncorrected for lensing magnification), that feature radio luminosities in the range $1.9 \times 10^{24} \lesssim L_{1.4\,\mathrm{GHz}}$ [W Hz^{-1}] $\lesssim 1.8 \times 10^{26}$ and integrated FIR luminosity in the range $1.3 \times 10^{13} \lesssim L_{\mathrm{FIR}}/\mathrm{L}_{\odot} \lesssim 1.1 \times 10^{14}$. By taking advantage of the source brightness possibly enhanced by lensing magnification I have reconstructed the FIRRC of the sample, identifying weak evolution with redshift out to $z \lesssim 4$ of the FIR-to-radio luminosity ratio q_{FIR}, consistent with previous determinations at lower redshift based on different selections.

Moreover, I found that the q_{FIR} parameter as a function of the radio power $L_{1.4\,\mathrm{GHz}}$ displays a clear decreasing trend, similar to the lensed quasars selected in optical/radio by Stacey et al. (2018, 2019), yet covering a complementary region in the $q_{\mathrm{FIR}} - L_{1.4\,\mathrm{GHz}}$ diagram.

Finally, in Section 3.4 I have discussed how the behaviour of the FIR-radio correlation can be interpreted according to an in-situ galaxy evolution scenario, as the result of the transition from an early dust-obscured star-forming phase (mainly pinpointed by our FIR selection) to a late radio-loud quasar phase (preferentially sampled by the Stacey et al. 2018, 2019 selection).

Chapter 4

Singular Case Study within a Strongly Lensed DSFG Sample

In this Chapter, I will present the lens modelling, the source reconstruction, spectral line and continuum analysis of HATLASJ113526.3−014605 (J1135 hereafter), also called G12v2.43 or G12H43, an optical/NIR dark strongly lensed galaxy at $z = 3.1276$ belonging to the Negrello et al. (2017) lensed candidate sample, featuring a flux density at 500 μm of 204 ± 8.6 mJy.

This object serves as a remarkable illustration of an optical/NIR dark, sub-mm selected strongly lensed DSFG during the peak of the Cosmic SFRD. The availability of high angular and spectral resolution observations has enabled lens modelling and the reconstruction of the source's morphology. Furthermore, I will present an exhaustive examination of the dust, gas, and stellar content, evolutionary stage, and physical properties of this heavily obscured galaxy.

In Section 4.1 I describe the observed properties of optical/NIR dark galaxies. In Section 4.2 I will present J1135, its ALMA high-resolution observations (including continuum and spectral line analysis), and ancillary multiwavelength data. Section 4.3 describes the lens modelling and source reconstruction technique adopted to analyse ALMA data. In Section 4.4 I will illustrate the broad-band SED-fitting procedure and the resulting physical properties. Section 4.5 and 4.6.3 overview the ISM conditions of J1135, with a particular focus on the water spectral lines. In Section 4.7 I will investigate and provide interpretations of the outcomes within the context of the *in-situ* evolutionary framework. The concluding Section 4.8 offers an overview of the Chapter's contents.

This chapter is based on the discoveries presented in two publications: Giulietti et al. (2023) and Perrotta et al. (2023).

4.1 The most obscured objects

In the last years, an even more extreme population of heavily obscured SMGs has been discovered. These objects are missed in optical/NIR surveys and have been found up to very high redshifts (z∼ 6; Riechers et al. 2013, 2020, Marrone et al. 2018). These heavily obscured star-forming galaxies often lack a counterpart even in deep NIR observed-frame HST (Wang et al. 2019a, Alcalde Pampliega et al.

2019, Gruppioni et al. 2020) or either show extreme red colours ($H - 3.6\ \mu$m > 4; see e.g. Wang et al. 2016) and are visible only from observed-frame MIR images performed e.g. with the *Spitzer*/IRAC. Samples of optical/NIR dark objects have been detected by observing deep CO line emission (Riechers et al. 2020), and have been efficiently selected in sensitive radio observations (Talia et al. 2021, Enia et al. 2022). These peculiar objects provide a significant and previously unknown contribution to the cosmic SFRD at $z \gtrsim 3$ estimated to be at least 10% up to $25-40\%$ with respect to the one inferred from UV-selected populations (Wang et al. 2019a, Williams et al. 2019, Gruppioni et al. 2020, Talia et al. 2021, Enia et al. 2022).

The studies conducted so far concerning these elusive objects are however limited by the poor angular resolution and sensitivity in MIR/FIR and sub-mm bands, causing confusion problems and prohibiting a detailed investigation of the physical properties of optical/NIR dark galaxies and the conditions of their ISM. In the last years, ALMA deep field observations strongly improved the quality of the observations of high redshift dusty galaxies, detecting SMGs up to flux density limits of $S_{870\mu\mathrm{m}} \sim 0.1 - 1$ mJy (Aravena et al. 2016, Walter et al. 2016, Dunlop et al. 2017, Franco et al. 2018, Hatsukade et al. 2018), and were crucial to establishing the physical properties of these bright sources ($\mathrm{S}_{870\mu\mathrm{m}} > 1 - 2$ mJy), typically found in at z~2.5-3.0 (e.g. Simpson et al. 2014, 2017, Dudzevičiūtė et al. 2020, Simpson et al. 2020).

4.2 The Target

J1135 is part of the sample of 80 (candidate) strongly lensed galaxies (Negrello et al. 2017) located in the equatorial GAMA 12th field (RA=11:35:26, dec=-01:46:07, J2000). Among the other sources in the sample, it emerges for its rich profusion of available ancillary data, while its lensed nature is still being debated. J1135 is therefore chosen as the target for our analysis aiming to address its nature. The spectroscopic redshift of $z = 3.1276$ of the background lensed source was obtained from blind CO searches with the Zpectrometer ultrawideband spectrometer on the Green Bank Telescope (GBT) (Harris et al. 2012) and confirmed by the Northern Extended Millimeter Array (NOEMA) observations (Yang et al. 2017). So far, no redshift measurement is available for the foreground lens. Andreani et al. (2018) presented observations of high CO transition (J=7-6) obtained with the APEX/SEPIA band 5 receiver for the background object. From the comparison of the CO(7-6) transition with the CO(1-0) and CI(2-1) the authors pointed out the presence of a large excitation status in the ISM of J1135.

Moreover, Vishwas et al. (2018) reported bright [OIII] 88 μm emission for J1135 detected through the ZEUS-2 instrument on APEX, attributed to ionised hydrogen regions around massive stars. From the SED-fitting of the multi-band photometry of J1135, the authors predicted J1135 to be a young, gas-rich starburst galaxy.

The object has also been targeted by the SMA high spatial resolution (~ 0.8 arcsec) observations described in Bussmann et al. (2013) but only marginally resolved. For this reason, its lensed nature has been debated in the works described above.

In the following, I will describe the data publicly available for J1135 exploited in the analysis of this target.

4.2.1 ALMA observations

The object is part of low ($\lesssim 2$ arcsecs) resolution observations in Band 3 (2017.1.01694.S, PI: Oteo) aimed at tracing dense molecular gas through J=4-3 transitions of HCN, HCO+, and HNC molecules. In this thesis, this data set is used for a preliminary analysis of these spectral lines and is further described in Section 4.7.1.
J1135 was also included in a project (2019.1.00663.S, PI: Butler) whose main goal was to investigate outflows in high redshift star-forming galaxies by tracing OH+ and CO(9-8) lines.

In the following, we describe the calibration, imaging, and analysis of further data sets with the highest angular resolution available in the ALMA Science Archive for J1135. These spatially resolved ALMA follow-ups reveal an almost complete Einstein ring, confirming out of any doubt the lensed nature of this system.

The object has been the target of ALMA Cycle 4 high-resolution follow-up in band 8 (2016.1.01371.S, PI: Vishwas) aimed at resolving the lensed morphology of the source and tracing the continuum at ~ 0.7 mm and the [CII] 158 μm FIR line. The continuum was observed exploiting four basebands of width 1.98 GHz, centred at 472.284, 470.451, 460.409, 458.534 GHz, each one composed of 128× 15.62 MHz channels.
The second examined data set is part of the ALMA Cycle 6 project (2018.1.00861.S, PI: Yang) carried out with the goal of tracing H_2O and CO (J=8−7) lines in candidate lensed galaxies at high redshift ($z \sim 2-4$) in Band 6 and 7. Both observations are performed with the same configuration with a maximum baseline of 1397 m, corresponding to a ~ 0.2 arcsec resolution in both bands. Band 6 targets the spectral line emission of $H_2O(J=2_{0,2}\text{-}1_{1,1})$ and CO(J=8-7) with two spectral windows centred at 239.376 GHz and 223.583 GHz respectively, while other two windows centred at 235.940 and 221.705 GHz are dedicated to continuum observations. The $H_2O(J=3_{2,1}\text{-}3_{1,2})$ and $H_2O(J=4_{2,2}\text{-}4_{1,3})$ spectral lines are targeted in Band 7 with two spectral windows, centred at 281.766 and 292.621 GHz respectively. The remaining two windows centred at 280.314 and 294.266 GHz observe the continuum emission. In both the bands, each spectral window has 1.875 GHz bandwidth and 240×7.8 MHz channels.

I calibrated the raw data calibration by running the available pipeline scripts using the Common Astronomy Software Applications (CASA, McMullin et al. 2007) package version 4.7.2 and 5.4.0-68 for Cycle 4 and Cycle 6 data respectively. I have manually subtracted the continuum using the task `uvcontsub` and performed interactively imaged the data adopting a Briggs weighting scheme, which assumes a robustness factor of 0.5. The properties of the generated images are reported in Table 4.1, and the continuum-cleaned images are shown in Figure 4.3.

In Figure 4.4 I have reported the image plane moment maps of J1135 from ALMA observations, showing zero, first, and second momenta for the [CII], the CO(8-7), and the three H_2O line transitions observed in J1135, corresponding

	Cycle 4 B8	Cycle 6 B6	Cycle 6 B7
Project ID	2016.1.01371.S	2018.1.00861.S	2018.1.00861.S
Spectral set-up [MHz]	4×128×15.63	4×240×7.81	4×240×7.81
Restored beam axes [arcsec^2]	0.14× 0.07	0.29×0.25	0.23×0.2
Continuum sensitivity [mJy beam^{-1}]	0.541	0.043	0.025

Table 4.1: Overview of ALMA observations used in the analysis of J1135.

Transition	$\nu_{\rm rest}$	E$_{\rm up}$	log A$_{ij}$	ALMA	$\nu_{\rm obs}$	Beam	P.A.	pixel scale	rms
	[GHz]	[K]	[s^{-1}]	Band	[GHz]	[arcsec^2]	[deg]	[arcsec]	[mJy beam^{-1} km s^{-1}]
p-H$_2$O 2$_{02}$-1$_{11}$	987.927	100.8	-2.23	6	239.376	0.305 × 0.270	-86.74	0.048	0.44
o-H$_2$O 3$_{21}$-3$_{12}$	1162.912	305.2	-1.64	7	281.766	0.259 × 0.226	-77.51	0.039	0.26
p-H$_2$O 4$_{22}$-4$_{13}$	1207.639	454.3	-1.55	7	292.621	0.251 × 0.220	-78.19	0.039	0.24
CO(J=8-7)	921.800	199.1	-4.29	6	223.583	0.328 × 0.289	-85.21	0.048	0.35
[CII]	1900.548	91.25	-5.6	8	460.510	0.142 × 0.076	-62.45	0.011	3.30

Table 4.2: Properties of water, [CII], and CO(J=8-7) spectral lines and their respective ALMA images. From the left: the line transition, rest-frame frequency, upper-level energy, the logarithm of the critical density, observed frequency, angular resolution, position angle, pixel scale, and rms.

respectively to the integrated brightness, velocity distributions, and velocity dispersion. Moments are computed considering the velocity range v$_p$ ± FWHM reported in Table 4.3 (see Section 4.2.2) and including only pixels above a 5σ threshold, where σ is the rms of the map.

The main features of the ALMA data analysed in this work and the properties of the final images are reported in Table 4.1.

The flux densities derived for the continuum emission of the lensed source are reported in Tab. 4.4. We also include the flux density value measured from the archival image of the Band 3 continuum emission mentioned in Section 4.2. Flux density uncertainties are computed including at least a 5% estimation of the flux calibration accuracy:

$$\delta S_{\rm image} = \sqrt{N(\sigma_{\rm image})^2 + (0.05 \times S_{\rm image})^2}, \tag{4.1}$$

with $\sigma_{\rm image}$ being the rms and N the number of resolution elements inside the aperture adopted to extract the flux density.

4.2.2 Spectral line profiles

Figure 4.1 reports the observed (magnified) [CII], CO(8-7), p-H$_2$O ($2_{02} - 1_{11}$), o-H$_2$O ($3_{21} - 3_{12}$), and p-H$_2$O ($4_{22} - 4_{13}$) lines of J1135. The intensity of the water lines is smaller (by a factor 2-4) but comparable to that of CO, with H$_2$O covering the same velocity range as CO and [CII]. The [CII], CO(8-7), and water emission line profiles, scaled to the peak value of the [CII] profile for better visualisation of the line profiles, are shown in Figure 4.2. The CO(8-7) and the water vapour lines show consistent velocity dispersion, suggesting that they plausibly stem from the very same physical region inside the galaxy.

The shape of each spectral line was reconstructed exploiting a Bayesian Monte Carlo Markov Chain (MCMC) framework, implemented numerically via the Python package `emcee` (Foreman-Mackey et al. 2013; further details on the fit procedure and the resulting contour plots can be found in Appendix B). Each spectral line is fitted with a single Gaussian function, described by the parameter vector $\theta = \{\mathrm{S_p}, \mathrm{v_p}, \sigma_\mathrm{v}\}$ where $\mathrm{S_p}$ stands for the peak flux, $\mathrm{v_p}$ represents the position of the peak in the velocity axis, and σ_v is the standard deviation of the Gaussian (also called Gaussian RMS width). The main parameters of the spectral line fit are reported in Table 4.3, along with estimates of the FWHM of the fitting functions, line flux, the mean, and the standard deviation of the residuals of the fits.

The FWHM values for all the spectral lines are in concordance with what is found by GBT and NOEMA CO and H_2O lines analysed in Harris et al. (2012) and Yang et al. (2017). The peak of the brightest spectral lines is detected at $\nu_\mathrm{obs} = 460.504 \pm 0.003$ GHz for [CII] and $\nu_\mathrm{obs} = 223.356 \pm 0.0011$ GHz for the CO(8-7), confirming the redshift estimate by Harris et al. (2012) of 3.127 whose associated uncertainties are $\delta z_\mathrm{[CII]} = \pm 0.005$ and $\delta z_\mathrm{CO(8-7)} = \pm 0.003$ respectively. In order to identify possible signatures of rotations or outflows, we also performed a fit of the profiles using two (and even three) Gaussian components, without finding any striking statistical evidence in favour of any of these supplementary components.

The observed magnified line profiles measured within a region containing the whole source emission are shown in Figures 4.1. Following Carilli & Walter (2013a) we compute the observed magnified line luminosities expressed in units of K km s^{-1} as:

$$L'_\mathrm{line} = 3.25 \times 10^7 \times S_\mathrm{line} \Delta v \frac{D_L^2}{(1+z)^3 \nu_\mathrm{obs}^2}. \tag{4.2}$$

Where $S_\mathrm{line}\Delta v$ is the measured flux of the line profile (in units of Jy km s^{-1}) and D_L is the luminosity distance. The luminosities expressed in $\mathrm{L_\odot}$ are computed as $L_\mathrm{line} = 3 \times 10^{-11} \nu_\mathrm{rest}^3 L'_\mathrm{line}$. The final values computed for the [CII], the CO(8-7), and water lines are summarised in Table 4.3.

4.2.3 Other bands

J1135 is covered by several surveys, such as the Kilo-Degree Survey (KiDS, de Jong et al. 2013) and the Hyper Suprime-Cam Subaru Strategic Program in the UV/optical bands (HSC, Aihara et al. 2018, 2022), the VIKING (Edge et al. 2013), and the UKIDSS-LAS (Lawrence et al. 2007) surveys in the NIR, the Wide-field Infrared Survey Explorer (WISE, Wright et al. 2010) in the MIR. PACS and SPIRE FIR observations are reported in H-ATLAS First and Second Data Release catalogues (Valiante et al. 2016, Maddox et al. 2017). Moreover, the source is covered by the VLA FIRST survey (Becker et al. 1995) in the radio band, where no emission is detected.

High-resolution NIR follow-up observations are available for J1135. The target was observed as part of the Cycle 19 HST/WFC3 snapshot program (PI: Negrello) at a wavelength of $\lambda = 1.15$ μm (see Negrello et al. 2014 for further details of the

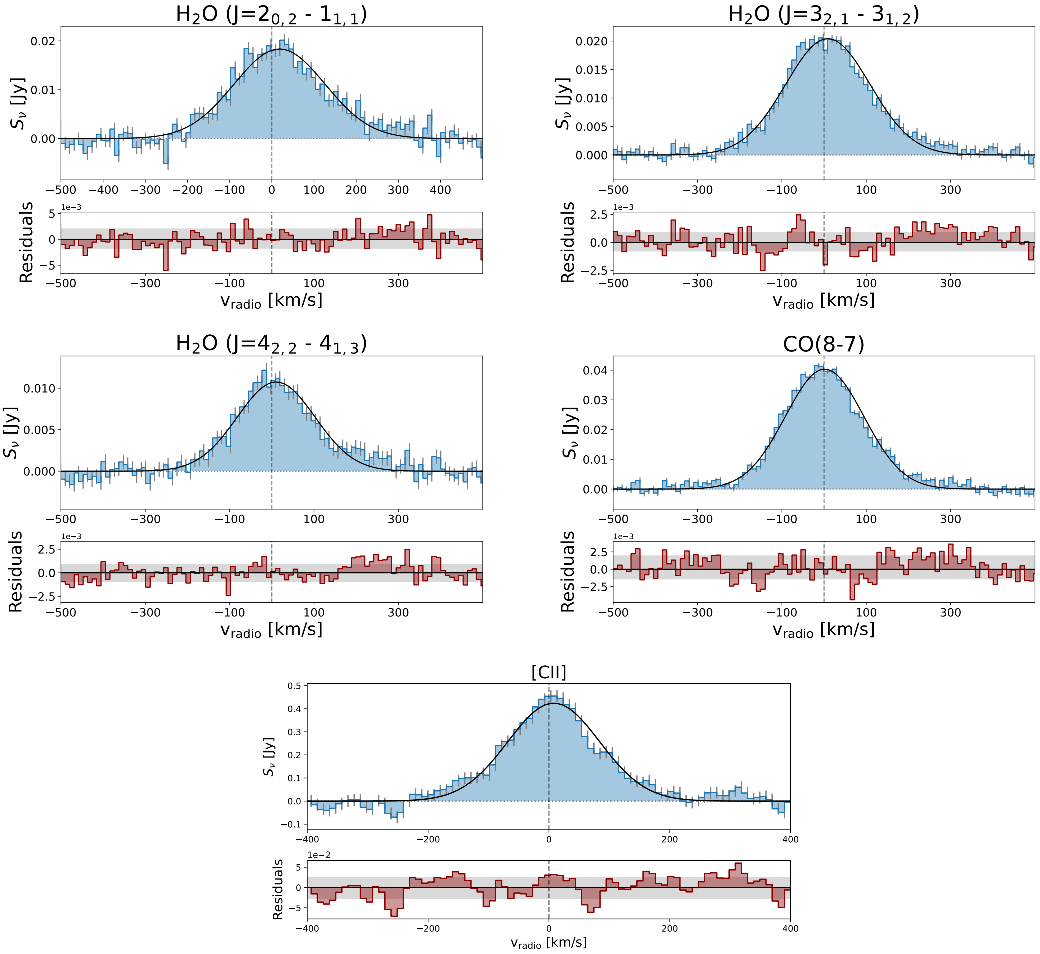

Figure 4.1: Targeted lines as observed in ALMA Bands 6, 7, and 8. Lines are extracted within a region enclosing pixels above ∼5σ drawn from the moment-0 map. The zero velocity corresponds to the rest-frame frequency of the spectral line. Data are represented by the blue step function along with the associated errors, i.e., the grey bars. The fit of the spectral lines is represented by the black solid line. In the bottom boxes, we have shown the magnitude of the residuals (red step function) relative to each fit together with their mean value (black solid line) and their standard deviation (spanning the grey-filled area).

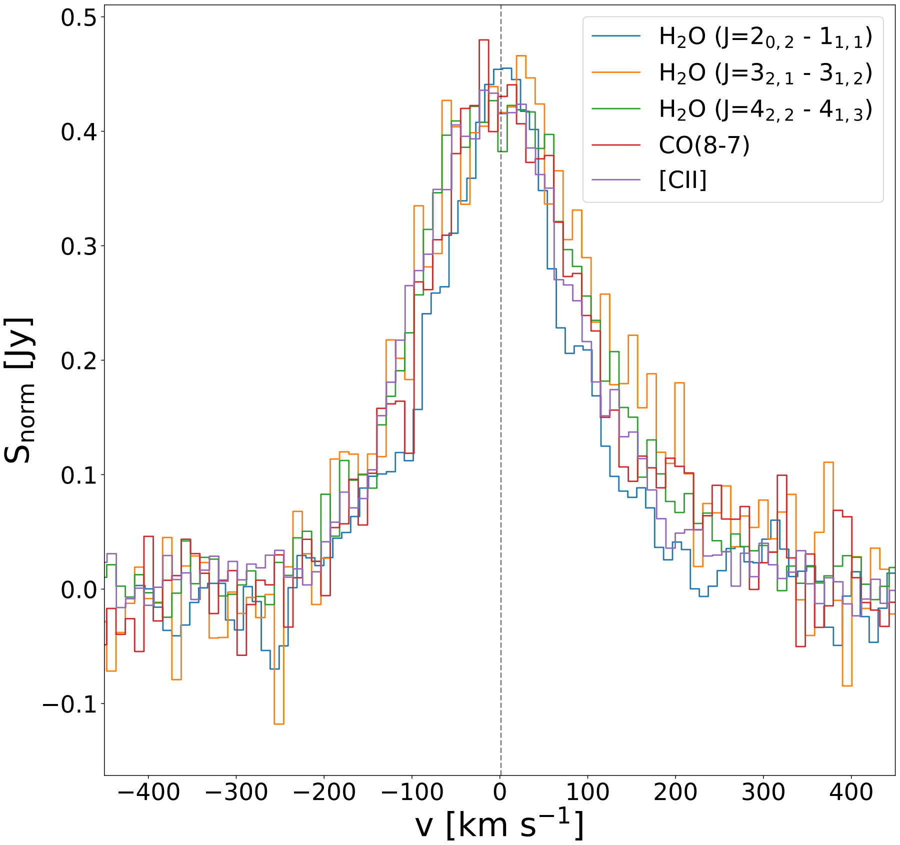

Figure 4.2: Water emission line profiles superimposed to the CO(J=8-7) and [CII] lines and scaled to the [CII] peak. The velocity scale is relative to the systemic velocity of J1135.

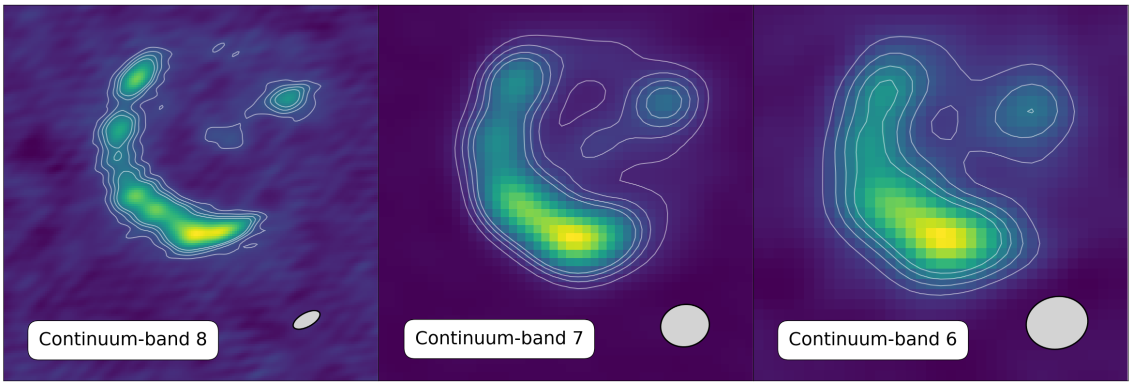

Figure 4.3: ALMA Bands 8, 7, and 6 continuum emission for J1135. White contours display the emission at 9,7,5 and 3 σ. The synthesised beam is displayed in the bottom-right corner, postage stamps are 3×3 arcseconds.

Line	S_p [mJy]	v_p [km s^{-1}]	σ_v [km s^{-1}]	FWHM [km s^{-1}]	$S_p \times$ FWHM [Jy km s^{-1}]	$\langle S_r \rangle$ [10^{-4} Jy]	σ_r [10^{-4} Jy]	μL [10^8 L$_\odot$]	$\mu L'$ [10^9 K km s^{-1}]
p-H_2O 2_{02}-1_{11}	18.3 ± 4	18 ± 3	108 ± 3	255 ± 7	4.7 ± 0.2	1.5	19	8.22 ± 0.35	28.4 ± 0.1
o-H_2O 3_{21}-3_{12}	20.4 ± 4	9 ± 2	100 ± 2	235 ± 4	4.8 ± 0.2	0.43	8.2	9.88 ± 0.41	20.9 ± 0.9
p-H_2O 4_{22}-4_{13}	10.7 ± 3	10 ± 3	92 ± 3	218 ± 8	2.3 ± 0.2	−0.17	8.9	4.92 ± 0.43	9.31 ± 0.81
CO(8-7)	40.4 ± 5	1 ± 1	92.9 ± 0.8	219 ± 2	8.8 ± 0.2	2.7	17	14.4 ± 0.3	61 ± 1.4
[CII]	424 ± 11	8 ± 2	76 ± 2	179 ± 5	71 ± 4	−15	260	240 ± 12	116 ± 6

Table 4.3: Observed emission lines parameters derived from the Bayesian MCMC Gaussian fit. Here S_p is the Gaussian's peak, v_p is the peak position on the velocity axis, σ_v is the standard deviation (or the Gaussian RMS width) and FWHM represents the full width at half maximum of the Gaussian, computed as FWHM = $2\sqrt{2\ln 2}\sigma_v$. The product $S_p \cdot$ FWHM represents the line flux. $\langle S_r \rangle$ and σ_r respectively represent the mean fit residuals and their standard deviation. The last two columns report the inferred magnified line luminosity expressed in L$_\odot$ and K km^{-1} pc^2. The fit refers to the lensing-magnified line profiles in Figure 4.1.

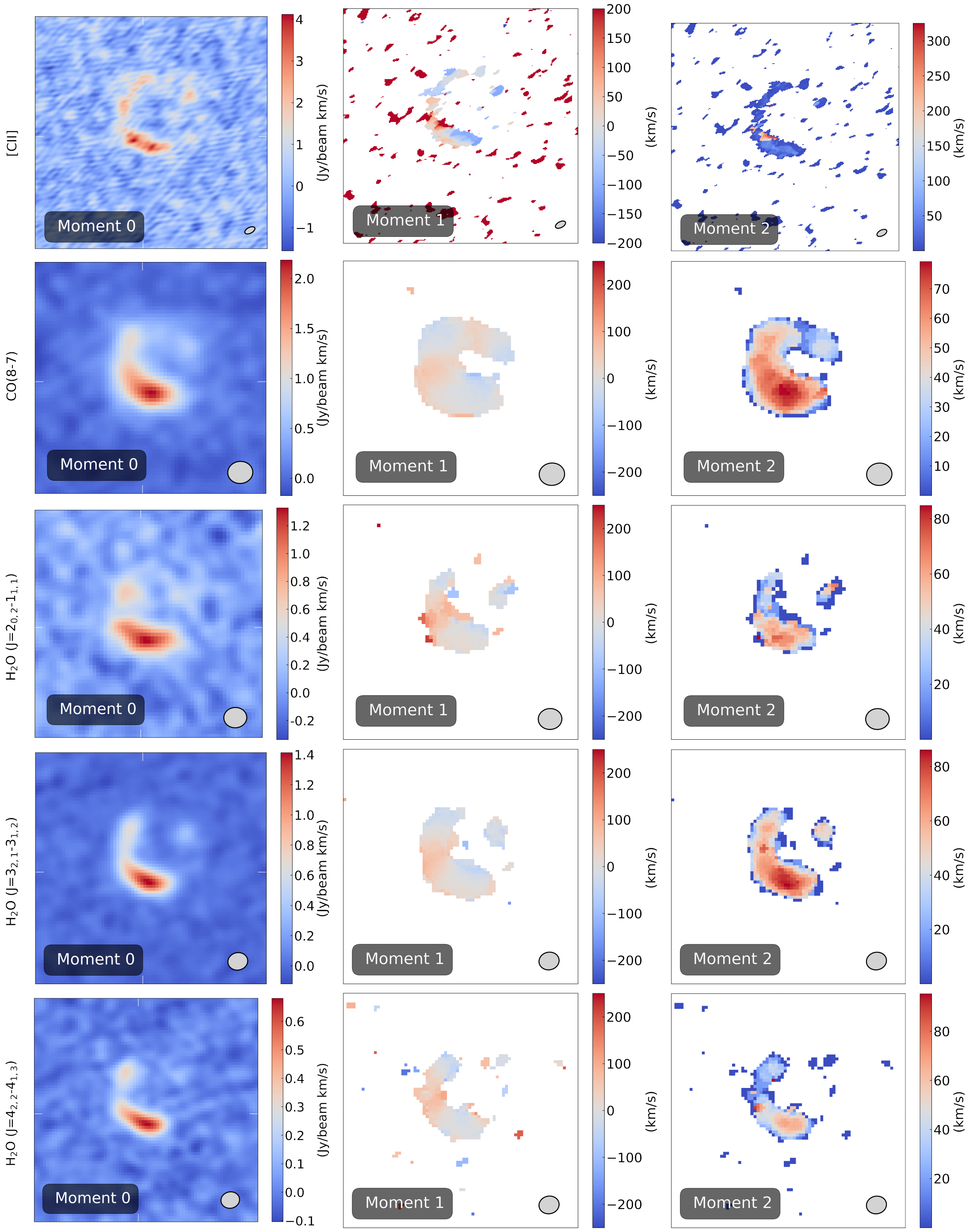

Figure 4.4: Moment maps for the spectral lines of J1135. From the left: integrated intensity, line-of-sight velocity, and velocity dispersion. The synthesised beam is displayed in the bottom-right corner, postage stamps are 3×3 arcseconds.

observations) and with the *Keck* telescope in Adaptive Optics (AO) in the Ks band (Calanog et al. 2014). No successful detection has been found in the Ks image, while a marginal emission ($\lesssim 3\sigma$) is present in the HST image, however, given the insufficient sensitivity and angular resolution it is not possible to unambiguously confirm whether it is associated with the foreground lens or the background source.

The object is also detected in MIR observations available in the *Spitzer*/IRAC Data Archive (PI: Cooray, ID: 80156) and described in Ma et al. (2015), covering IRAC channel 1 and channel 2, at 3.6 μm and 4.8 μm respectively.

The target also benefits from EVLA radio data available from the NRAO Archive. In particular, follow-ups in C-band centred ad ~ 6 GHz (project code: 16A-240, PI: Smith). I have processed the data by running the calibration scripts, cleaning is performed manually with CASA adopting an interactive mask. The final image reaches a mean rms of ~ 0.013 mJy beam^{-1} and a restored beam ellipse of 1.13×0.84 arcsec (see Figure 4.5).

The multi-band (optical-to-MIR) image cutouts of J1135 are reported in Figure 4.5. A faint emission at $\sim 4\ \sigma$ emerges starting from the VIKING H-band and is detected in both IRAC channels with a SNR $\gtrsim 6$, but the angular resolution is not sufficient to resolve any lensing features (e.g. arcs) in the NIR/MIR regime. Flux densities are estimated by performing aperture photometry with a diameter of 2 arcsecs for NIR VIKING images and 6 arcsecs for *Spitzer*/IRAC images. Table 4.4 summarises the photometry for J1135, also reporting upper limits for non-detections (i.e. emission with S/N $\lesssim 3$).

4.3 Lens modelling and source reconstruction

In order to reconstruct the intrinsic background source morphology I have performed the lens modelling analysis with the open source Python 3.6+ code `PyAutoLens` (Nightingale et al. 2018, 2021b). The code's features include a fully automated strong lens modelling for galaxies and galaxy clusters, exploiting the probabilistic programming language `PyAutoFit` (Nightingale et al. 2021a).

`PyAutoLens` includes several model-fitting algorithms (e.g. MCMC, maximum likelihood estimators, etc...) used to determine the best-fit parameters for mass and light profiles. For this analysis, the non-linear search fit is performed through the nested sampling algorithm `Dynesty` (Speagle 2020), which samples the parameter space and computes the posterior probability distributions for the parameters of a given lens model.

`PyAutoLens` also implements the Regularised SLI Method (Warren & Dye 2003) together with the adaptive source plane pixelisation scheme described in Nightingale & Dye (2015) extended to interferometric data as done in Massardi et al. (2017), Dye et al. (2018), Enia et al. (2018), Dye et al. (2022), Maresca et al. (2022) and detailed in Chapter 2.

For a fixed mass model, the image plane pixels are traced back to the source plane and grouped together by means of a k-clustering algorithm, comparing each source pixel with the neighbours sharing a direct vertex. This procedure results

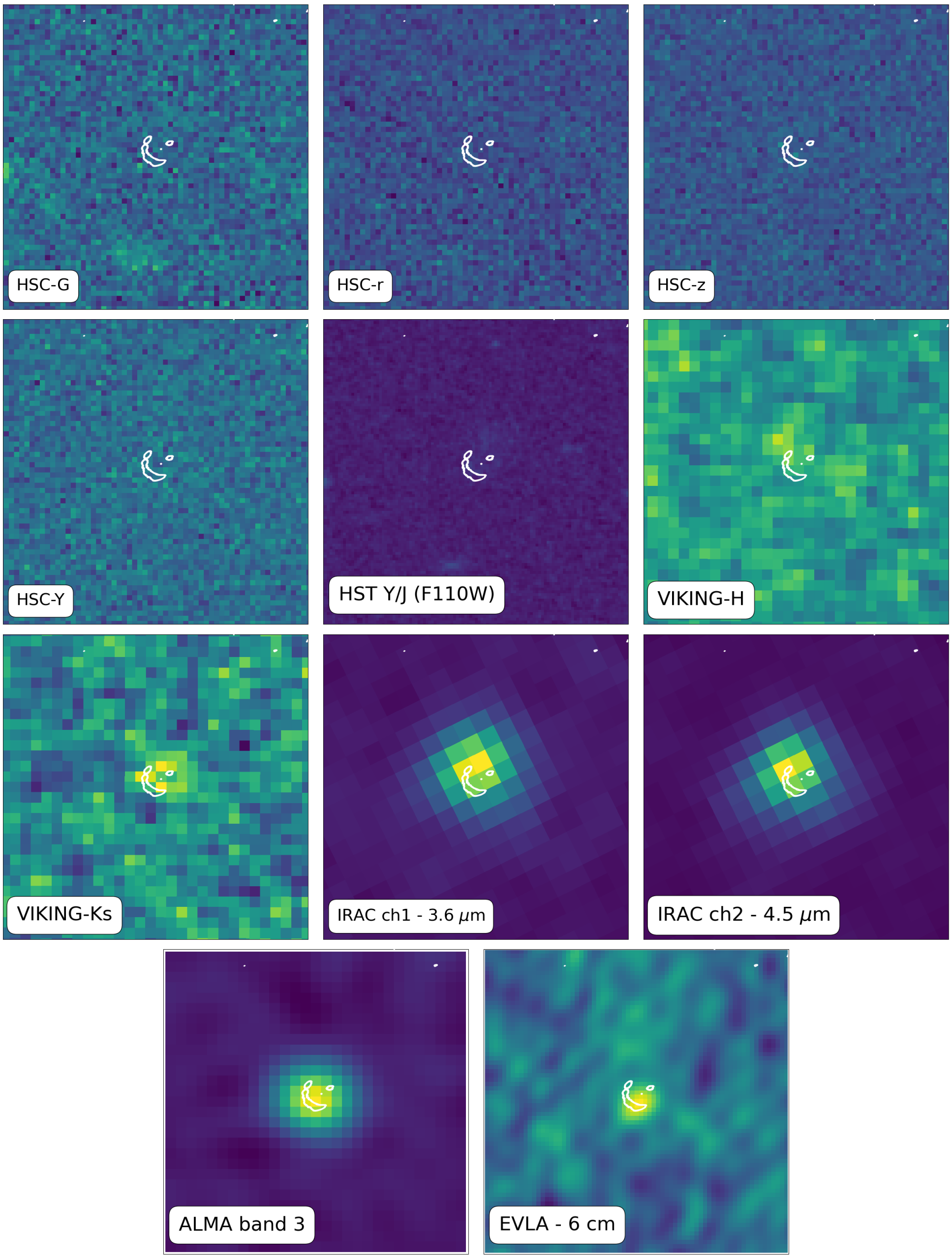

Figure 4.5: Cutouts of optical-to-radio images for J1135 centred on the *Herschel* position. Contours display ALMA Band 8 continuum emission at 9,7,5×σ The postage stamps are 10×10 arcsec.

[1] From the WISE All-sky Data Release Wright et al. (2010)
[2] From the H-ATLAS Data Release 1 catalog described in Valiante et al. (2016)
[3] From the H-ATLAS Data Release 2 catalog described in Maddox et al. (2017)
[4] From the HerBS sample (Bakx et al. 2018)
[5] From SMA observations described in Bussmann et al. (2013)

Wavelength (μm)	Flux density (mJy)	Instrument
0.47	$\lesssim 0.09\times10^{-3}$	HSC/g
0.61	$\lesssim 0.17\times10^{-3}$	HSC/r
0.77	$\lesssim 0.26\times10^{-3}$	HSC/i
0.89	$\lesssim 0.41\times10^{-3}$	HSC/z
0.97	$\lesssim 0.43\times10^{-3}$	HSC/y
1.15	$\lesssim 0.91\times10^{-3}$	HST/WFC3
1.64	$(6.9\pm1.2)\times10^{-3}$	VIKING/H
2.15	$(7.8\pm1.2)\times10^{-3}$	VIKING/Ks
3.55	$(37.1\pm6.2)\times10^{-3}$	*Spitzer*/IRAC1
4.49	$(58.2\pm7.5)\times10^{-3}$	*Spitzer*/IRAC2
11.6	$\lesssim 0.45$	WISE/W3[1]
22.1	$\lesssim 3.83$	WISE/W4[1]
100	$\lesssim 136.3$	*Herschel*/PACS[2]
160	151.5±50.3	*Herschel*/PACS[2]
250	278.8±7.4	*Herschel*/SPIRE[2,3]
350	282.9±8.2	*Herschel*/SPIRE[2,3]
500	204.0±8.6	*Herschel*/SPIRE[2,3]
640	163.7±8.4	ALMBA/B8
850	118.8±8.5	SCUBA-2[4]
880	48.6±2.3	SMA[5]
1043	29.4±1.5	ALMA/B7
1300	16.2±0.8	ALMA/B6
3450	0.71±0.04	ALMA/B3
48100	0.09±0.01	EVLA/BC

Table 4.4: Photometric data for J1135. References for flux densities (in mJy) taken from the catalogs described in Sec 4.2.3 are shown, while the remaining values are extracted through aperture photometry. Upper limits are reported at the 3σ level.

$\theta^{\text{mass}}_{\text{Ein}}$	y^{mass}	x^{mass}	q	ϕ
$0.4241^{+0.0005}_{-0.0005}$	$-0.2329^{+0.0005}_{-0.0005}$	$0.1494^{+0.0011}_{-0.0009}$	$0.637^{+0.001}_{-0.001}$	$-35.31^{+0.04}_{-0.04}$

Table 4.5: Fit parameters of the lens modelling of J1135. From the left: the Einstein radius, the lens centroid positions, the ratio between the semi-major and semi-minor axis, and the positional angle defined counter-clockwise from the positive x-axis.

in a new source plane's centres, used to trace a Delaunay grid. When dealing with a large number of visibilities, the computational efficiency and the memory costs are greatly improved by performing non-uniform Fast Fourier Transform (NUFFT) algorithm, implemented in `PyAutoLens` exploiting the `PyNUFFT` (Lin 2018) library and the linear algebra package `PyLops` (Ravasi & Vasconcelos 2020).

4.3.1 Lens model

In reconstructing the source's light profile we first need to assume a density profile for the mass of the foreground object. The lens is modelled as a SIE profile (Kormann et al. 1994), i.e. an elliptical power-law density distribution which goes as $\rho \propto r^{-\gamma}$, with r being the elliptical radius and with a fixed slope value $\gamma = 2$. The profile is described by five parameters: the Einstein radius θ_{E}, the lens centroid positions x_c, y_c, the first and the second ellipticity components of the elliptical coordinate system (e_x, e_y). The latter originates from two quantities: the positional angle (ϕ), defined counter-clockwise from the positive x-axis, and the factor $f = (1 - q)/(1 + q)$ where q is the ratio between the semi-major and semi-minor axis. The final expressions for the elliptical components are:

$$\begin{aligned} e_y &= f \times \sin(2\phi), \\ e_x &= f \times \cos(2\phi). \end{aligned} \tag{4.3}$$

From several tests, I have verified that the shear component does not improve the model, but instead worsens the fit results, and for this reason, it is omitted.

The search chain consists of two steps: 1) I searched for the best-fit lens model through non-linear parametric fitting. I assumed the source light to be described by a Sérsic profile and fit simultaneously the ALMA data in all of the three bands (including spectral lines). 2) Using the best-fit lens model parameters obtained in the first step as priors, I performed the inversion.

The fit is performed on several pixels delimited by a circular mask, where the radius changes according to the resolution of the cleaned ALMA image, to obtain a satisfactory fit without exceeding in terms of computational cost.

4.3.2 Results of the lens modelling

The best-fit lens model parameters and their uncertainties are reported in Table 4.5

The resulting reconstructed source contains only pixels excluded from the masked lensed image area. Magnification factors are computed as $\mu = A_{\mathrm{IP},5\sigma}/A_{\mathrm{SP},5\sigma}$. Where $A_{\mathrm{IP},5\sigma}$ and $A_{\mathrm{SP},5\sigma}$ are the areas enclosing significant (i.e. $> 5\sigma$) pixels in the reconstructed image plane (IP) and the reconstructed source plane (SP) respectively. The noise is estimated as the rms in the reconstructed source map. From the area enclosing all the pixels with signal-to-noise ratio $\gtrsim 3$ and $\gtrsim 5$ in the reconstructed source plane, the effective radius can be computed as $r_{\mathrm{eff}} = (A_{\mathrm{SP}}/\pi)^{0.5}$. In order to determine the uncertainties of these parameters, we exploit the set of samples provided by the non-linear search performed during the inversion. Each sample corresponds to a set of inversion parameters (i.e. the regularisation coefficient and the pixelisation's shape) that were evaluated and accepted by the non-linear search. Uncertainties are then retrieved as the 16th and 84th quantiles of the parameter distribution drawn from ~ 200 accepted samples. The results are reported in Table 4.6. This key information allows us to retrieve the intrinsic properties of the lensed background object, which will be discussed in detail in Section 4.5.

It is crucial to point out that the robustness of these quantities strongly depends on the noise covariance which, in the case of interferometric source reconstruction is difficult to quantify (Stacey et al. 2021, Rizzo et al. 2021). In order to understand how much the estimation of the noise impacts our results, we compare the effective radii inferred from the source reconstruction with the best-fit effective radii of the Sérsic profile ($\mathrm{R}_{\mathrm{eff,par}}$) used in the non-linear parametric fit described in Section 4.3.1. The values are shown in Table 4.6. The effective radii inferred from the two different methods are broadly consistent with each other. The only exception is for Band 7, where $\mathrm{R}_{\mathrm{eff,par}}$ is higher with respect to the values computed from the source reconstruction, likely due to a higher noise level. Therefore, the parameter uncertainties from the inversion are likely to be underestimated. Figure 4.6 and Figure 4.7 show the original lens-plane image, the model image, the normalised residual map, and the reconstructed source for the three ALMA continuum bands and the CO(8-7) and [CII] emission lines respectively. Differences in the retrieved physical scale values reflect the heterogeneity of the data adopted in this work, which are the product of different array configurations and angular resolutions. The central feature emerging in the normalised residuals of the continuum in Bands 8, 7, and 6 could originate from the faint foreground lens, whose nature is discussed in detail in the next Section. The attempt to remove the emission by light-profile subtraction was unsuccessful, mainly because of its extremely compact size and faintness compared to the background lensed source. However, the presence of this central feature in the continuum bands is not impacting considerably on the lens model in bands 8 and 7, where its contribution is estimated to be not higher than $\sim 4\%$ with respect to the lensed source flux density (i.e. computed including only the light originated by the arcs in the lens plane). One caveat concerns the Band 6 continuum, where the contribution of the central emission is estimated to be up to $\sim 28\%$ of the lensed source flux density, and where the lens modelling results are more difficult to interpret. In this case, the uncertainties impact the estimates of the magnification factors and effective radii and are included in the errors of these quantities. Since the Band 6 continuum is

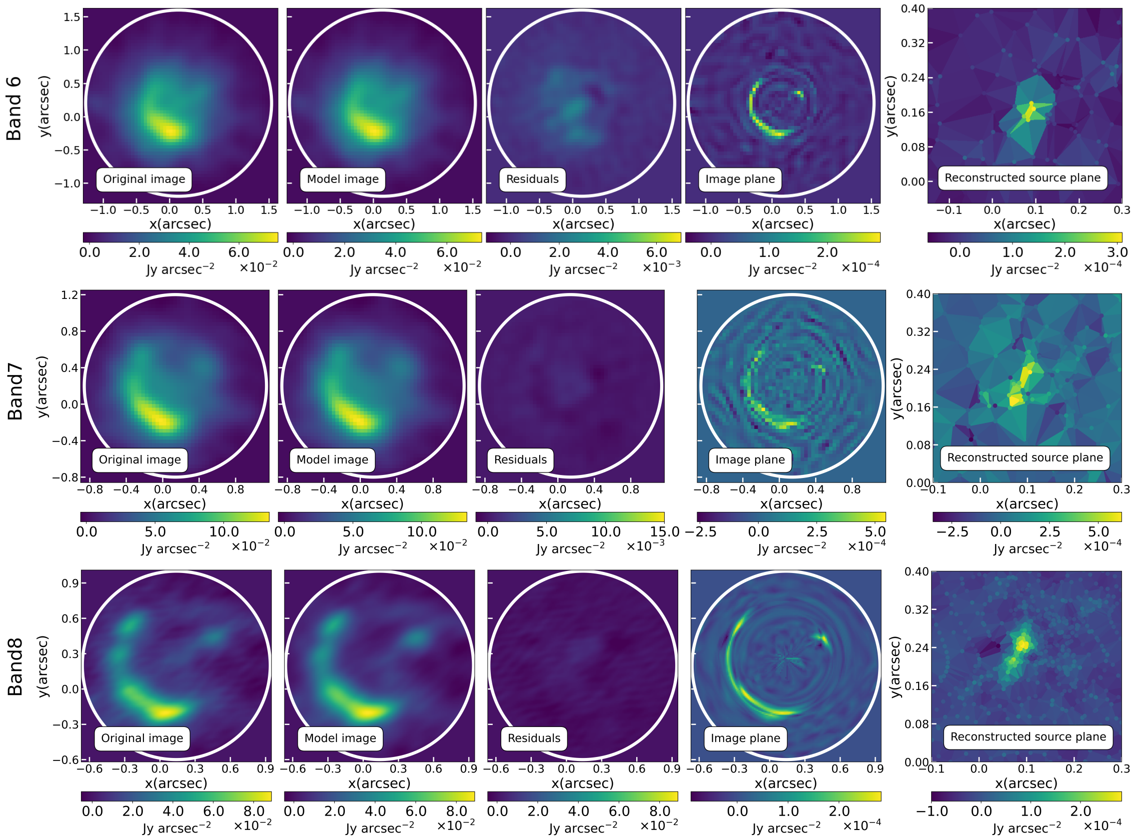

Figure 4.6: Results of the lens modelling and source reconstruction procedure for continuum data. From the first column to the right: the ALMA dirty image, the best-fit lensed model dirty image, the residuals, the image plane's model, and the reconstructed source plane. The white circle represents the mask used in the lens modelling. Note that surface brightness values of the former are de-magnified. The colour bar indicates the surface brightness in units of Jy arcsec^{-2}.

only used in the SED fitting (see Section 4.4) its overall impact on our analysis is negligible. Even if uncertain, the lens modelling and the estimated quantities are still reported in Table 4.6 and Figure 4.6, since they can be informative for future works regarding J1135.

Moreover, I have reconstructed the velocity map for the CO(8-7) line by dividing and modelling the emission in three different velocity bins. As there is no significant difference in the reconstructed emission in the bins, we cannot claim any indication of rotation or outflow (see Figure 4.8). This is also noticeable in the CO(8-7) first moment maps shown in Figure 4.4, where no strong velocity gradients are visible along the width of the arcs. The velocity dispersion peak is co-spatial with the integrated brightness peak, located in the southern region of the arc and corresponding to the northern clump in the reconstructed. The attempt to reconstruct the [CII] velocity field was unsuccessful, because of the poor signal-to-noise of the individual velocity bins, even though a modest velocity gradient is visible in 4.4 peaking at the same position as the velocity dispersion.

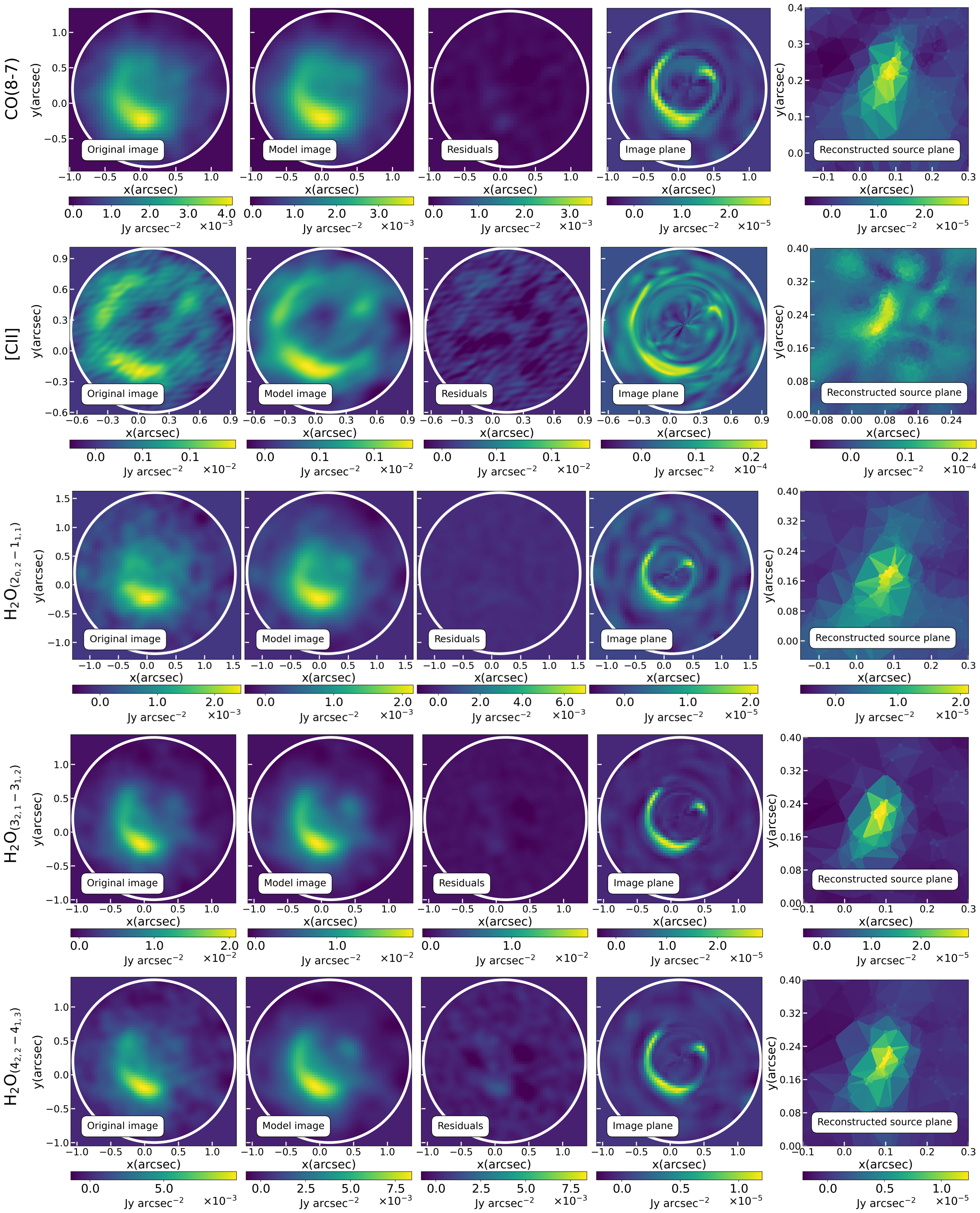

Figure 4.7: Same input and output as is Figure 4.6 for spectral line emissions.

	$\mu_{3\sigma}$	$\mu_{5\sigma}$	$R_{\mathrm{eff},3\sigma}$ (pc)	$R_{\mathrm{eff},5\sigma}$ (pc)	$R_{\mathrm{eff,par}}$ (pc)
Band 8	$12.65^{+0.67}_{-1.38}$	$12.80^{+0.32}_{-0.18}$	541^{+18}_{-10}	392^{+5}_{-13}	571^{+160}_{-142}
Band 7	$7.51^{+0.23}_{-0.05}$	$8.34^{+0.2}_{-0.05}$	518^{+35}_{-70}	314^{+64}_{-24}	995^{+38}_{-34}
Band 6	$6.51^{+1.48}_{-1.56}$	$5.59^{+0.95}_{-1.13}$	1146^{+149}_{-158}	770^{+157}_{-183}	789^{+75}_{-65}
[CII]	$8.94^{+0.9}_{-1.15}$	$6.01^{+0.44}_{-0.38}$	596^{+43}_{-42}	525^{+40}_{-50}	764^{+110}_{-50}
CO(8-7)	$6.22^{+0.75}_{-0.52}$	$5.49^{+0.39}_{-0.33}$	1200^{+106}_{-89}	970^{+84}_{-105}	936^{+248}_{-270}
p-H_2O (2_{02}-1_{11})	$7.67^{+0.68}_{-0.31}$	$6.73^{+0.99}_{-0.78}$	1043^{+55}_{-56}	912^{+67}_{-65}	1148^{+273}_{-247}
o-H_2O (3_{21}-3_{12})	$12.74^{+0.27}_{-0.66}$	$12.23^{+0.31}_{-0.47}$	739^{+57}_{-64}	672^{+33}_{-31}	611^{+79}_{-105}
p-H_2O (4_{22}-4_{13})	$12.04^{+1.49}_{-1.82}$	$10.83^{+1.06}_{-1.01}$	782^{+76}_{89}	745^{+62}_{-75}	530^{+102}_{-180}

Table 4.6: Output properties of the lens-modelling and source reconstruction analysis. From the left: magnification factors and effective radii computed for the 3σ and 5σ emission. For comparison, the last column reports the output effective radius of the Sérsic profile adopted in the non-linear search.

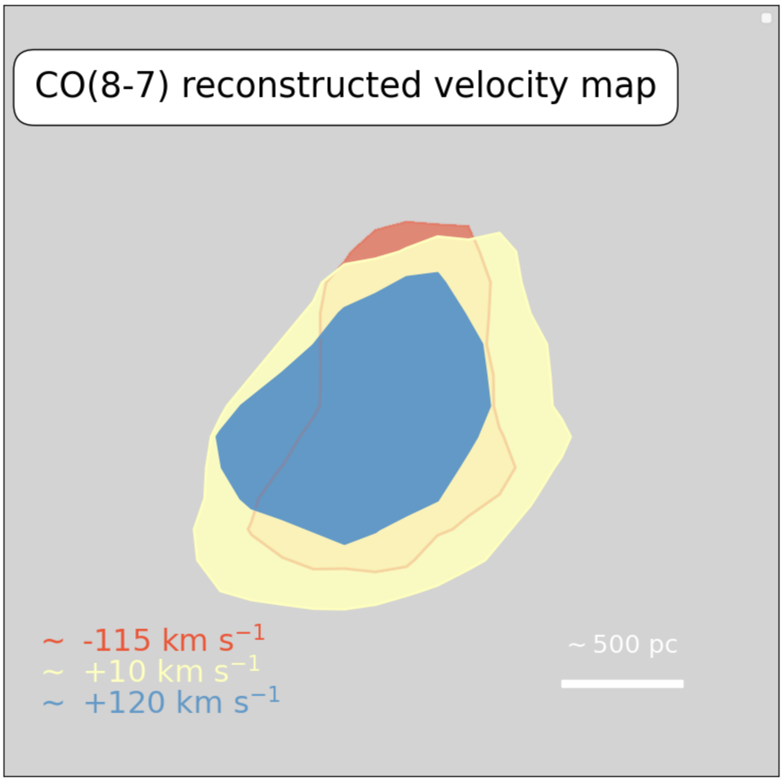

Figure 4.8: Reconstructed velocity map for CO(8-7) line emission. Each contour encloses the reconstructed $\sim 3\sigma$ surface brightness for 3 different velocity bins.

4.3.3 The lens

A peculiar aspect of J1135's foreground lens is its lack of clear detection in the deepest UV/optical images available from Hyper Suprime-Cam Subaru Strategic Program (Aihara et al. 2022, capable of detecting a 5σ limiting magnitude of 27.5 in the g band). As shown in analogous studies and as revealed by HST/NIR high-resolution images (e.g. Negrello et al. 2014), the foreground object usually dominates the emission in those bands, with a progressively higher contribution coming from the background source at higher wavelengths. For this reason, in order to achieve reliable results from the SED-fitting procedure, it is essential to fit and subtract the light profile of the foreground galaxy. In this case, however, only a marginal emission ($\lesssim 3\sigma$) comes from HST WFC3/F110 data and it is not possible to establish a priori whether it originated by the lens or by the lensed object.

Albeit this, the reason for the unusual faintness of this galaxy in the spectral bands in which one would expect it to dominate the total emission of the system is still unclear.

The first possibility assumes the lens to be itself a dust-obscured star-forming galaxy. Indeed, a faint ($\gtrsim 4\sigma$) central emission is detected in the normalised residuals of the lens modelling and visible in Figure B.1 in Appendix B.

Moreover, the resulting best-fit lens centroid displacement with respect to the centre of ALMA observations coincides with the origin of the faint residual emission. This hypothesis would also be reinforced by the lack of the optical/NIR image of the lens and by the ALMA flux density values measured from the central component (see right panel of Figure 4.9), which are consistent with the threshold sub-mm galaxy (e.g. Casey et al. 2014). However, with the current observations, it is not clear whether it could be unambiguously associated with the lens or with some spurious emission related to the noise.

A second possibility is that the faintness of such a foreground object could be due to its unusually high redshift. Assuming that the lens is a massive elliptical and its mass consists mainly of stars, its lack of detection in the optical and NIR bands would place upper limits on its SED, making such galaxy likely to be at $z \gtrsim 1.5$, as shown in the left panel of Figure 4.9, where the SED contributions of template massive ellipticals are shown as a function of the lens redshift. The SED of the foreground object is modelled constraining its from the Einstein (total) mass resulting from the lens modelling ($M_E \sim 1.15 \times 10^{11}\ M_\odot$), which is compatible with the lens to be a massive elliptical galaxy. Specifically, I adopted the template for an elliptical galaxy with 2 Gyr age from the SWIRE library (Polletta et al. 2007). The threshold $z \gtrsim 1.5$ is well distant from the redshift distribution's bulk of lenses in systems like this one, typically around $z \sim 0.7 - 0.8$ (Lapi et al. 2012, Negrello et al. 2017). Moreover, finding the lens at $z \gtrsim 2$ would make this definitely a rare object, whereas we do not expect at all such a massive elliptical to be at $z > 2.5$ since the redshift distribution of these lenses tends to zero after such threshold (Lapi et al. 2012).

In such a case, the central feature detected through ALMA observations could correspond to a third, highly de-magnified image of the source located close to the centre of the lens. Several works attempted to detect this feature in similar objects

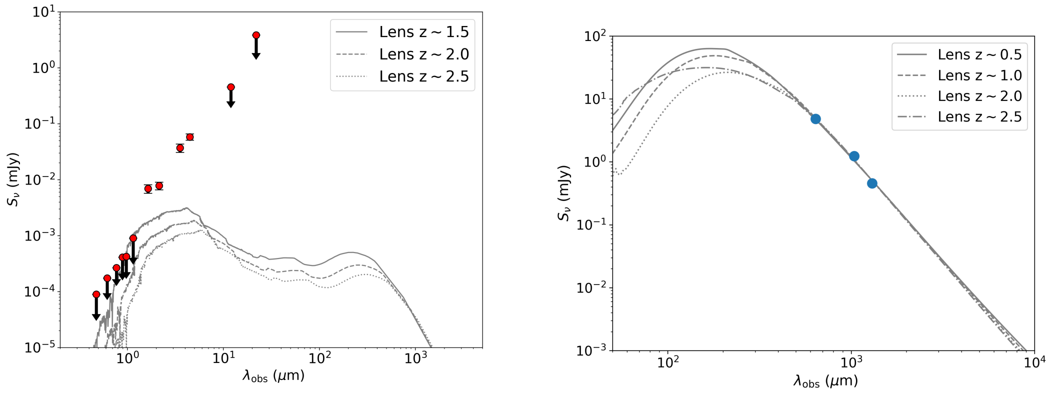

Figure 4.9: *Left:* SED templates of a passive elliptical galaxy at redshift $1.5 < z < 2.5$ compared with the photometry of J1135. The flux densities reported in Table 4.4 from HSC/g to WISE-4 (22μm) are represented as red points. Upper limits at 3σ are shown as arrows. *Right:* best-fit SED obtained with CIGALE (see Appendix D) for the ALMA Band 8, 7, and 6 flux densities extracted from the central component including optical-to-MIR upper limits, here assumed to belong to the lensing object. Here I have assumed a redshift range $0.5 < z < 2.5$.

drawn from the same sample of J1135 (e.g. SDP.81 and SDP.9, Wong et al. 2015; Wong et al. 2017) without success, given that the lens modelling theory predicts a de-magnification reaching factors of $\sim 10^2 - 10^4$ (Muller et al. 2020).

In both assumptions, the contribution from the lens is negligible for flux densities from the H and Ks VIKING bands up to the higher wavelengths. Hence, with the current data and under this assumption, lens subtraction is not needed. The situation is less clear for the marginal HST WFC3/F110 detection, and, for this reason, I have considered this value as an upper limit. From the lens modelling of ALMA observations, I inferred the intrinsic emission coming from the two images of J1135, however, uncertainties remain for flux densities probed by *Herschel*, where the poor angular resolution prevents disentangling between the contribution of the lens and the background source.

In the following analysis, I will adopt the second hypothesis (i.e. the lens is a massive elliptical galaxy at high redshift), however, it should be noted that if the first hypothesis (i.e. the lens is a DSFG) is confirmed, it could affect the estimate of physical properties such as the SFR, the dust mass, and the dust temperature of the lensed galaxy. Further observations are needed to probe this assumption, and correctly settle the actual contribution of J1135's background and foreground objects to the total emission.

4.4 SED fitting

As described in the previous Section, in the following analysis I assumed that the contribution of the lens to the total light is negligible. By correcting the available photometric information for the magnification factors we can retrieve the *intrinsic* physical properties of J1135. For this purpose, we have adopted

GalaPy, a new extensible API for broadband galaxy SEDs modelling (Ronconi et al. 2023, submitted to ApJ).

GalaPy enables the modelling and fitting of galactic SEDs from the X-ray to the radio band, as well as the evolution of their components and dust attenuation/reradiation. GalaPy incorporates both empirical and physically-motivated SFHs (e.g. constant, delayed exponential, etc.), in which the physical properties of the synthetic galaxy are derived analytically with a minimal parameterization, and also non-parametric interpolated SFHs that allow modelling the emission from galaxies simulated with hydro-dynamical N-body codes. The unattenuated stellar emission is computed via state-of-the-art single stellar population synthesis libraries. The dust model features two components: a compact warmer medium, rendering the contribution due to birth clouds, and a colder one rendering diffuse dust. As in the classic code GRASIL (Silva et al. 1998), this dust model evolves with time, encoding the gradual evaporation of birth clouds due to intense high energy emissions from young stars, implementing an age-dependent energy conservation scheme to account for the absorption and emission at longer wavelengths due to dust, in order to bypass the computational cost of radiative transfer and to account for the absorption and emission at longer wavelengths due to dust. This age-dependent scheme self-consistently computes the total energy absorbed and re-emitted by dust at each galactic age instead of assuming the temperatures of dust as free parameters. This approach allows the derivation of physical attenuation curves that vary with time due to the co-evolution of stellar populations and dust components. This latter feature is becoming increasingly relevant for the analysis of galaxies at their formation epoch, a regime that has been disclosed by the advent of JWST. Furthermore, GalaPy also includes additional sources of stellar continuum such as synchrotron, nebular/free-free emission, and X-ray radiation from low and high-mass binary stars.

On the computational side, GalaPy exploits a fully Bayesian parameter space sampling, which allows for the inference of parameter posteriors and thus facilitates the study of the correlations between the free parameters and the other physical quantities that can be derived from modelling. Two libraries for parameter-space sampling are available for the user: the Markov-chain Monte Carlo affine-invariant ensemble sampler provided by `emcee` (Foreman-Mackey et al. 2013) and the dynamic nested sampling approach offered by `dynesty` (Speagle 2020), offering different possibilities for addressing the challenge of multi-dimensional sampling. Moreover, GalaPy is the fastest SED generation tool of its kind, with a peak performance of almost 1000 SEDs per second. The models are generated on the fly without relying on templates, thus minimising memory consumption.

I have exploited the available broad-band photometry described in Section 4.2.3 and the continuum ALMA emission, including upper limits for non-detections. For ALMA Bands 8, 7, and 6 I have corrected the flux density values for the respective magnification factors reported in Table 4.6, while I used an average value of $\mu \sim 9.2$ for low-resolution photometric data. As described in Section 4.3.3, I have adopted the assumption that the observed photometry belongs only to the lensed source. In Appendix C I describe the hyper-parameters chosen for the SED-fitting procedure of J1135. Upper limits are treated by GalaPy by considering them as

SED-fitting results		
log age [yr]	$8.40^{+0.39}_{-0.48}$	[8.62]
log SFR [$\mathrm{M_\odot\ yr^{-1}}$]	$2.91^{+0.08}_{-0.07}$	[2.77]
$T_{\rm MC}$[K]	$45.14^{+24.27}_{-25.90}$	[63.23]
$T_{\rm DD}$[K]	$45.50^{+3.89}_{-5.84}$	[43.06]
$\log M_{\rm dust}$ [$\mathrm{M_\odot}$]	$9.36^{+0.36}_{-0.48}$	[9.34]
$\log M_{\rm gas}$ [$\mathrm{M_\odot}$]	$10.76^{+0.52}_{-0.48}$	[10.57]
$\log M_\star$ [$\mathrm{M_\odot}$]	$\lesssim 11.19$	[11.54]

Table 4.7: Output properties from GalaPy. From the first raw: galaxy age, SFR, temperatures of the dust for the MC and DD components, dust, gas and stellar masses. The median values are reported with the uncertainties of the parameters, corresponding to the 68% percentile around the median. The best-fit value of each quantity is enclosed in square brackets.

regular points entering the same χ^2 likelihood used for detections.

The resulting best-fit SED and parameters, along with their posteriors are shown in Figure 4.10, Table 4.7 and Figure 4.11. In Figure 4.10 upper limits are marked as circles with arrows, while detections are round markers with error bars. The lower panel shows standardised residuals and the χ^2 associated with the best-fitting model. Figure 4.11 also shows the median and the uncertainties of the parameters, corresponding to the 68% percentile around the median.

Besides the solid value of the reduced χ^2 statistics, we can notice that the grey 2σ confidence contour in the upper panel shows the NIR-MIR region of the spectrum is just upper-limited, as a result of having just observed upper limits in this wavelength range. This is of course expected, as one of the free parameters of the model (i.e. the fraction of diffuse dust emission that is in PAH, $f_{\rm PAH}$) is completely and only determined by measurements in the NIR to MIR.

I conclude this Section by highlighting the excellent agreement between the parameter values derived with GalaPy with respect to the values obtained from CIGALE (Boquien et al. 2019), where the analysis has been performed with different, but compatible, methods. The SED-fitting procedure performed CIGALE is described in detail for comparison in Appendix D. I note that in this case, I have adopted a delayed exponential SFH, a Bruzual & Charlot (2003) synthesis spectra library for the stellar component, a modified Charlot & Fall (2000) law for dust attenuation, and Draine et al. (2014) model for dust emission. It is also worth noticing that the synchrotron emission is treated with a separate module.

4.5 The Interstellar Medium of J1135

Taking advantage of the SED-fitting results and the reconstructed morphologies, we are able to investigate the ISM conditions of J1135 and its evolutionary state. In the first part of this Section, I will focus on the dust, gas, and stellar properties of J1135, inferred from the continuum data and [CII] and CO(8-7) spectral lines. As the water lines warrant a separate discussion, their analysis will be treated

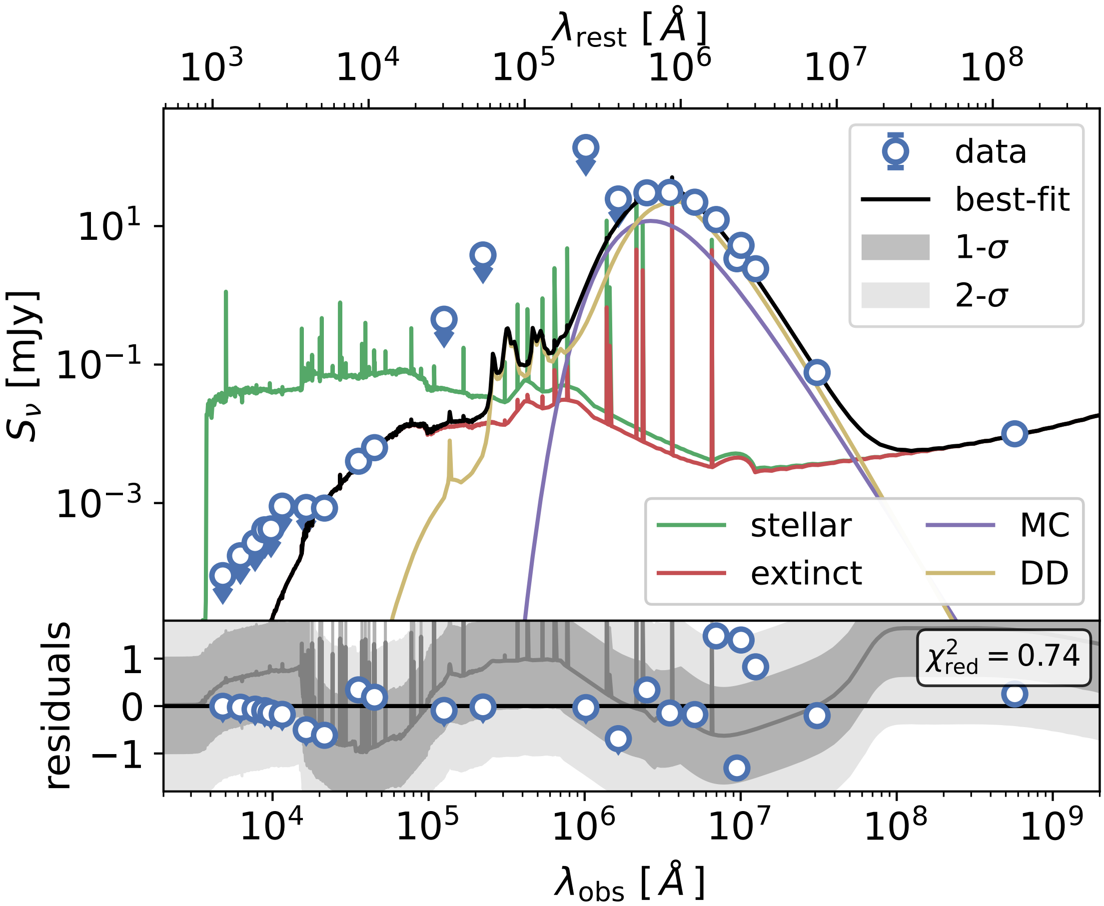

Figure 4.10: Best-fit model (black line) and 1- and 2-σ confidence intervals around the mean of samples (dark and light grey shaded areas, respectively) of the UV-to-radio SED of J1135 performed with GalaPy (Ronconi et al. 2023, submitted to ApJ). The total best-fitting model is decomposed into the different emission components: green and red solid lines show respectively the un-attenuated and dust-attenuated stellar emission (including line and free-free emission from nebular regions as well as the supernova synchrotron continuum), the yellow and purple solid lines mark the grey-body emitted by the two assumed dust components with temperatures of about $\sim$ 40 K and $\sim$ 60 K respectively. Round markers with error bars represent the detected fluxes while round markers with downward arrows represent 1σ upper limits.

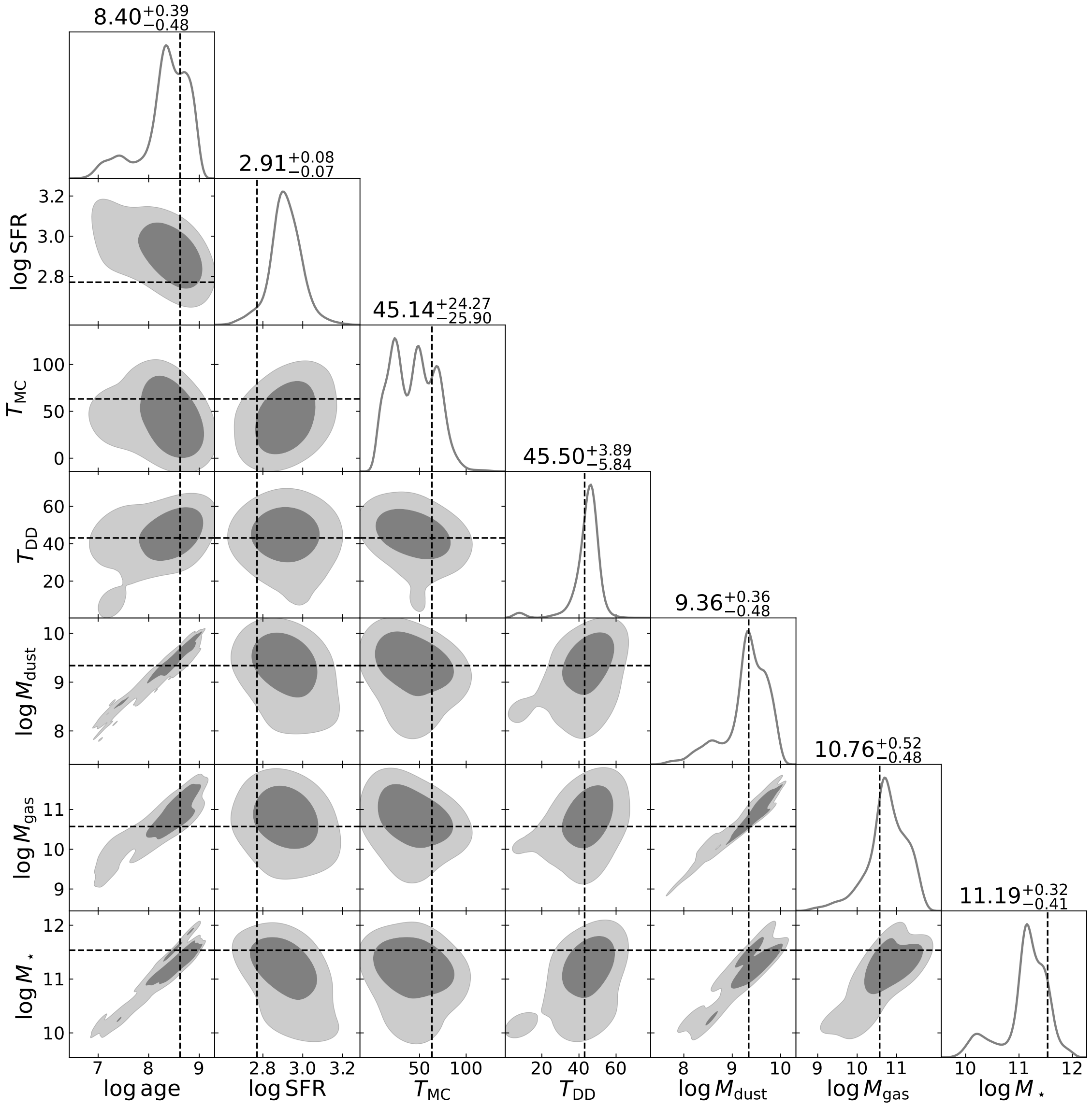

Figure 4.11: Corner plot obtained with GalaPy for J1135, showing the 1- and 2-d marginalised posteriors for a subset of the parameter space dimensions. The dark (light) shaded area represents the $1-\sigma$ ($2-\sigma$) confidence interval. Dashed black lines mark the position of the best-fitting parameters, while the values above the diagonal show the median and 68% percentile around the median ($\sim 1\sigma$ confidence in a Gaussian approximation).

separately in Section 4.6.

4.5.1 Dust properties

Table 4.7 reports the best-fit dust mass estimated by GalaPy. The SED-fitting also provides the estimates of the dust luminosity of J1135. We got $\log L_{\mathrm{TIR}} = 13.03 \pm 0.06\,\mathrm{L}_{\odot}$ and $\log L_{\mathrm{FIR}} = 13.01 \pm 0.05\,\mathrm{L}_{\odot}$ for the total (estimated in the range $3-1100\,\mu$m) and the FIR (estimated in the range $8-1000\,\mu$m) luminosities, with a small difference between the two estimates. The value of M_{dust} is consistent with what is obtained with CIGALE by choosing the Draine et al. (2014) multi-parameter library. This is a physically motivated model, where the dust is described as a mixture of carbonaceous and amorphous silicate grains. This results in a more robust estimate of the dust mass (M_{dust}) with respect to a single-temperature MBB fit, which tends to underestimate M_{dust} by a factor of ~ 2 (Magdis et al. 2012, Berta et al. 2016), resulting in a wrong gas-mass derivation. I will further explore this discrepancy in the case of J1135 in Section 4.5.2.

Concerning the dust temperature estimation in high redshift SFGs, different results in the literature (e.g. Riechers et al. 2013, Spilker et al. 2016, Scoville et al. 2017a, Simpson et al. 2017, Jin et al. 2019, Cortzen et al. 2020, Jin et al. 2022) suggest that the widely adopted optically-thin MBB approximation, may not be sufficient to infer the highest dust temperatures for dusty and optically-thick galaxies. For example, Jin et al. (2019, 2022) reported the presence of a population of compact, high-redshift ($z \sim 4$) starburst selected in the FIR with *Herschel* and detected with ALMA and NOEMA, showing abnormally cold dust temperatures. This behaviour can be associated either with a low star formation efficiency accompanied by a rapid enrichment of metals or to dust continuum in a FIR optically thick regime (Cortzen et al. 2020).

Here, following Cortzen et al. (2020), I explore this problem by estimating different dust temperatures with three different approaches and then comparing the values with the results from GalaPy.

The first estimate comes from the results obtained with the alternative SED-fitting code adopted in this analysis (i.e. CIGALE, see Appendix D). The other two estimates are obtained assuming an optically thin, and an optically thick MBBs. For the first case, the Draine & Li (2007); Draine et al. (2014) model assumes an optically thin dust emission and does not provide a luminosity-weighted temperature. However, following Draine (2011) the retrieved dust temperature as $T_{\mathrm{dust,DL14}} = 20U_{\mathrm{min}}^{1/6}$ K, where U_{min} is the value of the minimum intensity of the radiation field inferred from CIGALE. From the best-fit value of $U_{\mathrm{min}} = 44.3 \pm 10.6$ we obtain a dust temperature of $T_{\mathrm{dust,DL14}} = 37.7 \pm 1.5\,$K.

Exploiting the available FIR-to-mm photometry I have then computed the dust temperature by fitting a single temperature MBB under the optically-thin approximation, described as:

$$S_{\nu} \propto \frac{\nu^{3+\beta}}{e^{(h\nu/k_{\mathrm{B}}T_{\mathrm{d,thin}})} - 1}. \tag{4.4}$$

k_{B} is the Boltzmann constant, and β is the dust emissivity index, here assumed

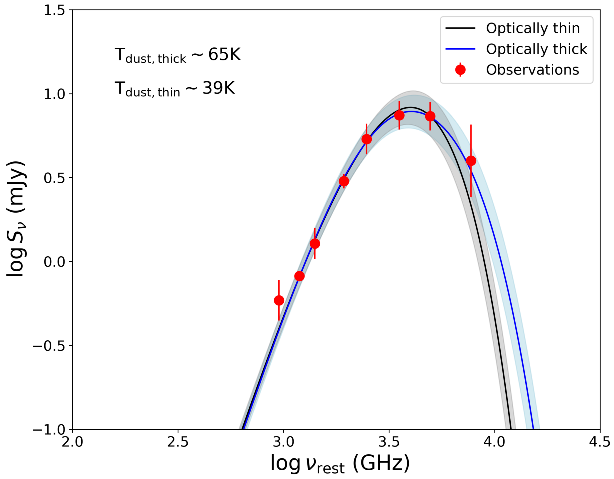

Figure 4.12: Best-fit FIR to sub-mm rest-frame SED of J1135. Red points are the observed flux densities and errors, and the black and the blue lines are the best-fitting modified black body spectrum in the optically thin and thick regime respectively. The grey shaded area represents the 68% confidence interval for the best-fit model.

to be $\beta = 2$.

Similarly, for the optically thick regime, I fit the single temperature MBB defined as:

$$S_\nu \propto (1 - e^{-\tau_\nu}) \frac{\nu^3}{e^{(h\nu/k_{\rm B}T_{\rm d,thick})} - 1}, \tag{4.5}$$

with $\tau_\nu = (\nu/\nu_0)^\beta$ and ν_0 being the rest-frame frequency corresponding to a dust opacity equal to unity.

The best-fit results for both the optically thin and optically thick approximations are represented in Figure 4.12. The resulting dust temperatures are respectively $T_{\rm dust,thin} = 38.6 \pm 1.1$ K and $T_{\rm dust,thick} = 64.8 \pm 2.8$ K, where the former is consistent with $\rm T_{dust,DL14}$.

From this analysis, I derived a significant discrepancy between $\rm T_{dust,thin}$ and $\rm T_{dust,thick}$, apparently in agreement with what is observed for similar objects in literature. This discrepancy, and the values obtained from the MBB fitting, are in agreement with the dust temperatures retrieved by GalaPy assuming the age-dependent two-component dust model. The recent work of Jin et al. (2022) presented useful diagnostics which can be used to identify whether an optically thick model is more appropriate to describe dust emission (e.g. the SFE, and their position relative to the infrared luminosity surface density diagram). Taking advantage of these indicators, I investigate here the nature of the dust continuum emission of J1135. The star-formation surface density computed in Section 4.5.3 is well above the threshold suggested by the authors for the optically thick regime (i.e. $\Sigma_{\rm SFR} \gtrsim 20\ \rm M_\odot yr^{-1} kpc^{-2}$). Moreover, the dust temperature inferred from the optically-thin approximation implies $\Sigma_{\rm IR} \gtrsim 1.5 \times 10^5 T^{4.21}_{\rm dust,thin}$, inconsistently with the Stefan-Boltzmann law, which represents an upper boundary for an object to emit as a black body. In Figure 4.13 I show the dust temperature against the intrinsic infrared luminosity ($\propto$ SFR) and colour-coded for the effective radius for J1135. J1135 is compared to other samples of DSFGs according to its position with respect to the modified Stefan-Boltzmann law inferred by Yan & Ma (2016) for different effective radii. As expected, temperatures of the order of $T_{\rm dust,thin}$ and $T_{\rm dust,DL14}$ (corresponding to the diffused component in the GalaPy model) would imply effective radii $\gtrsim$ 1.5 kpc at the inferred $L_{\rm TIR}$, which are well above with respect to what we measure from the reconstructed dust continuum morphology. In Figure 4.13 I have therefore assumed the case $T_{\rm dust} = T_{\rm dust,thick}$, obtaining a more consistent result. This is indeed in concordance with what was predicted by Jin et al. (2022) for apparently cold starburst, disfavouring the low-efficiency star-formation mechanism accompanied by a fast metal enrichment. In order to compare J1135 with other samples of DSFGs I have included the sample of FIR selected apparently cold starburst from Jin et al. (2022) in the redshift range $3 \lesssim z \lesssim 6$, the sample of FIR/sub-mm selected lensed quasars ($1.5 \lesssim z \lesssim 2.5$) from Stacey et al. (2021), and finally a sample of lensed DSFGs selected in by *Herschel* (Nayyeri et al. 2016, Negrello et al. 2017) analysed in the works by Nayyeri et al. (2016), Dye et al. (2018) distributed over the range $1 \lesssim z \lesssim 4$ (values are reported in Table A.1. of Stacey et al. 2021). J1135 shows smaller sizes compared to other lensed DSFGs at similar luminosities ($L_{\rm TIR} \gtrsim 10^{13}$ L$_\odot$) and temperatures comparable with some of the warmer lensed quasars.

In conclusion, I have shown that when considering the dust emission originated by the most compact component in J1135, an optically thin MBB is likely not appropriate to infer the dust temperature. Moreover, for starburst systems such as J1135, the dust emission is best reproduced by two components (diffuse + molecular clouds) which can be modelled with innovative approaches such as the one implemented with GalaPy. I will focus on this latter aspect in Section 4.6.3, in the context of the emission from water lines as thermal diagnostics for the dust.

4.5.2 Stellar and gas content

The bunch of available data allows us to estimate the gas content by adopting several empirical calibrators. First, we directly estimate the gas mass from the [CII] following Zanella et al. (2018), we assumed $\alpha_{\rm [CII]} \equiv M_{\rm gas}/L_{\rm [CII]} = 22 {\rm M}_\odot/{\rm L}_\odot$, which is calibrated on starburst galaxies spanning a redshift range $z \sim 2-6$. Secondly, the molecular gas content ($M_{\rm H_2}$) is estimated by deriving $L'_{\rm CO(1-0)}$ from the demagnified $L'_{\rm CO(8-7)}$ luminosity. We then follow Fujimoto et al. (2022) adopting a conversion factor of $L'_{\rm CO(1-0)} = 1.5 L'_{\rm CO(7-6)}$ estimated for high redshift starburst galaxies in literature (e.g. Riechers et al. 2013). This conversion factor is referred to a different transition, corresponding to higher luminosity values of the CO-SLED (Yang et al. 2017), for this reason, the resulting value of $L'_{\rm CO(1-0)} \sim 1.6 \times 10^{10}$ K km s^{-1} pc^2 is considered as an upper limit. This estimate is consistent with the value of $L'_{\rm CO(1-0)} \sim 1.5 \times 10^{10}$ K km s^{-1} pc^2 found by Harris et al. (2012) adopting an indicative magnification factor of 10. The molecular gas mass is then computed by assuming two different values of $\alpha_{\rm CO} = 0.8-4.6$. The value of $\alpha = 0.8$ is calibrated

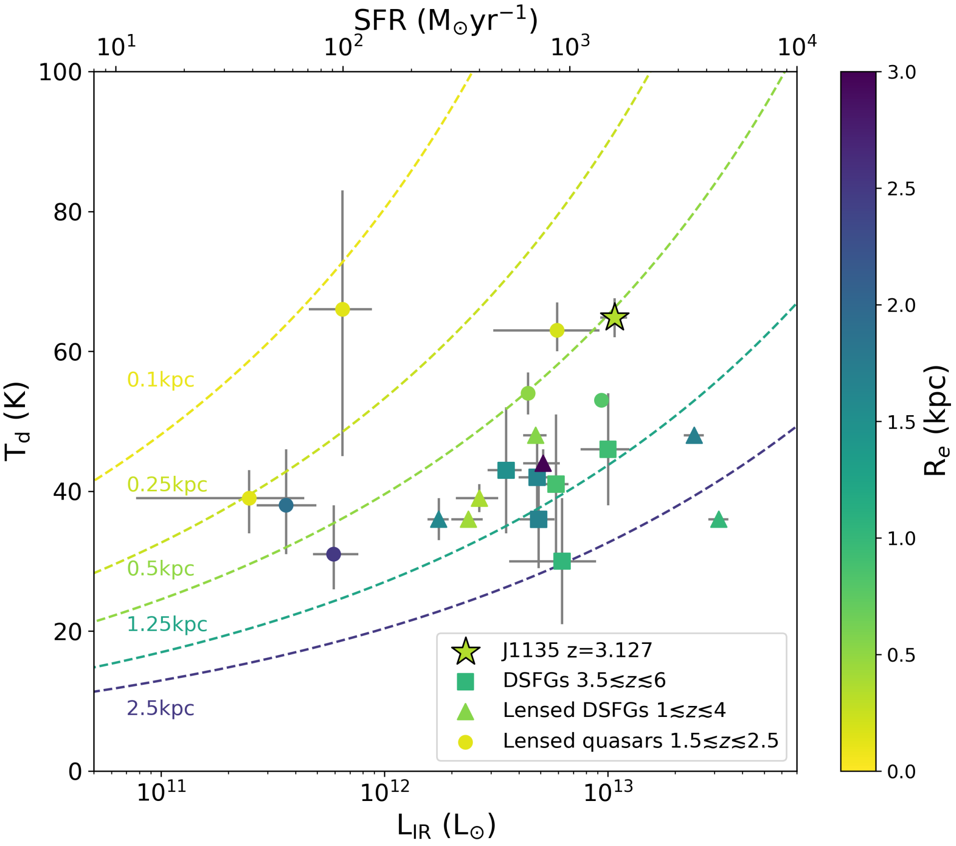

Figure 4.13: Dust temperature vs infrared luminosity colour-coded according to the effective radius. Dashed lines represent the modified Stefan-Boltzmann relation (Yan & Ma 2016). Circles show the sample of lensed quasars from Stacey et al. (2021). Triangles report the sample of FIR selected starburst from Jin et al. (2022); squares show a sample of lensed DSFGs selected by *Herschel* (Nayyeri et al. 2016, Dye et al. 2018), the original values are taken from Table A.1 of Stacey et al. (2021). The star symbol shows J1135.

Calibrator	log M_{gas} [$M_\odot$]
[CII]	11.04 ±0.04
CO(1-0)	$\lesssim$ (10.2-10.9)
850μm	11.5±0.2
α_{GDR}	(10.51-11.04)±0.05

Table 4.8: Values for the molecular mass computed from different calibrators.

from local ULIRGs with super-solar metallicity (Downes & Solomon 1998), while the higher value is calibrated in the Milky Way (Solomon & Barrett 1991).

The molecular gas content can also be estimated by means of the empirical calibration (Scoville et al. 2017b) as $\alpha \equiv < L_{850\mu m}/M_{gas} >= 6.7 \pm 1.7 \times 10^{19}$ erg s^{-1} Hz^{-1} M$_\odot^{-1}$.

Finally, the dust content can be converted into gas mass assuming a variable gas-to-dust ratio of $\delta_{GDR} = 30 - 92$ referred to typical solar and super solar metallicity following Magdis et al. (2012) and Fujimoto et al. (2022). The values obtained for the molecular gas masses are reported in Table 4.8. These estimates are in good agreement with the value inferred from GalaPy. For consistency we adopted the dust mass value inferred from GalaPy, however, it is worth checking how the dust opacity could affect our results. However, we caution the reader against deriving the dust mass through the effective dust temperatures inferred from a single-temperature MBB, as this estimate does not reflect the actual dust content of the ISM (see e.g. Scoville et al. 2016). The temperature-weighted dust masses in the optically thick regime are computed by adopting the value of $T_{dust,thick}$. obtained in Section 4.5.1 as. The inferred value is $\log M_{dust,thick} = 8.7 \pm 0.05$ M$_\odot$, which is ~ 4.6 times lower than the GalaPy estimate and would result in a gas mass range of $\log M_{gas,GDR} \sim (10.2 - 10.7)$ M$_\odot$.

The stellar mass estimate in output from the SED fitting must be considered as an upper limit. Indeed given the lack of a clear detection in NIR images it is not possible to correctly estimate the contribution coming from the lens (see Section 4.3.3 for a further discussion). Moreover, the dark nature of this object hinders a complete sampling of the optical and NIR parts of the SED. Aside from the values reported in Table 4.7 and D.1, I have computed the stellar mass assuming a typical stellar-to-dust mass ratio of $\delta_{SDR} \approx 100$, obtaining a value of $M_\star^{STD} \sim 2.2 \times 10^{11}$ M$_\odot$, in agreement with the SED fitting estimate.

4.5.3 Morphology and timescales

From the reconstructed continuum originated by the dust (Figure 4.6), a clear "clumpy" double-peaked structure is visible. First, I compare the effective radii inferred from the dust continuum at different wavelengths. Excluding the lower angular resolution reconstruction at 1.3 mm (Band 6), the most resolved 0.64 and 1.0 mm emissions do not show particular differences in their spatial extension ascribable to a dust-temperature gradient, even though further observations are needed in order to explore this possibility. Then, as shown in Figure 4.14 the source-plane maps reconstructed from our lens modelling for three different tracers are overlapped. The [CII] and CO(8-7) line emission and the dust continuum at 640 μm are shown, the latter corresponding to the data set with the highest angular resolution. The first visible difference between the three emissions concerns their spatial extension: while the [CII] and the dust continuum occupy a similar area, the CO(8-7) is more extended. The size discrepancy is most likely associated with the difference in angular resolution of the respective data set (see also $R_{\rm eff}$ and θ values reported in Tab.4.6) more than an intrinsic morphological difference. I also note that this difference is present in the dust continuum for the same data set as CO(8-7) (i.e. Band 6), where the estimated effective radii reach up to 1.1 kpc at 3σ. This comparison shows a co-spatial emission for the dust continuum and [CII] line, even though the peaks are located at different positions. The clumpy structures are also present in the reconstructed [CII] line emission, while it is likely to be not resolved for the CO(8-7) line, which extends in a more ellipsoidal profile. Further details on the CO(8-7) profile are provided in Section 4.6.2.

The [CII] is a fine structure line predominantly originated from high$-z$ photon-dominated regions and is typically used as a cool interstellar gas tracer and as a SFR estimator (see Casey et al. 2014 for a review). A well-known deficit in the [CII]/FIR ratio is observed in both nearby (e.g. Luhman et al. 2003, Díaz-Santos et al. 2017, Smith et al. 2017) and high-redshift star-forming galaxies (Stacey et al. 2010, Gullberg et al. 2015). This drop is found to reach very low values ($L_{\rm [CII]}/L_{\rm TIR} \approx 10^{-4}$) in spatially resolved studies (e.g. Gullberg et al. 2015, Lagache et al. 2018, Rybak et al. 2019). For J1135, I infer a [CII]/FIR ratio of $L_{\rm [CII]}/L_{\rm FIR} \approx 3.9 \times 10^{-4}$. Similar values are found for other strongly lensed galaxies among the H-ATLAS sample. For example, Rybak et al. (2020) reported a deficit down to $\sim 3{\times}10^{-4}$ for spatially resolved ALMA data of SDP.81 (Partnership et al. 2015, Dye et al. 2015, Hatsukade et al. 2015, Rybak et al. 2015a,b, Swinbank et al. 2015, Tamura et al. 2015, Hezaveh et al. 2016) at $z = 3.042$. Lamarche et al. (2018) found similar values ($\sim 2 \times 10^{-4}$) for SDP.11 at $z = 1.7$, even though our galaxy shows a more compact morphology in the [CII] emission with respect to other objects. I have computed the star-formation surface density using the mean of the effective radii of the 5σ continuum dust emission at 640μm and 1.1 mm reported in Table 4.6. The inferred value of $\Sigma_{\rm SFR} \gtrsim 1200\ {\rm M}_\odot\ {\rm yr}^{-1}\ {\rm kpc}^{-2}$ (higher when considering the SFR in output from CIGALE reported in Appendix D) is consistent with a galaxy being on the verge of the Eddington limit for a radiation pressure supported starburst (Andrews & Thompson 2011, Simpson et al. 2015). This result is compatible with the possible explanation of the deficit to be attributed to a lower increase of the [CII] emission with respect to the IR.

From the average of the gas mass values reported in Section 4.5.2, the estimated depletion timescale is $\tau_{\rm depl} \simeq M_{\rm gas}/{\rm SFR} \simeq 10^8$ yr, which translates to a high star formation efficiency reaching up to $\sim 10^{-8}\ {\rm yr}^{-1}$. Moreover, the inferred age of $\simeq$ few 10^8 yr is indicative of a young galaxy, offset from the main sequence locus of SFG at z~3 (Speagle et al. 2014).

Our results are consistent with the expectations reported in Vishwas et al. (2018), where the analysis of the Lyman continuum photons required to sustain the luminosity of the [OIII] 88 μm line pointed out the presence of young and massive stars ionising the surrounding HII regions. The same authors found no

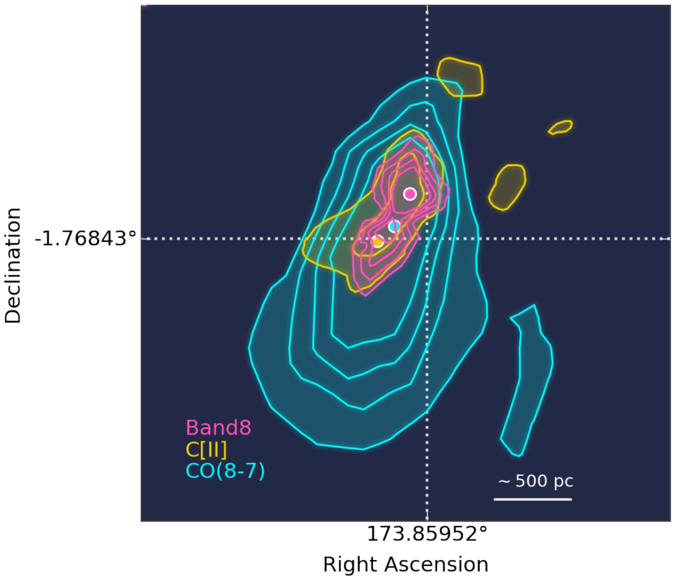

Figure 4.14: Comparison between the source reconstructed emissions of the ALMA continuum at 640 μm and the spectral emission of the CO(8-7) and [CII] lines. Contours are displayed at 9,7,5,3 $\times\sigma$, filled circles represent the position of the peak for each emission.

significant AGN contribution from the SED analysis, consistent with what we infer from the FIRRC for J1135 ($q_{IR} \approx 2.8$, see Table D.1), which is indicative of a star-formation-dominated object. However, it should be pointed out that lacking a good sampling of the MIR part of the SED, the presence of the AGN in J1135 is still arguable. Moreover, the CO(8-7) line associated with high transitions, can point towards the presence of large amounts of energy linked with a heavily dust-embedded central nucleus activity as well as a strong star-formation activity.

The hypothesis of J1135 being a compact starburst is also supported by the source reconstruction of the highest angular resolution ALMA dust continuum emission at 640 μm and 1.1 mm shown in Figure 4.6, where the effective radius reaches an average value of ~ 350 pc.

4.6 Resolving water emission in J1135

4.6.1 Water emission in high-redshift galaxies

Another interstellar molecule of key importance in the astrophysical environments of star-forming galaxies is H_2O. Milky Way observations (Caselli et al. 2010) suggest that water abundance in the gas phase, defined as $[H_2O]/[H_2] = X(H_2O)$, is quite low in cold molecular clouds, where it is strongly depleted on dust grains to levels $X(H_2O) < 10^{-9}$. However, water becomes the third most abundant species (after H_2 and CO) in dense warm regions, where star formation raises the dust temperature above the ice evaporation limit, or in shock-heated regions such as those dominated by AGN-driven winds (Bergin et al. 2003, Cernicharo et al. 2006, González-Alfonso et al. 2013). This makes water a unique and powerful tracer of the gas component involved in the highly energetic processes associated with compact nuclear starbursts or with the extreme environments of AGNs, potentially even more reliable than other molecular gas tracers (such as CO and HCN) traditionally used to probe the densest ISM regions. In fact, the H_2O lines offer diagnostics of warm gas regions which are usually deeply buried in dust and in star-forming regions and they can be almost as intense as CO lines and more prominent than HCN, as observed in the ULIRG Mkr 231 (Aalto et al. 1995, van der Werf et al. 2011,Feruglio et al. 2015). All in all, we can consider H_2O as a 'beacon' signalling the molecular clouds energy repository (Liu et al. 2017, hereafter L17, van Dishoeck et al. 2021).

Because of its high dipolar moment, extremely rich spectrum, and high-level spacing (compared to other molecules with low-level transitions in the millimetric range), H_2O is strongly coupled with the FIR radiation in compact and warm star-forming regions; in this vein, Omont et al. (2013) and Yang et al. (2013) found a strong correlation $L_{\mathrm{H_2O_{submm}}} \propto \mathrm{L_{IR}}^{\alpha}$, with $\alpha \sim 0.9-1.2$, extending from local to high-z sources. In addition, the excitation of water lines is also sensitive to collisions with Hydrogen molecules. Since the lowest vibrational band of H_2O lies at $\sim 6.3\,\mu$m (shorter than collisionally excited lines, e.g. HCN at $\sim$14.7μm), the continuum radiation is too weak to excite H_2O vibrational states: the relevant water transitions involve rotational states at the ground vibrational level. Pumping through *pure* rotational transitions, over the lowest vibrational level, is particularly important for an asymmetric top molecule like H_2O, since it makes the energy level structure more complex than the simple rotational ladder typical of linear or spinless molecules like HCN or CO.

The importance of radiative pumping in water vapour rotational transitions has been extensively discussed by González-Alfonso et al. (2004, 2008), Weiß et al. (2010), González-Alfonso et al. (2010, 2014), Pereira-Santaella et al. (2017) González-Alfonso et al. (2021, 2022), and L17. Absorption of FIR photons can populate mid/high-energy ($E_{\mathrm{up}} > 150$ K) rotational levels, which decay through a cascade process in which sub-mm photons are emitted; such energy levels are then radiatively excited even when collisions alone are ineffective due to their inadequate kinetic energy. However, the relative importance of collisions and IR pumping on water excitation in extragalactic sources turns out to be strongly dependent on the ambient ISM conditions.

4.6.2 Water excitation

H_2O lines are among the strongest molecular lines in high-z ultraluminous starburst galaxies. They serve as a powerful tool for investigating the physical, geometrical, and dynamic characteristics of the ISM within the unique and extreme conditions of star-forming molecular clouds. However, extracting essential information from these lines is not a straightforward task. This is primarily because most observed water lines have high optical depths, which hinders the direct inference of column densities from the measured line intensities. Additionally, the water spectrum is more intricate compared to other gas tracers, such as CO, due to the complex and fuddled interplay between collisional and radiative excitation

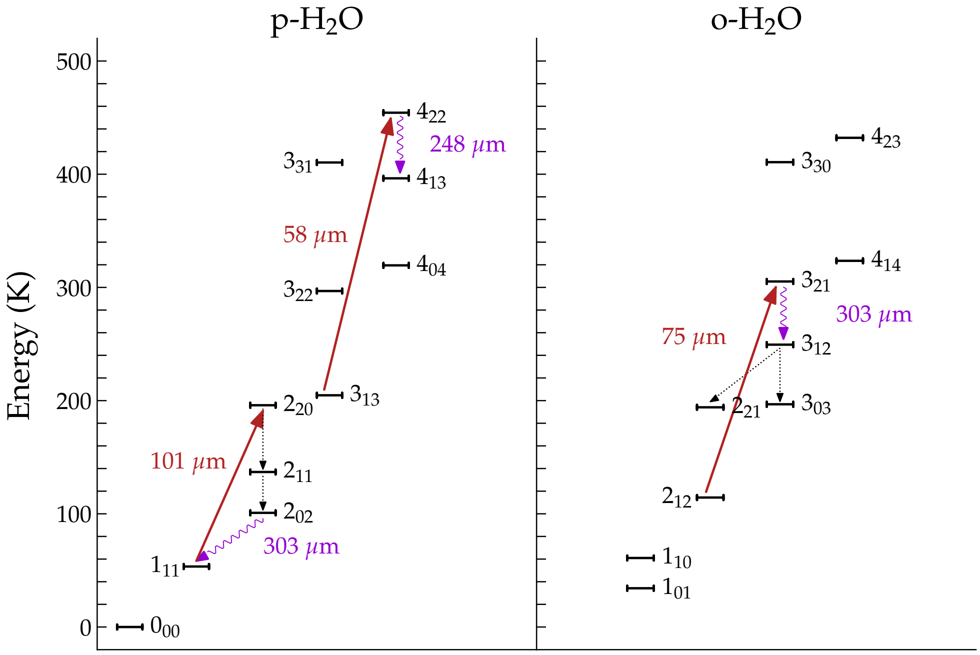

Figure 4.15: Energy levels of rotational water transitions. Red arrows indicate the FIR pumping from dust photons; the corresponding wavelengths are also indicated. Downward arrows indicate the radiative cascade of de-excitations in the pumping cycles. The three purple downward arrows highlight the three emission lines that are observed in J1135. Collisions may partially contribute to the population of the backbone levels. The energy levels are taken from LAMDA database, Schöier et al. (2005).

processes.

H_2O can effectively cool the dense, warm ISM when primarily excited through collisions below the critical density. In such cases, interactions with a colliding partner (typically H_2 or He) result in the release of kinetic energy from the gas through spontaneous decay, where each collision emits a photon (Draine 2011), leading to level de-excitation.

Nevertheless, the water molecule's high dipolar moment (1.85 Debye) and its strong coupling with the background radiation field introduce another significant excitation mechanism via the FIR continuum. FIR photons excite water molecules from low-lying "base" levels, initiating a cascade process that eventually returns the water molecules to their initial state. This cyclic process triggers the emission of observed sub-mm lines.

In other words, both collisions and photon absorption can potentially populate an energy level, but the de-excitation mechanism responsible for the observed lines is predominantly radiative and requires subcritical density. In Figure 4.15 the red downward arrows highlight the three water transitions targeted by ALMA observations of J1135: namely, a "low excitation" (E_{up} <250 K) line, p-H_2O $(2_{02}-1_{11})$, a "medium excitation" (150<E_{up} <350 K) line, o-H_2O $(3_{21}-3_{12})$, and a "high excitation" (E_{up} >350 K) line, p-H_2O $(4_{22}-4_{13})$. They are pumped in the corresponding cycles by dust-emitted photons at 101, 75, and 58 μm, respectively.

Radiative excitation and collisions are not mutually exclusive; in fact, collisions can play a significant role in populating the lower backbone level of a pumping cycle, thereby enhancing the FIR pumping process. Specifically, the collisional excitation of the 1_{11} and 2_{12} rotational energy levels can have a notable impact on the pumping cycles associated with the absorption of dust-emitted photons at 101 μm and 75 μm. This enhancement also leads to increased emission of two of the studied lines: the p-H_2O $(2_{02}-1_{11})$ and the o-H_2O $(3_{21}-3_{12})$.

Moreover, the emission of the p-H_2O $(2_{02}-1_{11})$ line may experience further enhancement in regions characterised by low continuum opacity but warm and dense gas. In such regions, the population of the upper-level p-H_2O 2_{02} may receive contributions from both collisional processes and the decay of 2_{11} within the FIR pumping cycle (González-Alfonso et al. 2014). To fully grasp the relative significance of FIR pumping and collisions, a comprehensive radiative transfer model must incorporate parameters related to the dust radiation field, as well as those describing the physical properties of the gas component. Generally, lines connected with the ground state levels of o-H_2O and p-H_2O serve as prime diagnostics of the cold gas (Yang et al. 2013, van Dishoeck et al. 2021). These lines often exhibit significant self-absorption or may even be entirely in absorption. On the other hand, the "medium level" lines are indicative of warm gas and are less influenced (if affected at all) by absorption. The "high-level" excited lines originate from energy levels that are exclusively populated in high-temperature gas and intense shock environments.

The analysis of observed line intensity ratios requires a radiative transfer model for the ISM in LTE, considering the interactions between collisions and FIR-pumping. However, this is beyond the scope of our current investigation. Nonetheless, an existing physical model (primarily focusing on in-situ processes)

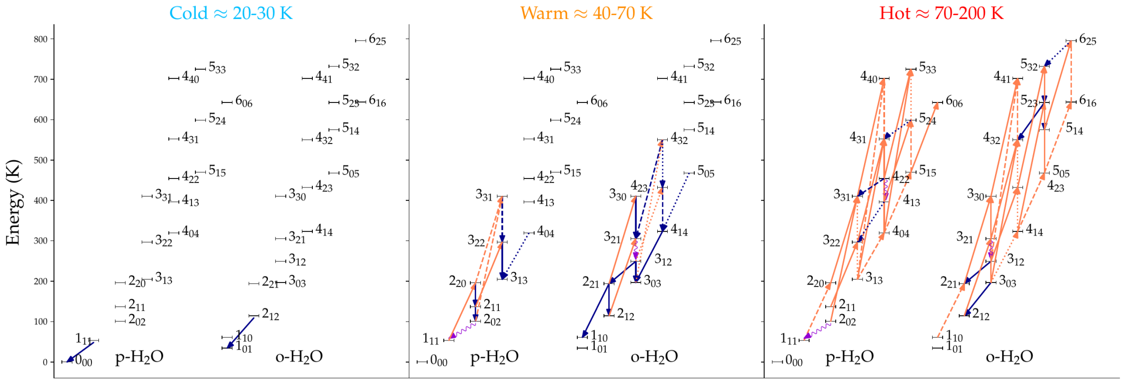

Figure 4.16: Water line transitions for cold, warm, and hot ISM components. Solid (dashed) arrows indicate the strongest (weaker) lines and dotted arrows show the weakest transitions. Purple arrows refer to the three transitions observed in the spectrum of J1135.

that is independent of the source's redshift can be utilised for this purpose. To do this, the radiative transfer models previously used in the study conducted by L17 on local star-forming galaxies can be used to derive some general insights about J1135.

L17's model was employed to analyse a survey involving multiple velocity-resolved water vapour FIR spectra from various local galaxies with diverse nuclear environments, ranging from pure nuclear starbursts to starburst nuclei hosting an AGN. To examine the significance of collisions and FIR pumping on line emission, they treated each component of the ISM as a collection of clumps with identical physical properties, while varying parameters related to the radiation field and gas within each clump model.

In this approach, water excitation within a multi-phase ISM is achieved using an extended 3D escape probability method to solve non-LTE radiative transfer, accounting for dust emission as well. The ultimate goal of this method is to explore the physical and chemical conditions within the nuclei of actively star-forming galaxies.

Water excitation is calculated for three typical ISM components: a cold extended component (with gas and dust temperatures of $20-30\,$K, the density of the order $\sim 10^4$ cm^{-3} and column density $\sim 10^{23}$ cm^{-2}); a warm component with gas and dust temperature between 40 and 70 K, typical densities of the order $\sim 10^5 - 10^6$ cm^{-3}, and column density of $\sim 10^{24}$ cm^{-2}; and a third, hot and dense component, needed to explain the high excitation transitions (such as those observed in Arp 220 and Mrk 231, which are commonly thought to host an AGN in their nuclei, see e.g, Soifer et al. 1999, Downes & Eckart 2007, Aalto et al. 2009, Fischer et al. 2010, Rangwala et al. 2011, van der Werf et al. 2011, González-Alfonso et al. 2014). The latter has gas and dust temperatures of $\sim 100-200$ K at densities $n(\mathrm{H}) \geq 10^6\,\mathrm{cm}^{-3}$, with high column densities $N_\mathrm{H} \geq 5\times10^{24}$ cm^{-2}. Figure 4.16 reports the excitation model of L17 for these ISM components; this will be used as a reference model to interpret ALMA water lines observations of J1135.

From the moment maps reported in Figure 4.4, besides random pixels of no statistical significance, the three water transitions in J1135 seem to arise from the same physical region, a nucleus stretched into an Einstein ring up to the size of a few kpc in the image plane. The observed emissions are consistent with a single molecular component, due to the strikingly similar kinematic properties; in addition, average velocities and velocity dispersions show no indication of merging nor rotation of the emitting cloud.

The left panel of Figure 4.17 shows the contour plots of the same lines at 5, 6, 9, and 12 σ and the peak of the corresponding emissions, superimposed to the continuum emission at 640 μm. For completeness, the figure also shows the emission peak and contours of the CO(8-7) emission. In the right panel of Figure 4.17, the 3σ and 11σ contours of the same lines in the source plane are superimposed to the continuum in Band 8. The reconstructed image reveals the H_2O with a resolution of < 500 pc scale. Notice that the comparison is made between observations at different ALMA resolutions: the low-level line is observed in Band 6, where the resolution is lower with respect to the other lines. However, it is still possible to locate a central nucleus, showing a clumpy structure corresponding to a region of less than 500 pc, where all the water lines have their peak of emission, superimposed to the CO(8-7) emission peak and adjacent to the 640 μm continuum peak. The reconstructed low-level transition peak is slightly ($\lesssim$500 pc) displaced from the peak of the other two lines but still located in the central region. The 3σ contours level of this line shows a tail of a few hundred parsecs stretching from the nucleus, resulting in a more extended region in which the low-level line emission is appreciably detectable, with respect to the medium and high-level lines. Noticeably, the peaks of CO(8-7) and $p-H_2O(4_{22}-4_{13})$ turn out to be completely superimposed to each other on both observed and reconstructed maps: the absence of differential lensing between these two emissions is another confirmation that they stem from the very same physical region. The extended emission tail of the water low-level transition is only weakly widening the velocity profile of the line shown in Figure 4.1. This result is confirmed by the mapping represented in Figure 4.17, evidencing a central, compact nucleus of <500 pc where CO (8-7) and the water lines have their maximum. As for the low-level line, the reconstructed emission of p-H_2O $(2_{02}-1_{11})$ (right panel of Figure 4.17) is spread over a larger zone, approximately delimited by its 3σ contour extending for about 1 kpc. In the next Section, I will focus on the observed emission of the water line transitions in J1135 in terms of the physical properties of the underlying gas and dust.

4.6.3 Qualitative thermal diagnostics

The $\lesssim$ 0.2 arcsecs resolution ALMA images presented here provide one of the highest angular resolutions of water emission ever reached in observations of high-z star-forming galaxies (see also Dye et al. 2022). As discussed in Section 4.6.2, the reconstructed emission of water of J1135 reveals that this target galaxy has a central, homogeneous, and compact zone ($<$ 500 pc) where low, medium, and high E_{up} water transitions are ignited by FIR pumping and collisions, together with collisional excitation of CO(8-7) and, partially, of the low-level water line. The latter is also weakly excited in a more extended region of the ISM. Though the rigorous diagnostic from these observations would require a full Ra-

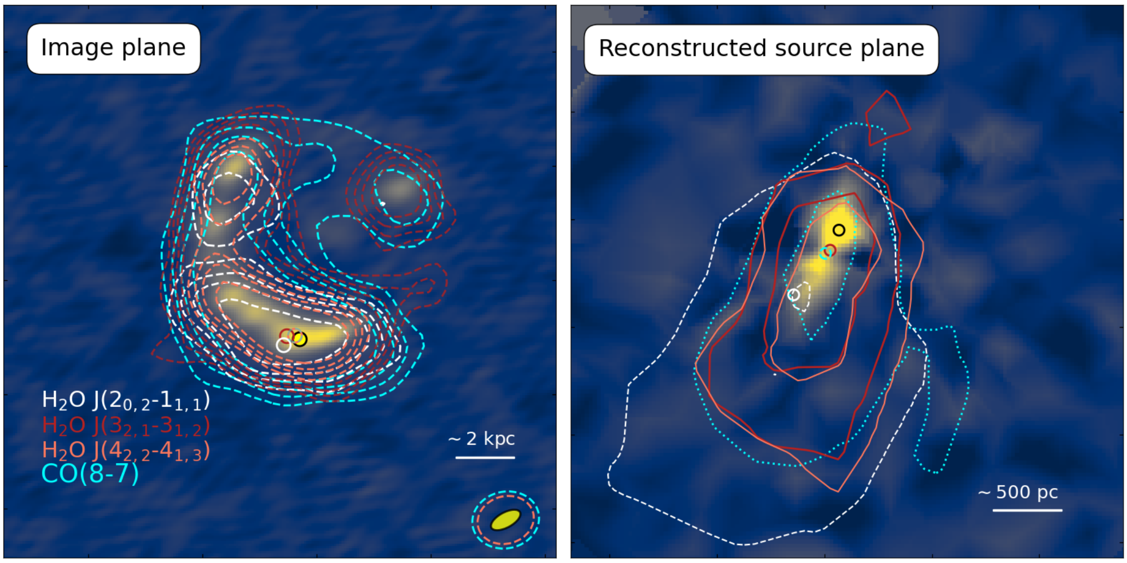

Figure 4.17: Left panel: Lensed image of J1135 ALMA Band 8 continuum at 640 μm. The superimposed contours of water lines and CO(8-7) moment 0 maps are shown at 5, 7, 9, 12 σ levels. Circles represent the position of the respective peak emissions. Right panel: reconstructed (de-lensed) source and line emissions. Contours are shown at 3 and 11 σ levels.

diative Transfer model, some general considerations can be done by sticking to the detailed models of L17 and González-Alfonso et al. (2010, 2014, 2022). The L17 model was specifically developed in order to produce a diagnostic tool for the ISM in the nuclei of star-forming galaxies. Several nuclear environments are covered, from pure nuclear starbursts to starburst nuclei hosting an AGN. Each galaxy is modelled with different ISM components, where each component is an ensemble of molecular clumps with identical physical properties. The excitation temperature and level population of the gas molecules in a cloud are determined under different physical conditions of the dust and of the gas itself. The SED modelling of J1135 by Ronconi et al. 2023 (submitted to ApJ), shown in Figure 4.10, successfully reproduces the continuum emission with two dust components: one is associated with the molecular clouds hosting star formation, where the young stellar populations, still embedded in their dense envelope, are heating the dust up to $T_{dust} \sim 60$ K; the second component is associated to the diffuse, optically thinner ISM: here, the diffuse dust is heated by the radiation field of the old stars populations and by the photons which could escape the molecular clouds sites of star formation, making a diffuse cold component at $T_{dust} \sim 40$ K. In the starburst core, the molecular clouds hosting young stellar populations are assumed to be embedded in the diffuse component. I will take these fiducial values of T_{dust} together with the L17 model as starting points to interpret the thermal status of the ISM associated with the observed water excitation. For each of the two dust components, the total flux (integrated over the whole galaxy) expected from the SED modelling at the water-pumping frequencies we are interested in is reported in Table 4.10, normalised to the flux at 101 μm.

The L17 model analyses, in particular, the water excitation, in terms of levels population, in a single clump having characteristic parameters of a typical warm molecular component, with gas kinetic temperature T_K=50 K, number density n(H)=10^5 cm^{-3} and water abundance X(H_2O)=10^{-5}, for increasing dust temperatures. Ignoring the effect of pumping (i.e., setting $T_{\rm dust}$=0 K), collisions alone excite p-H_2O (o-H_2O) up to levels with upper energy 250 K (350 K). This scheme is almost unchanged until the dust temperature increases to a value of 40-50 K when FIR pumping starts to populate levels with $250 - 350\mathrm{K} < \mathrm{E_{up}/K}_B < 500 - 700\mathrm{K}$. The line strength of transitions is sketched in Figure 5 of L17: the strength of transitions with $E_{\rm up}$ > 250 K (350 K) (as the p-$H_2O(4_{22} - 4_{13})$ line) increases rapidly with dust temperature, while the strength of transitions with $E_{\rm up}$ < 250 K (350 K) (as the o-$H_2O(3_{21} - 3_{12})$ line) has a weak dependence on $T_{\rm dust}$, and some of the lines with $E_{\rm up}$ < 200 K even tend to decrease for increasing $T_{\rm dust}$, due to the increased depopulation by the continuum photons. In this framework, line p-$H_2O(2_{02} - 1_{11})$ in this dense, warm gas ($T_{\rm gas} \sim 50$ K) component, and for dust temperatures $\gtrsim 50$ K, feels the combined effect of collisions (populating levels 1_{11} and 2_{02}) and the weak effect of pumping, which populates level 2_{20} through the transition 1_{11}-2_{20} while depopulating the same level 2_{20} through the transition 2_{20}-3_{31}. The last two effects balance, in such a way that the pumping effect on the transition p-$H_2O(2_{02} - 1_{11})$ is subdominant with respect to the collisional excitation. This explains the weak dependence on the dust temperature of this line at this relatively high density, and thus we can infer with a certain level of confidence that this line is mainly collisionally excited in the ISM component associated with the "molecular" warm dust.

The L17 analysis of the level population fractions shows that the collisional excitation drives the p-H_2O (o-H_2O) lines with $E_{\rm up}$ < 100 (200) K toward a Boltzmann distribution at the gas kinetic temperature (thermalising these levels) and dominates the population of levels with $E_{\rm up}$ < 250 (350) K, almost independently on the dust temperature. Therefore, line p-$H_2O(2_{02} - 1_{11})$ is collisionally excited, as long as the gas density is as large as n(H)=10^5 cm^{-3}.

Noticeably, this thermalisation can also occur at gas densities much smaller than the critical density of these water transitions ($n_{\rm crit} \sim 10^8 - 10^9 cm^{-3}$, reflecting the large values of the Einstein coefficients for water rotational transitions), due to the small escape probability of the emitted photons and the consequent large optical depth and important radiative trapping which lowers the effective density for thermalisation. For $E_{\rm up}$ > 250-350 K, the excitation is almost completely determined by the FIR pumping alone. In this range, the population of the levels is driven towards a Boltzmann distribution at the dust temperature.

At the typical gas density of dense molecular clouds, p-$H_2O(4_{22} - 4_{13})$ line is excited by pumping from dust photons (58 μm) only for dust temperatures above 50 K, and the level population of 4_{22} with respect to 3_{21} increases for increasing $\mathrm{T_{dust}}$. We can infer that also the intensity of line p-$H_2O(4_{22} - 4_{13})$ with respect to o-$H_2O(3_{21} - 3_{12})$ is increasing with $\mathrm{T_{dust}}$, although their ratio depends on line optical depths, and the solution of the radiative transfer equation is necessary to diagnostic the dust temperature from the line ratios.

Considering the nuclear region of J1135 depicted in Figure 4.17, roughly delimited by the 3σ contours of the medium and high-level water lines, we can compare the observed excitation of the lines with the trend arising from the thermal model of L17. I will analyse this nucleus separately from the extended tail of line p-$H_2O(2_{02} - 1_{11})$ later in this Section.

Adopting the continuum modelling of J1135 previously described, the observations of the water line in the central core are consistent with a ~500 pc extended ensemble of molecular clouds hosting bursts of star formation activity, featuring a warm "molecular" dust component at a temperature of $T_{\rm dust} \sim 60\,$K or higher, embedded in a diffuse dust component, and warm gas with density n(H)$\sim 10^5\,{\rm cm}^{-3}$ and $T_{\rm gas} \sim 50\,$K.

The contribution of the colder, diffuse dust component at ~40 K (in which the warm component is embedded), adds up to contribute FIR photons, in the central starburst region, although with fractional fluxes different than in the "molecular" warm component (see Table 4.9). This means that the FIR photons from the diffuse dust component are more effective in exciting the low-level line, with 101 μm photons than the medium and high-level, which require continuum injection of 75 μm and 58 μm photons respectively.

Summarising, the water emission in the core region of the starburst J1135 witnesses the effect of radiative pumping on all three water lines, due to FIR photons injected by both the molecular (warm) and diffuse (colder) dust component, as well as the effect of collisions on the low-level (and, partially, on the medium level) line. In the denser ISM, the p-H_2O $(2_{02} - 1_{11})$ line is mostly excited by collisions, while the medium and high-level lines are mostly excited by FIR pumping. In the diffuse, colder ISM, in which warm molecular clouds are embedded, FIR pumping is mostly exciting the low-level line. In the core of the galaxy, we assume these components are mixed.

It is important to stress here that the relative balance between FIR pumping and collisional excitation of the low-level lines is strongly dependent on the gas and dust environment parameters, which present a plethora of conditions in a different context (see, e.g. González-Alfonso et al. 2021).

While the aforementioned L17 model refers to a dense and warm gas component, we can then tentatively interpret the more extended emission of the low-level line (Figure 4.17) as arising far from the dense clouds cocooning young stellar populations, i.e. in a region where only the "diffuse dust" component is contributing to the local radiation field. Here, the effect of collisions is reduced with respect to the central nucleus, due to the lower gas density, though they are still efficient in populating level 1_{11}, the basis of the 101 μm pumping. The continuum from the diffuse dust component is then appreciably populating the low energy water levels by absorption of 101 μm photons, but it is ineffective in exciting the medium and high-level lines, due to a reduced injection of photons with the proper pumping frequencies (see the second row of Table 4.10). The abundance of H_2O molecules may also be reduced here since the lower temperature of the radiation field lowers the fraction of water evaporation from the dust grains ice mantles into the gas component. The low-level line in this extended tail is then plausibly FIR pumped by the 101 μm photons of the colder, diffuse dust component, in a less dense and more extended region where the other lines do not emit, owing to the weaker FIR continuum at 75 and 50 μm.

Translating level populations into line intensities is not trivial, since the observed emission lines are differently affected by radiative trapping and, ultimately, by their line and continuum optical depths. Usually, while the low-level lines in the water spectrum feature high optical depths ($\tau_{\rm line} > 1$) (and lower escape probabilities, which allows them to trace densities much lower than the line critical density), the medium-high lines are found to be optically thinner ($\tau_{\rm line} \sim 1$) because of the higher energy required for excitation. Because of the different optical depths of those lines, the interpretation of their flux ratios requires the solution of the full radiative transfer problem, which will be the subject of a forthcoming study (Perrotta et al. 2023, in preparation).

Finally, it is worth noticing that we assumed an *a priori* value of $T_{\rm dust} \sim 60$ K, as derived from the SED fitting, but the observed excitation of the high-level water line is also consistent with a higher dust temperature $T_{\rm dust} \sim 100$ K (the "hot" component in the L17 model). Nevertheless, the possible contribution of this hot dust component to the integrated continuum emission is expected to be subdominant, as it might be compact and deeply buried. The continuum emission by this component would be attenuated by the dense surrounding ISM, making J1135 strongly obscured at optical/NIR wavelengths. Due to the lack of MIR detections, this possible hot dust component is still largely unconstrained although it could still be included consistently with the upper limits in the MIR.

The ratios of the line intensities, after correcting for lensing magnification, are represented in the left panel of Figure 4.19, where they are compared with the results of Yang et al. (2013) for two samples taken from the NASA/IPAC Extragalactic Database (NED), and with the lensed QSO APM08279+5255 (van der Werf et al. 2011). One sample has optically identified, strong, AGN-dominated sources (Seyfert types 1 and 2), and the other sample has star-forming-dominated galaxies, possibly with mild AGNs (classes HII, composite, and LINER of Kewley et al. (2006), “HII+mild-AGN”). The two groups show similar ratios in H_2O emission, indicating that a strong AGN may have little impact on water excitation. Noticeably, the ratio of the high to the medium water lines of J1135 (which are the lines excited mostly by FIR photons from dust) is analogous to that of the sample containing a mild AGN. In each sample, as well as in our target galaxy, collisions alone cannot explain the relevant excitation of the medium and high-level transition. One could formulate a dubitative hypothesis since, up to date, there is no striking evidence for an obscured AGN (the radio luminosity of J1135 at 6 cm from available EVLA observations is consistent with the star-formation activity so that no significant contribution from a central AGN is emerging, see Vishwas et al. 2018). Our results seem to point to a hot nucleus possibly powered by a starburst and maybe hosting a mild AGN in J1135. This possibility will be further explored in Section 4.7.

4.6.4 The L_{H_2O}-L_{TIR} relation and SFR calibration

Multi-wavelength observations, ranging from UV to radio frequencies, have greatly improved our understanding of the SFR calibration. Direct tracers, like UV emission from newborn stars, recombination lines such as H_α or FIR cooling

Dust component	F_{58}/F_{101}	F_{75}/F_{101}
Dense molecular clouds	1.66	1.40
Diffuse dust	0.66	0.95

Table 4.9: Flux ratios of J1135 FIR pumping photons from dust associated with the dense molecular clouds (warm dust component) and from the diffuse (cold) dust component, having dust temperature, respectively, of $\sim 70\,\mathrm{K}$ and $\sim 40\,\mathrm{K}$ (from the SED modelling by Ronconi et al 2023, represented in Figure 4.3). F_{58}, F_{75}, F_{101} are the fluxes at 58, 75, 101 μm, respectively, integrated over all the source.

lines like [CII] at 158 μm are, however, largely affected by dust attenuation (Casey et al. 2014). In contrast, the TIR luminosity L_{TIR} is a promising SFR indicator precisely because of dust: in the limit of high obscuration, essentially all of the UV-optical light from young stars is absorbed and re-emitted into the IR. Thus, the TIR luminosity should be one of the best SFR indicators in those situations, such as for starburst galaxies. The SFR-L_{TIR} correlation is much more robust than it is for the [CII] fine structure line or for the CO(J=1-0) line, which is sublinearly correlated with L_{FIR} even when only pure star-forming galaxies are considered (Solomon et al. 1997, Díaz-Santos et al. 2013, Aravena et al. 2016). The TIR luminosity of galaxies has been used to infer the SFR of galaxies for decades (see Kennicutt 1998 and Kennicutt & Evans 2012 for reviews). The SFR is generally estimated from the scaling relations of Kennicutt & Evans (2012), that assumes a Salpeter IMF in the mass range 0.1-100 $M_\odot$, solar metallicity and for continuous bursts of age 10-100 Myr:

$$\mathrm{SFR}\left[M_\odot \mathrm{yr}^{-1}\right] \approx 1.47 \times 10^{-10} L_{TIR}\ [L_\odot] \tag{4.6}$$

A caveat to take into account is that L_{TIR} may overestimate the SFR in all those cases in which dust heating is enhanced by physical mechanisms other than star formation, for example, extra UV emission or X-rays, as arising in the light of evolved stars or AGNs (Kennicutt et al. 2009, Murphy et al. 2011, Hayward et al. 2014). In all those cases, converting the TIR luminosity into an SFR using a standard calibration will overestimate the true SFR. Besides this caveat, retrieving L_{TIR} requires a good sampling or modelling of the source SED, which is not always available. A way to encompass this possible lack of detailed information about the SED is to use tracers of L_{TIR} itself. L_{H_2O} was found to have a strong dependence on the IR luminosity, varying as $L_{H_2O} \sim {L_{TIR}}^{1.2}$ (Omont et al. 2013, Yang et al. 2013, Yang et al. 2016), slightly steeper than linear, and equivalent to a linear relation in log–log space with a slope very close to unity. It extends over four orders of magnitude of the luminosity range, regardless of whether or not a strong AGN signature is present. This relation is indicative of the fundamental role of radiative IR excitation of the water lines and implies that high-z galaxies with $L_{TIR} \gtrsim 10^{13}\ L_\odot$ tend to be very strong emitters in H_2O, that have no equivalent in the local universe.

The modelling of J1135 SED with a warm dust component and a cold, diffuse one (Section 4.4), allowed us to infer for the total IR luminosity a value of $L_{TIR} \sim$

1.1×10^{13} $L_{\odot}$ (consistent with the value obtained from the SED-fitting performed with CIGALE, see Table D.1) and a FIR luminosity, integrated into the (42.5-122.5 μm) band, $L_{FIR(42.5-122.5\mu m)} \approx 7.05 \times 10^{12}$ $L_{\odot}$, after correcting for lensing magnification. By inserting the value of $L_{FIR(42.5-122.5\mu m)}$ in Equation (4.6) it is then possible to estimate a SFR of $\sim 1.77 \times 10^{3}$ $M_{\odot}$ yr^{-1}. After the de-magnification of the water line intensities given in Table 4.6, for each transition, the corresponding ratio to the total IR luminosity is computed along with the steepness α for the relation L_{H_2O}= L_{IR}^{α}, where, for each water emission line, the luminosity L_{H_2O} is in units of 10^{7} $L_{\odot}$ and L_{IR} in units of 10^{12} $L_{\odot}$. The results are reported in Table 4.10 and compared with the best-fit values for the sample by Yang et al. (2013), initially performed on a sample of 45 water-emitting galaxies spanning a luminosity range (1-300$\times 10^{10}$ $L_{\odot}$) and on high-z dusty star-forming galaxies, and later also including lensed hyper-luminous IR galaxies at z$\sim 2-4$ (Yang et al. 2016, 2020).

Comparing the ratios reported in Table 4.10 with Yang et al. (2013), we find a consistent value (within 3σ) for all the transitions. In particular, this confirms the trend, already found in Yang et al. (2013), that the inclusion of high-z DSFGs at the high L_{TIR} end of the L_{H_2O}-L_{TIR} relation has the effect of slightly increasing L_{H_2O}/L_{TIR} when looking at the $2_{02}-1_{11}$ transition.

The effect is explained by noting that, according to the interpretation of the J1135 water emission described in Section 4.6.3, the 988 GHz line gets a significant boost due to collisions. As collisions do not directly indicate the warm/hot phase of the star-forming ISM, relying on this low-level line could introduce bias into the L_{H_2O}-L_{TIR} correlation. Therefore, using the $H2O_{2_{02}-1_{11}}$ line to trace IR emission might lead to an overestimation of the SFR. This mechanism might be at play in high-z DSFGs, which might explain the observed steeper increase in the L_{H_2O}-L_{TIR} relation for this specific group of sources, including J1135.

Likewise, the analysis of both J1135's source reconstruction and the modelling of its dust component suggests that relying solely on the total IR luminosity might not yield precise outcomes. The flux spanning from 3 to 1100 μm could indeed contain minor contributions from older stellar populations and potentially relevant AGNs. Consequently, using L_{TIR} as a direct indicator of dust emission closely tied to star formation could lead to an overestimation of the SFR. Conversely, employing water lines exclusively excited by IR pumping (like $H_2O_{4_{22}-4_{13}}$ or higher E_{up}) as calibrators might result in underestimating the SFR. This is because L_{TIR}, which is at the denominator of the ratio, is higher with respect to the emission from the effective warm/hot dust component (which is smaller than L_{TIR}). For this reason, the FIR($42.5-122.5$ μm) luminosity is a more reliable SFR indicator than the total IR luminosity.

According to Kennicutt (1998), the effectiveness of FIR luminosity as an indicator of SFR relies on the extent to which young stars contribute to heating dust and the optical depth of dust in star-forming areas. The simplest scenario occurs when newly formed stars dominate the UV-visible radiation and dust opacity is widespread, implying the FIR luminosity to be a reliable estimate of the starburst's bolometric luminosity. In this situation, FIR luminosity becomes the ultimate SFR tracer. Consequently, in cases of high optical depths commonly found in starbursts, integrating L_{FIR} across the 42.5-122.5 μm rest-frame wavelength range demonstrates its reliability as a star formation indicator, potentially surpassing ì$L_{\rm TIR}$.

In the context of this analysis, focusing on high FIR luminosities typical of starbursts ($L_{\rm FIR(42.5-122.5\mu m)} \geq 10^{12}{\rm L}_{\odot}$), we find a linear correlation between the luminosity of the p-$H_2O(2_{02}-1_{11})$ ($\nu_{\rm rest}$ = 988 GHz) spectral water line and $L_{\rm FIR}$. This suggests that the luminosity of this specific water line ($L_{\rm H_2O(2_{02}-1_{11})}$) could serve as a suitable SFR calibrator for high-redshift starbursts. Notably, this correlation is likely explained by the partial contribution of 101 μm photons from the diffuse dust component, within which the denser component is embedded (Jarugula et al. 2019, van der Werf et al. 2011, Yang et al. 2013, 2016). However, it is important to acknowledge that the excitation fraction resulting from this process depends on gas and dust parameters. The L17 model and our discussions in Section 4.6.3 demonstrate that FIR pumping of this line in a dense warm ISM component becomes relevant for $T_{\rm dust} > 40$ K, especially in the less dense ISM component, while collisions in a dense ISM contribute to line excitation even without a FIR radiation field.

Noticeably, Jarugula et al. (2019) found that the 988 GHz line is correlated with $L_{\rm FIR}$ not only on global scales but also on resolved kiloparsec scales within starbursts and AGNs, in source regions with uniform dust temperature and opacity. In this context, higher-resolution observations could effectively isolate water emissions originating from specific zones centred around the peaks of line luminosities, enabling a high signal-to-noise ratio and consistent physical conditions. Considering the entire emission area of the p-H2O($2_{02} - 1_{11}$) transition, we established a lower limit due to the inclusion of line flux from regions not directly connected to the molecular clouds hosting star formation. Specifically, we derived $L_{\rm H_2O}/{\rm L}_{\rm FIR} \sim (1.63 \pm 0.03) \times 10^{-6}$, which closely aligns with the findings of Jarugula et al. (2019) for a sample of gravitationally lensed DSFGs at around redshift z~3. This reinforces the hypothesis that p-$H_2O(2_{02} - 1_{11})$ in such galaxies is correlated with the FIR luminosity of the starburst. However, we suggest that a more reliable diagnostic of the SFR in dusty starburst galaxies based on the thermal dust emission should better rely on the high-level H_2O transitions (like the $4_{22} - 4_{13}$ transition detected in J1135). Indeed, in this case, the ratio $L_{\rm H_2O}$ / $L_{\rm FIR(42.5-122.5\mu m)}$ is dominated by IR pumping (actually, almost purely pumping induced), thus it is expected to increase for increasing dust temperatures and SFR, unlike the low-level transition at 988 GHz, whose upper energy level tends to depopulate at increasing temperatures. The J1135 calibrations for the SFR/$L_{\rm H_2O}$ are reported in Table 4.10 and are obtained from Equation 4.6. The $L_{\rm TIR}/L_{\rm FIR(42.5-122.5\mu m)}$ ratio, corresponding to the value 1.72, is computed from the values obtained from SED-fitting performed with GalaPy.

4.7 Evolutionary interpretation

In Chapter 2 I have provided a physical interpretation behind the evolution of the FIRRC for a sample of (mostly unresolved) candidate strongly lensed DSFGs. Here, I discuss how the observed *resolved* properties of a single strongly lensed

Line	L_{H_2O} [10^7 L$_\odot$]	$(L_{H_2O}/L_{TIR}) \times 10^6$	$(L_{H_2O}/L_{TIR})^{(a)} \times 10^6$	α	$\alpha^{(a)}$	SFR/L_{H_2O} [$M_\odot yr^{-1} L_\odot^{-1}$]
p-H_2O 2_{02}-1_{11}	11.4 ± 0.2	9.4 ± 1.6	7.6	0.97 ± 0.06	1.12 ± 0.04	1.56×10^{-5}
o-H_2O 3_{21}-3_{12}	7.9 ± 0.6	6.6 ± 0.6	10.7	0.83 ± 0.03	1.11 ± 0.05	2.25×10^{-5}
p-H_2O 4_{22}-4_{13}	4.3 ± 0.8	3.6 ± 0.6	5.7	0.58 ± 0.07	0.94 ± 0.12	4.13×10^{-5}

Table 4.10: From the left: de-magnified luminosities of J1135 water lines; ratios of water luminosities to the TIR total luminosity of J1135; where the index (a) refers to the results reported in Yang et al. (2013); α coefficient for the relation L_{H_2O}= L_{TIR}^{α}; SFR vs. water line luminosity. The SFRs were obtained from Equation 4.6 and linked to the luminosities of the water transitions.

galaxy can be exploited with the aim of interpreting and comprehending the evolutionary phase that this object is undergoing.

From the inspection of HST/WFC3 image, no evidence for galaxy companions of J1135 is found within a radius of at least ~ 5 arcsec, corresponding to ~ 40 kpc, although the detection of the possible closer and fainter source is hindered by the current data sensitivities and angular resolutions. Moreover, from the CO(8-7) reconstructed image and [CII] and water lines first-moment maps, we find no clear evidence of a complex kinematic possibly associated with an ongoing merging event. With no further hints pointing towards this scenario, we are led to interpret the ISM conditions and the physical properties discussed so far in the light of in-situ galaxy formation scenarios (Lapi et al. 2014, 2018, Mancuso et al. 2016a; Mancuso et al. 2016b, 2017, Pantoni et al. 2019). In particular, the properties of J1135 are consistent with a *compaction* phase (Barro et al. 2014, Ikarashi et al. 2015, 2017, Kocevski et al. 2017, Silverman et al. 2019, Stacey et al. 2021, Valentino et al. 2020, see Section 1.3) in which the dust-enshrouded star-formation activity increases at an almost constant rate in the inner regions of the galaxy where the stellar mass is being accumulated. At this stage, the in-situ scenario envisages the galaxy to be an off-main sequence object in an early evolutionary stage, which will eventually move towards the main-sequence locus as the stellar mass content increases. Finally, the star formation will either progressively decrease as the galaxy exhausts its gas reservoir or will be abruptly stopped by the action of the feedback from an AGN (Mancuso et al. 2016a; Mancuso et al. 2017).

4.7.1 Is J1135 hosting an AGN?

From the galactic evolutionary point of view, an important issue is to determine whether the obscured compact cores in high-z star-forming galaxies are powered by very compact starbursts and/or AGNs, from which strong emission is produced in very compact regions around the central accreting BH. The vigorous star formation requires a large amount of gas, suggesting that the host galaxy's ISM significantly contributes to the obscuration of the UV and X-ray emissions originating in the central nuclear region (Hickox & Alexander 2018), up to the Compton-thick regime ($N(H) > 10^{24}$ cm^{-2}), in addition to the pc-scale torus (D'Amato et al. 2020, Peca et al. 2021, Gilli et al. 2022). The fraction of obscured

AGNs is found to be higher at earlier epochs ($3 < z < 5$) up to ~ 80% (e.g. Vito et al. 2018) with respect to that in the local Universe (Burlon et al. 2011), likely driven by the increase of the gas content in distant galaxies (e.g., Carilli & Walter 2013b).

Given the hypothesised evolutionary stage of J1135, it is natural to inquire whether it contains an obscured AGN and if the inferred physical conditions of the object align with this possibility.

The analysis of the water excitation presented in this Chapter points toward the presence of a high excitation status in the ISM associated with the central region, but how could we distinguish between a pure starburst excitation and a (buried) starburst+AGN mechanism? Being J1135 obscured in the optical and NIR wavelengths, and due to the lack of data in the X-ray band, the question of whether it hosts a buried AGN is still open.

The CO high-J transition line (J=8-7) in J1135 reveals the presence of warm high-density molecular gas, which can be either associated with the far-UV photons produced by star formation processes or to the X-ray emission originated by the AGN (e.g. Vallini et al. 2018). Indeed, the inner regions of the galaxy (~ 0.5 kpc) are the most affected by the photons coming from the AGN, which penetrate deeply in the Giant Molecular Clouds (GMCs) generating X-ray-dominated regions (XDRs, Maloney et al. 1996).

Generally, the extremely compact nature of high-z galaxies hinders establishing the extension of the XDRs even with high-resolution observations performed with ALMA (e.g. Schleicher et al. 2010), and the effects of the AGN could be visible on the global CO SLED.

Moreover, the lack of a good sampling of the MIR part of the SED of J1135 prevents the characterisation of the central BH properties. Indeed, the AGN's emission heats up the surrounding dust creating an excess in the MIR band if compared with the MIR emission of galaxies with intense star formation but no strong AGN contribution. Such MIR excess is an important hint signalling the possible presence of AGN activity in these galaxies (Stern et al. 2012, Bonzini et al. 2013, Padovani et al. 2015, Delvecchio et al. 2021). The only hint of a possible MIR excess in J1135 is inferred from its CO-SLED. Figure 4.19 adapts the results of Kirkpatrick et al. (2019) adding the CO-SLED of J1135, which includes data from the IRAM-30 m (Yang et al. 2017) and the Green Bank telescopes (Harris et al. 2012). From this comparison, J1135 is found to be consistent with the CO-SLED of high-redshift sources with MIR AGN fraction > 0.5. However, Figure 4.19 should not be considered as a diagnostic, as one cannot find from the analysis of Kirkpatrick et al. (2019) a robust statistically significant difference between the CO excitation of star-formation dominated galaxies and AGN using the line flux alone.

The reconstructed and resolved CO(8-7) emission extension for J1135, leads to a quite large effective radius of $R_{\rm eff} \sim 1.2$ kpc (see Table 4.6). This result strongly hints toward the presence of a heavily obscured AGN activity in J1135 at the stage of its accretion or, alternatively, of feedback associated with the central star formation activity (Vallini et al. 2018).

Besides the indications from mid and high-water excitations and from the

CO(8-7) transition, previously discussed, one of the keys to discerning between a starburst and a putative AGN, or the ensemble of both, relies on the different mechanisms ruling their energetic mechanisms. Specifically, the main powering source in starbursts is nuclear fusion, while in AGNs is accretion into a supermassive BH. As a consequence, UV is the predominant energetic radiation in a starburst, while an AGN strongly emits in the X band in addition to the UV. However, this has consequences on the physical properties and on the excitation state of the dust and molecules surrounding the nuclei.

In particular, a peculiar and sensitive probe of the excitation mechanism resides in sub-mm and mm wavelength emission lines (weakly affected by dust extinction) from those molecules which mostly characterise these very dense regions where star formation takes place, i.e. HCN and HCO^+, and in their abundance ratio. Both HCN and HCO^+ are powerful tracers of the densest ($n_{H_2} > 10^4$ cm^{-3}) molecular gas, thanks to their high dipole moment, so their intensity ratio is insensitive to the fraction of dense molecular gas, relative to diffuse. While their typical ratio in our galactic molecular cloud is ~ 1 (Blake et al. 1987; Pratap et al. 1997; Dickens et al. 2000), an overabundance of HCN relative to HCO^+ is predicted for dense molecular gas when illuminated by an X-ray emitting source (Meijerink & Spaans 2005, Krips et al. 2008). Observations of the HCN and HCO^+ (J=1-0), (J=2-1), (J=3-2), and (J=4-3) transitions initially confirmed this trend since it was found that the HCN emission is systematically stronger than the HCO^+ in AGN-dominated galaxy nuclei than in starburst galaxies. The trend of a strong (> 1) HCN$(1-0)$ to HCO^+(1–0) emission ratio was further confirmed in luminous buried AGN candidates (Imanishi et al. 2004, Kohno 2005, Imanishi et al. 2006, Imanishi & Nakanishi 2006, Riechers et al. 2006, Gao et al. 2007, Imanishi et al. 2007, Krips et al. 2008, Bussmann et al. 2008, Graciá-Carpio et al. 2008, Imanishi et al. 2009, Juneau et al. 2009, Imanishi et al. 2010, Aalto et al. 2015, Imanishi et al. 2016, Oteo et al. 2017). For this reason, enhanced emission from the dense gas tracer HCN (relative to HCO^+) has been proposed as a signature of active galactic nuclei (AGN). However, this diagnostic was later questioned by Privon et al. (2020), following the hard X-ray observations of a sample of four galaxies with HCN/HCO^+(1-0) intensity ratios consistent with those of many AGN. No X-ray evidence of an obscured AGN was found, indicating that HCN/HCO^+ intensity ratios are not driven by the energetic dominance of AGN, nor are they reliable indicators of ongoing supermassive BH accretion (Costagliola et al. 2011, Snell et al. 2011). Low HCN/HCO^+(1-0) intensity ratios were also found in AGNs (Sani et al. 2012). This inconsistency could be due to spectral contamination from a coexisting starburst activity that dilutes emission from an AGN. Furthermore, the reason for the HCN /HCO^+ enhancement in AGNs is still not totally clear: it may reside in high temperature-driven chemistry (Izumi et al. 2013), a non-collisional excitation such as an IR pumping through the reradiation from UV/X-ray heated dust (Aalto et al. 1995, Sakamoto et al. 2010, García-Burillo et al. 2015), or in shocked regions at a few hundred parsecs from the supermassive black holes due to outflowing material (Martín et al. 2015). Different heating mechanisms, higher gas opacities, densities, and temperatures, abundance variations, can contribute to this enhancement.

The HCN and HCO^+ (J=1–0) transitions have rest wavelengths $\lambda_{\rm rest}$ = 3.385 mm and $\lambda_{\rm rest}$ = 3.364 mm respectively, thus suffering the limited resolutions of current observations. Izumi et al. (2013) proposed a possibly more reliable diagnostic based on the so-called "submillimeter HCN-enhancement", making use of the HCN/HCO^+ (J=4-3) ratio, whose integrated intensity seems again to be higher in AGNs than in starburst galaxies. These higher-J lines have sub-mm rest frame wavelengths so that higher angular resolution is easily achievable compared to (J=1–0) transitions; this is especially important to exclude contaminations from starburst activity to the line emission from AGN-heated gas. Moreover, such sub-mm lines can be covered by ALMA up to a redshift of ∼ 3-4. Since this feature could potentially be an extinction-free energy diagnostic tool for nuclear regions of galaxies (Izumi et al. 2015, 2016), I have performed a preliminary analysis in J1135 of the ratio HCN(J=4–3)/HCO^+(J=4–3) for purely rotational transition in the fundamental vibration state, whose rest frequencies are $\nu_{\rm rest}$ = 354.5 GHz for HCN (J=4-3) and $\nu_{\rm rest}$ = 354.5 GHz for HCO^+ (J=4-3). For the purpose of this analysis, I have adopted the pipeline-reduced ALMA Band 3 cubes directly available from the ALMA Science Archive (Project: 2017.1.01694.S, P.I. Oteo). Figure 4.18 represents the spectral profiles of the two lines extracted from a region of the cube images containing $\sim 3\sigma$ of the emission. The HCN/HCO^+ ratio turns out to be ∼ 2.2; this observed value of the HCN-to-HCO^+ (J=4-3) suggests possible AGN coexisting with a starburst-dominated region. Further observations are required, though, to confirm this result, which would be an important piece of information for the galaxy evolution scenarios.

4.8 Summary

In this Chapter, I have investigated the nature of the strongly-lensed galaxy HATLASJ113526.2-01460 (namely, J1135) at redshift $z \approx 3.1$, discovered by the *Herschel* satellite in the GAMA 12th field of the *Herschel*-ATLAS survey. I have performed detailed lens modelling and have reconstructed the source morphology in three different (sub-)mm continuum bands and the spectral emission of the [CII], CO(8-7), $H_2O(J=2_{0,2}\text{-}1_{1,1})$, $H_2O(J=3_{2,1}\text{-}3_{1,2})$ and $H_2O(J=4_{2,2}\text{-}4_{1,3})$ lines. I have also exploited a wealth of photometric ancillary data to perform broadband SED-fitting and to retrieve intrinsic (i.e., corrected for magnification) physical properties. Our main findings are summarised below:

- The lens modelling indicates that the foreground lens is constituted by a (likely elliptical) galaxy with mass $\gtrsim 10^{11}\,M_\odot$ at $z \gtrsim 1.5$, while the source is found to be an optical/NIR dark, dusty star-forming galaxy whose (sub-)mm continuum and line emissions are amplified by factors $\mu \sim 6 - 13$.

- The continuum emission of J1135 is extremely compact, with sizes $\lesssim$ 0.5 kpc for the star-forming region and $\lesssim$ 1 kpc for the gas component.

- An accurate fitting of the line profiles showed no evidence for outflows nor rotation of the central nucleus from which the water lines arise. This is also

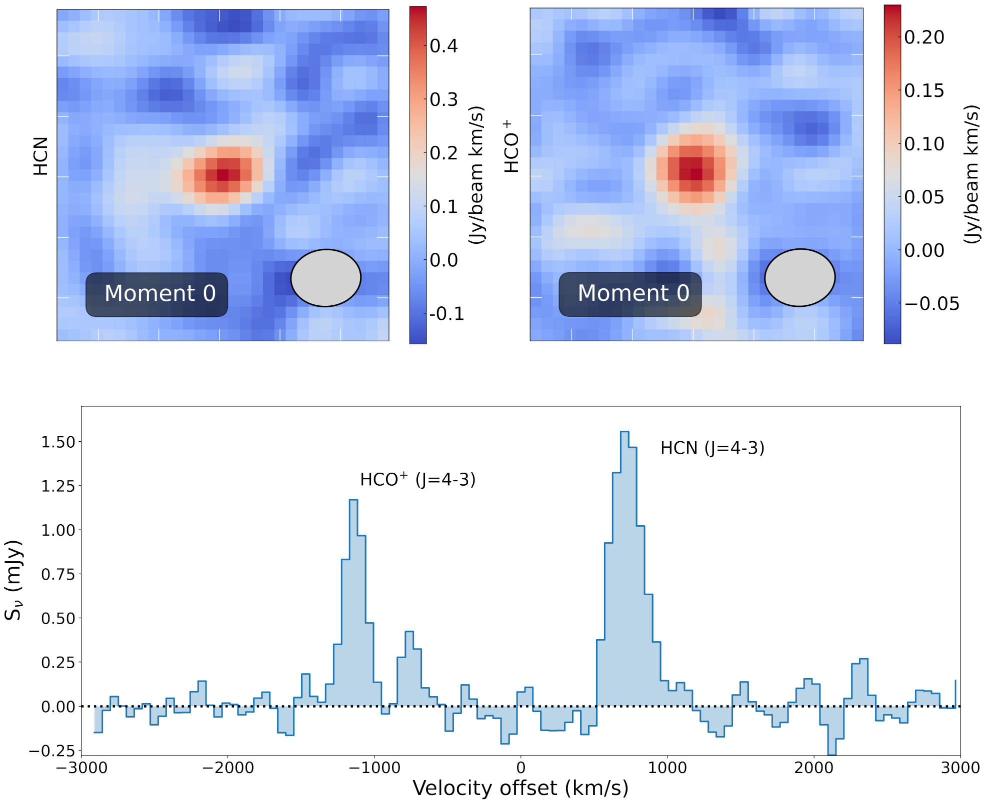

Figure 4.18: Top: intensity maps for the HCN and HCO$^+$ lines. Ellipses represent the restored beams, postage stamps are 10×10 arcsecs. Bottom: spectral profiles for the same lines

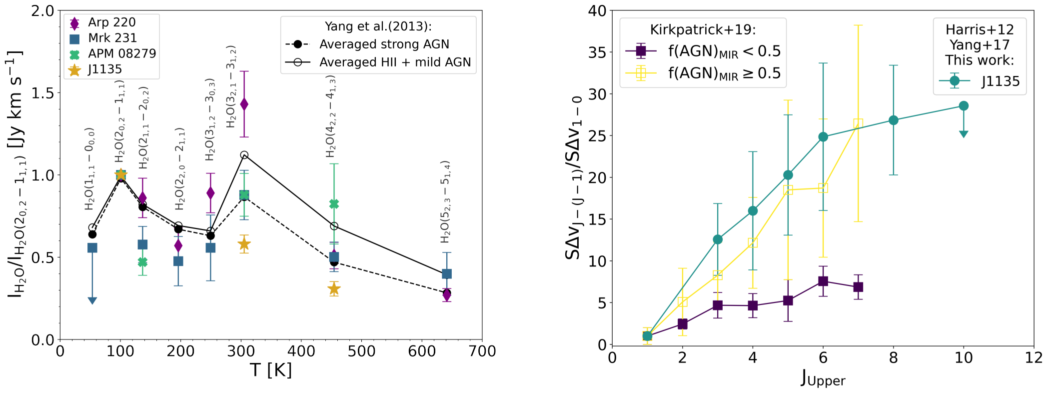

Figure 4.19: *Left:* integrated fluxes of the three J1135 de-magnified water lines (gold stars), in Jy km s^{-1}, compared with the sample analysed in Yang et al. (2013). The fluxes are normalised to the intensity of the p-H_2O ($2_{02} - 1_{11}$) line. *Right:* median CO SLEDs and line ratio uncertainties for selected sources with MIR AGN fractions ≥ 50%(yellow) and MIR AGN fractions < 50% (purple) from Kirkpatrick et al. (2019). Green points/line refer to J1135, including data from Harris et al. (2012) and Yang et al. (2017).

consistent with the reconstructed moment 1 of CO(8-7), obtained from 3 velocity bins. A single-Gaussian fit turned out to reproduce the water, the [CII], and the CO(8-7) emission lines at a high confidence level, indicating that the mid- and high-level water excitation region encompasses the same dense gas region where CO is collisionally excited.

- J1135 features a very high star-formation rate $\gtrsim 10^3\,\mathrm{M}_\odot\,\mathrm{yr}^{-1}$, that given the compact sizes is on the verge of the Eddington limit for starbursts. The radio luminosity at 6 cm from available EVLA observations is consistent with the star-formation activity, so no significant contribution from a central AGN is emerging (see also Vishwas et al. 2018).
- J1135 is found to be extremely rich in gas $\sim 10^{11}\,\mathrm{M}_\odot$ and dust $\gtrsim 10^9\,\mathrm{M}_\odot$. The stellar content $\lesssim 10^{11}\,\mathrm{M}_\odot$ places J1135 well above the main sequence of star-forming galaxies, indicating that the starburst is rather young with an estimated age $\sim 10^8$ yr and that the stellar mass should at least double before star formation is quenched.
- The imaging and line analysis of water transitions have been compared to the existing radiative transfer models which account for the effect of dust-emitted photons in the excitation of ISM molecules as well as of the collisional excitations. This comparison is suggestive of a warm, or even hot ($\gtrsim 70\,\mathrm{K}$), dust component in the central nucleus, which, together with a colder, diffuse component, could explain the observed excitations.
- The robustness of the water lines as possible SFR calibrators has been discussed, comparing water luminosity-IR luminosity correlation with the values obtained in literature for samples of local and high-z sources and strongly lensed dusty star-forming galaxies. The presented physically motivated analysis, based on the high-resolution imaging of the targeted source, suggested that the better SFR indicators should be the high-level water transitions, since they are exclusively excited by FIR pumping from dust, with negligible contribution from collision, and direct tracers of the warm and hot dust typically powered in star-forming environments
- The properties of J1135 can be consistently explained in terms of in-situ galaxy formation and evolution scenarios as typical of a rather young dusty star-forming galaxy caught in the compaction phase. The lack of X-ray observations and MIR detections of the continuum are currently preventing us from discerning the nature of this central hot nucleus. This perspective is further supported by the distribution of water lines, revealing a clear link between the central nucleus—potentially a site of starburst activity—and the most intense spectral lines. These lines are particularly sensitive to FIR photon emissions originating from a warm dust component with an approximate temperature of 60 K, reinforcing this connection. Specifically, lines such as o-$\mathrm{H_2O}(3_{21}-3_{12})$ and p-$\mathrm{H_2O}(4_{22}-4_{13})$ align with this central nucleus in visual imaging. Although there is a slight shift, the lower-intensity line p-$\mathrm{H_2O}(2_{02}-1_{11})$ also peaks within the same central nucleus, but exhibits

more widespread emission. The excitation of this line on both the core and the extended region is likely a result of diverse combinations of collisions and FIR photon pumping at 101 μm, stemming from a denser, warmer dust component and a diffuse, colder one.

In the future, observations coming from JWST will be crucial to shed further light on the nature of this obscured object and its foreground lens in the near- and MIR regime. Moreover, X-ray follow-up, coupled with the available ALMA data, is required to establish the presence of the dust-enshrouded AGN and to better investigate the interplay between star formation and nuclear activity (Massardi et al. 2017).

Chapter 5

Conclusions

This Chapter summarises the main results of this thesis and provides insights into possible future perspectives.

5.1 Main results of this work

The goal of this thesis is to gain insights into the properties and evolution of DSFGs by leveraging the physical phenomenon of gravitational lensing. To this purpose, I have exploited high-quality wavelength observations of multiple tracers and modern analysis techniques of SED-fitting, lens modelling, and source reconstruction. Using my composite approach, which combines exploring empirical relationships among samples of strongly lensed DSFGs and conducting a detailed investigation of the morphological and physical properties of individual objects, I have demonstrated that:

- Building a statistically significant sample of strongly lensed DSFGs at the peak of Cosmic SFH holds the potential to uncover empirical relationships among various physical properties of these objects, such as the FIRRC. This is especially valuable in a luminosity-redshift range that is typically challenging to observe.
- Resolved observations of strongly lensed DSFGs can efficiently be exploited to gain a comprehensive view of the chemical composition, morphology, and sub-structure distribution of individual objects. These results have been instrumental in probing the evolutionary stage of a single object and the analysis presented here can be expanded to similar sources.

In the following, I provide a summary of the work described in this thesis and possible future applications. My investigation started from a sample of (candidate) strongly lensed DSFGs in the *Herschel*-ATLAS survey ($\sim 570\,\mathrm{deg}^2$). This sample was originally selected in the work of Negrello et al. (2017), by means of a simple flux density threshold corresponding to $S_{500\,\mu\mathrm{m}} > 100\,\mathrm{mJy}$. The redshift distribution is in the range $1 \lesssim z \lesssim 4.5$, and the apparent IR luminosities are compatible with the most luminous systems in the Universe in these bands (ULIRGs and HyLIRGs), where $10^{13} \lesssim L_{\mathrm{IR}}/\mathrm{L}_{\odot} \lesssim 10^{14}$.

Thanks to these properties, this sample is the ideal test bench to investigate the evolution of DSFGs at the peak of the SFH and the interplay between black holes and their host galaxies.

The H-ATLAS survey offers a significant multi-wavelength coverage and a plethora of photometric and spectroscopic data, which are pivotal pieces of information in the understanding of the overall astrophysical properties characterising galaxy evolution.

5.1.1 Exploiting lensing for the investigation of DSFGs

To achieve this goal I followed two approaches: the first involved the study of a collection of objects, where the investigation focused on a few specific physical properties of the galaxy population. The second strategy relies on the detailed study of a few objects, exploiting a wealth of spectroscopic and broad-band photometric data. Both methodologies benefit from an additional advantage offered by gravitational lensing, which enables access to regions of the luminosity/redshift space that would otherwise be beyond the reach of current instrumentation or would require exorbitant amounts of observing time. For the former approach, lensing allows studies to be expanded toward fainter luminosity regimes, while for the latter, the magnification in sizes permits access to the details of the morphologies and structures composing the ISM of distant and compact objects such as DSFGs. This can be achieved through the accurate lens modelling and source reconstruction techniques which I have overviewed in Chapter 2.

In Chapter 3 I took advantage of available radio data from the literature, from the VLA-FIRST survey at 1.4 GHz, and from dedicated ATCA follow-up at 2.1 GHz, in order to build a sample of 28 candidate lensed DSFGs with a radio counterpart over the redshift range $1 \lesssim z \lesssim 4$ and reconstruct their FIRRC. The FIRRC is an empirical relationship observed between the FIR and radio continuum emissions from galaxies, strictly connected together by the star-formation process. This correlation suggests a connection between the processes of star formation, the generation of cosmic-ray electrons in galaxies, and the presence of magnetic fields and is widely used to estimate the SFR in galaxies, especially when other indicators are unavailable. Sub-mm-selected samples of gravitationally lensed galaxies provide a valuable opportunity for follow-up studies, offering insights into starburst characteristics in distant galaxies. This extends the FIR/radio correlation across a wide range of redshifts and radio luminosities, contributing to our understanding of how intense star formation influences the energy equilibrium in the ISM. This influence is seen through processes like cosmic ray injection, acceleration, magnetic field amplification, and their effects on star-forming regions. In Chapter 4 I have exploited a detailed-single object analysis. For this purpose, the target is the strongly optical/NIR lensed DSFGs J1135 at $z_{\rm spec} = 3.127$, belonging to the sample of Negrello et al. (2017). These heavily obscured galaxies represent a fraction ($\sim 20\%$, Chen et al. 2015) of sub-mm selected DSFGs, and often remain undetected even in deep HST imaging. The detailed knowledge of optical/NIR systems is still limited, however, it is becoming clear that they may play a crucial role in the determination of cosmic SFRD towards earlier epochs (e.g. Wang et al.

2019a, Talia et al. 2021, Enia et al. 2022). Therefore, J1135 presents an ideal case for investigating the physical characteristics of these elusive galaxies, for which only the average statistical properties have been examined so far. Moreover, the investigation involved detailed observations of sub-mm continuum and spectral emission lines such as [CII], CO(8-7), and multiple H_2O transitions.

5.1.2 Main achievements in the description of DSFGs properties

For what concerns the investigation of properties for a statistically relevant sample of DSFGs, in Chapter 3 I have presented the FIRRC for a sub-sample of (candidate) strongly lensed DSFGs with a radio counterpart, and originally drawn from the selection of Negrello et al. (2017). The key outcomes of this analysis are as follows.

- The resulting FIRRC for a sample of 28 (candidate) strongly lensed DSFGs with a radio counterpart demonstrates a weak redshift evolution, aligning with earlier findings based on different criteria at lower redshifts.
- The $q_{\rm FIR}$ parameter, when plotted against radio power $L_{\rm 1.4GHz}$, shows a clear decreasing pattern. This trend resembles the behaviour seen in lensed quasars identified through optical/radio methods by Stacey et al. (2018, 2019), but the lensed galaxies studied here occupy a distinct region on the $q_{\rm FIR} - L_{\rm 1.4GHz}$ graph.
- This trend can be effectively interpreted within the context of in-situ galaxy evolution, signifying a transition from an earlier phase of dust-obscured star formation (highlighted by our FIR selection) to a subsequent phase as radio-loud quasars (predominantly captured by the Stacey et al. (2018, 2019) criteria).

I have then analysed in detail the optical/NIR dark lensed system J1135. I have exploited all the available ancillary multi-wavelength photometry and ALMA high-resolution ($\lesssim$ 0.1 arcsec) (sub-)mm ($\lambda \sim 0.64 - 1.3$ mm) continuum and spectroscopic observations. The latter enabled the lens modelling and the source reconstruction of J1135's emission in different tracers. The main results of my analysis are the following:

- The analysis of the CO(8-7), [CII], and water spectral lines revealed no clear evidence of a complex kinematic, likely excluding the possibility of an ongoing merger.
- The lens modelling indicates a massive ($M_{\rm E} \gtrsim 10^{11}\,{\rm M}_\odot$) lens, which can be compatible with the assumption of an elliptical galaxy at $z \gtrsim 1.5$. On the other hand, the source galaxy exhibited high magnification factors ($\mu \sim 6 - 13$) and extreme compact sizes (~ 500 pc) in sub-mm emissions and ~ 1 kpc for the gaseous component.
- Through the SED fitting of broad-band photometry of J1135 I have retrieved the intrinsic physical properties of the object. The system showcases a large

reservoir of gas ($\sim 10^{11}\,\mathrm{M}_\odot$), which is being rapidly converted into new stars, placing this object well above the main sequence of SFGs.

- The high dust content ($\sim 10^{9}\,\mathrm{M}_\odot$) is well modelled by a two-component emission. The first one is associated with the molecular clouds embedding the star formation and heating the dust up to $T_{\mathrm{dust}} \sim 60$ K; the second component is associated with the diffuse, optically thinner ISM and corresponds to colder dust at $T_{\mathrm{dust}} \sim 40$ K.
- By reconstructing the de-lensed morphology of the different tracers I have found that the majority of the intense star formation takes place in a central and dusty region of the DSFG and settles the object close to the Eddington limit for starbursts, with radio luminosity favouring star-formation dominance over AGN activity.
- I have discussed the implications of water lines as SFR calibrators and the de-lensed morphology reconstruction indicates an alignment of specific water line transitions with the central nucleus, reinforcing J1135's characterisation.
- I have discussed how the presence of a hidden mild AGN activity in J1135 is suggested by the ratio of high-excitation emission lines such as HCN to HCO^+ and $H_2O(J=4_{2,2}\text{-}4_{1,3})$ to $H_2O(J=3_{2,1}\text{-}3_{1,2})$. This idea is backed up by the galaxy's global CO-SLED, consistent with the CO-SLED of a high-redshift source with MIR AGN fraction ≥ 0.5 compatible with (obscured) AGN activity.
- I have compared the above findings with the predictions of the I scenario of galaxy formation (Lapi et al. 2018), finding that these results are consistent with the hypothesis of J1135 being a young compact dusty starburst (see also Vishwas et al. 2018), likely to host an obscured, pre-quenching ANG, compatible with the "compaction" stage of its evolution.
- J1135 is therefore found to be a rather young object, with an estimated age and gas depletion time of $\sim 10^{8}$ yr. Its inferred stellar mass ($\lesssim 10^{11}\,\mathrm{M}_\odot$) should at least double before star formation is quenched.

In conclusion, my composite approach, which involves examining both samples of objects and individual sources, has demonstrated the efficiency of utilising the strong lensing phenomenon to gain valuable insights into the evolutionary sequence and the specific details of the evolutionary phases of massive objects during the Cosmic Star Formation peak.

5.2 Future Perspectives

5.2.1 Expanding the analysis to larger samples

Future applications of the analysis presented in this thesis will encompass extending the detailed investigation described in Chapter 4 to a significant number of objects within the sample of strongly lensed DSFGs selected in the H-ATLAS survey. So far, such lensing systems have been mostly analysed individually, because of the heterogeneity of data available. Achieving this goal implies confirming the lensing nature of the selected candidates (Negrello et al. 2017, Bakx et al. 2018, Ward et al. 2022), their spectroscopic redshifts, and the properties of the lenses. This forthcoming progression owes its feasibility to the increasing number of observations, and candidates strongly lensed sources, within H-ATLAS fields, predominantly facilitated by ALMA. This enhanced observational scope will permit performing the lens modelling, source reconstruction, magnification assessments, and finally an accurate SED-fitting analysis of a sample of objects sharing the same selection and, likely similar physical properties.

In this Section, I will describe the preliminary analysis and results achieved for a small sample of 3 sources. The findings discussed here will be the object of a forthcoming paper (Giulietti et al. in preparation).

Additionally to the Negrello et al. (2017) and Ward et al. (2022) targets, I have exploited the BEARS sample drawn from the HerBS survey (Bakx et al. 2018, Urquhart et al. 2022, Bendo et al. 2023, Hagimoto et al. 2023) which I have described in Section 2.5.2, and containing 85 bright SMGs. The sources have been selected following the criteria adopted by Bakx et al. (2018), obtaining a subset of 85 fields from the HerBS survey. In particular, sources have been identified applying a 500 μm flux density $\geq$ 80 mJy threshold, excluding known blazars or bright local galaxies (as described in Negrello et al. 2010), with photometric redshifts estimated from *Herschel*/SPIRE $z_{\rm phot} \geq 2$, and located in the H-ATLAS SGP field. Several ALMA observations have been conducted for the sources in the BEARS sample. Band 3 Cycle 4 and 6 observations (programmes 2016.2.00133.S and 2018.1.00804.S, PI: Serjeant) were obtained with the ACA, and all the 85 fields were observed during Cycle 7 in Band 3 and 4 with the 12-m Array (programme 2019.1.01477, PI: Urquhart) at low angular resolution ($\sim$ 2 arcsec). The latter follow-up was conducted in a frequency set-up optimised to efficiently measure robust redshifts (Bakx & Dannerbauer 2022).

From these observations, robust spectroscopic redshift measurements were obtained for 71 sources (Urquhart et al. 2022) by targeting the brightest mm-wavelength lines, such as the CO (J, J-1) transitions. Continuum emissions for the 85 fields were presented in Bendo et al. (2023), where almost half of the *Herschel* 500-μm sources were resolved into multiple ALMA sources. Moreover, a fraction of these sources are expected to be lensed because of the nature of their selection. ALMA continuum measurements were also utilised to improve the photometric redshift estimate based on *Herschel* photometry. Hagimoto et al. (2023) conducted an analysis of the CO, [CI], and H_2O emission lines of the 71 sources and their stacked spectrum, uncovering ISM conditions akin to those found in local IR-luminous galaxies and high-redshift DSFGs, albeit characterised by denser gas and more intense Far-UV radiation fields compared to typical SFGs.

Target sample selection

Starting from the ALMA Archival data, I have searched for candidate strongly lensed sources with no prior analysis, among the Negrello et al. (2017), Ward et al. (2022), and BEARS samples and with high angular resolution data sets available. In particular, I have exploited recent ALMA Cycle 8 observations for a sub-sample of 16 objects selected from the BEARS survey (project code 2021.1.01628.S, PI: Bakx), covering Band 3-to-Band 8. These follow-ups have been conducted with higher angular resolution than the previous observations described above, spanning from ∼ 0.09 for Bands 7 and 8 to ∼ 0.25 for Band 3. The angular resolutions are thus comparable with those of the ALMA observations of J1135 and represent the highest resolutions within the H-ATLAS survey, with the exception of other well-known gravitationally lensed sources analysed extensively in the literature (e.g. SDP.81, SDP.9, SDP.17, ID141).

The high quality and the broad spectral range of these ALMA data motivated the selection of the sources object of the analysis presented in this Section.

Among this sample, I have identified sources which appear clearly lensed from the ALMA images and with a high-resolution HST/NIR counterpart. As I mentioned in Sections 2.5.2 and 4.3.3, the presence of a counterpart in the NIR regime is crucial to disentangle the contributions of the lens and the background source to the overall SED (e.g. Negrello et al. 2014) and is therefore a minimum requirement for this selection. For this purpose, I have exploited Archival HST observations, finding 3 counterparts included in the Cycles 25 and 26 snap-shot programmes 15242 and 16015 respectively (PI: Marchetti).

The final sample consists of 3 strongly lensed sources among the SGP field, namely HerBS-22 (or HATLASJ002624.8-341737), HerBS-87 (HATLASJ002533.5-333825), and HerBS-155 (HATLASJ000330.6-321136).

HerBS-22 is part of the samples of Negrello et al. (2017) and Bakx et al. (2018), and it was also analysed in Chapter 3 as it shows a radio counterpart from ATCA follow-ups. HerBS-87 and HerBS-155 were originally selected from the sample of Bakx et al. (2018), and are also included in the BEARS sample, even though no robust spectroscopic redshift estimate is available for HerBS-87 to date.

I have calibrated and imaged the ALMA data following the same procedure described in Section 4.2.1, using the CASA version 6.2.1.7. The preliminary analysis described here focuses on continuum Bands 6 and 7 data and will be further expanded including data from Bands 3,4,5, and 8 and searching for spectral line emissions. Band 7 observations exploit four basebands of width 1.875 GHz, centred at 280.155, 282.010, 292.155, and 294.010 GHz, each one composed of 1920×0.97 MHz channels. Band 6 observations share an analogous set-up, with basebands centred at 223.879, 225.734, 238.379, and 240.234 GHz. The final cleaned images and their properties are reported in Figure 5.1 and Table 5.1.

Ancillary data

As for J1135, aside from ALMA, HST and *Herschel* observations, all three targets have ancillary multi-wavelength data in the KiDS, VIKING and WISE surveys, covering the UV/optical-to-MIR regime. Figures 5.2, 5.3, and 5.4 show the cutout

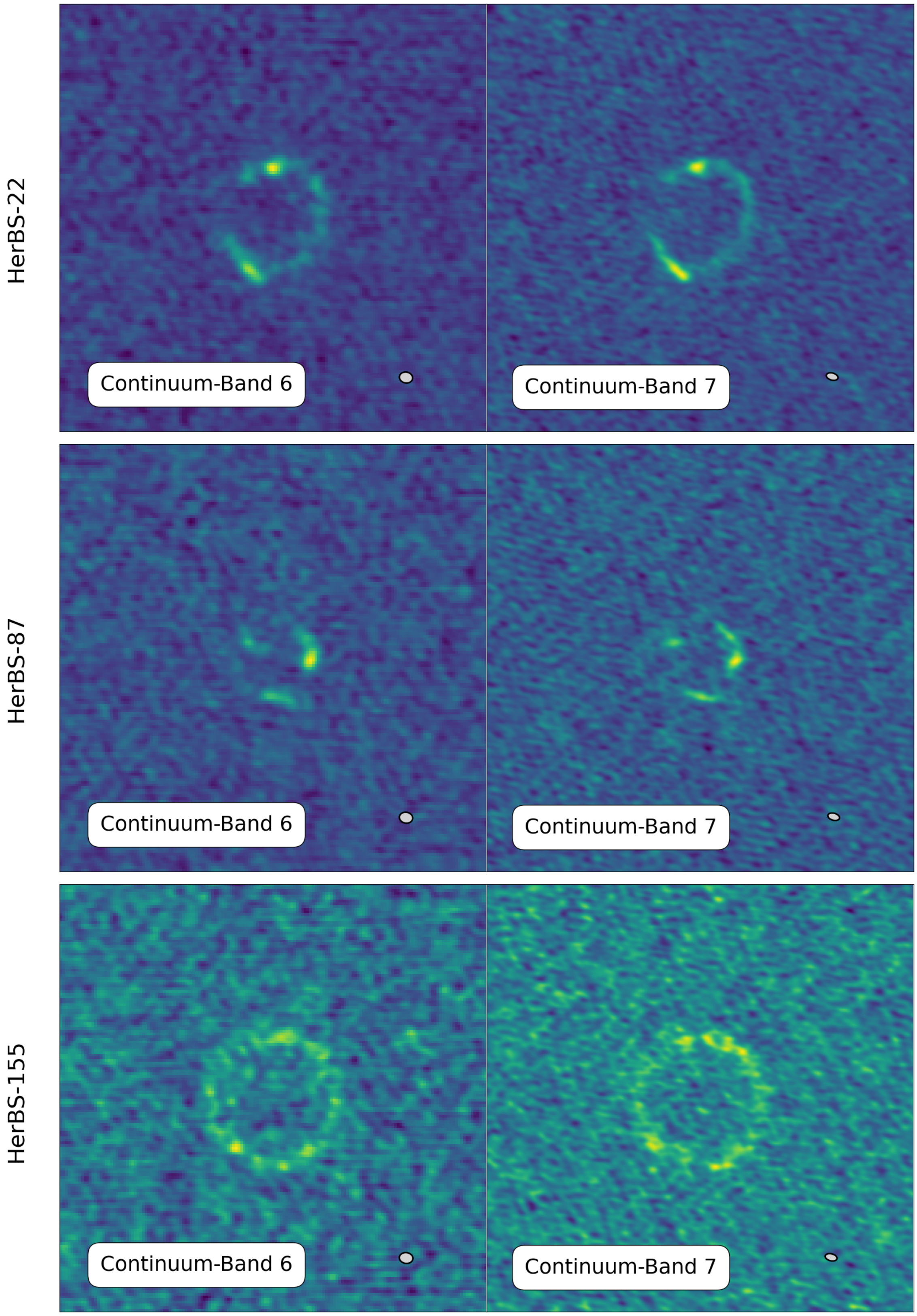

Figure 5.1: ALMA Band 7 and 6 images of the 3 HerBS sources, the beam is shown as a grey ellipse. Postage stamps are 5×5 arcseconds and are centred at $\mathrm{RA_{ALMA}}$ and $\mathrm{Dec_{ALMA}}$.

	Band 7			Band 6		
Source ID	Beam [arcsec^2]	PA angle [deg]	Cont. Sensitivity [mJy]	Beam [arcsec^2]	PA angle [deg]	Cont. Sensitivity [mJy]
HerBS-22	0.141×0.083	74.52	0.116	0.156×0.128	78.56	0.077
HerBS-87	0.140×0.082	75.06	0.101	0.157×0.127	80.27	0.071
HerBS-155	0.141×0.082	76.42	0.106	0.160×0.126	82.48	0.073

Table 5.1: Properties of ALMA Band 7 and 6 continuum images of the three HerBS targets. Columns show the final beam size, the positional angle, and the continuum sensitivity.

of the multi-band counterpart for each object in our sample with ALMA Band 7 contours superimposed. Conversely to J1135, the foreground object is clearly visible in the optical/NIR regime. The KiDS DR4 photometric catalogue (Kuijken et al. 2019) also provides an estimate of the photometric redshift of the lenses based on the 9-band optical-to-IR measurements. The properties of the sample of the three HerBS gravitationally lensed systems are summarised in Table 5.2.

Lens modelling

I have performed the lens modelling and source reconstruction of ALMA continuum Band 6 and 7 of the three systems following the same procedure described in Section 4.3 assuming an SIE mass profile for the lens. The best-fit lens model parameters are summarised in Table 5.4. The results of source reconstruction are reported in Figures 5.5, 5.6, and 5.7, and Table 5.3, where the parameters of the source reconstruction are computed as described in Section 4.3.1.

Lens subtraction

The availability of high-resolution NIR data from HST for the three sources enables us to infer the properties of the unobscured stellar component of these systems. A necessary step involves the subtraction of the lens light from the NIR image, where it dominates with respect to the background sources. For this purpose, I have modelled the lens emission in the HST/WFC3 F110W images through PyAutolens via a parametric non-linear fit with the same procedure adopted to model the source's light described in Section 4.3. Here I report the preliminary result of this procedure applied to HerBS-155. The lens emission is modelled with two Sérsic profiles, and the results are reported in Table 5.5 and Figure 5.8. The normalised residual map shows an arc-like structure similar to that present in the ALMA continuum maps of HerBS-155 belonging to the background source. The emission peak reaches a 5σ significance, and it should be tested whether or not the SNR of the background source is sufficient for the lens modelling.

I will extend the lens-subtraction analysis for the remaining two objects, with the goal of reconstructing the de-lensed NIR emission of the background source. The relative sizes of the dust and unobscured stellar emission will be then compared to investigate the evolutionary phase of these sources as done for J1135.

HerBS-ID	H-ATLAS ID	RA [deg]	Dec [deg]	RA_{ALMA} [deg]	Dec_{ALMA} [deg]	z_{source}	z_{lens}	$F_{250\mu m}$ [mJy]	$F_{350\mu m}$ [mJy]	$F_{500\mu m}$ [mJy]	$F_{850\mu m}$ [mJy]
HerBS-22	J002624.8-341737	6.6035	-34.2938	6.6042	-34.2939	3.05^{s}	1.11	137.7±5.2	185.9±5.8	148.8±6.8	91.9±12.8
HerBS-87	J002533.6-333826	6.3899	-33.6406	6.3903	-33.6406	2.36	0.98	114.7±5.2	127.8±6.1	96.0±7.3	30.3±8.0
HerBS-155	J000330.7-321136	0.8778	-32.1934	0.8777	-32.1931	3.077^{s}	0.43	59.9±5.8	94.2±5.8	85.6±7.2	46.0±10.6

Table 5.2: The table summarises the main information on the three HerBS sources object of this analysis. From the left: source name in the HerBS catalogue (Bakx et al. 2018), source name in the H-ATLAS survey (Eales et al. 2010), coordinates centred on *Herschel* position, coordinates centred on ALMA position, (J2000), redshift of the background source measured either from CO spectral lines (Urquhart et al. 2022, denoted by ^{s}) or from *Herschel* photometry. The photometric redshift of the foreground lens, retrieved from the optical-to-NIR photometry of the KiDS DR4 catalogue (Kuijken et al. 2019). The final four columns report the *Herschel*/SPIRE and SCUBA photometry from the H-ATLAS survey.

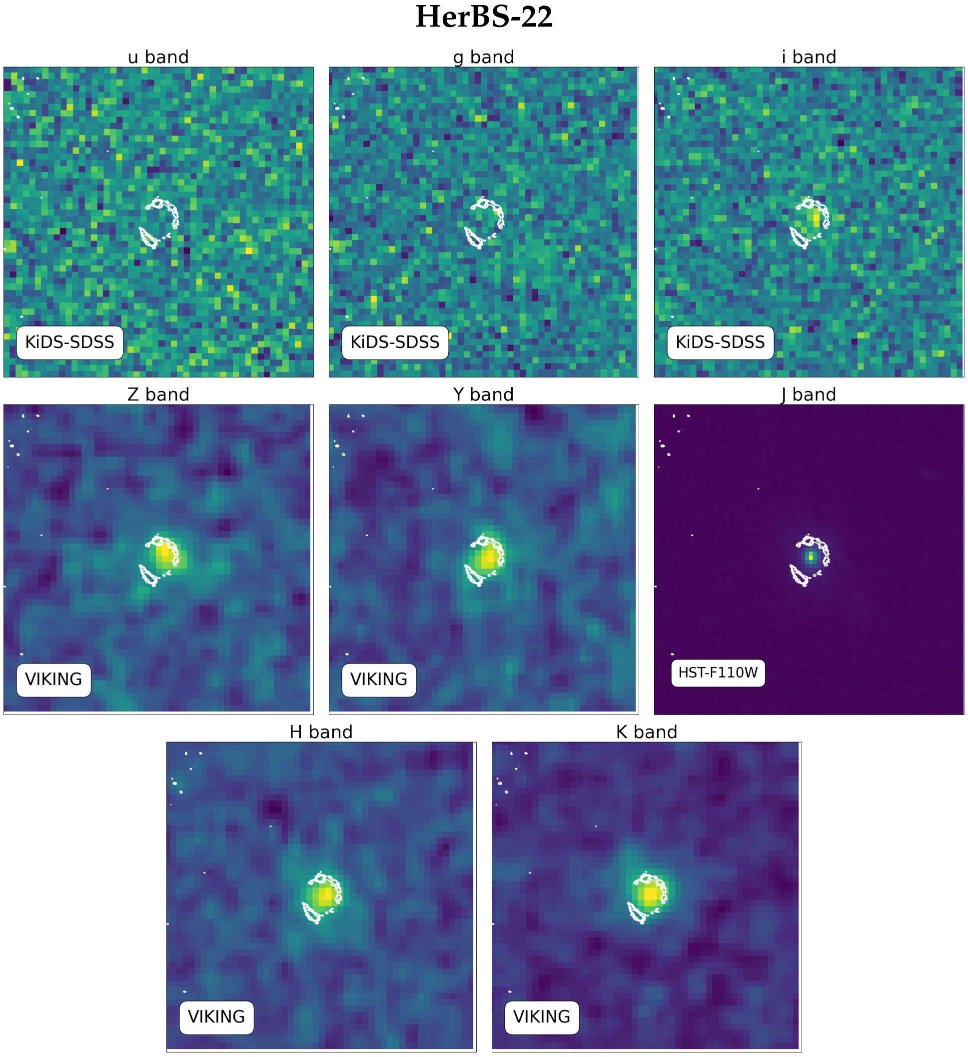

Figure 5.2: Cutouts of optical-to-NIR images for HerBS-22 centred on the ALMA position. Contours display ALMA Band 7 continuum emission at 9,7,5,3×σ The postage stamps are 10×10 arcsec.

	Band 6				Band 7			
Source ID	$\mu_{3\sigma}$	$\mu_{5\sigma}$	$R_{\mathrm{eff},3\sigma}$ [pc]	$R_{\mathrm{eff},5\sigma}$ [pc]	$\mu_{3\sigma}$	$\mu_{5\sigma}$	$R_{\mathrm{eff},3\sigma}$ [pc]	$R_{\mathrm{eff},5\sigma}$ [pc]
HerBS-22	$10.35^{+1.02}_{-1.16}$	$12.37^{+1.17}_{-1.08}$	1125^{+72}_{-86}	846^{+85}_{-92}	$13.66^{+3.62}_{-3.49}$	$15.30^{+2.39}_{-2.33}$	837^{+74}_{-67}	472^{+57}_{-63}
HerBS-87	$12.22^{+2.24}_{-2.82}$	$25.12^{+4.06}_{-3.53}$	1046^{+86}_{-79}	626^{+35}_{-43}	$9.35^{+1.87}_{-1.65}$	$18.47^{+1.93}_{-2.158}$	886^{+65}_{-74}	365^{+60}_{-60}
HerBS-155	$10.31^{+5.46}_{-3.86}$	$14.86^{+3.02}_{-3.31}$	1137^{+86}_{-80}	664^{+86}_{-80}	$17.52^{+1.55}_{-1.41}$	$14.81^{+1.67}_{-1.82}$	1028^{+52}_{-39}	960^{+40}_{-43}

Table 5.3: Parameters in output from the source reconstruction of ALMA continuum Band 6 and 7 data of the three HerBS sources. Columns report the 3σ and 5σ magnification factors and effective radii.

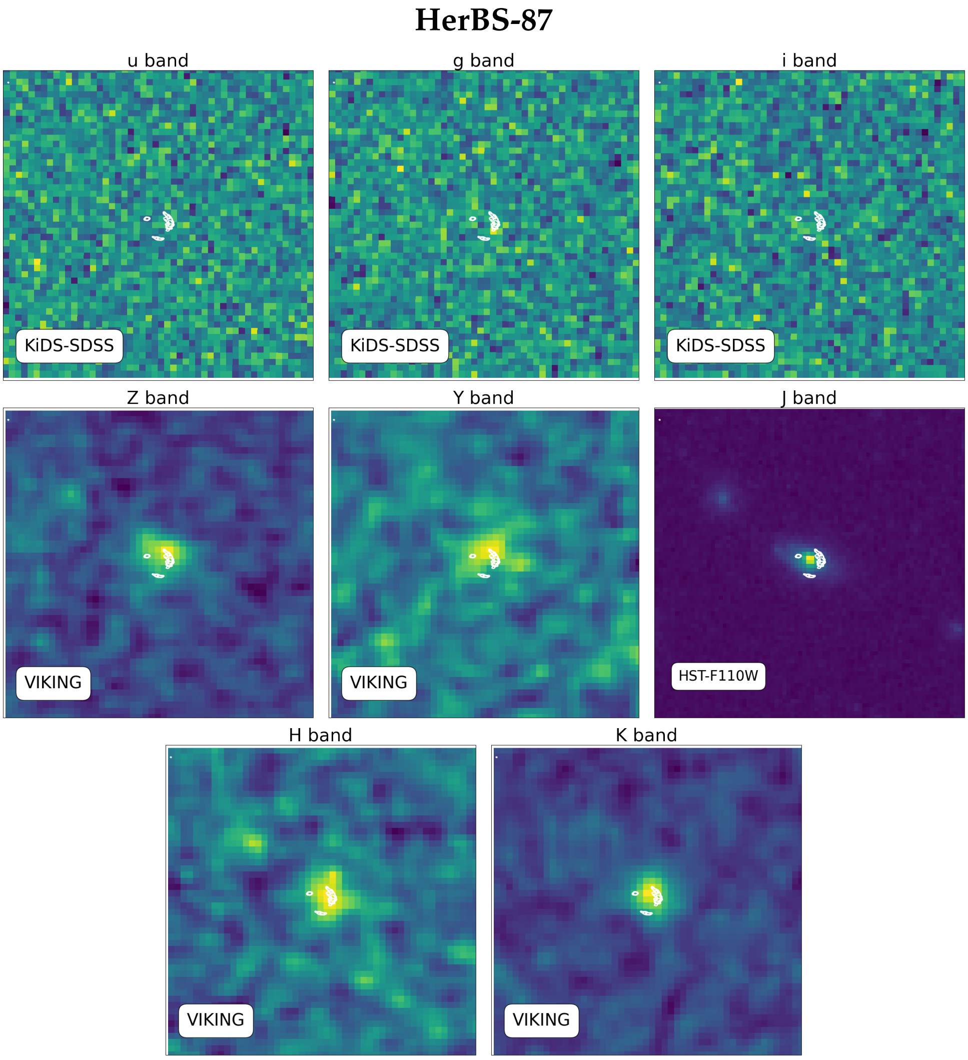

Figure 5.3: Same as Figure 5.2 for HerBS-87.

Source ID	$\theta_{\mathrm{Ein}}^{\mathrm{mass}}$ [arcsec]	$\mathrm{y}^{\mathrm{mass}}$ [arcsec]	$\mathrm{x}^{\mathrm{mass}}$ [arcsec]	q	ϕ [deg]	γ_1	γ_2
HerBS-22	$0.639^{+0.004}_{-0.003}$	$-0.016^{+0.004}_{-0.005}$	$0.1305^{+0.0057}_{-0.0055}$	$0.54^{+0.01}_{-0.01}$	$-46.19^{+0.01}_{-0.04}$	$-0.032^{+0.006}_{-0.007}$	$-0.157^{+0.006}_{-0.007}$
HerBS-87	$0.425^{+0.008}_{-0.004}$	$-0.027^{+0.004}_{-0.004}$	$-0.006^{+0.003}_{-0.005}$	$0.67^{+0.03}_{-0.04}$	$29.5^{+0.1}_{-0.1}$	$-0.0293^{+0.01}_{-0.01}$	$-0.0064^{+0.01}_{-0.02}$
HerBS-155	$0.731^{+0.004}_{-0.004}$	$-0.049^{+0.005}_{-0.005}$	$0.046^{+0.004}_{-0.004}$	$0.97^{+0.01}_{-0.01}$	8^{+3}_{-3}	$-0.0009^{+0.0048}_{-0.0048}$	$0.014^{+0.005}_{-0.004}$

Table 5.4: Best-fit parameters from the lens modelling of the three HerBS sources, as described in Table 4.5, the last two columns report the shear elliptical components of the mass profile.

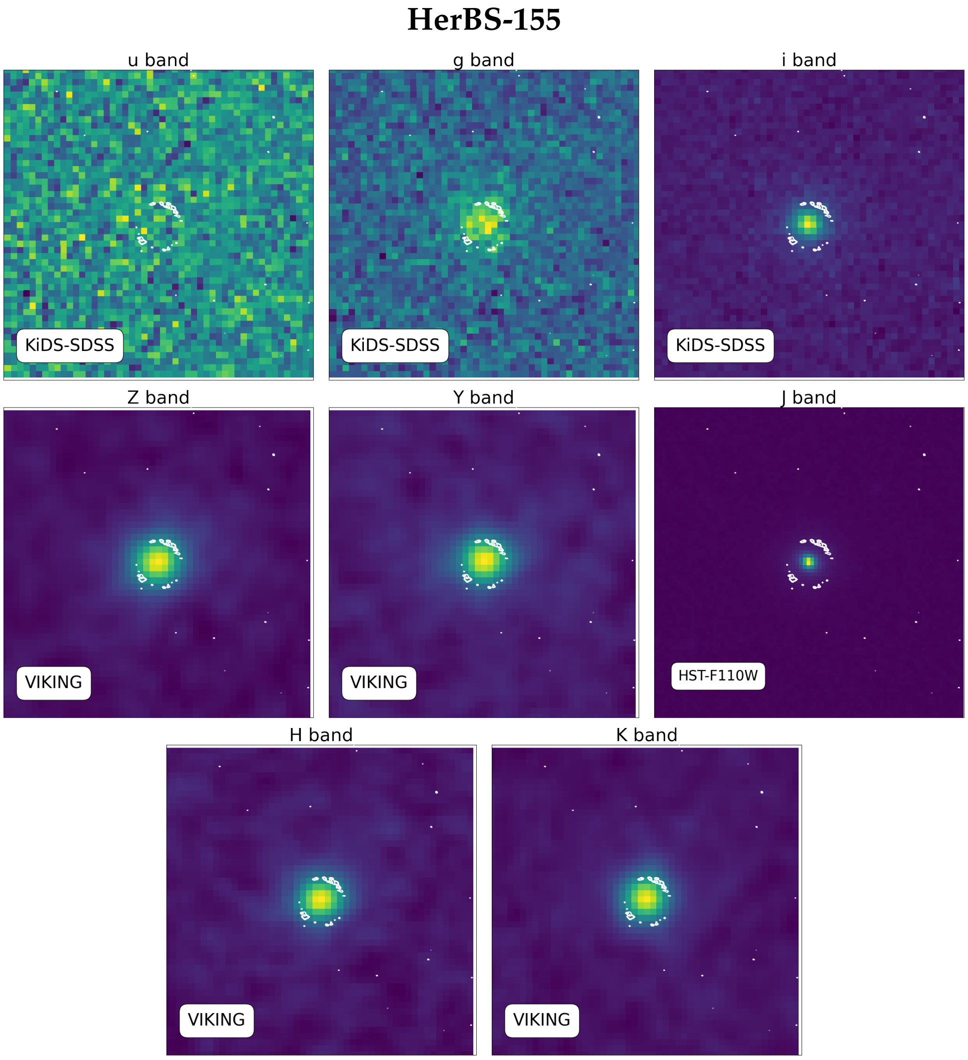
HerBS-155

Figure 5.4: Same as Figure 5.2 for HerBS-155.

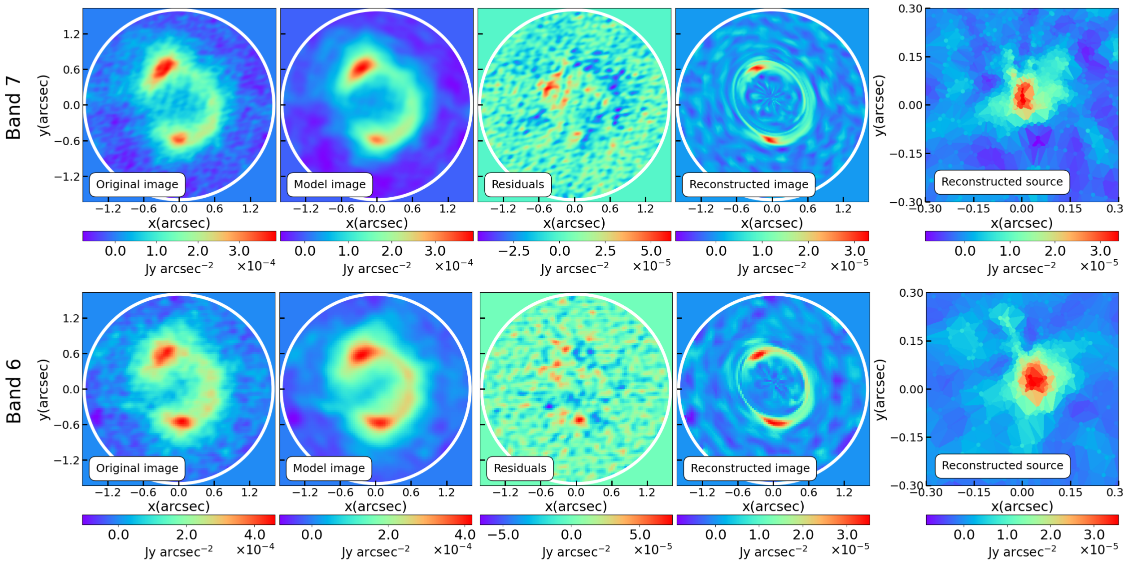

Figure 5.5: Same as 4.6 for HerBS-22.

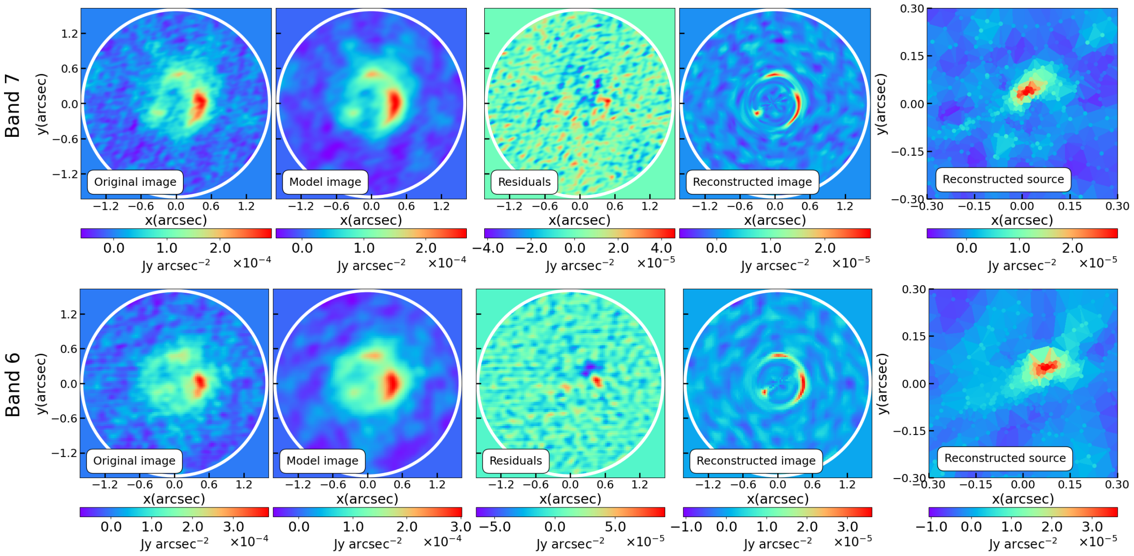

Figure 5.6: Same as 4.6 for HerBS-87.

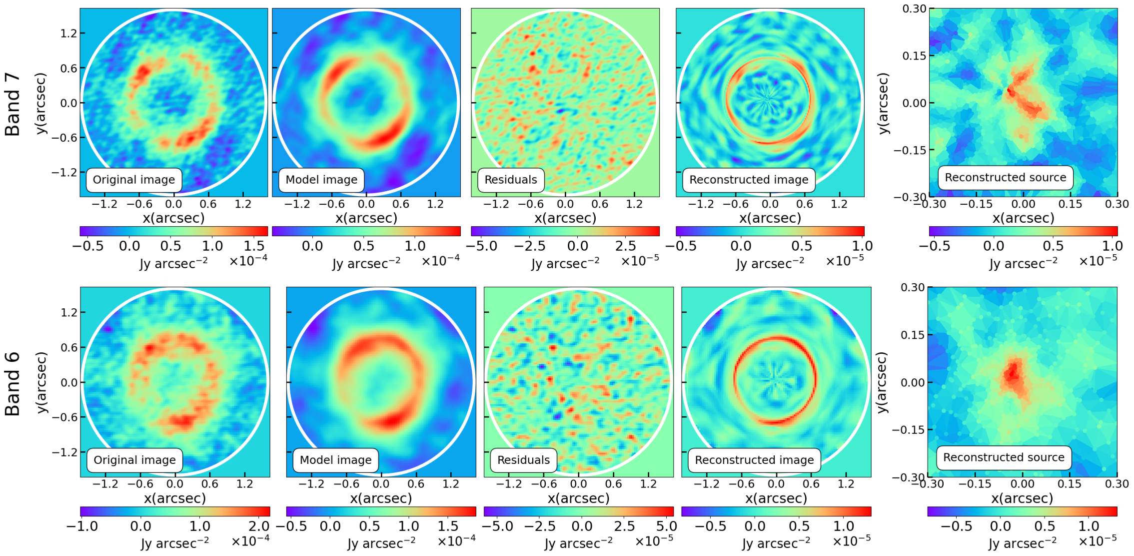

Figure 5.7: Same as 4.6 for HerBS-155.

Lens subtraction: HerBS-155

Components	q	ϕ [deg]	r_{eff} [arcsec]	n
Sérsic 1	0.79 ± 0.03	-29.2 ± 0.1	0.096 ± 0.002	0.34 ± 0.07
Sérsic 2	$0.857^{0.005}_{0.004}$	$-7.4^{+0.2}_{-0.1}$	0.88 ± 0.01	3.04 ± 0.04

Table 5.5: Output parameters from the lens-subtraction procedure performed with PyAutoLens for HerBS-155. The lens light is modelled with two Sérsic profiles. From the left: axis ratio, positional angle, effective radius and Sérsic index.

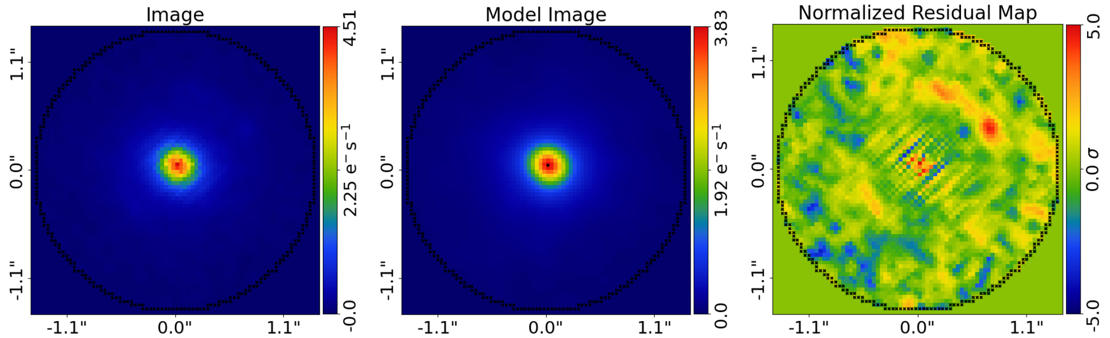

Figure 5.8: Results of the lens subtraction for HerBS-155 HST/WFC3 F110W image. Panels show the original map, the model and the normalised residuals.

5.2.2 Improving the information in the radio continuum domain

Addressing the issue of coevolution between galaxies and SMBHs involves not only a knowledge of the SFR but also of the AGN feedback mechanisms (jets or winds), concurring in the quenching of the star formation. Obtaining independent measurements of star formation and AGN activity is essential, especially in quasar-host galaxies which are rich in gas and dust (Hopkins et al. 2005).

One important issue regards the main driver of radio emission in heavily obscured accreting SMBHs (Alexander & Hickox 2012), and its connection with galaxy properties such as the age, the sSFR, and the obscuration.

From the FIRRC an excess in radio emission is expected from radio-loud AGNs, which is mainly detected at fluxes $S_{1.4,\mathrm{GHz}} \gtrsim 0.1\,\mathrm{mJy}$ (e.g. Mignano et al. 2008). This population progressively recedes towards fluxes below this threshold, making way for the emerging category known as radio-quiet AGNs (e.g., Simpson et al. 2006, Seymour et al. 2008, Smolčić et al. 2008). This also corresponds to a gradual change in the physical processes probed by deep radio surveys. However, the results of the radio emission mechanisms (AGN, star formation, or a composite of both) have been largely debated (e.g. Barthel 2006, Kimball et al. 2011, Padovani et al. 2011, Bonzini et al. 2013, Condon et al. 2013, Bonzini et al. 2015, Padovani et al. 2015, White et al. 2015, Herrera Ruiz et al. 2016, Kellermann et al. 2016, Herrera Ruiz et al. 2017, White et al. 2017).

I demonstrated that the in-situ scenario provides a plausible evolutionary framework for the evolution of radio-loud AGNs (see also Mancuso et al. 2017). In this view, samples of strongly lensed quasars and DSFGs can be exploited to overcome the limits in sensitivity of the current surveys, where the majority of these objects often remain undetected. However, most lensed quasars still lie below the detection limits of all-sky surveys such as FIRST and even forthcoming surveys such as VLASS, and samples of strongly lensed objects are still limited. Even though significant progress has been made in characterising the faint radio population with deep surveys of single fields, such as the VLA-COSMOS 3 GHz survey (Smolčić et al. 2017), these predictions need to be tested in detail in order to fully understand the mechanisms that give rise to radio emissions in radio-quiet AGNs, in particular, the impact of radiative feedback processes and whether or not radio emission in these objects is primarily governed by star formation.

In the future, the radio domain will soon open a new observational window, provided by the upcoming ultradeep radio continuum surveys planned on the Square Kilometre Array Observatory (SKAO) and its pathfinder telescopes, such as ASKAP, MeerKAT, and LOFAR (see Norris et al. 2013, Prandoni & Seymour 2015).

For what concerns SKA precursors, recent studies have exploited the low-frequency regime ($\nu \lesssim 150$ MHz), currently explored by LOFAR (van Haarlem, M. P. et al. 2013) and soon with SKA, to detect the emission originated by star formation at high-z through the steep negative spectrum of synchrotron radiation, where the observed radio luminosities are higher. This alternative method to identify extreme cases in which the radiative output from the AGN is heating the cold dust at FIR wavelengths can be also applied in the case of gravitationally lensed systems, where the magnification in sizes and luminosity enable the study of the FIR and radio properties for individual objects otherwise undetected (see Stacey et al. 2019).

SKA path-finders such as ASKAP are built to perform high-speed surveys with an instantaneous field of view up to 30 deg^2. The ASKAP Evolutionary Map of the Universe survey (EMU, Norris 2017; Norris et al. 2011) is planned to conduct all-sky deep observations. One of the key objectives of the survey is tracing the co-moving SFRD up to $z \sim 2$ for starburst galaxies and up to $z \sim 0.3$ for Milky Way-like galaxies, along with radio-loud AGNs up to $z > 4$ and radio-quiet AGNs up to $z \sim 2$. The pilot EMU survey (Norris et al. 2021) was conducted in the southern field (over ~270 deg^2) in the frequency range 800 – 1088 MHz, produced images reaching a sensitivity of $\sim 25-30\mu$Jy beam^{-1}, with an angular resolution of $\sim 11-18$ arcsec and resulted in a catalogue of ~ 220000 sources. At the end of 2022, the main EMU continuum survey started and is planned to reach a better sensitivity and dynamic range with respect to the pilot project.

In the context of future radio observations, the work described in this thesis has paved the way for new deep observations. In particular, my analysis of ATCA follow-up at 2 GHz conducted in 30 non-contiguous fields within the H-ATLAS SGP (Section 3.2) unveiled a substantial number of previously undetected radio sources. The identification of these new objects prompted the initiation of the Serendipitous H-ATLAS-field Observations in Radio-bands of Extragalactic Sources (SHORES) survey (PI M. Massardi). This comprehensive radio survey spanned over 200 hours of observing time and encompassed a total area of 15 deg^2, reaching sensitivities of approximately $\sim 30\mu$Jy. These depths are on par with surveys projected for the SKA pathfinders (see Figure 5.9). Notably, a specific deep field has been surveyed down to $\sim 5\mu$Jy at 2.1 GHz. Follow-up ATCA observations at 5.5 and 9 GHz were also in one (Deep) field, reaching down to 50 μJy. The SHORE's Deep Field also boasts a wealth of supplementary data, including partial coverage from ASKAP and data from *Spitzer*, WISE, and HST.

The main objectives of SHORES include the characterisation of the radio luminosity function and multi-band analysis of faint radio-emitting objects. Moreover, SHORES is observed in polarisation, which indicates AGN presence and opens the investigation of the extragalactic foreground (i.e. polarisation coming from star-forming galaxies and AGNs).

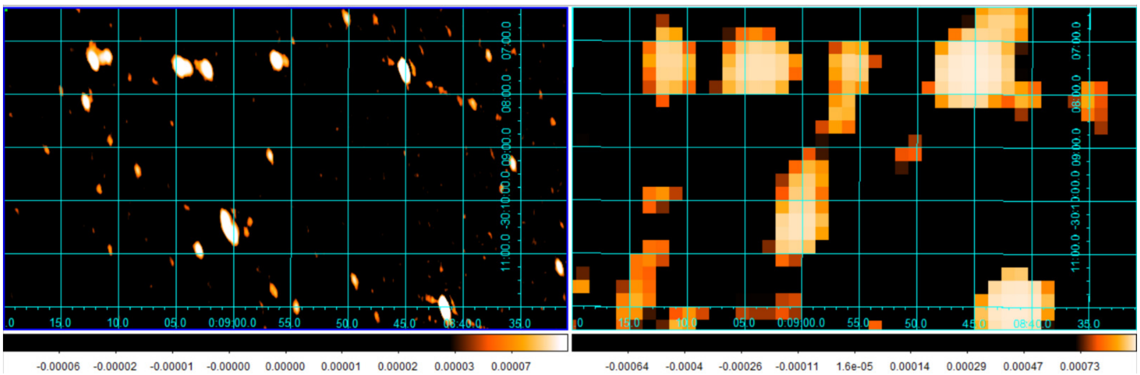

Figure 5.9: Cutout partially covering one of the SHORE's fields compared with previous NVSS observations of the same region of the sky.

The next-generation radio astronomy facility SKAO is planned to commence scientific operations by the end of the current decade. One of the primary objectives of SKAO is to investigate the history of cosmic star formation, even reaching extremely distant cosmic epochs. The initial phase, referred to as SKA1, was originally designed to be executed across two distinct locations, each with different arrangements of baselines. The first site, labelled SKA1-low, comprises 512 stations with 256 antennas each and is located at the Murchison Radio-astronomy Observatory in Western Australia. This array was designed to operate within the frequency range of 50 to 350 MHz. The second site, SKA-mid, was projected to incorporate a combination of 133 SKA 15-meter dishes and 64 MeerKAT 13.5-meter dishes situated at the Karoo site in South Africa. SKA-mid's observation range is planned to range from 350 MHz to 15.4 GHz, with the goal of reaching 24 GHz in the future, and is planned to be divided into at least 4 bands.

The first SKA science data challenge (Bonaldi et al. 2021) provided the properties of SKA-MID continuum imaging products, addressing the issues associated with their analysis. The images are simulated at three frequencies (150 MHz, 1.4 GHz and 9.2 GHz) and three depths (8 hours, 100 hours and 1000 hours). The rms for the deepest observations reaches ~ 250, 73 and 38 nJy in the three bands respectively.

According to projections from Mancuso et al. (2015), a survey reaching an rms sensitivity of $\sim 0.25\mu\text{Jy beam}^{-1}$ at 1.4 GHz could potentially identify ~ 1200 strongly lensed galaxies per square degree above a 5σ detection threshold, even at redshifts up to 10. Notably, the impressive angular resolution of SKA1-mid (ranging from 0.03 to 1.4 arcsec) ensures that at least two images from around 30% of these sources will be detected, allowing for the direct confirmation of their lensed nature.

The capabilities of SKA1-mid and its predecessors promise a comprehensive insight into the history of star formation during the EOR. This data will remain unaffected by dust extinction, thereby enabling a thorough exploration of both SFG and radio-quiet AGN populations. These observations will achieve unprecedented levels of sensitivity (sub-μJy) in the deepest fields. Additionally, they will generate extensive samples over wide areas at the same depth ($\sim \mu$Jy), to date attained only by the smallest and most in-depth radio surveys. In conjunction with in-depth multi-wavelength data, this approach will provide an unbiased perspective on the interplay between star formation and nuclear activity throughout cosmic history.

5.2.3 Improving the sub-mm/NIR spectral and continuum information

Aside from the radio band, the launch of JWST in 2022 has inaugurated a new perspective on the distant Universe in the NIR and MIR regime. Deep imaging of JWST's imaging cameras (NIRCam and MIRI), demonstrated the ability of JWST to identify optically and NIR dark sources missed even by Spitzer because of their fainter luminosities. By selecting galaxies based on their broadband colours and brightness drop (referred to as the Lyman Break or the Lyman Forest), the exploration of numerous extremely high-redshift (up to $\sim$ 16) Lyman-Break Galaxies (LBGs) *candidates* (e.g. Bradley et al. 2022, Castellano et al. 2022, Finkelstein et al. 2022, Naidu et al. 2022, Adams et al. 2023, Atek et al. 2023, Bouwens et al. 2023, Donnan et al. 2023, Finkelstein et al. 2023, Labbé et al. 2023, Harikane et al. 2023, Morishita & Stiavelli 2023, Rodighiero et al. 2023, Yan et al. 2023) was made possible. Along with this, the accuracy of JWST's spectrography (performed with NIRSpec and NIRIS) confirmed the presence of galaxies up to $z \sim 13.2$ (Robertson 2022, Curtis-Lake et al. 2023).

In addition to these thrilling discoveries, the high-resolution imaging capabilities of JWST to capture the stellar distribution of DSFGs hold a pivotal role in comprehending the mechanisms driving the triggering of starbursts, as well as their subsequent transformation into quiescent galaxies.

In particular, JWST can overcome the high-z DSFG's extremely low brightness in (rest-frame) optical wavelengths, the distribution of stars within intense starbursts remains largely unexplored and often beyond the capabilities of the HST and 8–10 m telescopes. Only a few galaxies have been detected by IRAC/Spitzer in the mid-infrared, but the resolution of these detections is insufficient for studying their structure. The JWST, combining sub-arcsecond angular resolution and significantly improved sensitivity compared to previous telescopes across the near- and mid-infrared spectrum (i.e., 1–28 μm), introduces the opportunity to, for the first time, investigate the stellar light and ionized gas structure within these galaxies at sub-kiloparsec scales.

NIRCam attains higher angular resolutions and sensitivities compared to HST, with its angular resolutions more closely resembling those of ALMA. This outcome will allow JWST to explore the spatial segregation between obscured and unobscured star formation, even in HST-dark entities like J1135, with an unprecedented level of detail. This factor holds significance in the evaluation of predictions made by evolutionary models. For instance, within the in-situ framework, the stellar component is anticipated to span an area larger than a kiloparsec, while obscured star formation occurs within a notably more concentrated sub-kiloparsec region (Lapi et al. 2018). This anticipation has undergone testing on DSFG samples (Pantoni et al. 2021) and a few strongly lensed DSFGs (e.g., Massardi et al. 2017), showcasing strong alignment with model projections. The capabilities of

JWST will expand these investigations to unprecedented angular resolutions and extend them to fainter and distant galaxies.

The unmatched angular resolution of MIRI overcomes the challenges of object blending commonly observed in instruments working within comparable wavelength ranges, such as *Spitzer* and WISE. Furthermore, MIRI imaging holds the capability to delve into the stellar and ionized gas structure in the rest-frame NIR of these galaxies, even during the Era of Reionization. For instance, a recent investigation by Álvarez-Márquez et al. (2023) showcased MIR sub-arcsecond imaging and spectroscopy of the farthest lensed hyper-luminous infrared system discovered to date (SPT0311-58, at z = 6.9). Through observations employing the MIRI IMager (MIRIM) and Medium Resolution Spectrometer (MRS), the study unveiled the structural characteristics of stellar emission (at rest-frame 1.26 μm) and the ionized medium on kiloparsec scales within the system.

Hence, MIRI and NIRCam possess the complete capability to distinguish arc-like characteristics within lensed galaxies at high redshifts, like J1135, during the peak of Cosmic SFH. This becomes notably significant when considering intricate lens modelling or conducting SED-fitting analyses, as the resolution and segregation of the background source's emission within the system are important aspects to be taken into account. Additionally, for the latter objective, JWST/MIRI can effectively track potential excess originating from obscured AGNs within such sources.

Finally, the synergy between JWST and ALMA can be exploited to identify the physical properties of candidate strongly lensed DSFGs and dig into the star formation events. Of particular importance will be the forthcoming ALMA2030 Wideband Sensitivity Upgrade (Carpenter et al. 2023), which will enhance the efficiency in spectral lines detection, also facilitating the redshift estimation of the lensed sources.

Appendix A

Relevant Astrophysical Processes in Galaxy Evolution

Here I overview the physical baryonic processes that constitute the fundamental elements shaping galaxy formation and evolution.

A.1 Radiative cooling

In Section 1.3 I have overviewed the main processes involved in the evolution of an ETG progenitor as described by Lapi et al. (2018). One of the main mechanisms involved in the early fast evolution is the *radiative cooling*. This process takes place when the astrophysical gas cools by emitting radiation and therefore loses the energy carried by the emitting photons. The result is the loss of kinetic energy of the gas particles.

In the context of galaxy formation, the relevant case involves an optically thin gas or a gas in which the photons can escape from the system because they are not absorbed by the gas itself.

Several mechanisms may be responsible for radiative cooling, depending on the gas temperature, density, and ionisation state. The discriminant temperature is $T \approx 10^4$ K, which in the case of Hydrogen, corresponds to the value separating regimes of ionised and neutral gas.

For $\mathrm{T} \gtrsim 10^4$ K the main mechanisms determining radiative cooling of the gas are processes involving electrons and ions (or atoms). These processes can be classified on the basis of whether the electron is in a bound or free state before or after the radiation emission.

- Bremsstrahlung (or free-free radiation): a free electron interacts with an ion and emits radiation because of its change in velocity when being deflected and accelerated in the ion field.
- Recombination (or free-bound radiation): a free electron recombines with an ion to form a neutral atom or a less ionised ion, and emits radiation.
- Radiative de-excitation (or bound-bound radiation): when transitioning

from a higher to a lower energy level, an electron bound to either a neutral atom or an ion emits radiation.

In addition to these three mechanisms, *collisional* processes are crucial in establishing the conditions for radiative cooling:

- Collisional ionisation (bound-free): through collision, usually involving a free electron, an electron that is initially bound to either a neutral atom or an ion is emitted.

- Collisional excitation (bound-bound): typically involving a free electron, a collision can cause a bound electron to be excited to a higher energy level or de-excited to a lower energy level. In case of a collisional excitation a photon is absorbed, in case of de-excitation, it is emitted.

The combined effect of the above mechanisms can be computed, provided we have information on the rate of ionisation and recombination of the various species involved. A useful approximation usually adopted is the *collisional ionisation equilibrium* (CIE). However, one has to keep in mind that this assumption may not be always applied in astrophysical systems, and in some cases, a more realistic treatment is required (e.g. Sutherland & Dopita 1993).

The collisional ionisation equilibrium assumes a perfect balance between the collisional and ionisation rates, neglecting photoionisation from external radiation fields. Moreover, the ions and neutral atoms are assumed to always be in the ground state, therefore they are not in thermodynamic equilibrium.
To fulfil these conditions, the gas number density must be much lower than a certain critical value n_{crit}. At these densities, collisional de-excitation is rare, favouring spontaneous decay and emission. Furthermore, in CIE excited ions and neutral atoms immediately emit radiation. As $n > n_{\mathrm{crit}}$, the upper energy levels become substantially populated due to collisional excitation, and concurrently, depopulated by collisional de-excitation. Meanwhile, spontaneous decay becomes progressively less likely. In such circumstances, a state of thermodynamic equilibrium is reached, leading to energy levels populated in accordance with the Boltzmann law.

Assuming a static fluid in the regime of $T \gtrsim 10^4$ and neglecting gravity, from the energy equation of fluids we can infer the energy loss per unit time per unit volume due to radiative cooling under the CIE approximation as:

$$\frac{\mathrm{d}\varepsilon}{\mathrm{d}t} = -n_t n_e \Lambda(T). \tag{A.1}$$

Here ϵ is the cooling rate of an optically thin gas, n_t and n_e are the atomic (atoms and ions) and the electron number densities respectively, such that $n = n_t + n_e$. Λ is the *cooling function* (in units of erg s^{-1} cm^3, which only depends on gas temperature and metallicity.

The left panel of Figure A.1 shows the cooling function $\Lambda(T)$ in the temperature interval 10^4K <T< 10^7K for plasmas with different metallicities. For $Z = 0$

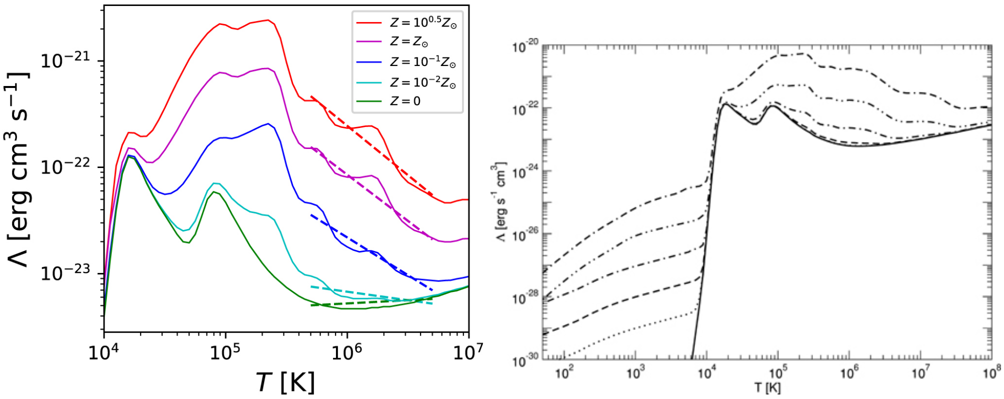

Figure A.1: *Left panel:* cooling functions from Sutherland & Dopita (1993) in the temperature range $10^4 <$ K T$< 10^7$ K and for different values of gas metallicities. Figure from Washinoue & Suzuki (2023). *Right panel:* Cooling functions for gases with $n_{\rm H} = 1$ cm^{-3} at different metallicities: $Z = 0$ (solid), $10^{-3} Z_\odot$ (dotted), $10^{-2} Z_\odot$ (dashed), $10^{-1} Z_\odot$ (dot-dash-dashed), 1 $Z_\odot$ (dot-dot-short dashed), $10 Z_\odot$ (dot-dot-long dashed). Image credits: Smith et al. (2008).

the gas is made only of hydrogen and helium, Λ peaks at T$\approx 2 \times 10^4$ K, corresponding to a regime in which collisional excitation (and radiative de-excitation) and ionisation (and recombination) of neutral hydrogen are most effective. With increasing temperatures hydrogen becomes ionised and its contribution to the radiative cooling rapidly drops, the second peak at $T \approx 10^5$ K is therefore originated by the helium. At even higher temperatures, also the helium is completely ionised and the free-free emission becomes the dominant process, enforcing the asymptotic dependence of $\Lambda(T) \sim T^{1/2}$. At a given temperature, the cooling rate is higher for higher metallicities. This is due to the fact that metal atoms and ions are characterised by several line transitions, which are the driving coolant mechanisms at T$\approx 10^5$.

The characteristic timescales of cooling can be approximated as

$$t_{\rm cool} = \frac{3}{2} \left(\frac{n}{n_t} \right) \left(\frac{n}{n_e} \right) \frac{k_{\rm B} T}{n \Lambda(T)} \approx \frac{6 k_{\rm B} T}{n \Lambda(T)}. \tag{A.2}$$

This quantity is the *cooling time*, corresponding to the time in which the gas would emit all of its thermal energy through radiation if the cooling rate was constant. $t_{\rm cool}$ is, in most cases, a reliable estimate of the cooling time, even if T and n vary during the process. This approximation holds for fully ionised gas. n_t/n and n_e/n depend on both metallicity and temperature, and for T$\gtrsim 3 \times 10^4$ K and $0 \leq Z \leq Z_\odot$ these ratios are ≈ 2 and are only weakly dependent on Z and T. Therefore, for a given metallicity and temperature $t_{\rm cool} \propto 1/n$, the outcome is that plasmas with higher densities have shorter cooling times.

In the case in which $T \lesssim 10^4$ K, all atoms are neutral and very few electrons are free. Within this temperature range, the cooling function is influenced not only by gas metallicity and temperature but also by gas density. At elevated densities, cooling becomes less effective, as collisional de-excitation replaces radiative de-excitation, leading to the suppression of metal cooling. The limited number of free

electrons lacks the required energy to excite the inner energy levels of hydrogen. Consequently, the atomic cooling of metal-poor gas markedly diminishes, quickly dropping down to zero for temperatures below 10^4 K.
The right panel of Figure A.1 illustrates this situation, also showing how, at these low temperatures, metal-rich gas cools more efficiently than metal-free gas. This is because heavier elements, such as the singly ionised Carbon, have low-energy transitions that can be excited at $T < 10^4$ K.

It is worth noticing that, even if metal-enriched gas cools more efficiently, the atomic cooling rate at $T < 10^4$ K is orders of magnitudes lower than at $T > 10^4$ K. Another important aspect, which becomes relevant in the context of the formation of galaxies and first stars, is that at lower temperatures atomic cooling is completely inefficient in metal-free gas. Instead, the gas can radiate its energy through molecules, whose contribution to the cooling function depends on the gas density. Even though molecular cooling has low rates in absolute terms, it can be very important since it peaks right at the drop of atomic hydrogen cooling.

A.2 Photoionisation and cosmic-ray heating

When an ionising background radiation field is present, the cosmic gas is heated by the mechanism of *photoionisation heating* (or photonheating).

A radiation field is considered ionising when its photons have sufficient energy to remove electrons from the atoms comprising the gas. For instance, hydrogen's binding energy is 13.6 eV, so it needs photons in the fuv or higher energy ranges to be ionised.

During the ionisation process, the gas experiences heating as free electrons absorb energy $\Delta E = h\nu - \chi$, where $h\nu$ represents the energy of an ionising photon and χ stands for the ionisation energy. This acquired energy is transformed into kinetic energy among the free electrons and subsequently transferred to other particles through collisions. Furthermore, photoionisation inhibits radiative cooling processes that involve bound electrons.

For photoheating to be effective, a reservoir of neutral atoms to ionise must be present. For example, the photoionisation of hydrogen is important only for $T < 10^5$ K; however, when present the effect is important since the peak of hydrogen cooling function can get strongly suppressed. In the context of galaxy formation, the most relevant ionising radiation stems from the extragalactic UV-background radiation, originating from massive stars and QSOs. The intensity of this radiation varies with redshift, intensifying as cosmic time progresses, starting from the reionisation era and reaching approximately $z \approx 2$. This aligns with the peak of cosmic SFRD and AGN emission before diminishing toward $z = 0$.

Moreover, cosmic rays, which are relativistic particles mainly composed of protons and electrons, generated by supernova remnants and AGNs, also contribute to heating. Even cosmic rays with relatively modest energies are effective at ionising atoms and dissociating molecules, thus injecting kinetic energy into the gas. This cosmic-ray heating holds particular significance for molecular clouds, which, due to their high densities, shield themselves from UV photons. Apart from the extragalactic UV background, gas within a galaxy is also subjected to photoionisation by internal sources within the same galaxy, including young massive stars and the AGN.

A.3 Compton Heating and Cooling

Other important cooling and heating processes in astrophysics are originated by Compton scattering. This mechanism is a quantum-mechanical process that involves the interaction between a photon and a free electron in the low-energy limit regime, in which quantum effects can be neglected ($h\nu \ll m_e c^2$).

In the context of thermal electrons within a population at temperature T and in the presence of background radiation, when the average energies of the photons significantly exceed the kinetic energies of the electrons ($h\nu \gg k_{\rm B}T$), energy transfers from the photons to the electrons. Through this phenomenon, known as *Compton heating*, the plasma can acquire energy through its interaction with the background radiation. This process, observed in the interstellar medium (ISM) and intergalactic medium (IGM), is thought to take place when there are X-ray and gamma-ray emissions originating from AGNs. In the opposite case in which the electrons' energies are much higher with respect to photons' energies ($h\nu \ll k_{\rm B}T$), energy is transferred from electrons to photons. This process is the *Compton cooling* or *inverse Compton scattering* and is important when hot gas interacts with low-energy photons from the CMB. This latter process is expected to impact the redshift evolution of the FIRRC, as discussed in Section 3.1.

A.4 Cooling and Infall

As mentioned in Section 1.3, cooling and infall are the main processes driving the galaxy formation and the set of the star-formation activity. The basic yet useful classical model of galaxy formation assumes that inside the DM halo, the infalling gas is heated to the virial temperature. Here I will overview the evolution of the gas at the viral temperature in DM halos.

Underlying early theories of galaxy formation (Binney 1977, Rees & Ostriker 1977, Silk 1977, White & Rees 1978b) there is the fact that the masses characterising galaxies are determined by different crucial timescales: the cooling time $t_{\rm cool}$, the Hubble time $t_{\rm H}$ and the dynamical time $t_{\rm dyn}$.

Assuming the most simple case of an isothermal gas distribution with average density n and temperature $T \approx T_{\rm vir}$ within a spherical virialised DM halo with mass $\mathcal{M}_{\rm vir}$ and radius $r_{\rm vir}$. The dynamical timescale is

$$t_{\rm dyn} \equiv \frac{1}{\sqrt{G\langle\rho\rangle}}, \tag{A.3}$$

where $\langle\rho\rangle = 3\mathcal{M}_{\rm vir}/(4\pi r_{\rm vir}^3)$ is the average halo mass density. In the assumption of $n = f_{\rm gas}\langle\rho\rangle/(\mu m_{\rm p}$, with $f_{\rm gas} \approx 0.16$ the universal fraction of baryons, the latter equation becomes:

$$t_{\rm dyn}(n) = \sqrt{\frac{f_{\rm gas}}{G\mu m_{\rm p} n}}. \tag{A.4}$$

Focusing on the cooling and dynamical time, in the case in which $t_{\rm cool} \ll t_{\rm dyn}$ the gas will cool, losing the support of the pressure and collapsing on timescales $\sim t_{\rm dyn}$. As a result of this catastrophic cooling, conditions conducive to star formation will emerge. In the opposite case in which $t_{\rm cool} \gg t_{\rm dyn}$ the gas will remain hot and in equilibrium in the potential well of the halo.

From these considerations, the discriminant threshold predicting whether or not the halo will form a galaxy is defined by $t_{\rm dyn} \approx t_{\rm cool}$.

Introducing now the Hubble time $t_{\rm H} \approx {\rm H}^{-1}$, the condition which permits the halo to virialise is $t_{\rm dyn} < t_{\rm H}$. Three possible regimes may occur:

- $t_{\rm cool} > t_{\rm H}$ (no cooling): the star formation is not triggered since the gas can not cool.
- $t_{\rm dyn} < t_{\rm cool} < t_{\rm H}$ (slow cooling): cooling becomes important on relatively long timescales yet shorter than the system age.
- $t_{\rm cool} < t_{\rm dyn}$ (rapid cooling): the cooling is efficient and the galaxy can form rapidly.

The average gas number density within halos having an overdensity of Δ_c and an average mass density of $\langle \rho \rangle = \Delta_c \rho_{\rm crit}$ is

$$n = f_{\rm gas} \frac{\Delta_c \rho_{\rm crit}(z)}{\mu m_{rmp}} = \frac{3\Delta_c f_{\rm gas}}{8\pi G \mu m_{\rm p}} H^2(z), \tag{A.5}$$

where $H(z)$ is defined from the Friedmann equation for a flat ΛCDM model. The number density of the gas (n) increases with the redshift, favouring galaxy formation inside halos with intermediate temperatures ($10^4 < T_{\rm vir} < 10^6$) and disfavouring the cases in which $T_{\rm vir} > 10^6$ K and $T_{\rm vir} < 10^4$. It should be also noted that higher metallicity favours cooling, therefore the range of virial temperatures allowed is actually larger.

The typical values of temperature and density are obtained from the loci of constant redshift and $\mathcal{M}_{\rm vir}$, inferred assuming $T \approx T_{\rm vir}$ and deleting $\Delta_c H^2$:

$$n = \frac{6k_{\rm B}^3}{\pi G^3 m_{\rm p}^4} \frac{f_{\rm gas} T^3}{\mu^4 \mathcal{M}_{\rm vir}^2}. \tag{A.6}$$

Summarising, the efficient galaxy formation is expected to occur in the range of halo masses $10^9 {\rm M}_\odot < \mathcal{M}_{\rm vir} < 10^{13} {\rm M}_\odot$. This is consistent with the typical value of stellar mass found in the most massive galaxies ($\mathcal{M}_\star \sim 10^{12}$ M$_\odot$). The model's predictions align with observations in higher-mass halos, indicating that the gas remains at high temperatures and lacks efficient star formation. This outcome corresponds to the regime of groups and clusters of galaxies, where favourable conditions for galaxy formation are lacking. Conversely, halos with masses below 10^9 M$_\odot$ are not anticipated to undergo efficient star formation.

A.4.1 Hot and Cold Accretion Modes

The model described previously in this Section does not accurately reflect the actual accretion dynamics of dark matter halos. This is because heating and cooling processes operate concurrently, and it is not always the case that the gas is heated to $T_{\rm vir}$ before cooling.

Both analytical calculations and numerical hydrodynamic simulations suggest that two distinct gas accretion modes are likely to take place. In the *hot mode*, the gas experiences shock heating up to the virial temperature, while in the *cold mode*, the gas remains cold as it reaches the halo's centre.

In practical terms, these two regimes are due to the occurrence of virial shocks exclusively in halos surpassing a certain mass threshold, denoted as $\mathcal{M}_{\rm sh}$. This critical mass remains relatively constant across different redshifts, typically around $\sim 10^{12}$ $\rm M_\odot$. $\mathcal{M}_{\rm sh}$ mainly depends on metallicity, reaching higher values for higher Z, given the major effectiveness of cooling. Another dependence is the shock-to-virial radius $r_{\rm sh}/r_{\rm vir}$, which according to numerical simulations can be as low as ≈ 0.1, even though major uncertainties remain.

The dependence of $\mathcal{M}_{\rm vir}$ on redshift is slight, spanning the range of $5-7\times10^{11}$ $\rm M_\odot$ for $0 \leq z \leq 5$, as shown in Figure A.2. For halos with $\mathcal{M}_{\rm vir} < \mathcal{M}_{\rm sh}$ at all redshifts, the gas infall doesn't result in shock heating, leading to the cold mode of accretion where the gas reaches the halo centre without being heated to $T_{\rm vir}$. Virial shocks are expected for halo masses surpassing the critical mass, indicating that the hot mode would be dominant based on simplistic isolated halo models. However, accretion is not spherically symmetric, and even in halos where $\mathcal{M}_{\rm vir} > \mathcal{M}_{\rm sh}$, cold gas streams can penetrate the centre due to their effectiveness along filament directions with shorter cooling times and higher density.

Cosmological hydrodynamic simulations support the idea that when $\mathcal{M}_{\rm vir}$ surpasses $\mathcal{M}_{\rm sh}$, virial shocks tend to occur at lower redshifts ($z < 1.5$). This is because higher-redshift gas can directly penetrate the halo centre as cold flows through filaments or streams, bypassing significant heating. Shocks are less effective along filament directions due to their elevated density and shorter cooling times.

Although the discussed aspects remain topics of debate, they possess minor significance at high redshifts when galaxy formation is driven by swift cooling. Whether the gas experiences shock heating and rapid cooling or enters cold mode, these details become inconsequential. Ultimately, the gas will descend toward the halo centre within the timescale $t_{\rm dyn}$.

After describing the processes guiding the gas infall and cooling into DM halo, the following sections will focus on the subsequent star formation process.

Star formation is the crucial process wherein gas transforms into stars, marking a significant stage in the formation and evolution of a galaxy, ultimately shaping its stellar component.

Key to star formation is cold ($T \lesssim 30$ K) and highly dense ($n \gtrsim 10^2$ $\rm cm^{-3}$) gas. To achieve these conditions, gas must initially form molecules, enabling highly efficient cooling to lower temperatures. Notably, cooling through CO rotational transitions is one effective mechanism. Subsequently, the gas progresses to the formation of molecular clouds with intricate and fractal internal structures.

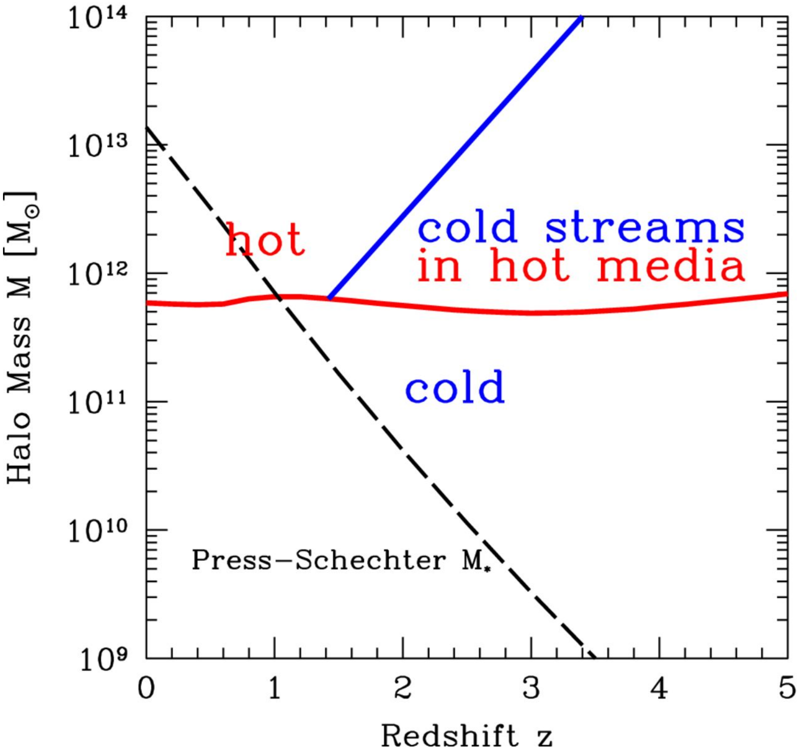

Figure A.2: Halo mass as a function of redshift. The values of $\mathcal{M}$sh are based on models of isolated spherically symmetric halos, assuming mean present-day metallicity and $r_{\rm sh} = 0.1 r_{\rm vir}$ and $Z = 0.1 Z_\odot$. Figure credits: Dekel et al. (2013).

In the densest regions of these clouds where gravity prevails over competing forces, conditions for gravitational collapse arise. Here, the gas undergoes the transformation into stars.

The phenomenon of star formation is remarkably intricate, involving a diverse array of physical and chemical processes that span an extensive range of scales, from galaxy size (tens of kpc) down to star size. Despite advancements, certain aspects of star formation remain enigmatic, especially at higher redshifts, where the individual star-forming regions cannot be resolved. In this thesis (see e.g. Chapter 4) I have highlighted how strong gravitational lensing can overcome this issue, revealing the observations of compact high-redshift galaxies down to sub-kpc scales.

A.5 Molecules Formation

Star formation commonly takes place within GMCs, which are observed in both the Milky Way and nearby star-forming galaxies. These GMCs typically possess masses around $\sim 10^{5-6}$ M$_\odot$ and encompass a hierarchical arrangement of diminishing structures, ultimately leading to dense cores where direct observations of star formation take place. In this thesis, I have discussed how molecules such as CO and water are important tracers of the star formation activity and of the energy budget of molecular clouds (see e.g. Section 4.6). The formation of molecules is the first crucial step required to trigger star formation within the ISM.

Radiative cooling is particularly efficient inside molecular clouds with respect to the more diffused ISM. The time evolution of the number density $n(M)$ of certain molecule M forming from two atoms or molecules A and B is expressed as

$$\frac{\mathrm{d}n(M)}{dt} = k_{\mathrm{f}}n(A)n(B) - n(M)\left[\beta + k_{\mathrm{d}}n(X)\right], \tag{A.7}$$

where $n(X)$ is the photon number density, k_f and k_d are formation and destruction coefficients of M respectively, and β is the molecule's photodissociation rate. Often the equilibrium condition is assumed to obtain a rough estimate of $n(M)$, under this assumption, the molecule formation and destruction processes are balanced, and Equation A.5 is equal to zero.

The molecular hydrogen H_2 is one of the most important components of molecular clouds. This molecule forms at $T < 40$ K and column densities $N_{\mathrm{H}} > 10^{21}$ cm^{-2}. In the complex ISM conditions of galaxies, the formation of this molecule occurs on the surface of *dust grains*. In brief, in the *adsorption* process hydrogen atoms collide with dust grains and stick to the surface of the grain. The H atom then can move on the grain's surface and likely can encounter another H atom, forming the H_2 molecule. The energy released during this event is absorbed by the dust grain and the H_2 molecule can escape from its surface through the so-called *desorption* process. The probability of the H atom to stick to the grain's surface, and therefore the rate of H_2 formation, depends on several factors, such as the atoms and grains density, the grain's cross-section, and the thermal speed of the atoms. Depending on the dust temperature, this probability diminishes for warmer dust. Additionally, dust grains can provide shielding against UV photodissociation for newly formed molecules.

A.6 Feedback

In Section 1.2.2 I have discussed how stellar and AGN feedback processes are pivotal in shaping the evolution in size of ETG progenitors, and their importance on regulating/quenching the star formation. In the following, I outline the main effects of astrophysical objects, such as stars and AGNs, in impacting the galaxy's evolution.

A.6.1 Feedback Processes from Stars

Stellar (or supernova) feedback arises when young and massive stars' winds or supernova explosions inject significant amounts of kinetic and thermal energy into the surrounding ISM. This phenomenon has dual effects: it can expel gas from the ISM and diminish or control the SFR (negative feedback), while also potentially compressing local gas and augmenting the star formation rate (positive feedback).

In particular, SN explosions affect the ISM rapidly producing large quantities of gas ejection moving at elevated speeds ($v_{\mathrm{ej}} \sim 10^3 - 10^4$ km s^{-1}). Type II SNe ejects the gas located on the outskirts of massive stars, which can constitute an important fraction of the initial mass of the star.

The ejected material moves at highly supersonic velocities, rapidly producing shocks in a few hundred years. The shock expansion consequently generates an approximately spherical shell of shocked ISM gas called *supernova remnant* (SNR), in which the equipartition between internal and kinetic energies is reached.

In its early phases, the shell evolves without radiative losses, conserving the total energy released by the SN explosion ($E_{\rm SN}$).

The radius and speed shell evolution are defined as:

$$r_{\rm sh} \simeq 14.1 \left(\frac{E_{\rm SN}}{10^{51}{\rm erg}}\right)^{1/5} \left(\frac{\mu n_0}{1~{\rm cm}^{-3}}\right)^{-1/5} \left(\frac{t}{10^4{\rm yr}}\right)^{2/5} {\rm pc} \tag{A.8}$$

$$v_{\rm sh} \simeq 552.9 \left(\frac{E_{\rm SN}}{10^{51}{\rm erg}}\right)^{1/5} \left(\frac{\mu n_0}{1~{\rm cm}^{-3}}\right)^{-1/5} \left(\frac{t}{10^4{\rm yr}}\right)^{-3/5} {\rm km~s}^{-1}, \tag{A.9}$$

known as *Sedov solution* (Sedov 1959) for a blastwave evolution in the ISM (with average density n_0), valid for $t > 100$ yr. Both solutions marginally depend on both the SN energy and ISM average density, implying that initial conditions do not strongly impact the normalisations. The adiabatic phase of a SNR lasts until the shock decelerates and radiative losses become significant, reducing the shell's temperature and causing the cooling time to match the system's age. Subsequently, in the radiative phase, a notable amount of energy is lost, and the shell's evolution can be described (using the principle of momentum conservation) as

$$\begin{aligned} r_{\rm sh} &\simeq 36.0 \left(\frac{E_{\rm SN}}{10^{51}{\rm erg}}\right)^{1/5} \left(\frac{\mu n_0}{1~{\rm cm}^{-3}}\right)^{-1/5} \left(\frac{t}{10^5{\rm yr}}\right)^{1/4} {\rm pc} \\ v_{\rm sh} &\simeq 88.0 \left(\frac{E_{\rm SN}}{10^{51}{\rm erg}}\right)^{1/5} \left(\frac{\mu n_0}{1~{\rm cm}^{-3}}\right)^{-1/5} \left(\frac{t}{10^5{\rm yr}}\right)^{-3/4} {\rm km~s}^{-1}. \end{aligned} \tag{A.10}$$

The above equations are referred to as *snowplough* solution, where the SNR experiences deceleration primarily due to the accumulation of ISM mass within the shell. Follows that the majority of the captured mass resides within the shell, with only a negligible mass gain within the bubble's interior.

The radiative phase ceases approximately at times $t_{\rm r} \approx 2 \times 10^6$ yr, when the shell velocity is approximately similar to the typical velocity of ISM random motions, corresponding to $\sigma \sim 10\,{\rm km\,s}^{-1}$. At this time, the SNR loses coherence, dispersing and releasing its residual kinetic energy to the ISM, which strongly impacts feeding turbulence. Most of the energy released during SN explosion is radiated in X-ray and UV/optical regimes via thermal emission, in addition to a synchrotron non-thermal emission.

The second feedback mechanism originated by stars involves stellar winds. Winds originate from radiation pressure during the evolution of massive O/B stars, impacting ions in the outermost regions of the stellar atmosphere. Consequently, the star loses a significant amount of mass. The *mechanical luminosity* is the wind's kinetic energy per unit of time and can be expressed as

$$L_{\mathrm{w}} \equiv \frac{1}{2}\dot{\mathcal{M}}_{\mathrm{w}} v_{\mathrm{w}}^{2} \simeq 1.3 \times 10^{36} \left(\frac{\dot{\mathcal{M}}_{\mathrm{w}}}{10^{-6} \mathcal{M}_{\odot} \mathrm{yr}^{-1}} \right) \left(\frac{v_{\mathrm{w}}}{2 \times 10^{3}\ \mathrm{km\ s}^{-1}} \right)^{2} \mathrm{ergs}^{-1}, \tag{A.11}$$

where $\dot{\mathcal{M}}_{\mathrm{w}}$ and v_{w} are respectively the wind mass outflow rate and velocity, and L_{w} can be considered approximately constant during the wind phase.

As a consequence of stellar winds, a bubble is generated, expanding into the ISM. As for SNR, also winds generate shocks when interacting with the ISM, however, in this case, the wind particles propagate as a continuous and fast flow from the central star. The flow impacts the shock material, forming a second *reverse* shock, which propagates through the wind perturbing it. Eventually, the freely expanding wind, the bubble of shocked wind, and the ISM shocked shell reach an equilibrium configuration. The velocity propagation of the two shocks is much lower than the wind flow's speed (v_{w}), for this reason, it is possible to estimate the thermodynamic state of the wind bubble. From the free wind's reference frame, the first shock would move toward the wind at a velocity $\sim v_{\mathrm{w}}$, producing a shock inside the wind, and creating a high-temperature bubble ($T \sim 10^{7}$ K). In this regime of temperature, cooling time is very long, therefore such a bubble can evolve nearly adiabatically. Conversely, the shocked ISM shell is perturbed by the second shock radiating away a significant fraction of its energy. The final system will be then composed of an adiabatic bubble and a radiative shell. The velocity and radius of the shell are defined as:

$$\begin{aligned} r_{\mathrm{sh}} &\simeq 7.0 \left(\frac{L_{\mathrm{w}}}{10^{36} \mathrm{ergs}^{-1}} \right)^{1/5} \left(\frac{\mu n_{0}}{1\ \mathrm{cm}^{-3}} \right)^{-1/5} \left(\frac{t}{10^{5} \mathrm{yr}} \right)^{3/5} \mathrm{pc} \\ v_{\mathrm{sh}} &\simeq 41.3 \left(\frac{L_{\mathrm{w}}}{10^{36} \mathrm{ergs}^{-1}} \right)^{1/5} \left(\frac{\mu n_{0}}{1\ \mathrm{cm}^{-3}} \right)^{-1/5} \left(\frac{t}{10^{5} \mathrm{yr}} \right)^{-2/5} \mathrm{km\ s}^{-1}. \end{aligned} \tag{A.12}$$

In conclusion, when a constant source of kinetic energy is present, in this case, stellar winds, the radius of the shell grows faster in time with respect to an instantaneous energy release such as the case of SN explosion, therefore the shell decelerates at a slower rate in a wind bubble than in an SNR.

Approximately half of the wind's total energy is channelled into the wind bubble's internal energy, while the remaining portion contributes to the shell's energy, distributed between kinetic and internal components. Around 20% of the wind's total energy is directed towards propelling the shell's expansion, and as the expansion concludes ($v \approx \sigma_{\mathrm{gas}}$), this energy will be conveyed to the ISM. Consequently, a stellar wind could potentially be more effective than a SNR in transmitting kinetic energy to the ISM.

Finally, the last stellar feedback mechanism involves *superbubbles and galactic winds*. Young star clusters, located within giant molecular clouds and referred to as O/B associations, host a significant number of O and B stars. When these stars are almost coeval, one can predict the simultaneous emission of robust stellar winds from approximately 100 stars within a confined spatial area. The collective effect of these emissions leads to the formation of a substantial bubble encompassing the entire stellar association, commonly known as a *superbubble*.

Given that superbubbles are re-scaled versions of single-star bubbles, they can be treated with the same formalism.

Around 1 Myr later, the most massive stars within the O/B associations interrupt the wind production and undergo SNe explosions, leading to both the heating of the bubble and the expansion of the shell. With the passage of time, an increasing number of stars experience SN explosions, resulting in the supershell becoming predominantly SN-driven. A rough estimation of the energy input can be derived by considering the main-sequence lifetime of an 8 $M_\odot$ star as the timescale for this phase, which amounts to approximately 30 Myr. Consequently, the average mechanical luminosity generated by SNe is

$$L_{\rm SN} \approx \frac{N_{\rm SN} E_{\rm SN}}{\tau_{\rm MS}\,(8\mathcal{M}_\odot)} \approx 10^{38} \left(\frac{N_{\rm SN}}{100}\right) \left(\frac{E_{\rm SN}}{10^{51}{\rm erg}}\right) {\rm ergs}^{-1}, \tag{A.13}$$

where $N_{\rm SN}$ is the number of SNe. The energy input per unit of time provided by SN is therefore similar to that of stellar winds. One has

$$r_{\rm sh} \approx 70 \left(\frac{N_{\rm SN}}{100}\right)^{1/5} \left(\frac{E_{\rm SN}}{10^{51}{\rm erg}}\right)^{1/5} \left(\frac{\mu n_0}{1\ {\rm cm}^{-3}}\right)^{-1/5} \left(\frac{t}{10^6{\rm yr}}\right)^{3/5} {\rm pc} \tag{A.14}$$

$$v_{\rm sh} \approx 41 \left(\frac{N_{\rm SN}}{100}\right)^{1/5} \left(\frac{E_{\rm SN}}{10^{51}{\rm erg}}\right)^{1/5} \left(\frac{\mu n_0}{1\ {\rm cm}^{-3}}\right)^{-1/5} \left(\frac{t}{10^6{\rm yr}}\right)^{-2/5} {\rm km\ s}^{-1} \tag{A.15}$$

It is worth highlighting that the phase of SN persists for roughly ten times the duration of the stellar wind phase, resulting in a larger energy input from SN within the superbubble due to comparable luminosities. Furthermore, the superbubble exhibits higher efficiency than individual SNRs in transmitting kinetic energy to the ISM. This advantage arises from the fact that supernovae exploding within a superbubble experience less resistance from the encompassing medium, which is comparatively less dense.

The power of a galactic wind can be linked to the global properties of a starburst galaxy, with a focus on its SFR. In particular, by multiplying the energy of a single SN by the rate of SNe, one can estimate the energy released per unit of time by a starburst galaxy. The supernova rate $R_{\rm SN}$ can be estimated from the number of stars having mass> 8 $M_\odot$. Given a Chabrier IMF,

$$R_{\rm SN} \approx 10^{-2} \left(\frac{\rm SFR}{\mathcal{M}_\odot {\rm yr}^{-1}}\right) {\rm yr}^{-1}. \tag{A.16}$$

Part of the SN energy can be injected into the galaxy ISM in the form of kinetic energy resulting in a galactic wind. The kinetic energy per unit of time available to drive the wind is

$$\dot{K} \approx 3 \times 10^{40} \left(\frac{\eta}{0.1}\right) \left(\frac{E_{\rm SN}}{10^{51}{\rm erg}}\right) \left(\frac{\rm SFR}{\mathcal{M}_\odot {\rm yr}^{-1}}\right) {\rm ergs}^{-1}, \tag{A.17}$$

with η being the efficiency in transferring energy to the wind. The kinetic power for a wind living in the galaxy, also called *energy-driven wind*, is $\dot{K} = \dot{\mathcal{M}}_{\rm out} v^2/2$, where $\dot{\mathcal{M}}_{\rm out}$ is the mass outflow rate, defined as

$$\dot{\mathcal{M}}_{\rm out\,,ED} \approx 1 \left(\frac{\eta}{0.1}\right) \left(\frac{\rm SFR}{\mathcal{M}_\odot {\rm yr}^{-1}}\right) \left(\frac{v_{\rm out}}{300\ {\rm km\ s}^{-1}}\right)^{-2} \mathcal{M}_\odot {\rm yr}^{-1}, \tag{A.18}$$

having $E_{\rm SN} = 10^{51}$ erg. The *mass loading factor* is the ratio between the mass outflow rate and the SFR of a galaxy and is expressed as

$$\beta \equiv \frac{\dot{\mathcal{M}}_{\rm out}}{\rm SFR}. \tag{A.19}$$

Energy-driven winds face a challenge: in order to achieve fast outflows, low outflow rates and correspondingly small values of β ($\beta \ll 1$) are required. To enable faster outflows with larger β, the concept of momentum-driven winds has been introduced. This approach posits that gas acquires momentum from the SFR at a rate $\sim {\rm SFR} \times v_{\rm out}$. This momentum transfer can occur through radiation pressure from massive stars onto dust grains, which then drag the remaining gas along (with the prerequisite that the ISM is optically thick). The mass outflow rate in a momentum-driven wind can be described by

$$\dot{\mathcal{M}}_{\rm out\,,MD} \approx 1 \left(\frac{\rm SFR}{\mathcal{M}_\odot {\rm yr}^{-1}}\right) \left(\frac{v_{\rm out}}{300\ {\rm km\ s}^{-1}}\right)^{-1} \mathcal{M}_\odot {\rm yr}^{-1} \tag{A.20}$$

which shows a milder dependence on the wind speed, and so could be more efficient than an energy-driven wind at fast speeds.

A.6.2 Feedback from AGNs

Gas located in a galaxy's central regions has a dual interaction with the SMBH hosted within it. On one hand, the gas is drawn in for accretion, fueling the AGN; on the other hand, the emissions and outflows from the AGN can influence the surrounding gas. This dynamic interaction is referred to as "AGN feedback". Since the mass difference between SMBH and its host bulge is of about three orders of magnitude, the quantity of gas which undergoes falls inside the SMBH is negligible in terms of the total energy, mass, and momentum budget of the host galaxy. Despite this, the feedback mechanism originating from AGNs has a considerable impact and significantly affects the evolution of the host galaxy. When these mechanisms suppress star formation through heating or cold gas expulsion from the galaxy's core, the feedback is negative. Conversely, positive feedback occurs when the star formation is enhanced, for example in the case in which the gas compression initiates the collapse of molecular clouds. Notably, AGN feedback encompasses various spatial scales. Indeed it links processes taking place at scales roughly corresponding to the Schwarzschild radius

$$r_\bullet \equiv \frac{2G\mathcal{M}_\bullet}{c^2} \simeq 9.57 \times 10^{-6} \left(\frac{\mathcal{M}_\bullet}{10^8 \mathcal{M}_\odot}\right) {\rm pc} \tag{A.21}$$

as well as additional mechanisms occurring within the characteristic scales of the host galaxies, groups, and clusters, spanning from a few kiloparsecs to several hundred kiloparsecs. In the above equation $\mathcal{M}_\bullet$ is the BH mass.

Even though AGN feedback is still a poorly understood mechanism, there are some fundamental properties useful to investigate its impact on galaxy evolution. AGN feedback is thought to manifest in two primary forms: *radiative feedback*, which is facilitated by photons, and *mechanical or kinetic feedback*, which is mediated through the expulsion of gas particles.

AGN's accretion rates can face high or low accretion rates, relative to the maximum accretion rate for a certain $\mathcal{M}_\bullet$.

A maximum luminosity resulting from the accretion of a pure hydrogen plasma onto a black hole in spherical symmetry can be defined. This is called *Eddington Luminosity*, defined as

$$L_{\mathrm{Edd}} \equiv \frac{4\pi c G m_{\mathrm{p}} \mathcal{M}_\bullet}{\sigma_{\mathrm{T}}} \simeq 1.26 \times 10^{46} \left(\frac{\mathcal{M}_\bullet}{10^8 \mathcal{M}_\odot} \right) \mathrm{erg s}^{-1}, \tag{A.22}$$

where σ_{T} is the Thomson cross section.
When $L = L_{\mathrm{Edd}}$, the radiation pressure force equals the gravitational force. Defining ϵ_{rad} as the radiative efficiency of the AGN, the *Eddington mass accretion rate* is

$$\dot{\mathcal{M}}_{\mathrm{Edd}} \equiv \frac{L_{\mathrm{Edd}}}{\epsilon_{\mathrm{rad}} c^2}. \tag{A.23}$$

$\dot{\mathcal{M}}_{\mathrm{Edd}}$, therefore, defines the maximum accretion rate for a black hole of mass $\mathcal{M}_\bullet$.

While the observed luminosity of AGNs is often below the Eddington limit, it is possible to have super-Eddington luminosities and mass accretion rates surpassing the Eddington rate if accretion is not spherically symmetric. The assumption of spherical symmetry amplifies the impact of radiation pressure. A scenario for super-Eddington accretion can arise when the accreting gas is distributed within a thin accretion disc.

The potential impact of AGN feedback on galaxy evolution can be summarised as follows: during its growth, a supermassive black hole with mass $\mathcal{M}_\bullet$ releases energy $E_\bullet = \langle \epsilon_{\mathrm{rad}} \rangle \mathcal{M}_\bullet c^2$. If the black hole resides in a galaxy with a bulge mass $\mathcal{M}_\star$ and velocity dispersion σ, the binding energy of the bulge is approximately $E_\star \approx \mathcal{M}_\star \sigma^2$. This provides a simple way to quantify the potential effects of AGN feedback. The energy released by the SMBH can largely exceed the binding energy of the host bulge, as indicated by the ratio between these two energies, which is expressed as follows:

$$\frac{E_\bullet}{E_\star} \approx \frac{\langle \epsilon_{\mathrm{rad}} \rangle \mathcal{M}_\bullet c^2}{\mathcal{M}_\star \sigma^2} \simeq 100 \left(\frac{\langle \epsilon_{\mathrm{rad}} \rangle}{0.1} \right) \left(\frac{\sigma}{300 \mathrm{~km~s}^{-1}} \right)^{-2} \left(\frac{\mathcal{M}_\bullet / \mathcal{M}_\star}{0.001} \right) \tag{A.24}$$

It is also useful to define the *Eddington Ratio* for a black hole with a given luminosity and mass accretion rate:

$$f_{\mathrm{Edd}} \equiv L / L_{\mathrm{Edd}} = \dot{\mathcal{M}}_{\mathrm{acc}} / \dot{\mathcal{M}}_{\mathrm{Edd}}. \tag{A.25}$$

Quasars are typically characterised by high $f_{\rm Edd}$ values, while radio galaxies exhibit low $f_{\rm Edd}$ values. As a result, the high and low accretion rate modes are commonly denoted as the *quasar mode* and *radio mode* feedback, respectively.

- The quasar mode feedback occurs when a supermassive black hole is accreting gas at a high rate and emitting a significant amount of energy as photons. This mode is characterised by a radiative luminosity comparable to $L_{\rm Edd}$ with $0.01 < f_{\rm Edd} < 1$, where both radiative and mechanical feedback is relevant. However, due to the high luminosity, radiative feedback tends to dominate. The presence of a relatively small accretion disc (approximately $10 - 100$ times the Schwarzschild radius) around the black hole results in limited electromagnetic emission. The energy emitted in radiation is

  $$E = \epsilon_{\rm rad}\mathcal{M}_{\rm acc}c^2, \tag{A.26}$$

  with $\epsilon \approx 0.1$ being the radiative efficiency. High-energy X-ray photons dominate the process of photoionisation heating, wherein photons can transfer energy to the gas, resulting in temperatures around 10^7 K.

  Photons can give rise to other feedback mechanisms, such as *AGN winds*. These emitted photons transfer their momentum to the surrounding gaseous medium, potentially driving an AGN wind.

  During the QSO mode phase, both radiative and mechanical feedback are significant factors, even if radiative feedback dominates. The AGN wind plays an important role with roughly half the mass accreted while the other half is ejected. In this phase, the AGN self-regulates through a cycle of powerful outbursts and quiescent periods, effectively heating and displacing cold, dense gas from the central galaxy regions, thus halting AGN fueling. The duty cycle, which is the fraction of time spent in an outburst, is relatively small at low redshifts, around $10^{-2} - 10^{-1}$, but can be more significant at high redshifts, lasting for hundreds of millions of years with a duty cycle exceeding 10^{-1}, thereby suppressing star formation in the host galaxy.

- Radio mode feedback operates in massive elliptical galaxies situated at the centres of groups and clusters. In this scenario, the BH is accreting at rates much lower than the Eddington limit, typically with $f_{\rm Edd} < 0.01$, from a surrounding environment primarily composed of hot gas at temperatures around $10^6 - 10^7$ K. While radiative feedback is minimal, mechanical power is significant due to the presence of powerful jets and radio lobes containing relativistic plasma. These jets create cavities or bubbles within the surrounding medium, where the relativistic plasma is confined by the pressure of the ambient gas.

  When the bubble is sufficiently distant from the centre the mechanical energy responsible for inflating the bubble is entirely transferred to the gas. The efficiency of energy transfer during AGN feedback is highest when the AGN is positioned at the core of a group or cluster, where the surrounding medium is denser. In this scenario, the potential well enhances energy transfer. In contrast, the efficiency is lower for isolated galaxies in a less dense medium, as jets can more easily propagate away from the core.

Radio mode feedback is characterised by intermittent production of jets, with a duty cycle of around $10^{-}3$ to $10^{-}2$. This leads to the formation of successive generations of radio lobes and cavities.

A.7 Galaxy Merging

Finally, in this Section, I describe the main physical processes involved in galaxy merging. As discussed in Section 1.3, dry merger events play an important role the late slow size and kinematic evolution of a massive ETG progenitor.

Merging is a phenomenon where two or more galaxies interact, resulting in the creation of a single new galaxy. The outcome of such an encounter is determined by factors such as orbital characteristics and the internal conditions of the galaxies involved. High-speed encounters are termed *gravitational flybys*, resulting in temporary perturbations and typically no merging. Conversely, low-speed encounters lead to galaxy mergers, where interacting galaxies combine to form a new entity within a relatively short time. Flybys play a minor role in galaxy evolution, however, they can have a significant role in the evolution of galaxy structures in galaxy clusters.

Mergers can take the form of binary interactions involving two galaxies or become more complex as multiple galaxies are involved. They can be categorised as *dissipationless* (dry) if the participating galaxies lack gas, or as *dissipative* (wet) mergers if gas is present. In cases where stars and dark matter are involved, the primary process is collisionless relaxation. However, if gas is present, additional mechanisms such as compressions, shock heating, and radiative cooling can also come into play.

Merging involves interactions among stars, dark matter, and gas. When considering the stellar component's evolution, the low stellar density prevents star-physical collisions, and both the stellar and dark matter components behave in a collisionless manner. In merging systems composed solely of stars and dark matter, collisionless relaxation drives their evolution. The behaviour of gas in merging is more intricate due to its dissipative and collisional nature. The merging process can lead to gas compression, shock heating, and radiative energy dissipation and, in some cases, conditions may allow gas to fragment and form stars. Numerical simulations combining N-body dynamics and hydrodynamics are therefore crucial for accurately describing the merging effects and predicting the properties of the resulting merger remnant, given the initial characteristics of the interacting galaxies and their encounter.

A galaxy merger begins with non-equilibrium initial conditions and progresses toward a state of equilibrium. The processes that lead to this eventual equilibrium are referred to as relaxation processes.

Collisionless systems, like galaxies, can attain virial equilibrium in a relatively brief period through collisionless relaxation. This involves two central processes: *violent relaxation*, which redistributes orbital energies in response to a rapidly changing gravitational field, and *phase mixing*, which disperses particle orbits in phase space. Working together, these mechanisms lead to the virialisation and development of the merger remnant within a timescale similar to the dynamic times of the merging galaxies.

For a minor merger scenario (when a satellite with mass M_{sat} is accreted by a much more massive host with mass $M_{\mathrm{host}} \gg M_{\mathrm{sat}}$), the process is driven by the dynamical friction. It is however important to note that major mergers cannot be adequately explained using the concept of dynamical friction, indeed when the masses involved in merging are similar, neither of them can be considered either host or satellite and the process is best described through phase mixing and violent relaxation.

When a satellite is in proximity to or embedded within a host galaxy, it experiences gravitational (tidal) forces that vary in intensity across its different regions. Consequently, the satellite can undergo a process called *tidal stripping*, wherein it sheds material. The extent of material loss is often determined by a tidal radius, representing the distance from the satellite's centre within which particles remain gravitationally bound. Outside this radius, particles become unbound and give rise to tidal tails, slender structures on both leading and trailing sides composed of the stripped material.

In scenarios where both the satellite and the host possess a gaseous component, *ram-pressure stripping* can play a role in depriving the satellite of its gas content. This phenomenon is particularly significant for galaxies with dominant bulges, characterised by a stellar velocity dispersion (σ) and an ISM density (ρ_{ISM}). The condition for ram pressure stripping is fulfilled when the ram pressure, represented by $\rho_{\mathrm{ISM}} v^2$, surpasses the gravitational force associated with the stellar velocity dispersion, $\rho_{\mathrm{ICM}} \sigma^2$. An example illustrating this process is observed in NGC4522, a galaxy situated within the extensive Virgo galaxy cluster (see Figure A.3).

The merging timescale (τ_{merg}) represents the duration between the initial close encounter and the eventual virialization of the resulting merger remnant. Within the context of specific internal properties of the galaxies involved, τ_{merg} becomes longer as both the orbital energy and angular momentum of the orbit increase.

Merging is more likely to occur in cases of elliptic/parabolic orbits and head-on encounters. Rapid merging is observed for low orbital energy ($E_{\mathrm{orb}} < 0$), as well as for orbits that are unbound, provided that the orbital angular momentum is also low. A general guideline is that galaxy merging is feasible if the relative velocity at the closest approach is approximately equal to or lower than the characteristic internal velocities (rotational or dispersion velocities) of the colliding galaxies. In equal mass parabolic mergers, $\tau_{\mathrm{merg}} \approx 10 t_{\mathrm{dyn}}$. For galaxies similar in size to the Milky Way, $t_{\mathrm{dyn}} \sim 10^8$ years, resulting in $\tau_{\mathrm{merg}} \sim 1$ Gyr. In the case of minor mergers, τ_{merg} is influenced by the dynamical friction timescale, which scales inversely with a parameter ζ, where $\zeta = M_{\mathrm{sat}}/M_{\mathrm{host}}$. From N-body simulations result that minor mergers can take place when $\zeta > 0.01$.

How are galaxies transformed by mergers? This question is non-trivial and can be addressed mostly for simple cases of merging through N-body simulations. Making quantitative predictions considering the gas presence is a challenging task

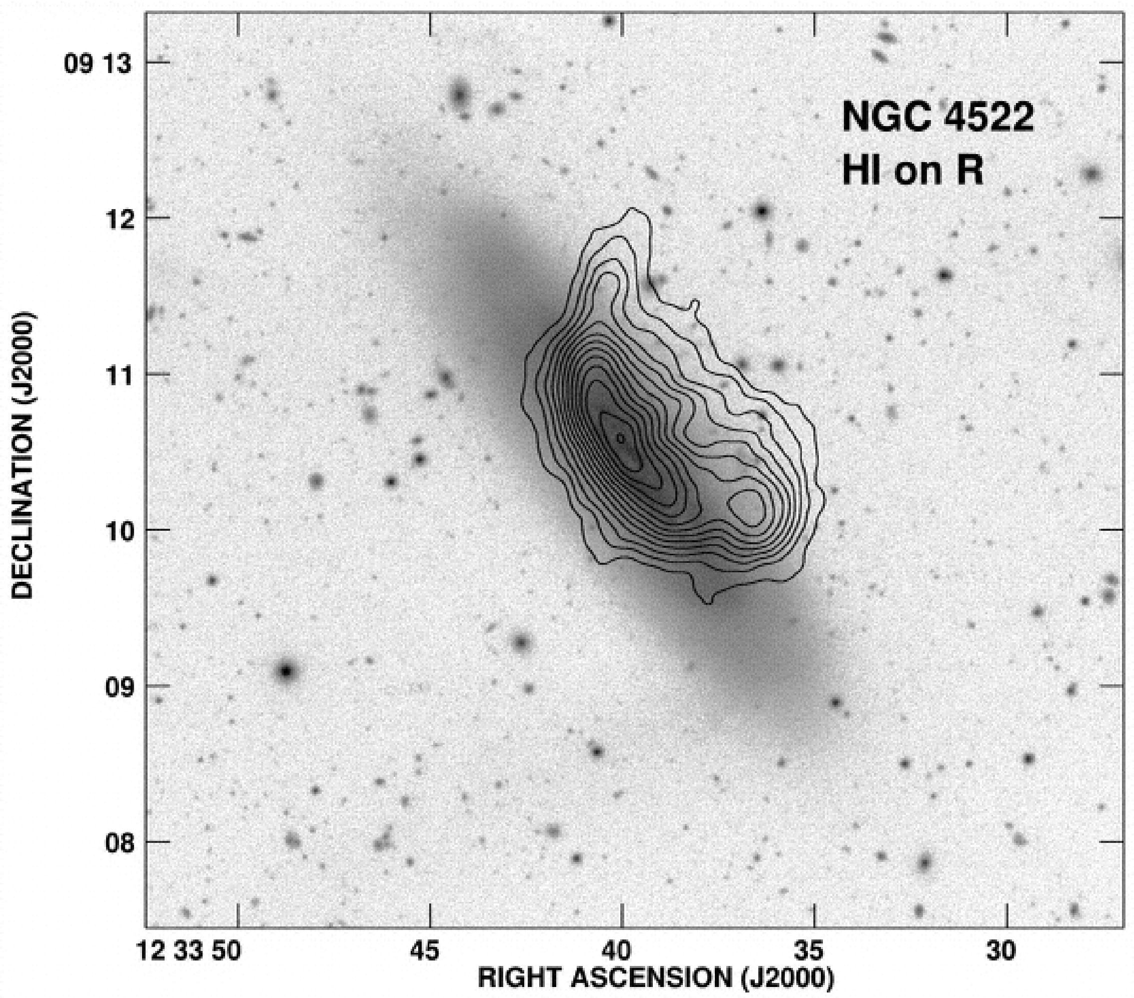

Figure A.3: The figure shows the R-band image and the 21 cm map of the gas (black contours) of the spiral galaxy NGC 4522 inside the Virgo cluster of galaxies. The distortion in the gas distribution can be traced back to the effect of the ram pressure. Image credits: Kenney et al. (2004).

even employing hydrodynamic simulations. This is due to the poor knowledge of the precise mechanisms regulating star formation and feedback from stars and AGN. Despite these complications, is it still possible to make some global analytic predictions.
For instance, in the simplest case involving gas-free (dry) mergers. These encounters happen between collisionless stellar systems made of stars and dark matter, such as two elliptical galaxies. In the absence of dissipation, the total energy remains constant. Ordered kinetic energy (associated with orbital energy) transforms into random kinetic energy, akin to an inelastic collision. Assuming no mass loss, the virial velocity dispersion of the merger remnant is

$$\sigma_{1+2}^2 = \frac{\mathcal{M}_1\sigma_1^2 + \mathcal{M}_2\sigma_2^2 - 2E_{\rm orb}}{\mathcal{M}_{1+2}}. \tag{A.27}$$

When two identical system merges, the final mass of the system is $2\mathcal{M}_1$ and the viral velocity dispersion is

$$\frac{\sigma_{1+2}^2}{\sigma_1^2} = 1 - \frac{E_{\rm orb}}{\mathcal{M}_1\sigma_1^2}, \tag{A.28}$$

hence, the gravitational radius $r_i = G\mathcal{M}_i/\sigma_i^2$ changes as

$$\frac{r_{1+2}}{r_1} = 2\left(1 - \frac{E_{\rm orb}}{\mathcal{M}_1\sigma_1^2}\right)^{-1}. \tag{A.29}$$

Dry mergers typically lead to systems with decreased density, resulting in larger remnant sizes and lower dispersions compared to the initial progenitors. However, the remnant's morphology can vary considerably; major mergers, for instance, often disrupt stellar disks, leading to a remnant characterised by a dominant spheroidal component.

On the other hand, in the context of wet mergers, the process is dissipative and total energy is not conserved. Due to this dissipation, gas accumulates at the remnant's centre, potentially leading to associated star formation and a deepening of the potential well. Consequently, the remnant becomes more concentrated, exhibiting a smaller size and higher dispersion compared to an equivalent dry merger. However, additional complexities arise as stellar and AGN feedback could be triggered, necessitating detailed hydrodynamic simulations for a thorough understanding of these effects.

A.8 The Initial Mass Function

The initial mass function (IMF) describes the distribution of masses for a population of newly formed stars in a stellar system. In other words, the IMF provides information about the number of stars that form with different masses. This quantity can be determined by counting single stars in young star clusters inside the Milky Way and measuring their masses. Even if uncertain, the results of this procedure suggest a certain similarity in the clusters observed in our Galaxy.

However, this approach cannot be extended to external galaxies, given that it is not possible to resolve single stars inside their clusters, with the exception of local systems such as the Large Magellanic Cloud. This constitutes a major problem in galaxy evolution, given that the IMF is likely to be not universal and may differ in environments denser than present-day galaxy discs.

The IMF is defined as $\phi(m)$, with m being the mass of the star in the unit of $\mathrm{M}_\odot$, and defines the number of stars with m and $m + \mathrm{d}m$. A classic description in the Salpeter IMF (Salpeter 1955), originally determined for masses in the range $m \sim 0.4 - 10$, and defined as

$$\mathrm{d}N = \phi(m)\mathrm{d}m = \phi_0 m^{-2.35}\mathrm{d}m, \tag{A.30}$$

where ϕ_0 is the normalization. Other forms of the IMF take into account that a deviation from a single power law has been observed.

In the SED-analysis performed in this thesis (see Section 4.4, and Appendix C and D) a Charbier IMF (Chabrier 2003) is assumed. This is formulated to describe the IMF across various environments within the Galaxy. For stars in the disc (normalised for $m = 1$) the IMF is

$$\phi(m) = \begin{cases} 3.58\frac{1}{m}\exp\left\{-1.050\left[\log\left(\frac{m}{0.079}\right)\right]^2\right\} & (m < 1), \\ m^{-2.3} & (m \geq 1), \end{cases} . \tag{A.31}$$

The Salpeter IMF is characterised as "bottom-heavy," emphasising its preference for generating a larger proportion of low-mass stars under 1 $\mathrm{M}_\odot$. The term "bottom" relates to the lower-mass star range, while "heavy" highlights the heightened mass concentration in this region. Conversely, an IMF favouring higher-mass stars (like the Chabrier IMF in comparison to the Salpeter IMF) is labelled as "top-heavy."

When observing a galaxy, whether by resolving individual stars or measuring its total stellar brightness, the dominance of intermediate and high-mass stars is evident. This is especially true in SFGs where young, massive, and highly luminous stars dominate. Despite this, a significant fraction of the galaxy's total mass resides in low-mass stars. Quantifying this quantity is not an easy task, given that it strongly depends on the chosen IMF. Consequently, adopting a specific IMF introduces systematic uncertainty into mass estimations. For example, using a Salpeter IMF leads to stellar mass calculations for a galaxy's optical/IR luminosity that is about 1.5 to 2 times greater than those derived from a Chabrier or Kroupa (2002) IMF.

A.9 Shaping the Theoretical Spectra of Evolving Galaxies

Galaxies emit light at different wavelengths according to the source originating the emission (stars, gas, dust). In the theory of galaxy formation, a critical aspect involves calculating the spectra that emerge from diverse types of galaxies as a function of their evolution over cosmic time. Theoretical spectra are particularly important in both numerical simulations and the physical interpretation of the properties emerging from observations, such as the continuum shape, colours, and emission/absorption lines. Simulated spectra are usually modelled including the components contributing to the SED: the stellar component, the ISM hot/warm/cold phases and dust, and an AGN component useful to determine the impact of high-energy sources on the spectrum.

In this Section, I will illustrate the basic theoretical ingredients required to model synthetic galaxy spectra which are also behind the SED-fitting codes exploited in this thesis (see Appendix C and D).

A.9.1 Stellar spectra

Due to resolution limitations, individual stars within galaxies can only be resolved within a range of a few Mpc from our own Galaxy. Consequently, the light observed from a distant galaxy represents the integrated output of radiation emitted by all its stars, rendering it unfeasible to deduce their individual characteristics and evolutionary paths.

An alternative method employs the concept of *stellar population synthesis* (SPS), wherein the spectra of stellar populations are predicted based on their properties and evolution over time.

The basic model is based on *simple stellar population* (SSP), which includes an ensemble of stars sharing the same age and metallicity. In this context, the monochromatic flux of an SSP with metallicity Z evolved from an initial time $t = 0$ to a given time t is

$$F_{\lambda,\mathrm{SSP}}(t, Z) = \int_{m_1}^{m_2} F_{\lambda,\,\mathrm{star}}(m, t, Z)\phi(m)\mathrm{d}m, \tag{A.32}$$

where the mass limits are $m_1 \approx 0.08$ and $m_2 \approx 100$, ϕ is the IMF, and $F_{\lambda,\,\mathrm{star}}(m, t, Z)$ is the flux of a single star with mass m, age t, and metallicity Z. In order to compute spectra from Equation A.9.1 the knowledge of isochrones, stellar spectral libraries, and IMF is required. A stellar spectral library is essential to translate quantities from stellar evolution calculations into spectra as a function of metallicity. Constructing such a library using observed spectra has limitations due to unobservable spectral regions, diverse spectrograph properties, and calibration differences. To overcome this, theoretical spectra based on detailed models of stellar atmospheres are sometimes employed for certain regions.

Additionally, an IMF must be chosen, which defines the distribution of stellar masses in the population. Often, a universal IMF, which remains constant across time and physical properties like SFR, is adopted along with a range of stellar masses.

All the above ingredients are also subjected to several uncertainties, for instance, the role of binary stars and pulsating AGB (TP-AGB) stars is still not completely understood.

The theoretical spectra of SSPs computed following Equation A.9.1, exhibit a significant dependence on the age of the galaxy. An example of computed

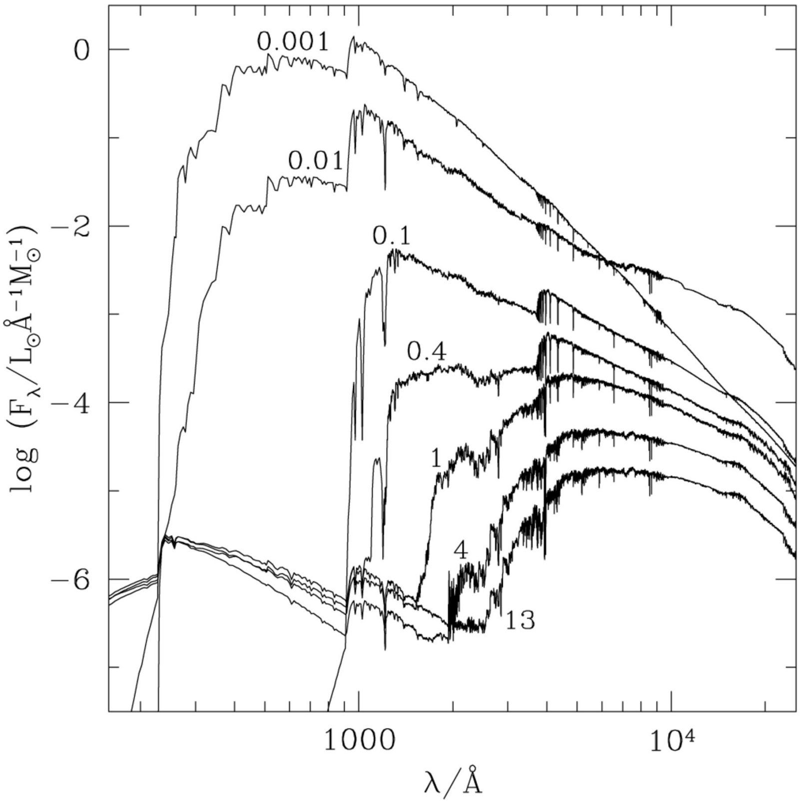

Figure A.4: Evolving SSP spectra obtained with SPS modelling with solar metallicity and Chabrier IMF. Ages are indicated next to the spectra in units of Gyr. Image credits: Bruzual & Charlot (2003).

synthetic spectra which is also used in D is shown in Figure A.4 (Bruzual & Charlot 2003). The impact of the galaxy age is visible from the suppression of the UV/optical light for increasing ages, as a consequence of the progressive disappearance of hot and massive stars.

The observed evolution of a SSP is also significantly contingent on the photometric filter employed for observation. Blue/UV filters are particularly responsive to the hottest stars, such as main sequence stars with ages less than 1 Gyr. Conversely, red/NIR filters are more influenced by the light emitted from cooler stars like low-mass main sequence stars, red giants, supergiants, and AGB stars. This results in a more rapid and distinct decrease in luminosity with short-wavelength filters. For instance, within a timespan from 10^7 to 10^9 years, the B-band luminosity of an SSP diminishes by two orders of magnitude, whereas it fades by 10 orders of magnitude in the K band.

The SSP evolution depends also on other relevant factors. One is the impact that the giant and supergiant phase stars have on the stellar spectrum of a galaxy. Indeed, when entering this phase of their evolution, stars dominate the overall radiation output in specific spectral ranges. For instance, TP-AGB stars momentarily enhance the NIR luminosity around ages of 0.5-1 Gyr and can contribute up to 50-70% of the total luminosity in the K band due to their positioning in the HR diagram characterised by high luminosity and low temperature. Second, the SSP evolution is strictly linked to its metallicity. Higher metal content leads to a decrease in luminosity in the blue and UV regions due to the increasing number and strength of metal absorptions, The result is the so-called blanketing effect, which shifts colours towards red (blanketing effect). Additionally, elevated metallicity results in higher opacity, leading to more energy absorption within stellar interiors. Consequently, red giants expand more, becoming cooler and redder. Therefore, the colour of an SSP can be reddened due to either its advanced age, higher metallicity, or both. Ultimately, the characteristics of an SSP are profoundly influenced by the IMF, which governs the balance between massive and low-mass stars, the stellar population's mass-to-light ratio, and the relative significance of type II SNe.

The major issue with the modelling based on SSPs is that these are based on the assumption of coeval stars, which is not a good representation of real stellar populations where stars form during an extended time interval.

A more sophisticated model relies on multiple SSP, called *composite stellar population* (CSP), thus a collection of stars formed at different times and with different chemical compositions.

Mathematically, a CSP is the sum of individual SSPs evolving as a function of time as

$$F_{\lambda,\mathrm{CSP}}(t) = \int_{t'=0}^{t'=t} \int_{Z=0}^{Z=Z_{\max}} \left[\mathrm{SFR}\,(t-t')\,\mathcal{P}\,(Z, t-t')\,F_{\lambda,\mathrm{SSP}}\,(t', Z)\right] \mathrm{d}t'\mathrm{d}Z, \quad \text{(A.33)}$$

where Z is the metallicity and $P(Z, t-t')$ is its distribution at time $t - t\prime$. SFR$(t-t')$ is the SFR at time $t-t'$, or the SFH. SFHs in galaxies are generally poorly constrained by observations, therefore computing the above equation requires the use of an analytic function describing SFR$(t - t')$. Usually, the SFR is assumed to be constant, exponentially declining, or exponentially delayed.

The contribution of the ISM must also be taken into account. Theoretical SEDs must include also the components involved in the emission and absorption of radiation. For example, the dust effects can be added to Equation A.9.1

$$\begin{aligned}F_{\lambda,\mathrm{CSP}}(t) = \int_{t'=0}^{t'=t}\int_{Z=0}^{Z_{\max}} &\Big[\mathrm{SFR}\,(t-t')\,\mathcal{P}\,(Z,t-t')\,F_{\lambda,\mathrm{SSP}}\,(t',Z)\,e^{-\tau_{\mathrm{d}}(t')} \\ &+AF_{\lambda,\mathrm{d}}\,(t',Z)\Big]\,\mathrm{d}t'\mathrm{d}Z,\end{aligned} \tag{A.34}$$

where $\tau_{\mathrm{d}}(t\prime)$ is the optical depth of the dust, $F_{\lambda,\mathrm{d}}$ is the dust emission spectrum and A is a absorption constant.

Also, nebular emission (lines and continuum) effects can be added via photoionisation models taking into account the evolution of the radiation field and the processes relevant to the emitted spectrum.

Appendix B

Normalised Residual Maps from the Lens Modelling

Here I report the lens-modelling residual maps in units of the rms noise for the continuum emission of J1135. The figures are reported to highlight an emerging central feature. Spectral lines' normalised residuals are not reported here, since they do not show this component.

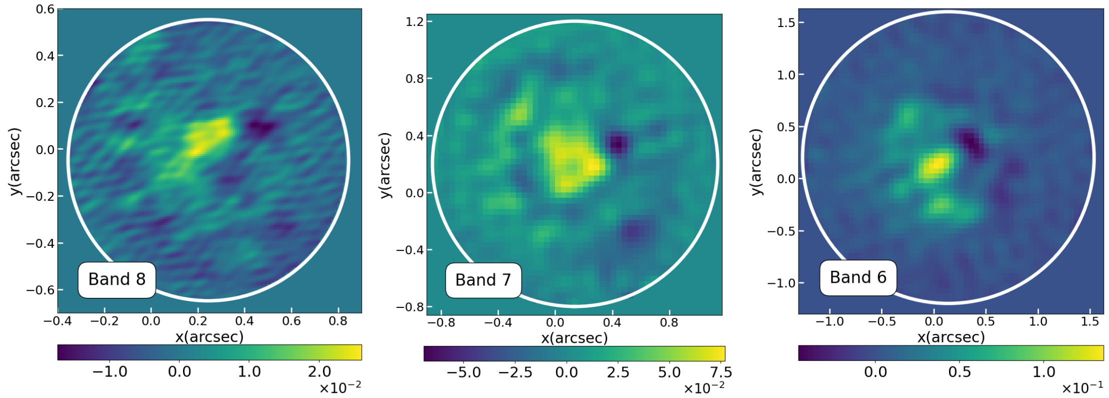

Figure B.1: Lens modelling normalised residual maps in units of rms noise for J1135.

Appendix C

Description of GalaPy Modules

C.1 Star Formation History model

The SFH is described by the in-situ model, implementing the galaxy formation model presented in Lapi et al. (2018) and Pantoni et al. (2019) for ETGs, and extended to LTGs in Lapi et al. (2020). This model is based on a self-consistent treatment of the black-hole/host-galaxy co-evolution, which captures the fast collapse, with low angular momentum, of the innermost gaseous regions of a galaxy, and the resulting stellar feedback. Such a regime is extremely important when interpreting data sets of galaxies at considerable redshift (i.e. $z \gtrsim 4$ and beyond). Furthermore, the model allows for the derivation of age-dependent analytical expressions of the evolution of the gas and dust content in galaxies.

This implementation also reduces the size of parameter space and gains access to analytically derived astrophysical properties of the galaxy, such as dust and gas mass/metallicity.

The SFR includes the effects of recycling and stellar feedback, expressed by the parameter γ, defined as:

$$\gamma \equiv 1 + \mathcal{R} + \epsilon_{\text{out}}, \tag{C.1}$$

where ϵ_{out} is the mass loading factor of the outflows from stellar feedback, and $\mathcal{R}$ is the fraction of recycled gas, expressed as:

$$\mathcal{R}(\tau) \approx 0.05 \ln\left(1 + \frac{\tau}{0.4\text{Myr}}\right). \tag{C.2}$$

The former parameter is $\epsilon_{\text{out}} \approx 3[\psi_{\max}/M_{\odot} yr^{-1}]^{-0.3}$, gauged according to the hydrodynamic simulations of stellar feedback from Hopkins et al. (2012). Therefore γ is determined in terms of the free parameter $\psi_{\max}$ and the age of the galaxy τ.

The evolution of the gas/dust masses and of the gas/stellar metallicity can be followed analytically as a function of the galactic age and self-consistently with respect to the evolution of the SFR. The gas mass is thus computed as

$$M_{\text{gas}}(\tau) = \psi(\tau)\tau_{\star}, \tag{C.3}$$

and the dust mass is computed in terms of the gas mass and of the dust-to-gas mass ratio $D_{\mathrm{in-situ}}$ as:

$$M_{\mathrm{dust}}(\tau) = M_{\mathrm{gas}}(\tau) D_{\mathrm{in-situ}}. \tag{C.4}$$

Following Lapi et al. (2020) and Pantoni et al. (2019), the latter quantity can be derived analytically as the expression:

$$\begin{aligned} D_{\text{in-situ}}(\tau) \approx \; & \frac{s^3 \epsilon_{\mathrm{acc}} y_D y_Z}{[s\gamma - 1]\,[s\,(\gamma + \kappa_{\mathrm{SN}}) - 1]\,[s(\gamma + \tilde{\epsilon}) - 1]} \times \\ & \times \left\{ 1 - \frac{(s\gamma - 1)x}{e^{(s\gamma - 1)x} - 1} \left[1 + \frac{s\gamma - 1}{s\tilde{\epsilon}} \left(1 - \frac{1 - e^{-s\tilde{\epsilon}x}}{s\tilde{\epsilon}x} \right) \right] \right\}; \end{aligned} \tag{C.5}$$

with

$$\tilde{\epsilon} \equiv \kappa_{\mathrm{SN}} + \epsilon_{\mathrm{acc}} s y_D / [s\,(\gamma + \kappa_{\mathrm{SN}}) - 1] \tag{C.6}$$

being the measure of the efficiency of dust grain formation in terms of the metal coagulation efficiency $\epsilon_{\mathrm{acc}} \approx 10^6$ onto dust grains, of the dust spallation efficiency $\kappa_{\mathrm{SN}} \approx 10$ by SN shock-waves, and of the dust production yield $y_D \approx 3.8 \times 10^{-4}$.

As a consequence, assuming an abrupt quenching event has the consequence of depleting the diffuse matter reservoir of the galaxy in question. Consequently, the galaxy loses its main source of star formation and undergoes an ageing process. The expressions for the gas and stellar metallicity are:

$$\begin{cases} Z_{\mathrm{gas}}(\tau) \approx \frac{s y_Z}{(s\gamma - 1)} \left[1 - \frac{(s\gamma - 1)x}{e^{(s\gamma - 1)x} - 1} \right], \\ Z_{\star}(\tau) \approx \frac{y_Z}{\gamma} \left[1 - \frac{s\gamma}{s\gamma - 1} \frac{e^{-x} - e^{-s\gamma x}[1 + (s\gamma - 1)x]}{s\gamma - 1 + e^{-s\gamma x} - s\gamma e^{-x}} \right], \end{cases} \tag{C.7}$$

where $x \equiv \tau / s\tau_{\star}$, and $y_Z \approx 0.04$ is the metal production yield, including the recycling, for a Chabrier IMF. Utilising analytical age-evolution expressions for previously unknown parameters in SED fitting offers several benefits. It reduces the parameter space needed, leading to faster convergence and improved estimation accuracy of optimal SEDs. This approach also differs from typical SED-fitting libraries based on energy conservation. GalaPy stands out as an innovative tool, providing non-parametric estimates of galaxy components and their age evolution, highlighting a consistent interplay between these elements.

C.2 Stellar Component

The stellar component is treated by GalaPy by using pre-computed SSP libraries. In this analysis, I have chosen the libraries computed with the PARSEC code (namely PARSEC22 library) for a Chabrier IMF and varying ages and metallicities. This module also includes nebular thermal emission, nebular line emission, and non-thermal synchrotron emission from core-collapse SNe. The PARSEC22 SSP libraries have the main advantage of reducing the total amount of computations, given that this module includes the radio and nebular characterisation, which are usually described with separated modules in other SED-fitting codes (see the comparison with the CIGALE SED-fitting procedure described in Appendix D). It is worth noticing that GalaPy also offers the classic Bruzual & Charlot (2003) libraries in its updated version (v2016). As discussed in Section A.9, the intrinsic luminosity of coeval stars sharing the same ISM in a galaxy is the result of the evolution of several SSPs formed and aged within the structure in all of its history. At a given age τ, a galaxy that has followed a SFH $\psi(\tau)$ will host a CSP resulting from all the SSPs formed and evolved up to that moment. The overall unattenuated intrinsic (i) stellar luminosity of the CSP, $L^{\mathrm{i}}_{\mathrm{CSP}}$, is therefore computed by summing up the contribution of SSPs properly sampled at different ages and stellar metallicities weighted by the formed stellar mass:

$$L^{\mathrm{i}}_{\mathrm{CSP}}(\lambda,\tau) = \int_0^\tau \mathrm{d}\tau_{\mathrm{SSP}} L_{\mathrm{SSP}}\left[\lambda, \tau_{\mathrm{SSP}}, Z_\star\left(\tau-\tau_{\mathrm{SSP}}\right)\right]\psi\left(\tau-\tau_{\mathrm{SSP}}\right), \tag{C.8}$$

where τ_{SSP} is the age of the SSP, L_{SSP} is the luminosity of the SSP per unit stellar mass defined, and $Z_\star(\tau-\tau_{\mathrm{SSP}})$ is the metallicity of stars at a given instant in the galactic history of metal enrichment. Integrating the above equation, the contribution of all the stellar ages defined in the SSP pre-computed library is summed up. For both the BC03 tables and the PARSEC22 tables, the time grid is constituted by an irregular grid that reaches a maximum accuracy of $\delta\tau = 10^5$ years.

The age-dependent, two-component dust model implemented in GalaPy is composed of a typically hotter molecular cloud phase (or birth clouds, here dubbed BC), and colder diffuse medium (or cirrus, here dubbed DD). GalaPy treats the fraction of dust contained in molecular clouds (f_{MC}) as a free parameter, which assumes typical values around 0.5, reaching higher values for starburst galaxies at higher redshift.

Therefore, the overall SED will consist of dust-attenuated emission from stars including nebular thermal emission, nebular line emission, and non-thermal synchrotron as well as thermal emission coming from the two different components of the age-dependent dust model. As mentioned at the beginning of this section, GalaPy implements energy conservation in an age-dependent way, calculating time-step by time-step the dust temperatures across the galaxy's lifetime.

C.3 Dust extinction and attenuation

Dust extinction and attenuation are characterised as follows. In the DD phase, the extinction normalisation scaling is assumed to be

$$A_V^{\mathrm{DD}} = C_V^{\mathrm{DD}} \frac{1-f_{\mathrm{MC}}}{0.5}\frac{M_{\mathrm{DD}}}{10^8 M_\odot}\left(\frac{R_{\mathrm{DD}}}{1\mathrm{kpc}}\right)^{-2}, \tag{C.9}$$

where M_{DD} is the age-dependent mass of the dust within the galaxy, R_{DD} is the characteristic radius of the diffuse dust component, and C_{V}^{DD} is a normalisation constant of order unity. The extinction law for the diffuse component follows the power-law

$$A_{\mathrm{DD}}(\lambda) = A_V^{\mathrm{DD}} \left(\frac{\lambda}{5500\text{Å}}\right)^{-\delta_{\mathrm{DD}}^{1/\mathrm{u}}}, \tag{C.10}$$

where δ_{DD}^{1} is ≈ 0.7 for $\lambda \lesssim 100\,\mu$m and $\delta_{\mathrm{DD}}^{\mathrm{u}} \approx 2$ for $\lambda \gtrsim 100\,\mu$m. Both these parameters can be set as free and directly fitted by GalaPy. The flatter power-law dependence is motivated by the observed relations between the ratio of far-infrared to UV luminosity and the UV spectral slope for nearby starburst galaxies (Charlot & Fall 2000, da Cunha et al. 2008). On the other hand, the transition to a steeper slope is indicative of the scattering and absorption cross-section behaviour of dust grains at longer wavelengths (e.g. Draine & Li 2007, Silva et al. 1998).

The MC component is expressed by adopting a V-band extinction depending on the average mass of a molecular cloud $M_{\mathrm{gas}}^{\mathrm{MC}}/10^6 M_\odot = \left(f_{\mathrm{MC}} M_{\mathrm{gas}}\right)/\left(N_{\mathrm{MC}} 10^6 M_\odot\right)$, on the cloud's radius R_{MC}, on the total number of MCs in the system and on the gas metallicity Z_{gas}, and is expressed as:

$$A_V^{\mathrm{MC}} = C_V^{\mathrm{MC}} \frac{Z_{\mathrm{gas}}}{Z_\odot} \frac{f_{\mathrm{MC}} M_{\mathrm{gas}}}{N_{\mathrm{MC}} 10^6 M_\odot} \left(\frac{R_{\mathrm{MC}}}{16\mathrm{pc}}\right)^{-2}. \tag{C.11}$$

The extinction for the MCs is therefore expressed as

$$A_{\mathrm{MC}}(\lambda) = A_V^{MC} \left(\frac{\lambda}{5500\text{Å}}\right)^{-\delta_{\mathrm{MC}}^{1/\mathrm{u}}}, \tag{C.12}$$

where δ_{MC}^{1} is ≈ 1.3 for $\lambda \lesssim 100\,\mu$m and $\delta_{\mathrm{MC}}^{\mathrm{u}} \approx 1.6$ for $\lambda \gtrsim 100\,\mu$m. These slopes correspond respectively to the middle range of the optical properties of dust grains between the Milky Way, the Large and the Small Magellanic Clouds (Charlot & Fall 2000,da Cunha et al. 2008) and to the values reproducing the sub-mm emission for ULIRGs (Silva et al. 1998, Lacey et al. 2016). From the extinction curves presented in Equations C.3 and C.3 the attenuated galaxy luminosity is given by

$$\begin{aligned} &L_{\mathrm{CSP}}^{\mathrm{a}}(\lambda,\tau) = \mathcal{A}_{\mathrm{DD}}(\lambda)\times \\ &\times \int_0^\tau \mathrm{d}\tau_{\mathrm{SSP}} \mathcal{A}_{\mathrm{MC}}\left(\lambda,\tau_{\mathrm{SSP}}\right) L_{\mathrm{SSP}}\left[\lambda,\tau_{\mathrm{SSP}},Z_\star\left(\tau-\tau_{\mathrm{SSP}}\right)\right] \psi\left(\tau-\tau_{\mathrm{SSP}}\right), \end{aligned} \tag{C.13}$$

with $\mathcal{A}_{\mathrm{DD}}(\lambda)$ and $\mathcal{A}_{\mathrm{MC}}(\lambda,\tau)$ being the attenuation factors originated by the DD and the MCs respectively. These factors are expressed as:

$$\mathcal{A}_{\mathrm{DD}}(\lambda) = 10^{-0.4 A_{\mathrm{DD}}(\lambda)} \mathcal{A}_{\mathrm{MC}}(\lambda) = 1 - \eta(\tau) + \eta(\tau) 10^{-0.4 A_{\mathrm{MC}}(\lambda)}, \tag{C.14}$$

by assuming that the attenuation suffered by radiation from stars already escaped from their birth MCs are independent of stellar age, while the birth clouds tend to be evaporated as the hosted SSPs evolve, therefore $\mathcal{A}_{\rm MC}$ is age-dependent. $\eta(\tau)$ defines the fraction of stars with age τ sill inside their MC. From GRASIL, this quantity is expressed as

$$\eta(\tau) = \begin{cases} 1 & \tau \leq \tau_{\rm esc} \\ 2 - \frac{\tau}{\tau_{\rm esc}} & \tau_{\rm esc} < \tau \leq 2\tau_{\rm esc} \\ 0 & \tau > 2\tau_{\rm esc}, \end{cases} \tag{C.15}$$

with $\tau_{\rm esc}$ being a free parameter defining the typical time for stars to start escaping MCs. By taking the luminosity-weighted average over stellar ages on the MC attenuation law, and re-writing Equation C.3, one obtains

$$L^{\rm a}_{\rm CSP}(\lambda, \tau) = \mathcal{A}_{\rm DD}(\lambda) \left\langle \mathcal{A}_{\rm MC} \right\rangle_\tau (\lambda) L^{\rm i}_{\rm CSP}(\lambda, \tau), \tag{C.16}$$

where $L^{\rm i}_{\rm CSP}(\lambda, \tau)$ is the intrinsic CSP luminosity (see Equation C.2, and

$$\left\langle \mathcal{A}_{\rm MC} \right\rangle_\tau (\lambda) = 1 - \langle\eta\rangle_\tau(\lambda) \left[1 - 10^{-0.4 A_{\rm MC}(\lambda)}\right], \tag{C.17}$$

with

$$\begin{aligned} &\langle\eta\rangle_\tau(\lambda) = \\ &= \frac{\int_0^\tau {\rm d}\tau_{\rm SSP} \eta\left(\tau_{\rm SSP}\right) L_{\rm SSP}\left[\lambda, \tau_{\rm SSP}, Z_\star\left(\tau - \tau_{\rm SSP}\right)\right] \psi\left(\tau - \tau_{\rm SSP}\right)}{\int_0^\tau {\rm d}\tau_{\rm SSP} L_{\rm SSP}\left[\lambda, \tau_{\rm SSP}, Z_\star\left(\tau - \tau_{\rm SSP}\right)\right] \psi\left(\tau - \tau_{\rm SSP}\right)} . \end{aligned} \tag{C.18}$$

Finally, the wavelength- and age-dependent total galactic extinction curve is

$$A_{\rm TOT}(\lambda, \tau) = -2.5 \log_{10}\left[\mathcal{A}_{\rm DD}(\lambda) \left\langle \mathcal{A}_{\rm MC} \right\rangle_\tau (\lambda)\right] . \tag{C.19}$$

C.3.1 Energy conservation and dust emission

The bolometric intrinsic luminosity originated from the CSP is computed integrating Equation C.2 all over the spectrum:

$$L^{\rm i}_{\rm bol}(\tau) = \int_0^\infty {\rm d}\lambda L^{\rm i}_{\rm CSP}(\lambda, \tau) \tag{C.20}$$

In GalaPy, the absorption of this luminosity occurs in two stages for stars that are still within their birth cloud. Initially, it must traverse the molecular cloud (MC) phase, followed by passing through the diffuse and dense (DD) region. The quantification of the bolometric luminosity that is absorbed by dust within the molecular clouds is determined by applying the age-dependent law defined in Equation C.3 to the above integral. The luminosity not transferred to MCs is then further absorbed by DD. Therefore one has:

$$L_{\rm abs}^{\rm MC}(\tau) = \int_0^\infty \mathrm{d}\lambda \left[1 - \langle \mathcal{A}_{\rm MC} \rangle_\tau (\lambda)\right] L_{\rm CSP}^{\rm i}(\lambda, \tau) \tag{C.21}$$

$$L_{\rm abs}^{\rm DD}(\tau) = \int_0^\infty \mathrm{d}\lambda \left[1 - \mathcal{A}_{\rm DD}(\lambda)\right] \langle \mathcal{A}_{\rm MC} \rangle_\tau (\lambda) L_{\rm CSP}^{\rm i}(\lambda, \tau). \tag{C.22}$$

Because of energy conservation, the two dust components emit radiation approximately as two optically thick grey bodies, depending on the attenuation laws for the two respective dust phases. Therefore one can define the DD and MC phases respectively:

$$L_{\rm DD}\left(\lambda, \tau \mid T_{\rm DD}\right) = \frac{16\pi^2}{3} R_{\rm DD}^2 \left[1 - 10^{-0.4 A_{\rm DD}(\lambda,\tau)}\right] B\left(\lambda, T_{\rm DD}\right), \tag{C.23}$$

$$L_{\rm MC}\left(\lambda, \tau \mid T_{\rm MC}\right) = \frac{16\pi^2}{3} N_{\rm MC} R_{\rm MC}^2 \left[1 - 10^{-0.4 A_{\rm MC}(\lambda,\tau)}\right] B\left(\lambda, T_{\rm MC}\right). \tag{C.24}$$

In the above equations, luminosity is given in terms of the black body spectrum.

The temperatures are age-dependent outputs obtained by imposing energy conservation and, thus are not free parameters. By integrating the spectrum given in the second expression in Equation C.3.1 and using Equation C.3.1 one obtains:

$$\int_0^\infty \mathrm{d}\lambda L_{\rm MC}\left[\lambda, \tau \mid T_{\rm MC}(\tau)\right] = L_{\rm abs}^{\rm MC}(\tau). \tag{C.25}$$

which is the expression relative to the emission coming from MCs, where $T_{\rm MC}$ is its related temperature.

Furthermore, the emission from polycyclic aromatic hydrocarbons (PAH) is assumed to be suppressed in MCs but included in the emission from the DD phase (Vega et al. 2008). By defining the free parameter regulating the fraction of absorbed power ($L_{\rm abs}(\tau)^{\rm DD}$) as $0 \leq f_{\rm PAH} \leq 1$, the temperature of the DD grey-body is computed by imposing

$$\int_0^\infty \mathrm{d}\lambda L_{\rm DD}\left[\lambda, \tau \mid T_{\rm DD}(\tau)\right] = \left(1 - f_{\rm PAH}\right) L_{\rm abs}^{\rm DD}(\tau). \tag{C.26}$$

GalaPy implements the PAH template $L_{\rm PAH}(\lambda)$ by da Cunha et al. (2008) and is based on the photo-dissociation regions of the Milky Way. It includes PAH line emission primarily in MIR, PAH continuum emission in the NIR, and MIR continuum emission stemming from very small, hot dust grains. All in all, the overall emission arising from diffuse dust, including PAH, is expressed as

$$L_{\rm DD+PAH}(\lambda, \tau) = L_{\rm DD}\left[\lambda, \tau \mid T_{\rm DD}(\tau)\right] + f_{\rm PAH} L_{\rm abs}^{\rm DD}(\tau) L_{\rm PAH}^{\rm norm}(\lambda), \tag{C.27}$$

with $L_{\rm PAH}^{\rm norm}(\lambda) = L_{\rm PAH}(\lambda) / \int_0^\infty \mathrm{d}\lambda L_{\rm PAH}(\lambda)$ being the normalized PAH spectrum. Finally, the total dust bolometric luminosity is given by the all-spectrum integral

$$L_{\rm dust}\,(\tau) = \int_0^\infty {\rm d}\lambda\,[L_{\rm MC}(\lambda,\tau) + L_{\rm DD+PAH}(\lambda,\tau)] == \int_0^\infty {\rm d}\lambda L_{\rm dust}\,(\lambda,\tau). \qquad (C.28)$$

Appendix D

SED-fitting with CIGALE

For comparison, I report here the results of the SED fitting of J1135's photometry performed with the e Code Investigating GAlaxy Emission (CIGALE, Boquien et al. 2019). CIGALE is a Python SED fitting code able to reproduce broad-band uv-to-radio photometric data according to the energy balance (i.e. the energy coming from the stellar uv-NIR emission is the same as the one re-emitted by the dust in the MIR and FIR regime). The main physical properties are estimated by comparing the observed galaxy SED with the modelled one by means of χ^2 and Bayesian statistics.

The stellar emission is computed following the Bruzual & Charlot (2003) (BC03) population synthesis models, associated with a Chabrier (2003) IMF and metallicity values of Z= 0.004, 0.008, 0.02, 0.05. I assume a delayed exponential star formation history, which predicts a nearly linear increase in the SFR:

$$SFR(t) \propto \frac{t}{\tau^2} \times \exp\left(-\frac{t}{\tau}\right) \qquad \text{for} \quad 0 \leq t \leq t_0, \tag{D.1}$$

where t_0 is the age of the onset of star formation, and τ is the time at which the SFR peaks.

In order to model the effect of the dust attenuation on FUV-optical light I adopt the modified Charlot & Fall (2000) prescriptions, where the attenuation is age-dependent and described by two different power-laws, one for the ISM and one for the Birth Clouds (BC). The attenuation slopes are assumed to be -0.7 and the V-band attenuation is computed as:

$$\kappa = \frac{A_{\rm V}^{\rm ISM}}{A_{\rm V}^{\rm ISM} + A_{\rm V}^{\rm BC}}. \tag{D.2}$$

In this analysis, I assume $A_{\rm V}^{\rm ISM}$ spanning from 0.3 to 5.0 and a κ spanning from 0.3 to 0.6.

Following Draine & Li (2007), dust emission is modelled as two separated components: a diffuse one, illuminated with a single radiation field (U_{min}) originated by a general stellar population; and a second component is closely associated to regions in which the star-formation occurs, heated by a variable radiation field described with a power-law profile and defined between two values U_{min} and

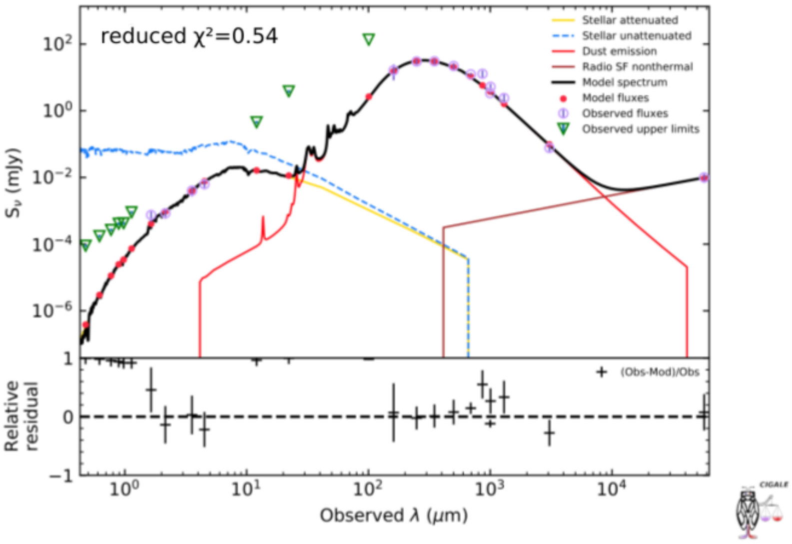

Figure D.1: Best-fit UV to radio observed-frame SED of J1135. Green arrows are 3σ upper limits, purple circles are the observed flux densities and errors. The black line is the best-fitting modified black body spectrum.

SED-fitting results	
$\log L_{\rm dust}$ ($L_\odot$)	13.03 ± 0.06
$\log M_{\rm dust}$ ($M_\odot$)	9.06 ± 0.04
$\log {\rm SFR}$ ($M_\odot$ yr^{-1})	2.97 ± 0.08
$\log M_\star$ ($M_\odot$)	$\lesssim$ 11.75
$q_{\rm IR}$	2.84±0.09

Table D.1: Output properties from CIGALE. From the first raw: dust luminosity, dust mass, star formation rate, stellar mass, and the Infrared-Radio correlation parameter.

U_{max}. In particular, I use the most recent and refined version of this model which accounts also for dust-mass renormalization (Draine et al. 2014).

The radio emission is treated by CIGALE with the `synchrotron` module, relying on the radio-IR correlation $q_{\rm IR}$ of Helou et al. (1985), a free power-law spectral slope α, and on the assumption that non-thermal emission dominates the 21 cm spectrum. The luminosity density at 21 cm is therefore computed from the IR emission of the galaxy through the $q_{\rm IR}$ parameter. The only free parameter requested from the module is the power slope α, which is used to compute the spectrum so that it matches the estimated luminosity.

The best-fit model is presented in Fig. D.1 and the resulting best physical properties are summarised in Table D.1.

Appendix E

Bayesian lines shape reconstruction

Here I summarise the spectral line fitting analysis performed in Chapter 4. The MCMC fit adopted in this analysis maximises the likelihood $\mathcal{L}(\theta) \equiv -\chi^2(\theta)/2$, where $\chi^2 = [\mathcal{M}(\theta) - \mathcal{D}]^2/\sigma^2_{\mathcal{D}}$ is obtained by comparing the expectations of our empirical model $\mathcal{M}(\theta)$ with the data $\mathcal{D}$ having uncertainties $\sigma^2_{\mathcal{D}}$. We adopted flat prior $\pi(\theta)$ on the fit parameters, sampling the posterior distribution $\mathcal{P}(\theta) \propto \mathcal{L}(\theta)\pi(\theta)$ by running `emcee` with 10^4 iterations and 300 walkers. Each walker has been initialised with a random position uniformly sampled from the (flat) priors and discarded a fraction of the initial iterations of the MCMC to allow the chain to reach statistical equilibrium. The fraction of the chain to discard was determined from the Markov Chain's autocorrelation time computed for each parameter thanks to the Gelmen-Rubin criterion (Gelman & Rubin 1992). In our case, the fraction of the rejected chain is about 18% of the MCMC on average for each fitted spectral line. In Figure E.1 I show the contour plots obtained from the chains via the Python package `getdist` (Lewis 2019).

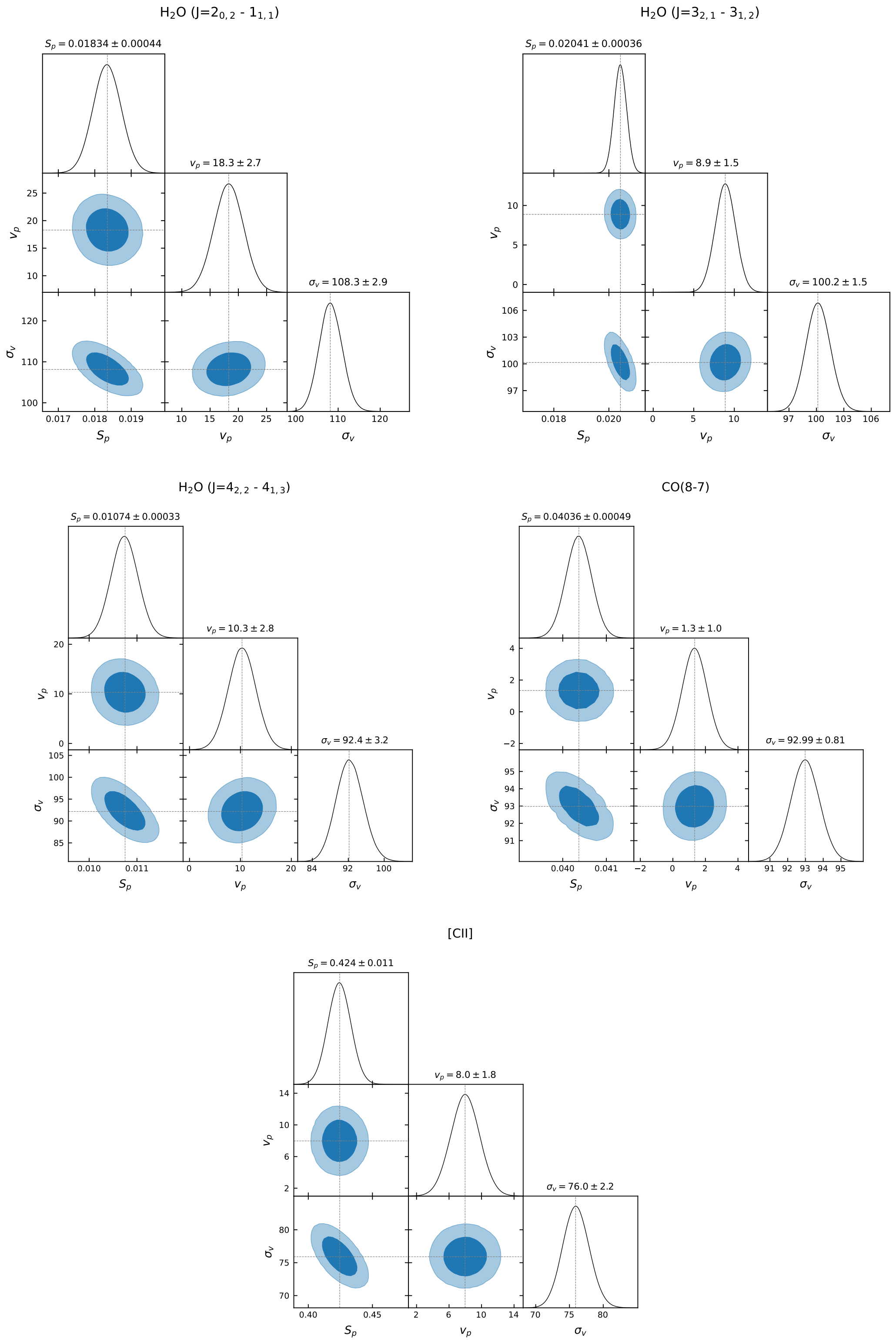

Figure E.1: Contour plots for our Bayesian lines shape reconstruction obtained with the `getdist` Python package.

Bibliography

[1] Aalto S., Booth R. S., Black J. H., Johansson L. E. B., 1995, A&A, 300, 369

[2] Aalto S., Wilner D., Spaans M., Wiedner M. C., Sakamoto K., Black J. H., Caldas M., 2009, VizieR Online Data Catalog, pp J/A+A/493/481

[3] Aalto S., et al., 2015, A&A, 574, A85

[4] Adams N. J., et al., 2023, MNRAS, 518, 4755

[5] Aihara H., et al., 2018, PASJ, 70, S8

[6] Aihara H., et al., 2022, PASJ,

[7] Aird J., et al., 2010, MNRAS, 401, 2531

[8] Aird J., Coil A. L., Georgakakis A., Nandra K., Barro G., Pérez-González P. G., 2015, MNRAS, 451, 1892

[9] Alcalde Pampliega B., et al., 2019, ApJ, 876, 135

[10] Alexander D. M., Hickox R. C., 2012, New Astron. Rev., 56, 93

[11] Algera H. S. B., et al., 2020, ApJ, 903, 138

[12] Álvarez-Márquez J., et al., 2023, A&A, 671, A105

[13] An F., et al., 2021, MNRAS, 507, 2643

[14] Andreani P., Retana-Montenegro E., Zhang Z.-Y., Papadopoulos P., Yang C., Vegetti S., 2018, A&A, 615, A142

[15] Andrews B. H., Thompson T. A., 2011, ApJ, 727, 97

[16] Andrews B. H., Weinberg D. H., Schönrich R., Johnson J. A., 2017, ApJ, 835, 224

[17] Aoyama S., Hou K.-C., Shimizu I., Hirashita H., Todoroki K., Choi J.-H., Nagamine K., 2017, MNRAS, 466, 105

[18] Aoyama S., Hou K.-C., Hirashita H., Nagamine K., Shimizu I., 2018, MNRAS, 478, 4905

[19] Aravena M., et al., 2016, ApJ, 833, 71

[20] Aretxaga I., et al., 2011, MNRAS, 415, 3831

[21] Arrigoni M., Trager S. C., Somerville R. S., Gibson B. K., 2010, MNRAS, 402, 173

[22] Asano R. S., Takeuchi T. T., Hirashita H., Inoue A. K., 2013, Earth, Planets and Space, 65, 213

[23] Atek H., et al., 2023, MNRAS, 519, 1201

[24] Auger M. W., Treu T., Bolton A. S., Gavazzi R., Koopmans L. V. E., Marshall P. J., Bundy K., Moustakas L. A., 2009, ApJ, 705, 1099

[25] Aversa R., Lapi A., de Zotti G., Shankar F., Danese L., 2015, ApJ, 810, 74

[26] Bakx T. J. L. C., Dannerbauer H., 2022, MNRAS, 515, 678

[27] Bakx T. J. L. C., et al., 2018, MNRAS, 473, 1751

[28] Barger A. J., Cowie L. L., Sanders D. B., Fulton E., Taniguchi Y., Sato Y.,

Kawara K., Okuda H., 1998, Nat, 394, 248
[29] Barro G., et al., 2014, ApJ, 791, 52
[30] Barro G., et al., 2016a, ApJ, 820, 120
[31] Barro G., et al., 2016b, ApJL, 827, L32
[32] Barro G., et al., 2017, ApJL, 851, L40
[33] Barthel P. D., 2006, A&A, 458, 107
[34] Basu A., Wadadekar Y., Beelen A., Singh V., Archana K. N., Sirothia S., Ishwara-Chandra C. H., 2015, ApJ, 803, 51
[35] Becker R. H., White R. L., Helfand D. J., 1995, ApJ, 450, 559
[36] Behroozi P. S., Wechsler R. H., Conroy C., 2013, ApJ, 770, 57
[37] Beifiori A., Courteau S., Corsini E. M., Zhu Y., 2012, MNRAS, 419, 2497
[38] Bekki K., 2013, MNRAS, 436, 2254
[39] Bekki K., 2015, MNRAS, 449, 1625
[40] Belli S., Newman A. B., Ellis R. S., 2017, ApJ, 834, 18
[41] Bendo G. J., et al., 2023, MNRAS, 522, 2995
[42] Benson A. J., 2010, PR, 495, 33
[43] Benson A. J., 2012, New Astron., 17, 175
[44] Bergin E. A., Kaufman M. J., Melnick G. J., Snell R. L., Howe J. E., 2003, ApJ, 582, 830
[45] Berta S., Lutz D., Genzel R., Förster-Schreiber N. M., Tacconi L. J., 2016, A&A, 587, A73
[46] Binney J., 1977, ApJ, 215, 483
[47] Blain A. W., 1996, MNRAS, 283, 1340
[48] Blain A. W., Smail I., Ivison R. J., Kneib J. P., Frayer D. T., 2002, PR, 369, 111
[49] Blake G. A., Sutton E. C., Masson C. R., Phillips T. G., 1987, ApJ, 315, 621
[50] Bolton A. S., Burles S., Koopmans L. V. E., Treu T., Moustakas L. A., 2006, ApJ, 638, 703
[51] Bonaldi A., et al., 2021, MNRAS, 500, 3821
[52] Bonato M., et al., 2021, A&A
[53] Bonzini M., Padovani P., Mainieri V., Kellermann K. I., Miller N., Rosati P., Tozzi P., Vattakunnel S., 2013, MNRAS, 436, 3759
[54] Bonzini M., et al., 2015, MNRAS, 453, 1079
[55] Boquien M., Burgarella D., Roehlly Y., Buat V., Ciesla L., Corre D., Inoue A. K., Salas H., 2019, A&A, 622, A103
[56] Bouché N., et al., 2010, ApJ, 718, 1001
[57] Bournaud F., Dekel A., Teyssier R., Cacciato M., Daddi E., Juneau S., Shankar F., 2011, ApJL, 741, L33
[58] Bourne N., Dunne L., Ivison R. J., Maddox S. J., Dickinson M., Frayer D. T., 2011, MNRAS, 410, 1155
[59] Bouwens R. J., et al., 2015, ApJ, 803, 34
[60] Bouwens R. J., et al., 2023, MNRAS, 523, 1036
[61] Bower R. G., Benson A. J., Malbon R., Helly J. C., Frenk C. S., Baugh C. M., Cole S., Lacey C. G., 2006, MNRAS, 370, 645
[62] Boyle B. J., Terlevich R. J., 1998, MNRAS, 293, L49
[63] Bradley L. D., et al., 2022, arXiv e-prints, p. arXiv:2210.01777
[64] Brinchmann J., Charlot S., White S. D. M., Tremonti C., Kauffmann G., Heck-

man T., Brinkmann J., 2004, MNRAS, 351, 1151
[65] Browne I. W. A., et al., 2003, MNRAS, 341, 13
[66] Brownstein J. R., et al., 2012, ApJ, 744, 41
[67] Bruzual G., Charlot S., 2003, MNRAS, 344, 1000
[68] Burlon D., Ajello M., Greiner J., Comastri A., Merloni A., Gehrels N., 2011, ApJ, 728, 58
[69] Bussmann R. S., et al., 2008, ApJL, 681, L73
[70] Bussmann R. S., et al., 2013, ApJ, 779, 25
[71] Bussmann R. S., et al., 2015, ApJ, 812, 43
[72] Butler K. M., et al., 2021, ApJ, 919, 5
[73] Cañameras R., et al., 2015, A&A, 581, A105
[74] Cai Z.-Y., et al., 2013, ApJ, 768, 21
[75] Calanog J. A., et al., 2014, ApJ
[76] Calistro Rivera G., et al., 2017, MNRAS, 469, 3468
[77] Cappellari M., 2016, ARA&A, 54, 597
[78] Cappellari M., et al., 2013, MNRAS, 432, 1862
[79] Carilli C. L., Walter F., 2013a, ARA&A, 51, 105
[80] Carilli C. L., Walter F., 2013b, ARA&A, 51, 105
[81] Carlstrom J. E., et al., 2011, PASP, 123, 568
[82] Carpenter J., Brogan C., Iono D., Mroczkowski T., 2023, in Physics and Chemistry of Star Formation: The Dynamical ISM Across Time and Spatial Scales. p. 304 (`arXiv:2211.00195`), doi:10.48550/arXiv.2211.00195
[83] Caselli P., et al., 2010, A&A, 521, L29
[84] Casey C. M., et al., 2012a, ApJ, 761, 139
[85] Casey C. M., et al., 2012b, ApJ, 761, 140
[86] Casey C. M., Narayanan D., Cooray A., 2014, PR, 541, 45
[87] Castellano M., et al., 2022, ApJL, 938, L15
[88] Cernicharo J., Pardo J. R., Weiss A., 2006, ApJL, 646, L49
[89] Chabrier G., 2003, PASP, 115, 763
[90] Charlot S., Fall S. M., 2000, ApJ, 539, 718
[91] Chen C.-C., et al., 2015, ApJ, 799, 194
[92] Cheng C., et al., 2020, ApJ, 898, 33
[93] Chiappini C., Matteucci F., Romano D., 2001, ApJ, 554, 1044
[94] Chiosi C., 1980, A&A, 83, 206
[95] Cimatti A., et al., 2008, A&A, 482, 21
[96] Cole S., Lacey C. G., Baugh C. M., Frenk C. S., 2000, MNRAS, 319, 168
[97] Collacchioni F., Cora S. A., Lagos C. D. P., Vega-Martínez C. A., 2018, MNRAS, 481, 954
[98] Condon J. J., Cotton W. D., Broderick J. J., 2002, AJ, 124, 675
[99] Condon J. J., Kellermann K. I., Kimball A. E., Ivezić Ž., Perley R. A., 2013, ApJ, 768, 37
[100] Cortzen I., et al., 2020, A&A, 634, L14
[101] Costagliola F., et al., 2011, in Röllig M., Simon R., Ossenkopf V., Stutzki J., eds, EAS Publications Series Vol. 52, EAS Publications Series. pp 285–286, doi:10.1051/eas/1152049
[102] Cousin M., Buat V., Boissier S., Bethermin M., Roehlly Y., Génois M., 2016,

A&A, 589, A109
[103] Cox P., et al., 2011, ApJ, 740, 63
[104] Cox P., et al., 2023, arXiv e-prints, p. arXiv:2307.15732
[105] Croton D. J., et al., 2006, MNRAS, 365, 11
[106] Curtis-Lake E., et al., 2023, Nature Astronomy, 7, 622
[107] D'Amato Q., et al., 2020, A&A, 641, L6
[108] Daddi E., et al., 2005, ApJL, 631, L13
[109] Daddi E., et al., 2007, ApJ, 670, 156
[110] Davé R., Finlator K., Oppenheimer B. D., 2012, MNRAS, 421, 98
[111] Davis M., Efstathiou G., Frenk C. S., White S. D. M., 1985, ApJ, 292, 371
[112] De Lucia G., Tornatore L., Frenk C. S., Helmi A., Navarro J. F., White S. D. M., 2014, MNRAS, 445, 970
[113] De Lucia G., Fontanot F., Hirschmann M., 2017, MNRAS, 466, L88
[114] Decarli R., et al., 2016, ApJ, 833, 70
[115] Dekel A., Mandelker N., 2014, MNRAS, 444, 2071
[116] Dekel A., Sari R., Ceverino D., 2009, ApJ, 703, 785
[117] Dekel A., Zolotov A., Tweed D., Cacciato M., Ceverino D., Primack J. R., 2013, MNRAS, 435, 999
[118] Dekel A., Sarkar K. C., Jiang F., Bournaud F., Krumholz M. R., Ceverino D., Primack J. R., 2019, MNRAS, 488, 4753
[119] Delhaize J., et al., 2017, A&A, 602, A4
[120] Delvecchio I., et al., 2014, MNRAS, 439, 2736
[121] Delvecchio I., et al., 2015, MNRAS, 449, 373
[122] Delvecchio I., et al., 2021, A&A, 647, A123
[123] Díaz-Santos T., et al., 2013, ApJ, 774, 68
[124] Díaz-Santos T., et al., 2017, ApJ, 846, 32
[125] Dickens J. E., Irvine W. M., Snell R. L., Bergin E. A., Schloerb F. P., Pratap P., Miralles M. P., 2000, ApJ, 542, 870
[126] Dickinson M., Papovich C., Ferguson H. C., Budavári T., 2003, ApJ, 587, 25
[127] Diemand J., Kuhlen M., Madau P., 2008, ApJ, 679, 1680
[128] Donnan C. T., McLeod D. J., McLure R. J., Dunlop J. S., Carnall A. C., Cullen F., Magee D., 2023, MNRAS, 520, 4554
[129] Downes D., Eckart A., 2007, A&A, 468, L57
[130] Downes D., Solomon P. M., 1998, ApJ, 507, 615
[131] Draine B. T., 2003, ARA&A, 41, 241
[132] Draine B. T., 2011, Physics of the Interstellar and Intergalactic Medium. Princeton University Press
[133] Draine B. T., Li A., 2007, ApJ, 657, 810
[134] Draine B. T., et al., 2014, ApJ, 780, 172
[135] Dubinski J., Carlberg R. G., 1991, ApJ, 378, 496
[136] Dubois Y., Volonteri M., Silk J., 2014, MNRAS, 440, 1590
[137] Dubois Y., Peirani S., Pichon C., Devriendt J., Gavazzi R., Welker C., Volonteri M., 2016, MNRAS, 463, 3948
[138] Dudzevičiūtė U., et al., 2020, MNRAS, 494, 3828
[139] Dunlop J. S., et al., 2016, MNRAS, 466, 861–883
[140] Dunlop J. S., et al., 2017, MNRAS, 466, 861

[141] Dwek E., 1998, ApJ, 501, 643
[142] Dwek E., Cherchneff I., 2011, ApJ, 727, 63
[143] Dye S., et al., 2014, MNRAS, 440, 2013
[144] Dye S., et al., 2015, MNRAS, 452, 2258
[145] Dye S., et al., 2018, MNRAS, 476, 4383
[146] Dye S., et al., 2022, MNRAS, 510, 3734
[147] Eales S. A., 2015, MNRAS, 446, 3224
[148] Eales S., et al., 2010, PASP, 122, 499
[149] Edge A., Sutherland W., Kuijken K., Driver S., McMahon R., Eales S., Emerson J. P., 2013, The Messenger, 154, 32
[150] Edmunds M. G., 1990, MNRAS, 246, 678
[151] Elbaz D., et al., 2007, A&A, 468, 33
[152] Enia A., et al., 2018, MNRAS, 475, 3467
[153] Enia A., et al., 2022, ApJ, 927, 204
[154] Erb D. K., 2008, ApJ, 674, 151
[155] Everett W. B., et al., 2020, ApJ, 900, 55
[156] Falgarone E., et al., 2017, Nat, 548, 430
[157] Fall S. M., 2002, in Athanassoula E., Bosma A., Mujica R., eds, Astronomical Society of the Pacific Conference Series Vol. 275, Disks of Galaxies: Kinematics, Dynamics and Peturbations. pp 389–396
[158] Fanidakis N., et al., 2012, MNRAS, 419, 2797
[159] Feldmann R., 2015, MNRAS, 449, 3274
[160] Ferrarese L., Ford H., 2005, Space Sci. Rev., 116, 523
[161] Ferrarese L., Merritt D., 2000, ApJL, 539, L9
[162] Feruglio C., et al., 2015, A&A, 583, A99
[163] Finkelstein S. L., et al., 2022, ApJL, 940, L55
[164] Finkelstein S. L., et al., 2023, ApJL, 946, L13
[165] Fischer J., et al., 2010, A&A, 518, L41
[166] Fontanot F., De Lucia G., Hirschmann M., Bruzual G., Charlot S., Zibetti S., 2017, MNRAS, 464, 3812
[167] Forbes J. C., Krumholz M. R., Burkert A., Dekel A., 2014, MNRAS, 443, 168
[168] Forbes J. C., Krumholz M. R., Speagle J. S., 2019, MNRAS, 487, 3581
[169] Foreman-Mackey D., Hogg D. W., Lang D., Goodman J., 2013, PASP, 125, 306
[170] Franceschini A., Hasinger G., Miyaji T., Malquori D., 1999, MNRAS, 310, L5
[171] Franco M., et al., 2018, A&A, 620, A152
[172] Frenk C. S., White S. D. M., 2012, Annalen der Physik, 524, 507
[173] Fu H., et al., 2012, ApJ, 753, 134
[174] Fujimoto S., Ouchi M., Shibuya T., Nagai H., 2017, ApJ, 850, 83
[175] Fujimoto S., et al., 2022, Nat, 604, 261
[176] Gao Y., Carilli C. L., Solomon P. M., Vanden Bout P. A., 2007, ApJL, 660, L93
[177] García-Burillo S., et al., 2015, A&A, 580, A35
[178] Gavazzi R., Treu T., Marshall P. J., Brault F., Ruff A., 2012, ApJ, 761, 170
[179] Gebhardt K., et al., 2000, ApJL, 543, L5
[180] Gelman A., Rubin D. B., 1992, Statistical Science, 7, 457
[181] Genzel R., et al., 2014, ApJ, 785, 75

[182] George R. D., et al., 2013, MNRAS, 436, L99
[183] Gilli R., et al., 2022, A&A, 666, A17
[184] Gioannini L., Matteucci F., Vladilo G., Calura F., 2017, MNRAS, 464, 985
[185] Giulietti M., et al., 2022, MNRAS, 511, 1408
[186] Giulietti M., et al., 2023, ApJ, 943, 151
[187] Glazebrook K., et al., 2017, Nat, 544, 71
[188] Glenn J., et al., 2010, MNRAS, 409, 109
[189] González-Alfonso E., Smith H. A., Fischer J., Cernicharo J., 2004, ApJ, 613, 247
[190] González-Alfonso E., Smith H. A., Ashby M. L. N., Fischer J., Spinoglio L., Grundy T. W., 2008, ApJ, 675, 303
[191] González-Alfonso E., et al., 2010, A&A, 518, L43
[192] González-Alfonso E., et al., 2013, A&A, 550, A25
[193] González-Alfonso E., Fischer J., Aalto S., Falstad N., 2014, A&A, 567, A91
[194] González-Alfonso E., et al., 2021, A&A, 645, A49
[195] González-Alfonso E., Fischer J., Goicoechea J. R., Yang C., Pereira-Santaella M., Stewart K. P., 2022, A&A, 666, L3
[196] Graciá-Carpio J., García-Burillo S., Planesas P., Fuente A., Usero A., 2008, A&A, 479, 703
[197] Graham A. W., 2007, MNRAS, 379, 711
[198] Graham A. W., Onken C. A., Athanassoula E., Combes F., 2011, MNRAS, 412, 2211
[199] Granato G. L., De Zotti G., Silva L., Bressan A., Danese L., 2004, ApJ, 600, 580
[200] Greene J. E., Ho L. C., 2007, ApJ, 667, 131
[201] Greggio L., 2005, A&A, 441, 1055
[202] Grillo C., Lombardi M., Bertin G., 2008, A&A, 477, 397
[203] Grisoni V., Spitoni E., Matteucci F., 2018, MNRAS, 481, 2570
[204] Gruppioni C., et al., 2013, MNRAS, 432, 23
[205] Gruppioni C., et al., 2020, A&A, 643, A8
[206] Gullberg B., et al., 2015, MNRAS, 449, 2883
[207] Gültekin K., et al., 2009, ApJ, 698, 198
[208] Hagimoto M., et al., 2023, MNRAS, 521, 5508
[209] Harikane Y., et al., 2023, ApJS, 265, 5
[210] Häring N., Rix H.-W., 2004, ApJL, 604, L89
[211] Harris A. I., et al., 2012, ApJ, 752, 152
[212] Hartwick F. D. A., 1976, ApJ, 209, 418
[213] Hatsukade B., Tamura Y., Iono D., Matsuda Y., Hayashi M., Oguri M., 2015, PASJ, 67, 93
[214] Hatsukade B., et al., 2018, PASJ, 70, 105
[215] Hayward C. C., et al., 2014, MNRAS, 445, 1598
[216] Heckman T. M., Kauffmann G., Brinchmann J., Charlot S., Tremonti C., White S. D. M., 2004, ApJ, 613, 109
[217] Helou G., Soifer B. T., Rowan-Robinson M., 1985, ApJ, 298, L7
[218] Herrera Ruiz N., Middelberg E., Norris R. P., Maini A., 2016, A&A, 589, L2
[219] Herrera Ruiz N., et al., 2017, A&A, 607, A132

[220] Hezaveh Y. D., et al., 2016, ApJ, 823, 37
[221] Hickox R. C., Alexander D. M., 2018, ARA&A, 56, 625
[222] Hill R., et al., 2018, MNRAS, 477, 2042
[223] Hirashita H., 2000, PASJ, 52, 585
[224] Hirashita H., Nozawa T., Villaume A., Srinivasan S., 2015, MNRAS, 454, 1620
[225] Hirschmann M., De Lucia G., Fontanot F., 2016, MNRAS, 461, 1760
[226] Ho L. C., Kim M., 2014, ApJ, 789, 17
[227] Hodge J. A., da Cunha E., 2020, Royal Society Open Science, 7, 200556
[228] Hodge J. A., et al., 2013, ApJ, 768, 91
[229] Hodge J. A., et al., 2016, ApJ, 833, 103
[230] Hopkins P. F., Hernquist L., Cox T. J., Di Matteo T., Martini P., Robertson B., Springel V., 2005, ApJ, 630, 705
[231] Hopkins P. F., Hernquist L., Cox T. J., Di Matteo T., Robertson B., Springel V., 2006, ApJS, 163, 1
[232] Hopkins P. F., Quataert E., Murray N., 2012, MNRAS, 421, 3522
[233] Hopkins P. F., Kereš D., Oñorbe J., Faucher-Giguère C.-A., Quataert E., Murray N., Bullock J. S., 2014, MNRAS, 445, 581
[234] Hopkins P. F., et al., 2018, MNRAS, 480, 800
[235] Hughes D. H., et al., 1998, Nat, 394, 241
[236] Ikarashi S., et al., 2015, ApJ, 810, 133
[237] Ikarashi S., et al., 2017, ApJL, 849, L36
[238] Imanishi M., Nakanishi K., 2006, PASJ, 58, 813
[239] Imanishi M., Nakanishi K., Kuno N., Kohno K., 2004, AJ, 128, 2037
[240] Imanishi M., Nakanishi K., Kohno K., 2006, AJ, 131, 2888
[241] Imanishi M., Nakanishi K., Tamura Y., Oi N., Kohno K., 2007, AJ, 134, 2366
[242] Imanishi M., Nakanishi K., Tamura Y., Peng C.-H., 2009, AJ, 137, 3581
[243] Imanishi M., Nakanishi K., Yamada M., Tamura Y., Kohno K., 2010, PASJ, 62, 201
[244] Imanishi M., Nakanishi K., Izumi T., 2016, AJ, 152, 218
[245] Imara N., Loeb A., Johnson B. D., Conroy C., Behroozi P., 2018, ApJ, 854, 36
[246] Inada N., et al., 2012, AJ, 143, 119
[247] Inoue A. K., 2003, PASJ, 55, 901
[248] Irwin M. J., Webster R. L., Hewett P. C., Corrigan R. T., Jedrzejewski R. I., 1989, AJ, 98, 1989
[249] Ishigaki M., Kawamata R., Ouchi M., Oguri M., Shimasaku K., Ono Y., 2018, ApJ, 854, 73
[250] Ivison R. J., et al., 2010a, MNRAS, 402, 245
[251] Ivison R. J., et al., 2010b, A&A, 518, L31
[252] Izumi T., Kohno K., Martín S., Sheth K., Matsushita S., Espada D., NGC 1097 collaborators 2013, in Kawabe R., Kuno N., Yamamoto S., eds, Astronomical Society of the Pacific Conference Series Vol. 476, New Trends in Radio Astronomy in the ALMA Era: The 30th Anniversary of Nobeyama Radio Observatory. p. 309
[253] Izumi T., et al., 2015, ApJ, 811, 39
[254] Izumi T., et al., 2016, ApJ, 818, 42

[255] Jackson N., Rampadarath H., Ofek E. O., Oguri M., Shin M.-S., 2012, MNRAS, 419, 2014

[256] Jarugula S., et al., 2019, ApJ, 880, 92

[257] Jarvis M. J., et al., 2010, MNRAS, 409, 92

[258] Jarvis M., et al., 2015, in Advancing Astrophysics with the Square Kilometre Array (AASKA14). p. 68 (`arXiv:1412.5753`)

[259] Jarvis M., et al., 2016, in MeerKAT Science: On the Pathway to the SKA. p. 6 (`arXiv:1709.01901`)

[260] Jin S., et al., 2019, ApJ, 887, 144

[261] Jin S., et al., 2022, A&A, 665, A3

[262] Juneau S., Narayanan D. T., Moustakas J., Shirley Y. L., Bussmann R. S., Kennicutt R. C. J., Vanden Bout P. A., 2009, ApJ, 707, 1217

[263] Karim A., et al., 2011, ApJ, 730, 61

[264] Karim A., et al., 2013, MNRAS, 432, 2

[265] Katz N., Weinberg D. H., Hernquist L., 1996, ApJS, 105, 19

[266] Kauffmann G., White S. D. M., Guiderdoni B., 1993, MNRAS, 264, 201

[267] Kauffmann G., et al., 2003, MNRAS, 341, 33

[268] Kaviraj S., et al., 2017, MNRAS, 467, 4739

[269] Kellermann K. I., Condon J. J., Kimball A. E., Perley R. A., Ivezić Ž., 2016, ApJ, 831, 168

[270] Kenney J. D. P., van Gorkom J. H., Vollmer B., 2004, AJ, 127, 3361

[271] Kennicutt Robert C. J., 1998, ARA&A, 36, 189

[272] Kennicutt R. C., Evans N. J., 2012, ARA&A, 50, 531

[273] Kennicutt Robert C. J., et al., 2009, ApJ, 703, 1672

[274] Kewley L. J., Groves B., Kauffmann G., Heckman T., 2006, MNRAS, 372, 961

[275] Khandai N., Di Matteo T., Croft R., Wilkins S., Feng Y., Tucker E., DeGraf C., Liu M.-S., 2015, MNRAS, 450, 1349

[276] Kimball A. E., Ivezić Ž., 2008, AJ, 136, 684

[277] Kimball A. E., Ivezić Ž., Wiita P. J., Schneider D. P., 2011, AJ, 141, 182

[278] Kirkpatrick A., Sharon C., Keller E., Pope A., 2019, ApJ, 879, 41

[279] Klypin A. A., Trujillo-Gomez S., Primack J., 2011, ApJ, 740, 102

[280] Kocevski D. D., et al., 2017, ApJ, 846, 112

[281] Kochanek C. S., Falco E. E., Impey C. D., Lehaár J., McLeod B. A., Rix H.-W., 1999, The 9th astrophysics conference: After the dark ages, when galaxies were young (the Universe at 2<Z<5),

[282] Kohno K., 2005, in Hüttmeister S., Manthey E., Bomans D., Weis K., eds, American Institute of Physics Conference Series Vol. 783, The Evolution of Starbursts. pp 203–208 (`arXiv:astro-ph/0508420`), doi:10.1063/1.2034987

[283] Kormann R., Schneider P., Bartelmann M., 1994, A&A, 284, 285

[284] Kormendy J., Bender R., 2009, ApJL, 691, L142

[285] Kormendy J., Ho L. C., 2013, ARA&A, 51, 511

[286] Kormendy J., Richstone D., 1995, ARA&A, 33, 581

[287] Krips M., Neri R., García-Burillo S., Martín S., Combes F., Graciá-Carpio J., Eckart A., 2008, ApJ, 677, 262

[288] Kroupa P., 2002, Science, 295, 82

[289] Kuijken K., et al., 2019, A&A, 625, A2

[290] Labbé I., et al., 2023, Nat, 616, 266
[291] Lacey C., Cole S., 1993, MNRAS, 262, 627
[292] Lacey C. G., et al., 2016, MNRAS, 462, 3854
[293] Lacki B. C., Thompson T. A., 2010, ApJ, 717, 196–208
[294] Lagache G., Cousin M., Chatzikos M., 2018, A&A, 609, A130
[295] Lagos C. d. P., Tobar R. J., Robotham A. S. G., Obreschkow D., Mitchell P. D., Power C., Elahi P. J., 2018, MNRAS, 481, 3573
[296] Lamarche C., et al., 2018, ApJ, 867, 140
[297] Lapi A., Shankar F., Mao J., Granato G. L., Silva L., De Zotti G., Danese L., 2006, ApJ, 650, 42
[298] Lapi A., et al., 2011, ApJ, 742, 24
[299] Lapi A., Negrello M., González-Nuevo J., Cai Z. Y., De Zotti G., Danese L., 2012, ApJ, 755, 46
[300] Lapi A., Raimundo S., Aversa R., Cai Z. Y., Negrello M., Celotti A., De Zotti G., Danese L., 2014, ApJ, 782, 69
[301] Lapi A., et al., 2018, Astrophys. J. 857 (2018), 22
[302] Lapi A., Pantoni L., Boco L., Danese L., 2020, ApJ, 897, 81
[303] Lauer T. R., et al., 2007, ApJ, 664, 226
[304] Lawrence C. R., Bennett C. L., Hewitt J. N., Langston G. I., Klotz S. E., Burke B. F., Turner K. C., 1986, ApJS, 61, 105
[305] Lawrence A., et al., 2007, MNRAS, 379, 1599
[306] Le Floc'h E., et al., 2005, ApJ, 632, 169
[307] Lewis A., 2019, GetDist: MCMC sample analysis, plotting and debugging tools, doi:10.5281/zenodo.3376730
[308] Lilly S. J., Le Fevre O., Hammer F., Crampton D., 1996, ApJL, 460, L1
[309] Lilly S. J., Carollo C. M., Pipino A., Renzini A., Peng Y., 2013, ApJ, 772, 119
[310] Lin J.-M., 2018, Journal of Imaging, 4
[311] Liu L., et al., 2017, ApJ, 846, 5
[312] Luhman M. L., Satyapal S., Fischer J., Wolfire M. G., Sturm E., Dudley C. C., Lutz D., Genzel R., 2003, ApJ, 594, 758
[313] Ma B., et al., 2015, ApJ, 814, 17
[314] Madau P., Dickinson M., 2014, ARA&A, 52, 415
[315] Maddox S. J., et al., 2017, ApJ, 236, 30
[316] Magdis G. E., et al., 2012, ApJ, 760, 6
[317] Magnelli B., et al., 2015, A&A, 573, A45
[318] Magnelli B., et al., 2019, ApJ, 877, 45
[319] Maiolino R., Mannucci F., 2019, A&A Rev., 27, 3
[320] Maloney P. R., Hollenbach D. J., Tielens A. G. G. M., 1996, ApJ, 466, 561
[321] Mancini M., Schneider R., Graziani L., Valiante R., Dayal P., Maio U., Ciardi B., Hunt L. K., 2015, MNRAS, 451, L70
[322] Mancuso C., et al., 2015, ApJ, 810, 72
[323] Mancuso C., Lapi A., Shi J., Gonzalez-Nuevo J., Aversa R., Danese L., 2016a, ApJ, 823, 128
[324] Mancuso C., Lapi A., Shi J., Cai Z. Y., Gonzalez-Nuevo J., Béthermin M., Danese L., 2016b, ApJ, 833, 152
[325] Mancuso C., et al., 2017, ApJ, 842, 95

[326] Marconi A., Hunt L. K., 2003, ApJL, 589, L21

[327] Marconi A., Risaliti G., Gilli R., Hunt L. K., Maiolino R., Salvati M., 2004. pp 49–52 (`arXiv:astro-ph/0409542`), doi:10.1017/S1743921304001437

[328] Maresca J., et al., 2022, MNRAS,

[329] Marrone D. P., et al., 2018, Nat, 553, 51

[330] Martín S., et al., 2015, A&A, 573, A116

[331] Massardi M., et al., 2017, A&A, 610, A53

[332] Matteucci F., Greggio L., 1986, A&A, 154, 279

[333] McAlpine S., et al., 2016, Astronomy and Computing, 15, 72

[334] McAlpine S., et al., 2019, MNRAS, 488, 2440

[335] McConnell N. J., Ma C.-P., 2013, ApJ, 764, 184

[336] McKinnon R., Torrey P., Vogelsberger M., Hayward C. C., Marinacci F., 2017, MNRAS, 468, 1505

[337] McKinnon R., Vogelsberger M., Torrey P., Marinacci F., Kannan R., 2018, MNRAS, 478, 2851

[338] McLeod D. J., McLure R. J., Dunlop J. S., 2016, MNRAS, 459, 3812

[339] McLure R. J., Dunlop J. S., 2004, MNRAS, 352, 1390

[340] McMullin J. P., Waters B., Schiebel D., Young W., Golap K., 2007, in Shaw R. A., Hill F., Bell D. J., eds, Astronomical Society of the Pacific Conference Series Vol. 376, Astronomical Data Analysis Software and Systems XVI. p. 127

[341] Meijerink R., Spaans M., 2005, A&A, 436, 397

[342] Messias H., et al., 2014, A&A, 568, A92

[343] Messias H., et al., 2019, MNRAS, 486, 2366

[344] Mignano A., Prandoni I., Gregorini L., Parma P., de Ruiter H. R., Wieringa M. H., Vettolani G., Ekers R. D., 2008, A&A, 477, 459

[345] Mocanu L. M., et al., 2013, ApJ, 779, 61

[346] Mollá M., Cavichia O., Gavilán M., Gibson B. K., 2015, MNRAS, 451, 3693

[347] Molnár D. C., et al., 2021, MNRAS, 504, 118

[348] Molnár D. C., et al., 2017, MNRAS, 475, 827–838

[349] More A., Cabanac R., More S., Alard C., Limousin M., Kneib J. P., Gavazzi R., Motta V., 2012, ApJ, 749, 38

[350] More A., et al., 2016a, MNRAS, 455, 1191

[351] More A., et al., 2016b, MNRAS, 456, 1595

[352] Morishita T., Stiavelli M., 2023, ApJL, 946, L35

[353] Muñoz J. A., Kochanek C. S., Keeton C. R., 2001, ApJ, 558, 657

[354] Mullaney J. R., et al., 2012, ApJL, 753, L30

[355] Muller S., Jaswanth S., Horellou C., Martí-Vidal I., 2020, A&A, 641, L2

[356] Munoz J. A., Falco E. E., Kochanek C. S., Lehar J., McLeod B. A., Impey C. D., Rix H. W., Peng C. Y., 1999, Ap&SS

[357] Murphy E. J., 2009, ApJ, 706, 482

[358] Murphy E. J., 2019, Proceedings of the International Astronomical Union, 15, 177–186

[359] Murphy E. J., et al., 2011, ApJ, 737, 67

[360] Naab T., Ostriker J. P., 2017, ARA&A, 55, 59

[361] Naidu R. P., et al., 2022, ApJL, 940, L14

[362] Narayanan D., et al., 2015, Nat, 525, 496

[363] Navarro J. F., Steinmetz M., 2000, ApJ, 538, 477
[364] Navarro J. F., Frenk C. S., White S. D. M., 1996, ApJ, 462, 563
[365] Nayyeri H., et al., 2016, ApJ, 823, 17
[366] Nayyeri H., et al., 2017, ApJ, 844, 82
[367] Negrello M., Perrotta F., González-Nuevo J., Silva L., de Zotti G., Granato G. L., Baccigalupi C., Danese L., 2007, MNRAS, 377, 1557
[368] Negrello M., et al., 2010, Science, 330, 800
[369] Negrello M., et al., 2014, MNRAS, 440, 1999
[370] Negrello M., et al., 2017, MNRAS, 465, 3558
[371] Nelson E. J., et al., 2019, ApJ, 870, 130
[372] Neri R., et al., 2020, A&A, 635, A7
[373] Nightingale J. W., Dye S., 2015, MNRAS, 452, 2940
[374] Nightingale J. W., Dye S., Massey R. J., 2018, MNRAS, 478, 4738
[375] Nightingale J., Hayes R., Griffiths M., 2021a, The Journal of Open Source Software, 6, 2550
[376] Nightingale J., et al., 2021b, The Journal of Open Source Software, 6, 2825
[377] Noeske K. G., et al., 2007, ApJL, 660, L43
[378] Norris R. P., 2017, Nature Astronomy, 1, 671
[379] Norris R. P., et al., 2011, Publ. Astron. Soc. Aust, 28, 215
[380] Norris R. P., et al., 2013, Publ. Astron. Soc. Aust, 30, e020
[381] Norris R. P., et al., 2021, Publ. Astron. Soc. Aust, 38, e046
[382] Novak M., et al., 2017, A&A, 602, A5
[383] Ocran E. F., Taylor A. R., Vaccari M., Ishwara-Chandra C. H., Prandoni I., Prescott M., Mancuso C., 2020, MNRAS, 491, 5911
[384] Oesch P. A., Bouwens R. J., Illingworth G. D., Labbé I., Stefanon M., 2018, ApJ, 855, 105
[385] Oguri M., et al., 2006, AJ, 132, 999
[386] Oliver S. J., et al., 2012, MNRAS, 424, 1614
[387] Omont A., et al., 2013, A&A, 551, A115
[388] Oteo I., Zwaan M. A., Ivison R. J., Smail I., Biggs A. D., 2016, ApJ, 822, 36
[389] Oteo I., et al., 2017, ApJ, 850, 170
[390] Padovani P., Miller N., Kellermann K. I., Mainieri V., Rosati P., Tozzi P., 2011, ApJ, 740, 20
[391] Padovani P., Bonzini M., Kellermann K. I., Miller N., Mainieri V., Tozzi P., 2015, MNRAS, 452, 1263
[392] Page M. J., et al., 2012, Nat, 485, 213
[393] Pagel B. E. J., Patchett B. E., 1975, MNRAS, 172, 13
[394] Pallottini A., Ferrara A., Gallerani S., Vallini L., Maiolino R., Salvadori S., 2017, MNRAS, 465, 2540
[395] Pantoni L., Lapi A., Massardi M., Goswami S., Danese L., 2019, ApJ, 880, 129
[396] Pantoni L., et al., 2021, MNRAS, 507, 3998
[397] Paraficz D., et al., 2016, A&A, 592, A75
[398] Partnership A., et al., 2015, ApJL, 808, L4
[399] Peca A., et al., 2021, ApJ, 906, 90
[400] Peebles P. J. E., 1982, ApJL, 263, L1

[401] Peng Y.-j., et al., 2010, ApJ, 721, 193

[402] Pereira-Santaella M., et al., 2017, A&A, 601, L3

[403] Perrotta F., Baccigalupi C., Bartelmann M., De Zotti G., Granato G. L., 2002, MNRAS, 329, 445

[404] Perrotta F., et al., 2023, ApJ, 952, 90

[405] Pilbratt G. L., et al., 2010, A&A, 518, L1

[406] Pipino A., Lilly S. J., Carollo C. M., 2014, MNRAS, 441, 1444

[407] Polletta M., et al., 2007, ApJ, 663, 81

[408] Popping G., Somerville R. S., Galametz M., 2017, MNRAS, 471, 3152

[409] Porter L. A., Somerville R. S., Primack J. R., Croton D. J., Covington M. D., Graves G. J., Faber S. M., 2014, MNRAS, 445, 3092

[410] Prandoni I., Seymour N., 2015, in Advancing Astrophysics with the Square Kilometre Array (AASKA14). p. 67 (`arXiv:1412.6512`), doi:10.22323/1.215.0067

[411] Pratap P., Dickens J. E., Snell R. L., Miralles M. P., Bergin E. A., Irvine W. M., Schloerb F. P., 1997, ApJ, 486, 862

[412] Privon G. C., et al., 2020, ApJ, 893, 149

[413] Ragone-Figueroa C., Granato G. L., 2011, MNRAS, 414, 3690

[414] Rangwala N., et al., 2011, ApJ, 743, 94

[415] Ravasi M., Vasconcelos I., 2020, SoftwareX, 11, 100361

[416] Recchi S., Kroupa P., 2015, MNRAS, 446, 4168

[417] Rees M. J., Ostriker J. P., 1977, MNRAS, 179, 541

[418] Reuter C., et al., 2020, ApJ, 902, 78

[419] Richardson M. L. A., Scannapieco E., Devriendt J., Slyz A., Thacker R. J., Dubois Y., Wurster J., Silk J., 2016, ApJ, 825, 83

[420] Riechers D. A., Walter F., Carilli C. L., Weiss A., Bertoldi F., Menten K. M., Knudsen K. K., Cox P., 2006, ApJL, 645, L13

[421] Riechers D. A., et al., 2013, Nat, 496, 329

[422] Riechers D. A., et al., 2020, ApJ, 895, 81

[423] Rizzo F., Vegetti S., Powell D., Fraternali F., McKean J. P., Stacey H. R., White S. D. M., 2020, Nat, 584, 201

[424] Rizzo F., Vegetti S., Fraternali F., Stacey H. R., Powell D., 2021, MNRAS, 507, 3952

[425] Rizzo F., Kohandel M., Pallottini A., Zanella A., Ferrara A., Vallini L., Toft S., 2022, A&A, 667, A5

[426] Robertson B. E., 2022, ARA&A, 60, 121

[427] Rodighiero G., et al., 2010, A&A, 518, L25

[428] Rodighiero G., et al., 2011, ApJL, 739, L40

[429] Rodighiero G., et al., 2015, ApJL, 800, L10

[430] Rodighiero G., Bisigello L., Iani E., Marasco A., Grazian A., Sinigaglia F., Cassata P., Gruppioni C., 2023, MNRAS, 518, L19

[431] Rodríguez-Puebla A., Primack J. R., Behroozi P., Faber S. M., 2016, MNRAS, 455, 2592

[432] Romanowsky A. J., Fall S. M., 2012, ApJS, 203, 17

[433] Rowan-Robinson M., et al., 2016, MNRAS, 461, 1100

[434] Rujopakarn W., et al., 2016, ApJ, 833, 12

[435] Rybak M., McKean J. P., Vegetti S., Andreani P., White S. D. M., 2015a, MNRAS, 451, L40

[436] Rybak M., Vegetti S., McKean J. P., Andreani P., White S. D. M., 2015b, MNRAS, 453, L26

[437] Rybak M., et al., 2019, ApJ, 876, 112

[438] Rybak M., Hodge J. A., Vegetti S., van der Werf P., Andreani P., Graziani L., McKean J. P., 2020, MNRAS, 494, 5542

[439] Sakamoto K., Aalto S., Evans A. S., Wiedner M. C., Wilner D. J., 2010, ApJL, 725, L228

[440] Salpeter E. E., 1955, ApJ, 121, 161

[441] Sani E., et al., 2012, MNRAS, 424, 1963

[442] Sargent M. T., et al., 2010, ApJL, 714, L190

[443] Sault R. J., Teuben P. J., Wright M. C. H., 1995, in Shaw R. A., Payne H. E., Hayes J. J. E., eds, Astronomical Society of the Pacific Conference Series Vol. 77, Astronomical Data Analysis Software and Systems IV. p. 433 (`arXiv:astro-ph/0612759`)

[444] Scannapieco C., et al., 2012, MNRAS, 423, 1726

[445] Schaye J., et al., 2015, MNRAS, 446, 521

[446] Schiminovich D., et al., 2005, ApJL, 619, L47

[447] Schleicher D. R. G., Beck R., 2016, A&A, 593, A77

[448] Schleicher D. R. G., Spaans M., Klessen R. S., 2010, A&A, 513, A7

[449] Schmidt M., 1963, ApJ, 137, 758

[450] Schöier F. L., van der Tak F. F. S., van Dishoeck E. F., Black J. H., 2005, A&A, 432, 369

[451] Scott K. S., et al., 2008, MNRAS, 385, 2225

[452] Scoville N., et al., 2016, ApJ, 820, 83

[453] Scoville N., et al., 2017a, ApJ, 836, 66

[454] Scoville N., et al., 2017b, ApJ, 837, 150

[455] Sedov L. I., 1959, Similarity and Dimensional Methods in Mechanics

[456] Seymour N., et al., 2008, MNRAS, 386, 1695

[457] Shankar F., Weinberg D. H., Miralda-Escudé J., 2009, ApJ, 690, 20

[458] Shen S., Mo H. J., White S. D. M., Blanton M. R., Kauffmann G., Voges W., Brinkmann J., Csabai I., 2003, MNRAS, 343, 978

[459] Shi J., Lapi A., Mancuso C., Wang H., Danese L., 2017, ApJ, 843, 105

[460] Shu Y., et al., 2015, ApJ, 803, 71

[461] Shu Y., et al., 2016, ApJ, 824, 86

[462] Silk J., 1977, ApJ, 211, 638

[463] Silva L., Granato G. L., Bressan A., Danese L., 1998, ApJ, 509, 103

[464] Silverman J. D., et al., 2009, ApJ, 696, 396

[465] Silverman J. D., et al., 2019, ApJL, 887, L5

[466] Simpson C., et al., 2006, MNRAS, 372, 741

[467] Simpson J. M., et al., 2014, ApJ, 788, 125

[468] Simpson J. M., et al., 2015, ApJ, 799, 81

[469] Simpson J. M., et al., 2017, ApJ, 839, 58

[470] Simpson J. M., et al., 2020, MNRAS, 495, 3409

[471] Smail I., Walter F., 2014, The Messenger, 157, 41

[472] Smail I., Ivison R. J., Blain A. W., 1997, ApJL, 490, L5
[473] Smith B., Sigurdsson S., Abel T., 2008, MNRAS, 385, 1443
[474] Smith D. J. B., et al., 2014, MNRAS, 445, 2232
[475] Smith J. D. T., et al., 2017, ApJ, 834, 5
[476] Smith D. J. B., et al., 2021, A&A, 648, A6
[477] Smolčić V., et al., 2008, ApJS, 177, 14
[478] Smolčić V., et al., 2017, A&A, 602, A6
[479] Snell R. L., Narayanan G., Yun M. S., Heyer M., Chung A., Irvine W. M., Erickson N. R., Liu G., 2011, AJ, 141, 38
[480] Soifer B. T., Neugebauer G., Matthews K., Becklin E. E., Ressler M., Werner M. W., Weinberger A. J., Egami E., 1999, ApJ, 513, 207
[481] Solomon P. M., Barrett J. W., 1991. p. 235
[482] Solomon P. M., Downes D., Radford S. J. E., Barrett J. W., 1997, ApJ, 478, 144
[483] Somerville R. S., Davé R., 2015, ARA&A, 53, 51
[484] Sopp H. M., Alexander P., 1991, MNRAS, 251, 14P
[485] Speagle J. S., 2020, MNRAS, 493, 3132
[486] Speagle J. S., Steinhardt C. L., Capak P. L., Silverman J. D., Elvis M., Feldstein B. S., SPLASH 2014, in American Astronomical Society Meeting Abstracts #223. p. 246.44
[487] Spilker J. S., et al., 2016, ApJ, 826, 112
[488] Spitoni E., Vincenzo F., Matteucci F., 2017, A&A, 599, A6
[489] Springel V., 2005, MNRAS, 364, 1105
[490] Springel V., et al., 2008, MNRAS, 391, 1685
[491] Springel V., et al., 2018, MNRAS, 475, 676
[492] Stacey G. J., Hailey-Dunsheath S., Ferkinhoff C., Nikola T., Parshley S. C., Benford D. J., Staguhn J. G., Fiolet N., 2010, ApJ, 724, 957
[493] Stacey H. R., et al., 2018, MNRAS, 476, 5075–5114
[494] Stacey H. R., et al., 2019, A&A, 622, A18
[495] Stacey H. R., et al., 2021, MNRAS, 500, 3667
[496] Stadel J., Potter D., Moore B., Diemand J., Madau P., Zemp M., Kuhlen M., Quilis V., 2009, MNRAS, 398, L21
[497] Stanley F., Harrison C. M., Alexander D. M., Swinbank A. M., Aird J. A., Del Moro A., Hickox R. C., Mullaney J. R., 2015, MNRAS, 453, 591
[498] Stanley F., et al., 2017, MNRAS, 472, 2221
[499] Stern D., et al., 2012, ApJ, 753, 30
[500] Sutherland R. S., Dopita M. A., 1993, ApJS, 88, 253
[501] Swinbank A. M., et al., 2010, Nat, 464, 733
[502] Swinbank A. M., et al., 2015, ApJL, 806, L17
[503] Tabatabaei F. S., et al., 2016, ApJ, 836, 185
[504] Tacchella S., Bose S., Conroy C., Eisenstein D. J., Johnson B. D., 2018, ApJ, 868, 92
[505] Tacconi L. J., Genzel R., Sternberg A., 2020, ARA&A, 58, 157
[506] Tadaki K.-i., et al., 2015, ApJL, 811, L3
[507] Tadaki K.-i., et al., 2017a, ApJ, 834, 135
[508] Tadaki K.-i., et al., 2017b, ApJL, 841, L25
[509] Talbot Raymond J. J., Arnett W. D., 1971, ApJ, 170, 409

[510] Talia M., et al., 2018, MNRAS, 476, 3956
[511] Talia M., Cimatti A., Giulietti M., Zamorani G., Bethermin M., Faisst A., Le Fèvre O., Smolçić V., 2021, ApJ, 909, 23
[512] Tamura Y., Oguri M., Iono D., Hatsukade B., Matsuda Y., Hayashi M., 2015, PASJ, 67, 72
[513] Thompson T. A., Quataert E., Murray N., 2005, ApJ, 630, 167
[514] Thomson A. P., et al., 2014, MNRAS, 442, 577
[515] Timmons N., et al., 2015, ApJ, 805, 140
[516] Tinker J., Kravtsov A. V., Klypin A., Abazajian K., Warren M., Yepes G., Gottlöber S., Holz D. E., 2008, ApJ, 688, 709
[517] Tinsley B. M., 1974, ApJ, 192, 629
[518] Toft S., et al., 2014, ApJ, 782, 68
[519] Toft S., et al., 2017, Nat, 546, 510
[520] Toomre A., 1964, ApJ, 139, 1217
[521] Torrey P., et al., 2019, MNRAS, 484, 5587
[522] Tremaine S., et al., 2002, ApJ, 574, 740
[523] Treu T., 2010, ARA&A, 48, 87
[524] Tyson J. A., Valdes F., Wenk R. A., 1990, ApJL, 349, L1
[525] Übler H., et al., 2017, ApJ, 842, 121
[526] Urquhart S. A., et al., 2022, MNRAS, 511, 3017
[527] Valentino F., et al., 2020, A&A, 641, A155
[528] Valiante R., Schneider R., Bianchi S., Andersen A. C., 2009, MNRAS, 397, 1661
[529] Valiante E., et al., 2016, MNRAS, 462, 3146
[530] Vallini L., Pallottini A., Ferrara A., Gallerani S., Sobacchi E., Behrens C., 2018, MNRAS, 473, 271
[531] Valtchanov I., et al., 2011, MNRAS, 415, 3473
[532] Vega O., Clemens M. S., Bressan A., Granato G. L., Silva L., Panuzzo P., 2008, A&A, 484, 631
[533] Vegetti S., Koopmans L. V. E., 2009, MNRAS, 400, 1583
[534] Vieira J. D., et al., 2010, ApJ, 719, 763
[535] Vieira J. D., et al., 2013, Nat, 495, 344
[536] Viero M. P., et al., 2014, ApJS, 210, 22
[537] Vika M., Driver S. P., Graham A. W., Liske J., 2009, MNRAS, 400, 1451
[538] Vincenzo F., Matteucci F., Spitoni E., 2017, MNRAS, 466, 2939
[539] Vishwas A., et al., 2018, ApJ, 856, 174
[540] Vito F., et al., 2018, MNRAS, 473, 2378
[541] Voelk H. J., 1989, A&A, 218, 67
[542] Vogelsberger M., et al., 2014, Nat, 509, 177
[543] Walter F., et al., 2016, ApJ, 833, 67
[544] Wang T., et al., 2016, ApJ, 816, 84
[545] Wang T., et al., 2019a, Nat, 572, 211
[546] Wang L., et al., 2019b, A&A, 631, A109
[547] Ward B. A., et al., 2022, MNRAS, 510, 2261
[548] Wardlow J. L., et al., 2013, ApJ, 762, 59
[549] Warren S. J., Dye S., 2003, ApJ, 590, 673

[550] Washinoue H., Suzuki T. K., 2023, ApJ, 953, 74
[551] Weinberg D. H., Andrews B. H., Freudenburg J., 2017, ApJ, 837, 183
[552] Weiß A., et al., 2010, A&A, 521, L1
[553] Weiß A., et al., 2013, ApJ, 767, 88
[554] White S. D. M., Frenk C. S., 1991, ApJ, 379, 52
[555] White S. D. M., Rees M. J., 1978a, MNRAS, 183, 341
[556] White S. D. M., Rees M. J., 1978b, MNRAS, 183, 341
[557] White S. V., Jarvis M. J., Häußler B., Maddox N., 2015, MNRAS, 448, 2665
[558] White S. V., Jarvis M. J., Kalfountzou E., Hardcastle M. J., Verma A., Cao Orjales J. M., Stevens J., 2017, MNRAS, 468, 217
[559] Williams C. C., et al., 2019, ApJ, 884, 154
[560] Wong K. C., Suyu S. H., Matsushita S., 2015, ApJ, 811, 115
[561] Wong K. C., Ishida T., Tamura Y., Suyu S. H., Oguri M., Matsushita S., 2017, ApJ, 843, L35
[562] Wright E. L., et al., 2010, AJ, 140, 1868
[563] Yan H., Ma Z., 2016, ApJL, 820, L16
[564] Yan H., Ma Z., Ling C., Cheng C., Huang J.-S., 2023, ApJL, 942, L9
[565] Yang C., Gao Y., Omont A., Liu D., Isaak K. G., Downes D., van der Werf P. P., Lu N., 2013, ApJL, 771, L24
[566] Yang C., et al., 2016, A&A, 595, A80
[567] Yang C., et al., 2017, A&A, 608, A144
[568] Yang C., González-Alfonso E., Omont A., Pereira-Santaella M., Fischer J., Beelen A., Gavazzi R., 2020, A&A, 634, L3
[569] York D. G., et al., 2000, AJ, 120, 1579
[570] Yun M. S., Reddy N. A., Condon J. J., 2001, ApJ, 554, 803
[571] Zanella A., et al., 2018, MNRAS, 481, 1976
[572] Zhukovska S., Gail H. P., Trieloff M., 2008, A&A, 479, 453
[573] Zhukovska S., Dobbs C., Jenkins E. B., Klessen R. S., 2016, ApJ, 831, 147
[574] da Cunha E., Charlot S., Elbaz D., 2008, MNRAS, 388, 1595
[575] de Jong J. T. A., et al., 2013, The Messenger, 154, 44
[576] van Dishoeck E. F., et al., 2021, A&A, 648, A24
[577] van Dokkum P. G., et al., 2015, ApJ, 813, 23
[578] van Haarlem, M. P. et al., 2013, A&A, 556, A2
[579] van de Sande J., et al., 2013, ApJ, 771, 85
[580] van der Wel A., van der Marel R. P., 2008, ApJ, 684, 260
[581] van der Wel A., et al., 2014, ApJ, 788, 28
[582] van der Werf P. P., et al., 2011, ApJL, 741, L38